

**IN-SITU DETERMINATION OF THE THERMO-PHYSICAL PROPERTIES OF  
NANO-PARTICULATE LAYERS DEVELOPED IN ENGINE EXHAUST GAS  
HEAT EXCHANGERS AND OPPORTUNITES FOR HEAT EXCHANGER  
EFFECTIVENESS RECOVERY**

**by**

**Ashwin Ashok Salvi**

A dissertation submitted in partial fulfillment  
of the requirements for the degree of  
Doctor of Philosophy  
(Mechanical Engineering)  
in The University of Michigan  
2013

Doctoral Committee:

Dionissios N. Assanis, Co-Chair  
Professor Claus Borgnakke, Co-Chair  
Associate Research Scientist John W. Hoard, Co-Chair  
Professor Arvind Atreya  
Professor John W. Barker  
Daniel J. Styles, Ford Motor Company

© Ashwin Ashok Salvi 2013  
All Rights Reserved

To my parents Dr. Ashok Salvi and Dr. Usha Salvi

## ACKNOWLEDGMENTS

I would like to start off by acknowledging my advisors Dr. Dennis Assanis and John Hoard. Dr. Assanis, you inspired me to pursue my graduate studies in the Walter E. Lay Automotive laboratory after taking your Internal Combustion Engines course. You have always supported me from the beginning of my Master's and all the way throughout my Ph.D. Your enthusiasm and passion for science is truly contagious and your desire to see your students succeed has kept me going throughout my graduate career. Thank you for everything. John, your mentorship and advice has been invaluable to me. I have thoroughly enjoyed our scientific and worldly conversations and admire not only your curiosity for all things research, but also philosophical. Thank you for giving me the opportunity to work with and learn from you.

A sincere thank you to my committee members: Dan Styles, Dr. Claus Borgnakke, Dr. John Barker, and Dr. Arvind Atreya. Dan, thank you for giving me the opportunity to contribute to Ford research. Your ability to assimilate and distill information makes you a great leader and your thoughts and advice on this project have been instrumental to its success. Thank you for all the financial and more importantly intellectual support from Ford Motor Company. Dr. Borgnakke, thank you for all of the conversations related to my research and to the field of science in general. It has been a pleasure exchanging ideas and information with you and partaking in numerous lab tours with you. Dr. Barker, thank you for joining my committee. Thank you for opening my eyes to the world of atmospheric chemistry. AOSS 578 still ranks amongst the top of my all-time favorite classes. Dr. Atreya, thank you for teaching me about advanced heat

transfer. It was a subject that was very helpful in my research and helped me to make sense of my work.

Thank you to Scott Sluder, Michael Lance, and John Storey from Oak Ridge National labs for their thoughts and advice. Thank you Dr. Lance for performing thermogravimetric analysis on our deposit samples.

There are far too many people that I am grateful for. Dr. Mehdi Abarham, thank you so much for all of your help. My research truly would not have been possible without you. Mitchell Bieniek, Kevin Collao, Theerapat Yangyuenthanasan, Pavan Jagarlapudi, Rajagopal Jayaraman – thank you for all your help in the lab. You are all truly exceptional students. Dr. Rajit Johri and Dr. Fernando Tavares, thank you guys for all the support throughout these years and for all the great conversations. Dr. Mark Hoffman, I enjoyed all of our scientific and non-scientific conversations alike. Dr. Josh Lacey, Dr. Anne Marie Lewis, Dr. Ben Lawler, Luke Hagen, Dr. Michael Mosburger, Dr. Michael Cundy, Jerry Fuschetto, Kevin Zaseck, Louise Lu, Dr. Brian Peterson, Dr. Karl Zelik, Dr. Jonathan Hagen, Dr. Bruno Vanzieleghem, Dr. Tulga Ersal, William Lim, Melissa McGeorge, Kathie Wolney, Laurie Stoianowski, Kent Pruss, Bill Kirkpatrick, and everybody else in the autolab – thank you for making the past few years such a fond memory. I truly believe the students, former and current, make this lab one of the most unique, social, intellectual, and passionate labs on campus. Thanks for all the support and good times.

Thanks to all my family and friends for the years of unconditional support. Special thanks to Dr. Ajay Jetley, Andrea Callas, Dr. Amar Desai, and Dr. Keshav Deshpande for their friendship. Thanks especially to my parents, Dr. Ashok Salvi and Dr. Usha Salvi, who have always been there for me. I am incredibly fortunate to have you in my life. You guys are my inspiration, role models, moral compass, and foundation. Thank you for all your sacrifice. I would not be the person I am today without you.

Always and forever GO BLUE!

## TABLE OF CONTENTS

<b>DEDICATION.....</b>	<b>ii</b>
<b>ACKNOWLEDGMENTS .....</b>	<b>iii</b>
<b>LIST OF FIGURES .....</b>	<b>x</b>
<b>LIST OF TABLES .....</b>	<b>xxi</b>
<b>LIST OF ABBREVIATIONS .....</b>	<b>xxii</b>
<b>ABSTRACT.....</b>	<b>xxiv</b>
<b>CHAPTER 1 INTRODUCTION.....</b>	<b>1</b>
1.1 EGR Cooler Fouling.....	2
1.2 Deposits .....	12
1.2.1 What are deposits.....	12
1.2.2 Properties of deposits.....	17
1.3 Deposition mechanisms.....	24
1.4 Stabilization and recovery .....	26
1.5 Models .....	31
1.6 References .....	38
<b>CHAPTER 2 MEASUREMENT PRINCIPLE AND EXPERIMENTAL EQUIPMENT .....</b>	<b>42</b>
2.1 Measurement Principle.....	42
2.2 Experimental hardware.....	45
2.2.1 Visualization rig.....	45
2.2.2 Infrared camera .....	49
2.2.3 Infrared and optically transmissible window .....	53
2.2.4 Microscope.....	55
2.2.5 Heat flux probe .....	55

2.2.6 Diesel engine.....	57
2.2.7 Gaseous emissions analyzer.....	59
2.2.8 Particulate analyzers .....	61
2.3 References .....	64
<b>CHAPTER 3 EXPERIMENTAL IN-SITU METHODOLOGY .....</b>	<b>65</b>
3.1 Reflected temperature.....	65
3.2 Deposit layer emissivity .....	67
3.2.1 Isothermal experiment .....	68
3.3 Infrared window .....	70
3.3.1 Transmissivity.....	70
3.3.2 Infrared camera angle .....	73
3.4 Deposit layer transparency .....	75
3.5 References .....	82
<b>CHAPTER 4 DEPOSIT LAYER EVOLUTION ON STAINLESS STEEL SUBSTRATE.....</b>	<b>83</b>
4.1 Experimental conditions.....	83
4.1.1 Engine conditions.....	84
4.1.2 Exhaust gas composition.....	88
4.2 24-hour deposition experimental results .....	95
4.2.1 Deposit layer thickness .....	95
4.2.2 Deposit layer topography and surface area.....	97
4.2.3 Infrared surface temperature .....	104
4.3 Conclusions .....	110
4.4 References .....	112
<b>CHAPTER 5 IN-SITU DEPOSIT LAYER PROPERTIES.....</b>	<b>113</b>
5.1 24-hour deposition experimental results .....	113
5.1.1 Deposition.....	113

5.1.2 Deposit layer thickness .....	115
5.1.3 Deposit surface area .....	116
5.1.4 Deposit temperature .....	117
5.1.5 Heat flux.....	121
5.1.6 Thermal conductivity .....	123
5.1.7 Thermal resistance .....	129
5.2 Conclusions .....	130
5.3 References .....	133
<b>CHAPTER 6 EFFECT OF VOLATILES ON DEPOSIT LAYER PROPERTIES.....</b>	<b>134</b>
6.1 Volatile removal results.....	135
6.1.1 Deposit thickness and surface area .....	135
6.1.2 Thermal measurements .....	138
6.1.3 Heat flux.....	141
6.1.4 Deposit thermal conductivity.....	144
6.2 Addition of volatiles.....	149
6.2.1 Layer collapse .....	149
6.2.2 Heat flux analysis.....	153
6.2.3 Infrared surface temperature .....	154
6.3 Conclusions .....	157
6.4 References .....	160
<b>CHAPTER 7 REMOVAL MECHANISMS .....</b>	<b>161</b>
7.1 Experimental Setup .....	162
7.1.1 Visualization rig.....	162
7.1.2 Optical Equipment .....	164
7.2 Results .....	164
7.2.1 Downstream tee-junction solenoid .....	164



7.2.2 Upstream in-line solenoid.....	170
7.2.3 Condensation and flow transient.....	177
7.2.4 Angle of attack.....	180
7.3 Conclusions .....	182
7.4 Acknowledgements .....	183
7.5 References .....	184
<b>CHAPTER 8 UNCERTAINTY ANALYSIS .....</b>	<b>186</b>
8.1 Measurement uncertainty .....	186
8.1.1 Accuracy .....	186
8.1.2 Precision.....	191
8.1.3 Accuracy and precision uncertainty improvement .....	195
8.2 Experimental error reduction.....	196
8.2.1 Infrared camera .....	196
8.2.2 Optical microscope .....	200
8.2.3 Heat flux measurement .....	201
8.3 Conclusion.....	212
<b>CHAPTER 9 CONCLUSIONS, CONTRIBUTIONS, AND FUTURE WORK .....</b>	<b>214</b>
9.1 Summary of conclusions .....	214
9.1.1 In-situ measurement accuracy.....	214
9.1.2 Deposit conductivity with thickness .....	215
9.1.3 Deposit conductivity with surface temperature .....	216
9.1.4 Volatile influence on deposit conductivity .....	216
9.1.5 In-situ conductivity compared to previous results .....	217
9.1.6 Deposit surface area.....	217
9.1.7 Deposit porosity .....	217
9.1.8 Velocity based removal.....	218

9.2 Summary of contributions .....	218
9.3 Recommendations for future work.....	219
9.3.1 Porosity measurement.....	219
9.3.2 Impact of hydrocarbons on the thermal properties of deposit layers	220
9.3.3 Full factorial experiment.....	220
9.3.4 Longer term exposure .....	221
9.3.5 Reduced cross sectional area .....	221
9.3.6 Live deposition.....	222
9.3.7 In-situ thickness measurement.....	223
9.3.8 Flow geometry .....	224
9.3.9 Alternative fuels.....	224
<b>APPENDIX A .....</b>	<b>226</b>
A.1 MATLAB script for microscope image processing and surface area .....	226
A.2 Close up infrared lens.....	228
A.3 Heat flux conditions .....	228

## LIST OF FIGURES

Figure 1.1: Cross section of a fouled diesel EGR cooler [6] .....	2
Figure 1.2: EGR cooler effectiveness loss with time for ULSD, 5% biodiesel, and 20% biodiesel [7] .....	3
Figure 1.3: Deposit mass as a function of exhaust exposure time for ULSD, 5% biodiesel, and 20% biodiesel [7] .....	4
Figure 1.4: Increase in EGR outlet temperature for unfiltered (BASE) and filtered (DPF) exhaust gas [9] .....	4
Figure 1.5: Pressure drop across EGR cooler for unfiltered (BASE) and filtered (DPF) exhaust gas [9] .....	5
Figure 1.6: EGR cooler effectiveness for catalyzed and un-catalyzed exhaust gas [6] .....	6
Figure 1.7: Exhaust gas temperature post EGR cooler for catalyzed and un-catalyzed exhaust gas [5] .....	6
Figure 1.8: Effect of EGR coolant temperature on deposit mass gain [10] .....	8
Figure 1.9: Effect of flow rate on deposit mass gain as a function of coolant temperature [10] .....	8
Figure 1.10: Effect of inlet gas temperature on deposit mass [11] .....	10
Figure 1.11: Effect of inlet gas mass flow rate (effectively Reynolds number) on deposit mass [11] .....	10
Figure 1.12: Effect of inlet gas particulate concentration on deposit mass [11] .....	11
Figure 1.13: Effect of inlet gas pressure on deposit mass [11] .....	11
Figure 1.14: Effect of HC concentration on EGR cooler effectiveness loss and mass gain [12] .....	12

Figure 1.15: Hydrocarbon extraction from a Canadian market diesel fuel with ~400 ppm sulfur in a twin series EGR cooler configuration [6].....	14
Figure 1.16: Speciation of certification diesel fuel with 300 ppm sulfur [10].....	15
Figure 1.17: Hydrocarbon speciation of deposit layers found in heated, catalyzed, and cooled EGR tubes [10].....	16
Figure 1.18: Vapor pressure for select alkane species [10] .....	16
Figure 1.19: Volatile fraction of deposit mass for ULSD and 20% biodiesel [14] .....	17
Figure 1.20: Evolution of deposit thickness, deposit mass/area, and relative heat transfer coefficient versus time, adapted from [8] .....	18
Figure 1.21: Average effectiveness loss of ULSD, 5% biodiesel, and 20% biodiesel at 90, 65, and 40°C coolant temperature [7].....	19
Figure 1.22: Average differential pressure across tubes for ULSD, 5% biodiesel, and 20% biodiesel at 90, 65, and 40°C coolant temperatures [7] .....	19
Figure 1.23: Variation of combustion chamber deposit mass with manifold pressure at constant fuel/air ratio, adapted from [16] .....	20
Figure 1.24: Volatilization of deposit sample during Heating Run 1 [17] .....	21
Figure 1.25: Deposit density measurements of ULSD and 20% biodiesel with increasing exposure time [18] .....	23
Figure 1.26: Deposit density variation from wall to deposit surface [8] .....	24
Figure 1.27: Effect of low amplitude and high amplitude pressure waves on radial particle flow [8].....	26
Figure 1.28: Deposit thickness variation along tube length [24] .....	27
Figure 1.29: Deposit removal resulting from increasing gas velocity [26] .....	29
Figure 1.30: Comparison of removal mechanism in model to experimental data [12] ....	30
Figure 1.31: Numerical versus analytical prediction of pipe diameter [11] .....	33
Figure 1.32: Predicted and actual effectiveness versus time [29].....	34
Figure 1.33: PRCC values for parameters influencing deposit mass gain [29] .....	36

Figure 1.34: PRCC values of parameter influence on heat transfer reduction [29].....	36
Figure 1.35: Effect of porosity and surface temperature on deposit layer thermal conductivity [29].....	37
Figure 2.1: Schematic of heat conduction.....	43
Figure 2.2: Schematic of heat conduction through deposit layer with required measurements for thermal conductivity measurements.....	43
Figure 2.3: Schematic of heat conduction through deposit layer with required measurements and instruments.....	44
Figure 2.4: Visualization rig version 3 schematic.....	46
Figure 2.5: Schematic of test stand with exhaust flow through the test fixture [3].....	46
Figure 2.6: Visualization rig version 3 dimensioned drawing.....	48
Figure 2.7: Assembled and exploded views of visualization rig version 3.....	48
Figure 2.8: Molecular attenuation in the infrared spectrum[4].....	49
Figure 2.9: Total radiation received by infrared camera.....	51
Figure 2.10: Infrared window mounting.....	54
Figure 2.11: Heat flux probe installation schematic.....	56
Figure 2.12: Actual heat flux probe installation.....	56
Figure 2.13: 6.4L diesel engine.....	58
Figure 2.14: Thermal image of diesel engine highlighting exhaust gas flow path and on-board EGR cooler.....	59
Figure 2.15: AVL SESAM emissions analyzer.....	60
Figure 2.16: Combustion differential mobility spectrometer (DMS500).....	61
Figure 2.17: DMS500 classifier column schematic [5].....	62
Figure 2.18: AVL 415S variable smoke meter.....	63
Figure 3.1: Crumpled aluminum foil for reflection temperature.....	66
Figure 3.2: Aluminum foil experiment for infrared reflected temperature.....	66
Figure 3.3: Reflection temperature versus Reynolds number.....	67

Figure 3.4: Isothermal experiment schematic .....	68
Figure 3.5: Emissivity of deposit layer .....	69
Figure 3.6: Emissivity differences between deposit layer and stainless steel.....	70
Figure 3.7: Infrared image of deposit layer in absence of infrared window .....	71
Figure 3.8: Infrared image of deposit layer with one infrared window in line of sight....	72
Figure 3.9: Infrared image of deposit layer with two infrared windows in line of sight ..	72
Figure 3.10: ExaminIR object parameters .....	73
Figure 3.11: Infrared camera angle schematic .....	74
Figure 3.12: Infrared window transmissivity as a function of infrared camera angle for a two-window setup.....	75
Figure 3.13: Transparency of deposit layer compared to powdered charcoal .....	76
Figure 3.14: Evolution of deposit layer transparency with increasing layer thickness ....	77
Figure 3.15: Schematic of reflection through thin deposit layer .....	77
Figure 3.16: Experimental evidence of reflection through deposit layer but not on contact thermocouple.....	78
Figure 3.17: Schematic of reflection coating [1] .....	79
Figure 3.18: Effect of coating properties on substrate reflection [1].....	79
Figure 3.19: Evolution of reflection with increasing deposition .....	80
Figure 3.20: High emissivity paint applied across channel width in addition to a small strip of RTV along channel length.....	80
Figure 3.21: Infrared image of transmission of high emissivity paint through 60 micron thick deposit layer .....	81
Figure 3.22: Infrared image of negligible transmission of high emissivity paint through 140 micron thick deposit layer.....	81
Figure 4.1: Fueling quantity at conventional and post-injection conditions.....	85
Figure 4.2: A/F ratio for conventional and post-injection engine conditions.....	86

Figure 4.3: Rate of heat release during combustion for the conventional and post-injection engine condition.....	87
Figure 4.4: Cumulative heat release for the conventional and post-injection engine condition .....	87
Figure 4.5: Emissions levels for H <sub>2</sub> O, CO <sub>2</sub> , O <sub>2</sub> , EGR rate, and CO <sub>2</sub> EGR for conventional, post-injection, and idle engine conditions.....	90
Figure 4.6: Emissions levels for NO <sub>x</sub> , CO, and THC for conventional, post-injection, and idle engine conditions .....	90
Figure 4.7: NO <sub>x</sub> break-up for conventional, post-injection, and idle engine conditions..	91
Figure 4.8: Lambda values measured from the SESAM for conventional and post-injection conditions.....	91
Figure 4.9: Filter smoke number for conventional and post-injection conditions.....	92
Figure 4.10: Diluter schematic, courtesy of Joe Szente, Ford Motor Company.....	93
Figure 4.11: DMS particle profiles upstream and downstream of visualization rig.....	94
Figure 4.12: Count median diameter size for upstream and downstream rig locations, as measured by the DMS.....	94
Figure 4.13: 24 hour deposit thickness evolution on stainless steel substrate .....	95
Figure 4.14: Schematic of radiative layer heating in large and small cross sectional areas .....	96
Figure 4.15: Model prediction of deposit thickness for 22 mm and 6 mm wide channels	97
Figure 4.16: Topographical features on the deposit layer.....	99
Figure 4.17: Average surface area ratio with increasing deposit layer thickness.....	99
Figure 4.18: Model results for the impact of 100% compared to 120% surface area ratio on gas temperature for a 483 micron thick layer .....	102
Figure 4.19: Effect of surface area ratio on heat exchanger effectiveness for varying thicknesses .....	103

Figure 4.20: Percent increase in heat exchanger effectiveness as a function of surface area ratio for varying thicknesses .....	104
Figure 4.21: Infrared surface temperature evolution with deposit thickness for Point 6	106
Figure 4.22: Interface deposit surface temperature as a function of varying Reynolds number for constant deposit thickness.....	107
Figure 4.23: Interface deposit surface temperature evolution with layer thickness for constant Reynolds number.....	108
Figure 4.24: 1-D model estimates of surface temperature (both y-axes) for constant Reynolds number, varying thickness (solid lines without markers, corresponding to bottom x-axis) and constant thickness, varying Reynolds number (dashed lines with solid markers, corresponding to the top x-axis).....	108
Figure 4.25: Calculated deposit conductivity as a function of temperature and layer porosity [2].....	109
Figure 4.26: Close up of 3-hour deposit layer, 5.6 kg/hr at 202°C air flow rate .....	110
Figure 5.1: Heat flux probe temperatures during live deposition .....	114
Figure 5.2: Deposit layer growth on heat flux probe 1 and 2 with linear extrapolation.	116
Figure 5.3: Deposit surface area ratio for probes 1 and 2.....	117
Figure 5.4: Infrared surface temperature of deposit layers on heat flux probes 1 and 2	118
Figure 5.5: Infrared surface temperature versus deposit thickness.....	119
Figure 5.6: Temperature difference across deposit thickness as a function of Reynolds number .....	120
Figure 5.7: Temperature difference across deposit thickness as a function of deposit thickness.....	120
Figure 5.8: Heat flux for constant thickness and varying Reynolds number .....	122
Figure 5.9: Heat flux for fixed Reynolds number and varying thickness.....	122
Figure 5.10: Deposit conductivity for constant thickness as a function of Reynolds number .....	124



Figure 5.11: Estimated deposit conductivity as a function of porosity and temperature [1]	125
Figure 5.12: Estimated deposit thermal conductivity in air as a function of temperature and porosity	126
Figure 5.13: Probe 1 deposit conductivity as a function of probe 1 infrared surface temperature	127
Figure 5.14: Probe 2 deposit conductivity as a function of probe 2 infrared surface temperature	128
Figure 5.15: 18-hour layer conductivity for low surface temperature with estimated thermal conductivity at 98% porosity as a function of deposit surface temperature	128
Figure 5.16: Thermal resistance of deposit layer on heat flux probe 1	129
Figure 5.17: Thermal resistance of deposit layer on heat flux probe 2	130
Figure 6.1: 24hr pre-bake layer, 150x magnification	136
Figure 6.2: 24hr pre-bake layer, 250x magnification	136
Figure 6.3: 24hr bake-out layer, 150x magnification	137
Figure 6.4: 24hr bake-out layer, 250x magnification	137
Figure 6.5: Deposit surface temperature for 24hr pre-bake and post-bake layers on heat flux probe 1	139
Figure 6.6: Deposit surface temperature for 24hr pre-baked and post-bake layers on heat flux probe 2	139
Figure 6.7: Temperature across deposit layer thickness for 24hr pre-bake and post-bake layers on heat flux probe 1	140
Figure 6.8: Temperature across deposit layer thickness for 24hr pre-bake and post-bake layers on heat flux probe 2	141
Figure 6.9: Heat flux through 24hr pre-bake, bake 1, and bake 2 layers for heat flux probe 1	142

Figure 6.10: Heat flux through 24hr pre-bake, bake 1, and bake 2 layers for heat flux probe 2 .....	142
Figure 6.11: Deposit conductivity as a function of Reynolds number for heat flux probe 1 .....	145
Figure 6.12: Deposit conductivity as a function of Reynolds number for heat flux probe 2 .....	145
Figure 6.13: Estimated deposit conductivity as a function of porosity and temperature	146
Figure 6.14: Deposit conductivity as a function of deposit surface temperature on heat flux probe 1 .....	147
Figure 6.15: Deposit conductivity as a function of deposit surface temperature for heat flux probe 2 .....	147
Figure 6.16: TGA on 24hr pre-bake and post-bake layers.....	148
Figure 6.17: Time-lapse images of isopropyl alcohol addition to deposit layer on heat flux probe 2 (time interval is listed as min:sec.msec) .....	150
Figure 6.18: Image of deposit layer just after alcohol-induced collapse (time interval is listed as min:sec.msec).....	151
Figure 6.19: Image of contracted deposit layer (time interval is listed as min:sec.msec) .....	151
Figure 6.20: Image of a further contracted deposit layer and at the onset of mud-cracking (time interval is listed as min:sec.msec) .....	152
Figure 6.21: Image of contracted and mud-cracked deposit layer (time interval is listed as min:sec.msec).....	152
Figure 6.22: Heat flux measurements on heat flux probe 2 for pre- and post-IPA alcohol collapse .....	154
Figure 6.23: Frame-by-frame variations of surface temperature on 6-hour deposit layer. Imaged at 25 Hz .....	155

Figure 6.24: Frame-by-frame variations of surface temperature of 24-hour deposit layer. Imaged at 25 Hz .....	155
Figure 6.25: Frame-by-frame negligible variations in surface temperature on 30-hour collapsed layer. Imaged at 25 Hz .....	155
Figure 6.26: Porous flow diagram .....	157
Figure 7.1: Visualization rig version 2 cross-section schematic.....	162
Figure 7.2: Visualization rig version 2 image.....	163
Figure 7.3: Solenoid locations on visualization rig version 2.....	163
Figure 7.4: Qualitative analysis of deposit layer removal for condition 1 (high pressure, high flow) and condition 2 (low pressure, low flow) .....	165
Figure 7.5: Qualitative analysis of condition 2 compared to post-condition 2 with high pressure and low flow .....	166
Figure 7.6: Low pressure, high flow mild shear removal during flow-transient on a 3.5- hour layer (image colors converted to black and white).....	166
Figure 7.7: High pressure, low flow flow-transient layer shearing and particle bombardment .....	168
Figure 7.8: High-speed images of deposit shear.....	168
Figure 7.9: Schematic of flow-transient for high pressure, low flow condition.....	169
Figure 7.10: Flow-transients for upstream in-line solenoid valve; significant removal near inlet of channel.....	170
Figure 7.11: Zoomed-out and zoomed-in view at channel inlet of post-transient removal .....	171
Figure 7.12: 3-hour pre-transient layer with upstream, in-line solenoid .....	172
Figure 7.13: Optical surface images post-transient with upstream, in-line solenoid.....	173
Figure 7.14: Flow schematic of upstream, in-line solenoid transient flow event.....	174
Figure 7.15: High-speed images of deposit layer removal caused by upstream solenoid .....	174

Figure 7.16: Layer removal on a previously modified deposit layer with an upstream, in-line solenoid .....	176
Figure 7.17: Image of deposit surface after water condensation from exhaust gas .....	178
Figure 7.18: Water condensation plus flow-transient on a previously modified layer ...	179
Figure 7.19: Definition of angle of attack.....	180
Figure 7.20: Deposit surface spallation resulting from angled airflow .....	181
Figure 8.1: Total accuracy uncertainty as a function of Reynolds number at various thicknesses on heat flux probe 1 .....	188
Figure 8.2: Total accuracy uncertainty as a function of Reynolds number at various thicknesses on heat flux probe 2 .....	188
Figure 8.3: Thermal conductivity uncertainty breakdown for 109 micron thick deposit layer on heat flux probe 2 .....	190
Figure 8.4: Thermal conductivity uncertainty breakdown for 378 micron thick deposit layer on heat flux probe 2 .....	190
Figure 8.5: Thermal conductivity with maximum instrument uncertainty for 109, 279, and 378 micron thick deposit layers on heat flux probe 2.....	191
Figure 8.6: Precision of deposit interface temperature measurement on a 378 micron layer on heat flux probe 2 .....	192
Figure 8.7: Precision uncertainty for the 6-hour 109 micron, 18-hour 279 micron, and 24-hour 378 micron layers on heat flux probe 2 .....	194
Figure 8.8: Precision uncertainty for thermal conductivity as a function of deposit surface temperature for the 18-hour, 279 micron layer on heat flux probe 2.....	194
Figure 8.9: Thermal conductivity with precision uncertainty for the 24-hour bake-out layer on heat flux probe 2 .....	195
Figure 8.10: Interface temperature variation on a 378 micron thick layer using 5 second infrared video at 25 Hz .....	197

Figure 8.11: Variation of thermal conductivity due to temperature variations for the 378 micron thick layer on heat flux probe 2 .....	198
Figure 8.12: Interface temperature variation on a 109 micron thick layer using a 5 second infrared video at 25 Hz .....	199
Figure 8.13: Variation of thermal conductivity due to temperature variations for the 109 micron thick layer on heat flux probe 2 .....	200
Figure 8.14: Effect of side lighting compared to center lighting on a deposit layer.....	201
Figure 8.15: Schematic of surface mounted thermocouple .....	202
Figure 8.16: Experimental implementation of surface mounted thermocouple .....	204
Figure 8.17: Exhaust side stick-on and surface mounted thermocouple schematic .....	204
Figure 8.18: Exhaust side surface mounted, stick-on, and inlet temperature measurements .....	205
Figure 8.19: Surface mounted versus exposed tip thermocouple on coolant side .....	206
Figure 8.20: Calculated heat flux across a 1mm thick stainless steel substrate with a thermal conductivity of 14.6 W/mK and using the surface mounted thermocouple temperatures .....	207
Figure 8.21: Thermal resistance schematic.....	209
Figure 8.22: Thermostatic coolant heater influence on coolant temperature and measured heat flux .....	210
Figure 8.23: PID controlled coolant temperature .....	212
Figure 9.1: Air pocket design.....	222
Figure 9.2: Live interface temperature.....	223
Figure 9.3: Top down fixed reference point thickness measurement .....	224

## LIST OF TABLES

Table 2.1: Infrared window specifications.....	55
Table 2.2: Concept Engineering heat flux probe properties .....	57
Table 2.3: Diesel engine specifications .....	58
Table 4.1: Engine and visualization rig conditions.....	84
Table 4.2: Interface surface temperature experiment, compressed air conditions.....	105
Table 6.1: Thickness and surface area ratio pre- and post-bake .....	135
Table 6.2: Layer thickness reduction for bake-out events relative to 24hr pre-bake.....	143
Table 6.3: Heat flux increase for bake-out events relative to 24hr pre-bake .....	143
Table 6.4: Layer thickness reduction for 24hr bake 2 relative to bake 1 .....	144
Table 6.5: Heat flux increase for 24hr bake 2 relative to bake 1 .....	144
Table 6.6: Deposit thickness and surface area ratio for collapsed layer .....	153
Table 6.7: Standard deviation of measured surface temperature .....	156
Table 8.1: Instrument uncertainty for various parameters .....	187
Table 8.2: Optical microscope uncertainty at various experimental conditions.....	193
Table A.1: Close up infrared lens specifications .....	228
Table A.2: Standard heat flux conditions .....	228
Table A.3: Heat flux conditions for Reynolds number sweep at 18-hour interval .....	228

## LIST OF ABBREVIATIONS

A/F	Air fuel ratio
aTDC	After top dead center
BMEP	Brake mean effective pressure
CMD	Count median diameter
CO	Carbon monoxide
CO <sub>2</sub>	Carbon dioxide
EGR	Exhaust gas recirculation
F/A	Fuel air ratio
FSN	Filter smoke number
H <sub>2</sub> O	Water
HCCI	Homogeneous charge compression ignition
HF	Heat flux
HR	Heat release
IPA	Isopropyl alcohol
IR	Infrared
mg/stk	Milligram of fuel per engine stroke
MFB	Mass fraction burned
MFB50	Crank angle location of 50% mass fraction burned
Micron	Micrometer
NO <sub>x</sub>	Oxides of nitrogen
O <sub>2</sub>	Oxygen
PCI	Pre-mixed compression ignition

PM	Particulate matter
ppm	Parts per million
Re	Reynolds number
ROHR	Rate of heat release
RPM	Revolutions per minute
SA	Surface area
SLPM	Standard liters per minute
SS	Stainless steel
TGA	Thermogravimetric analyzer
THC	Total hydrocarbon
ULSD	Ultra low sulfur diesel
UMHR	University of Michigan Heat Release



## ABSTRACT

The use of exhaust gas recirculation (EGR) in internal combustion engines has significant impacts on engine combustion and emissions. EGR can be used to reduce in-cylinder NO<sub>x</sub> production, reduce particulate matter, reduce fuel consumption, and enable advanced forms of combustion such as HCCI and PCI. To maximize the benefits of EGR, the exhaust gases are often cooled with liquid to gas heat exchangers. A common problem with this approach is the build-up of a fouling deposit layer inside the heat exchanger due to thermophoresis of exhaust stream particulates and condensation of volatiles. This deposit layer lowers the effectiveness of the heat exchanger at decreasing the exhaust gas temperature.

The overall heat exchanger effectiveness is significantly influenced by the thermo-physical properties of the resulting deposit layer. Prior efforts have been made to quantify these properties, however measurements were performed ex-situ and in the absence of deposit volatiles. To generate more representative insights into the properties of these deposits, a novel optical measurement technique was developed to capture the native behavior of deposits in-situ.

The in-situ methodology utilizes 1-D conduction and measures heat flux, deposit wall temperature, deposit interface temperature, and the deposit thickness to calculate the deposit thermal conductivity. A visualization rig was designed and built to simulate an EGR cooler while providing optical and infrared access to the deposit. An optical microscope is used to measure deposit thickness and surface area, while an infrared camera is used to measure the deposit surface temperature. Combined with a heat flux

probe, the deposit conductivity at varying thicknesses and exhaust conditions was determined.

Results indicate that the novel methodology is capable of measuring and tracking deposit conductivity over a range of conditions. The measurement becomes more reliable with thicker deposit layers and at hotter interface temperatures. Deposit conductivity was shown to be independent of layer thickness, however varied with deposit surface temperature and volatile composition.

Hypothesized removal mechanisms were also investigated with the visualization rig. Results show that a high pressure upstream flow transient into a quiescent chamber is capable of removing 30% of a deposit layer down to the bare substrate while significantly thinning the remaining deposit layer. Velocity based removal was more effective when combined with water condensation, producing almost 50% deposit removal.

## **CHAPTER 1**

### **INTRODUCTION**

As emissions and fuel economy standards continue to tighten, advanced technologies are being employed to meet their criteria. Of these technologies, exhaust gas recirculation (EGR) introduces inert combustion products back into the combustion chamber, raising the specific heat capacity, increasing ignition delay, lowering the adiabatic flame temperature, reducing charge oxygen concentration, and thus reducing in-cylinder NO<sub>x</sub> emission. In addition, high rates of EGR enable advanced forms of combustion, such as pre-mixed compression ignition (PCI) or homogeneous charge compression ignition (HCCI). These combustion modes are being aggressively researched due to their ability to reduce NO<sub>x</sub> and particulate matter (PM) emission through low temperature combustion, with the possible unintended side-effect of increased hydrocarbon emission, and increased fuel efficiency through un-throttled engine operation [1-4].

EGR is more effective at reducing in-cylinder temperatures when cooled by an EGR heat exchanger or cooler. These EGR coolers are compact heat exchangers using liquid coolant, often of shell in tube design, however various other configurations exist [5]. In addition, numerous geometries of tubes exist; some are simple flat tubes while others incorporate turbulence-inducing components. The concept behind the turbulence enhancing geometries is enhanced heat transfer between the hot EGR gases and the cooled tube wall; thus producing lower EGR temperatures. Regardless of geometry,

previous work has shown that EGR coolers suffer from fouling as shown in Figure 1.1 [6].



Figure 1.1: Cross section of a fouled diesel EGR cooler [6]

### 1.1 EGR Cooler Fouling

EGR cooler fouling is the buildup of a deposit layer over time due to particle deposition, hydrocarbon condensation, and various other acid condensates resulting in the degradation of cooler effectiveness, as shown in Figure 1.2. The effectiveness of a cooler is ability to reduce the outlet temperature of the hot gas and is defined by the ratio of actual heat rejected by the gas to the maximum possible heat rejection by the gas:

$$\eta = \frac{\dot{m}C_{p,gas}(T_{gas,inlet} - T_{gas,outlet})}{\dot{m}C_{p,gas}(T_{gas,inlet} - T_{coolant})} = \frac{T_{gas,inlet} - T_{gas,outlet}}{T_{gas,inlet} - T_{coolant}}$$

Where  $\dot{m}$  is the mass flow rate of the gas,  $C_{p,gas}$  is the specific heat capacity of the gas,  $T_{gas,inlet}$  is the temperature of the gas at the cooler inlet,  $T_{gas,outlet}$  is the actual temperature of the gas at the cooler outlet, and  $T_{coolant}$  is the coolant temperature of the heat exchanger representing the lowest possible outlet gas temperature.

Fouling is also associated with an increase of deposit mass as shown in Figure 1.3 [7]. The deposit layer acts as an insulative barrier between the cooler wall and the hot exhaust gas passing through the tube [8]. This decreases the heat transfer between the

exhaust gas and cooler wall and results in an increased exhaust gas exit temperature. This effect is demonstrated by Zhan et al. illustrating a 90°C differential between a clean and fouled cooler in Figure 1.4 [9]. Increased EGR temperatures diminish the capability of the EGR to reduce the adiabatic flame temperature resulting in increased NO<sub>x</sub> emissions and could potentially upset the delicate chemical and thermal balance required for advanced forms of combustion. Zhan et al. also showed that fouling increases the pressure drop (Figure 1.5) across the cooler, potentially resulting in decreased flow rates, increased engine pumping work, and decreased fuel economy.

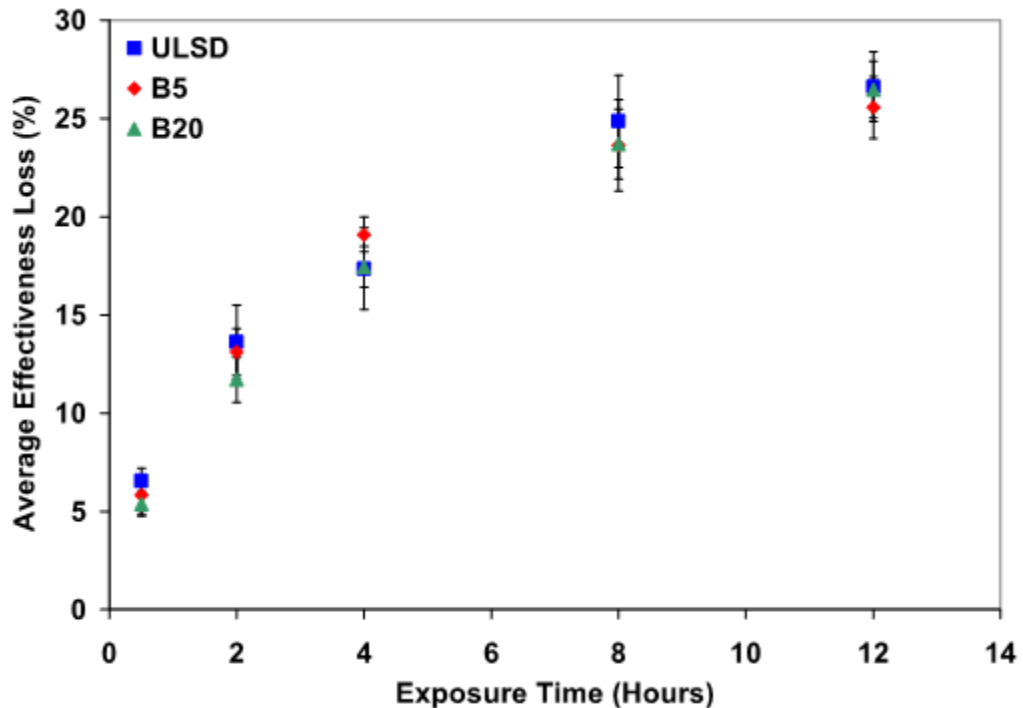


Figure 1.2: EGR cooler effectiveness loss with time for ULSD, 5% biodiesel, and 20% biodiesel [7]

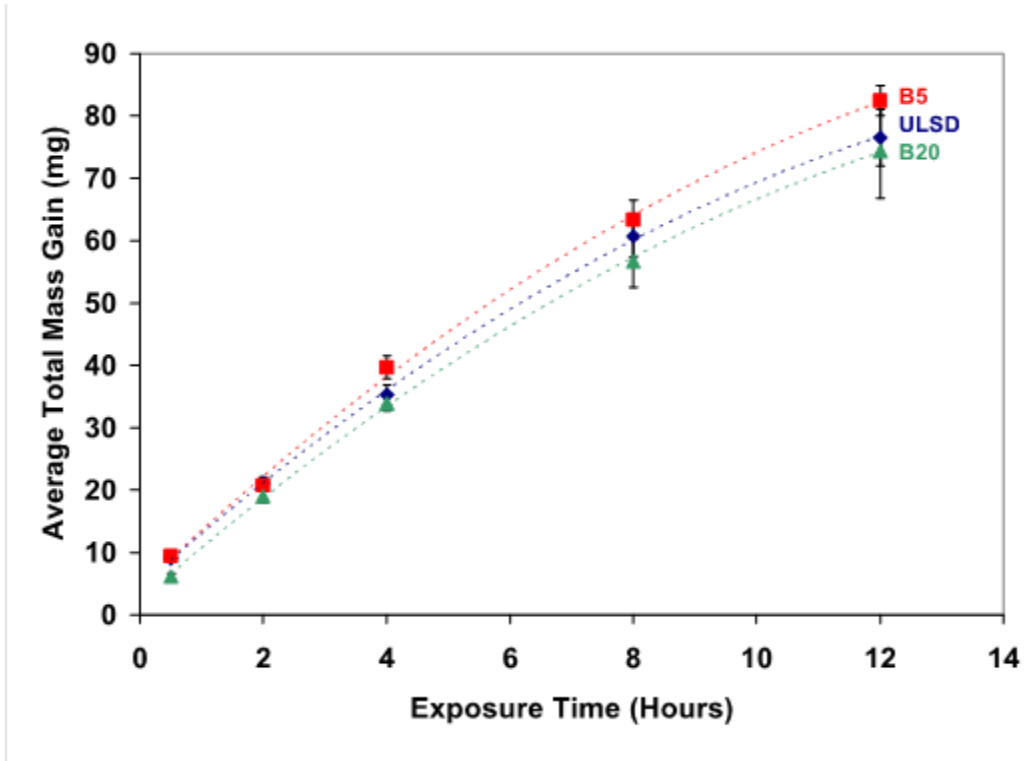


Figure 1.3: Deposit mass as a function of exhaust exposure time for ULSD, 5% biodiesel, and 20% biodiesel [7]

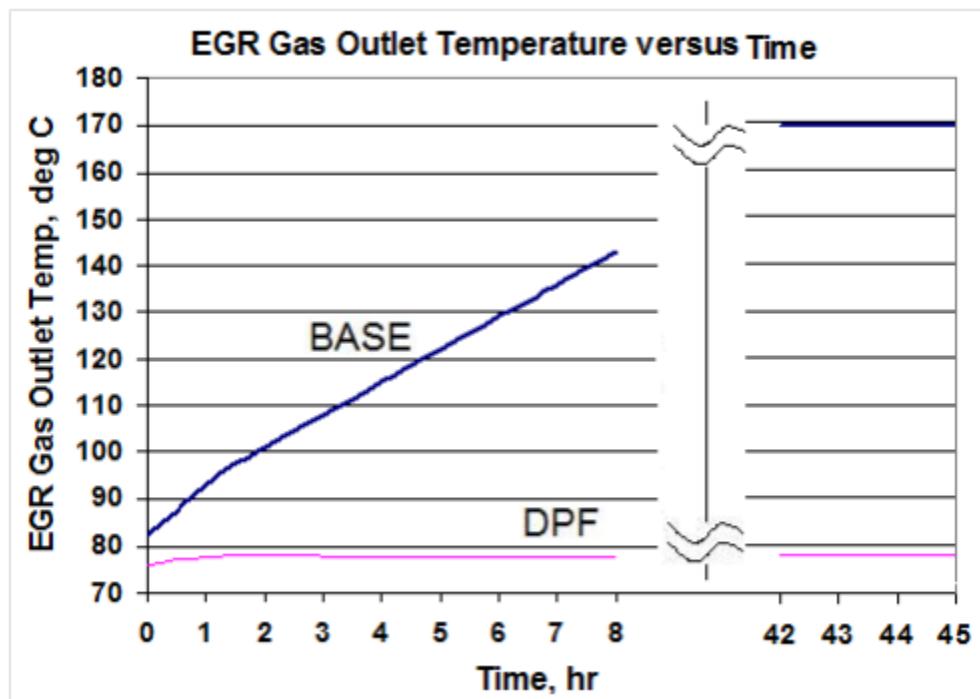


Figure 1.4: Increase in EGR outlet temperature for unfiltered (BASE) and filtered (DPF) exhaust gas [9]

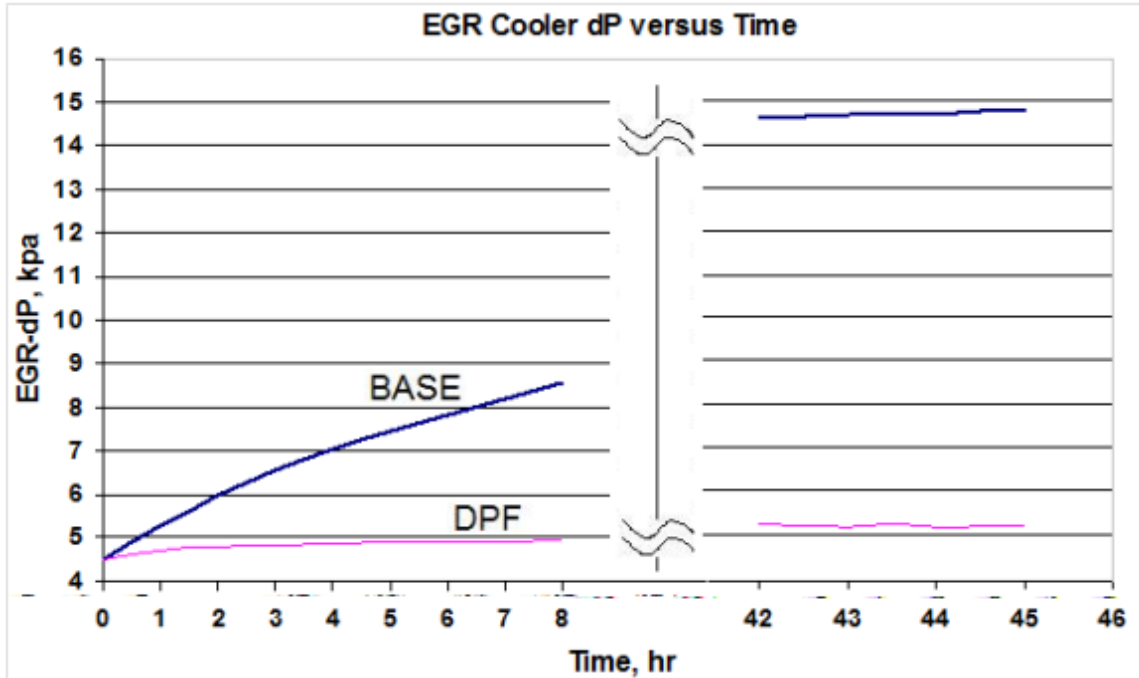


Figure 1.5: Pressure drop across EGR cooler for unfiltered (BASE) and filtered (DPF) exhaust gas [9]

While an in-line diesel particulate filter (DPF) system did show an improvement in fouling, Zhan et al. mentioned the system would need to be regenerated periodically. Regeneration would incur a fuel penalty as well as introduce hotter EGR into the cooler, causing an increase in the outlet temperature. In addition, an in-line high pressure DPF would cause difficulties maintaining EGR flow rates due to the increased pressure drop across the filter. When considering vehicle-packaging constraints, an in-line DPF is not a viable solution.

To determine the effect of hydrocarbons on EGR cooler fouling, Hoard et al. conducted experiments on two EGR coolers in series fed with diesel exhaust [6]. Two conditions were captured: one with straight engine out exhaust entering the cooler and the other with a diesel oxidation catalyst (DOC) before the cooler. The heat exchanger effectiveness in Figure 1.6 was seen to decrease for both cases, however less significantly for the catalyzed case. This data suggests that the reduction of hydrocarbons before the cooler inlet will help to prevent fouling and maintain heat exchanger effectiveness. Even

with a DOC in-line, the temperature of the EGR at the outlet of the second heat exchanger increased with time as shown in Figure 1.7.

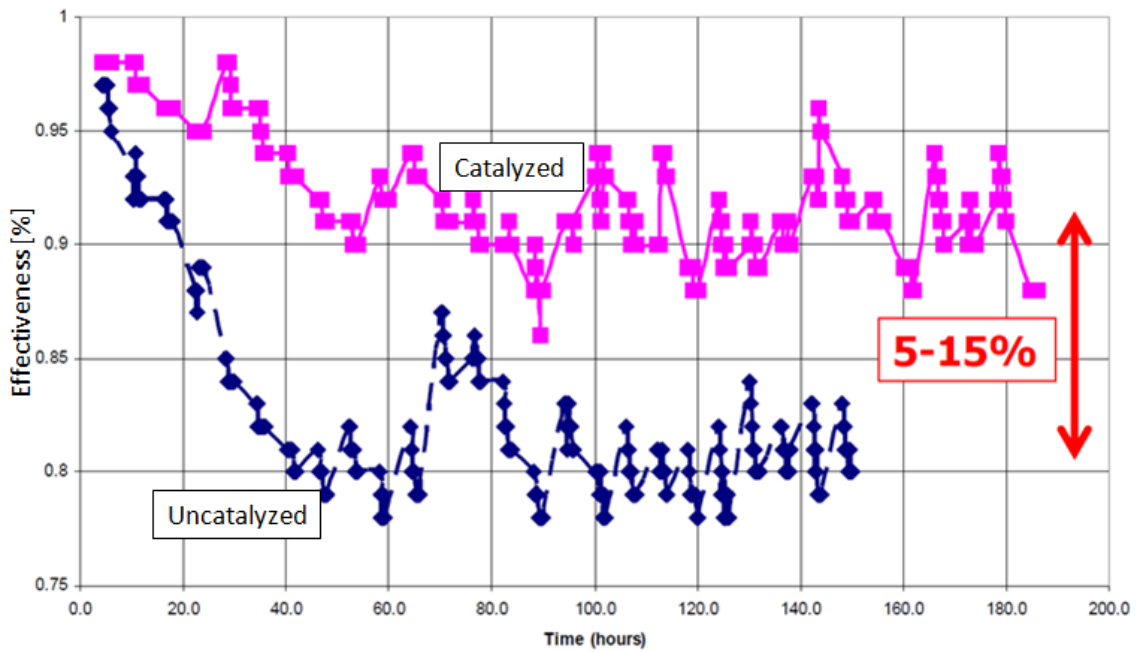


Figure 1.6: EGR cooler effectiveness for catalyzed and un-catalyzed exhaust gas [6]

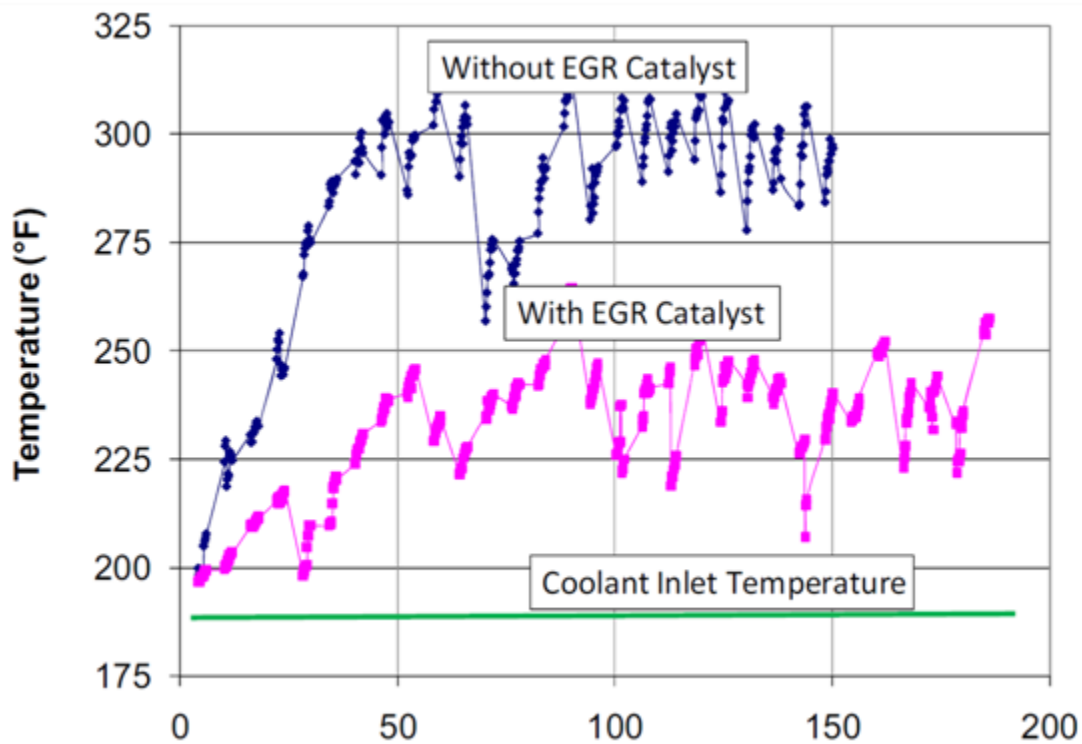


Figure 1.7: Exhaust gas temperature post EGR cooler for catalyzed and un-catalyzed exhaust gas [5]



The results from Zhan et al. and Hoard et al. show that particulates and hydrocarbons are critical to EGR cooler fouling. Sluder et al. also investigated parameters important to fouling and highlighted five: gas temperature at cooler inlet, coolant temperature, gas flow rate, PM concentration, and HC concentration [10]. Their study showed that lower coolant temperatures resulted in increased deposit mass gains (Figure 1.8). The authors noted that the coolant temperature to mass gain was non-linear with much higher mass gains at the lowest temperature.

In addition, Sluder et al. reported that with the use of an inline DOC (catalyst line in Figure 1.8), the deposit mass was much lower for the lower coolant temperatures. This indicates that a fouling layer still forms in the absence of HC and that HC condensation is not necessary for soot to adhere to the surfaces of the cooler. The DOC also reduced the sensitivity of the deposit mass to the coolant temperature. At 85°C, the catalyzed and uncatalyzed mass gain was similar. This potentially indicates condensation and mass gain from hydrocarbon species.

The authors also noted a strong relationship between coolant temperature and gas flow rate (Figure 1.9). High flow rates produced lower deposit mass at the coolest coolant temperature, however produced the largest mass at the mid and high coolant temperature levels.

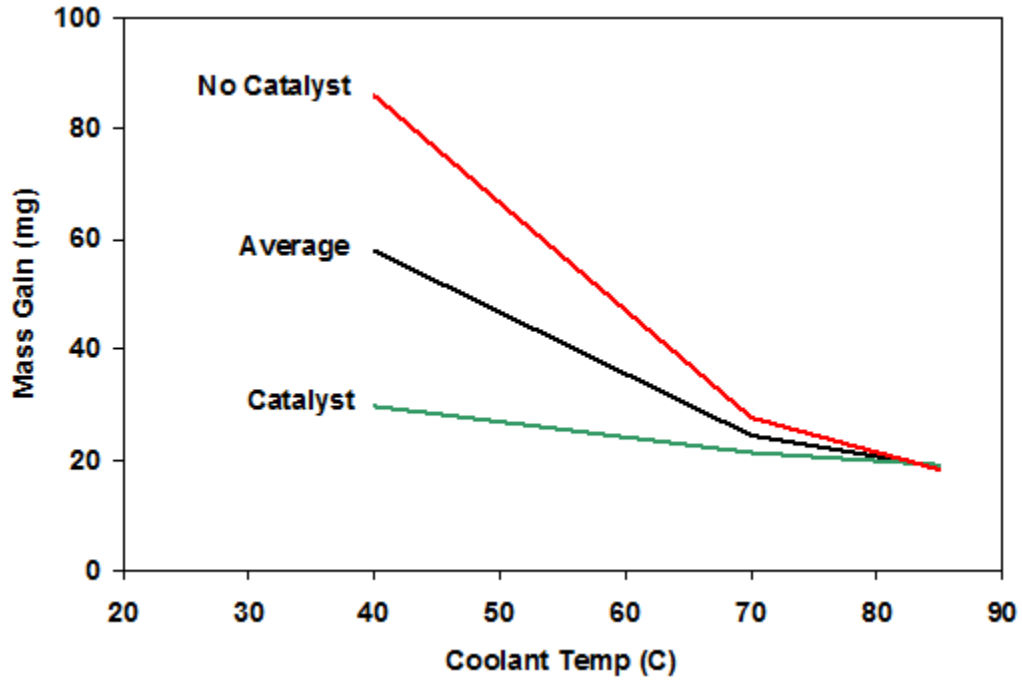


Figure 1.8: Effect of EGR coolant temperature on deposit mass gain [10]

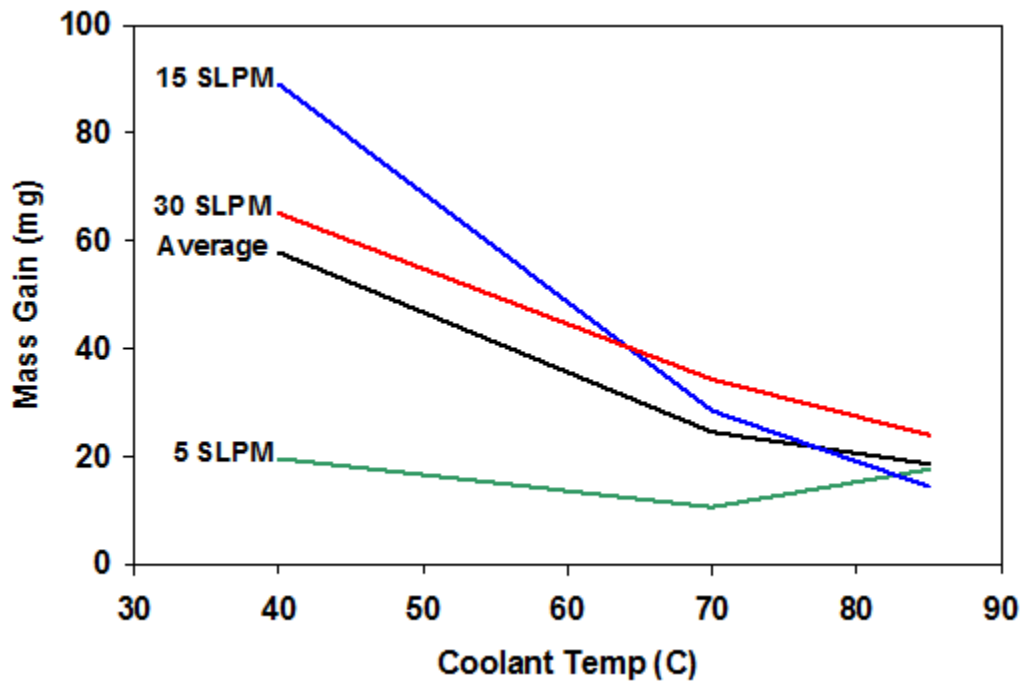


Figure 1.9: Effect of flow rate on deposit mass gain as a function of coolant temperature [10]

Using an analytical solution, Abarham et al. performed a parameter sweep on the boundary conditions at the inlet of an EGR cooler to determine the effects on deposit

particulate mass [11]. Varying one condition at a time, Abarham et al. determined the effects of gas mass flow rate, inlet gas temperature, inlet particulate concentration, and inlet pressure on deposit mass.

It was found that increasing the inlet gas temperature resulted in a higher deposit mass (Figure 1.10). The authors cite an increased thermophoretic driving force due to a larger temperature gradient between the hot gas and heat exchanger wall. In addition, an increase in the gas temperature reduces the gas density and increases the volumetric flow rate. To keep a constant particle concentration, the number of particles must increase. This can also add to increased particle deposition.

Increasing the gas mass flow rate (effectively Reynolds number) also increased the volumetric flow rate. The increase in volumetric flow rate required the number of particles to increase to maintain a set particle concentration, increasing the deposited mass (Figure 1.11).

Naturally, increasing the particulate concentration resulted in increased deposit mass (Figure 1.12). This is due to the presence of more particles in the gas flow.

Increasing the inlet pressure results in higher gas density and lowers the volumetric flow rate for a fixed mass flow rate. In order to maintain a constant particle density, the number of particles needs to be reduced as pressure increases. This results in a lower mass deposition (Figure 1.13).

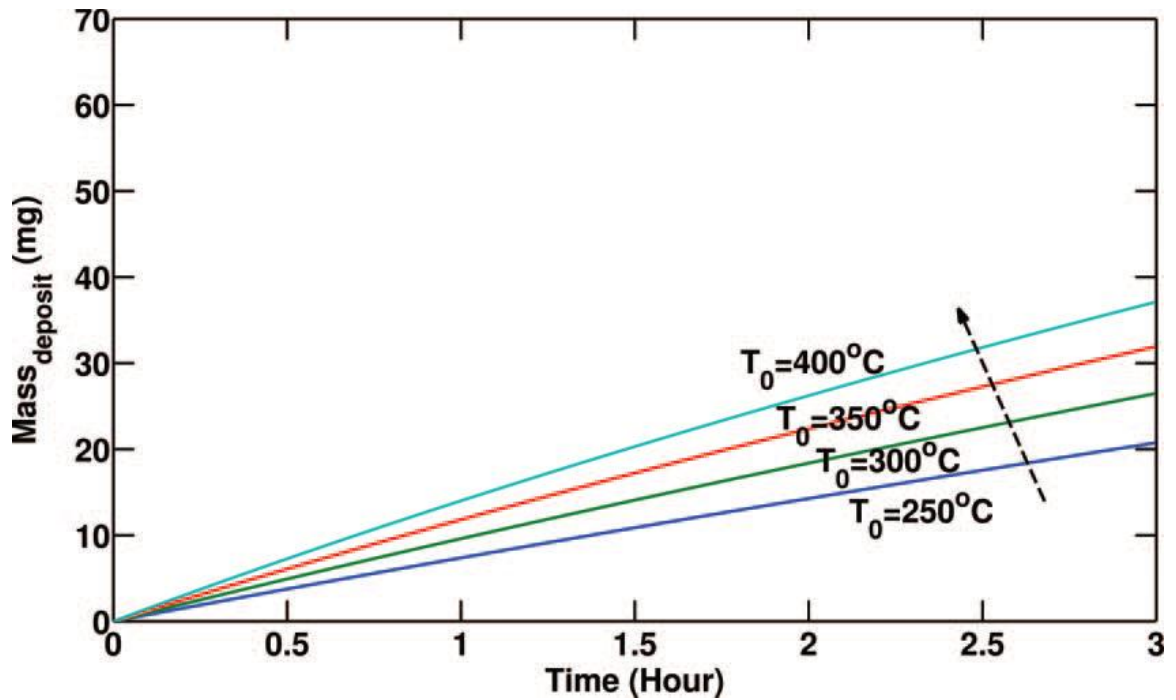


Figure 1.10: Effect of inlet gas temperature on deposit mass [11]

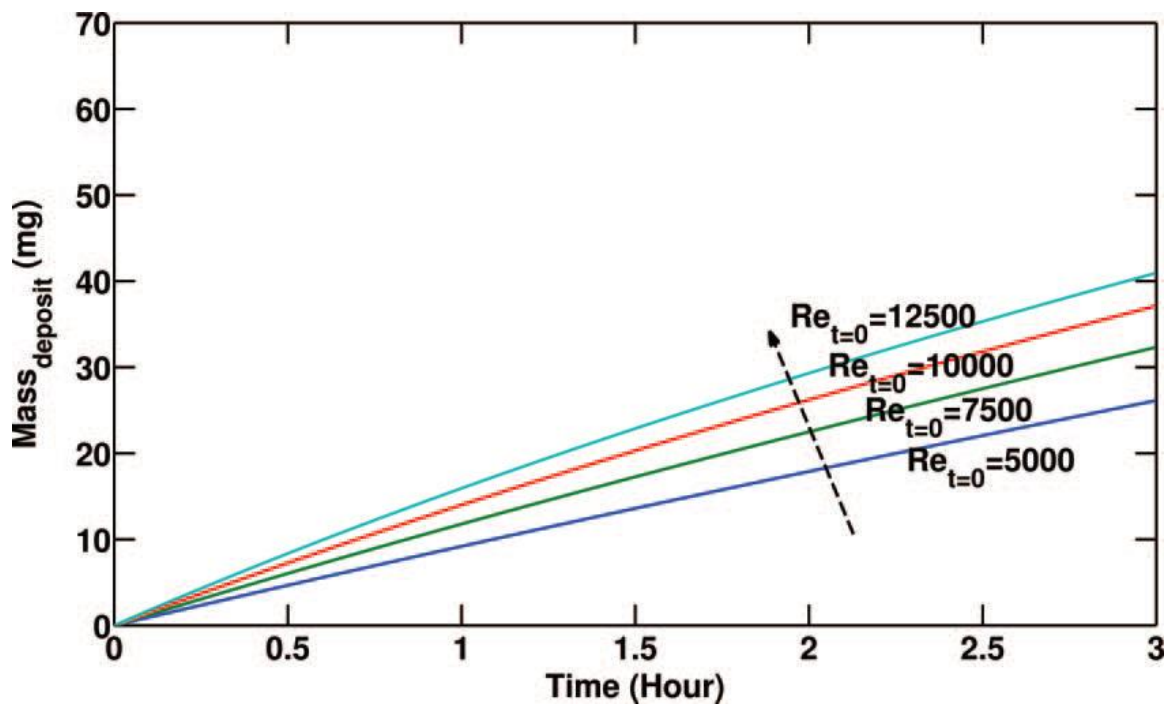


Figure 1.11: Effect of inlet gas mass flow rate (effectively Reynolds number) on deposit mass [11]

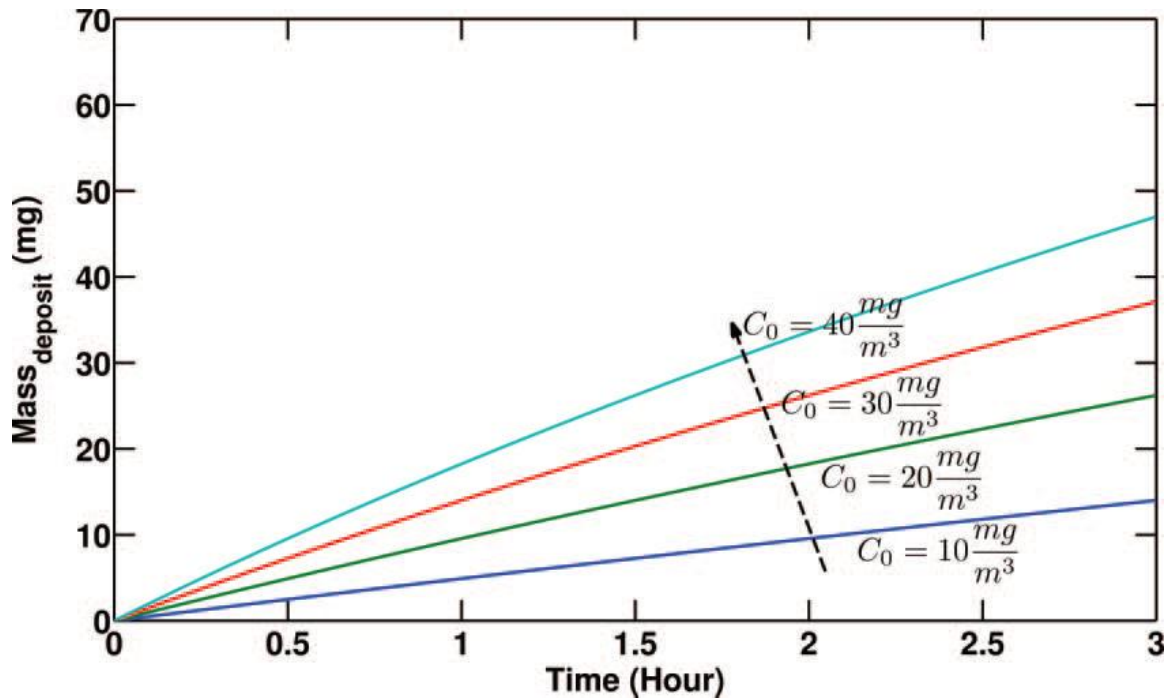


Figure 1.12: Effect of inlet gas particulate concentration on deposit mass [11]

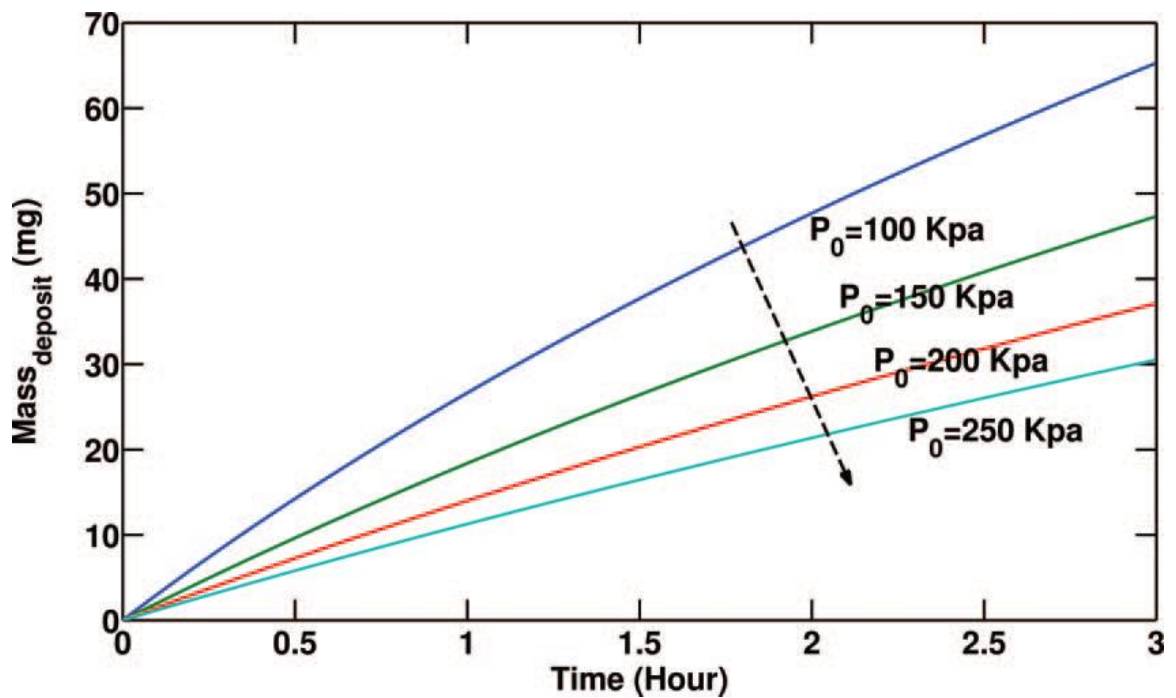


Figure 1.13: Effect of inlet gas pressure on deposit mass [11]

To determine the potential impact of hydrocarbons on EGR cooler fouling, Styles et al. varied the hydrocarbon concentration in the exhaust stream [12]. The study found that as hydrocarbon concentration increased, a marginal decrease in EGR cooler

effectiveness loss was experienced. However, a significant increase in deposit mass was also seen (Figure 1.14).

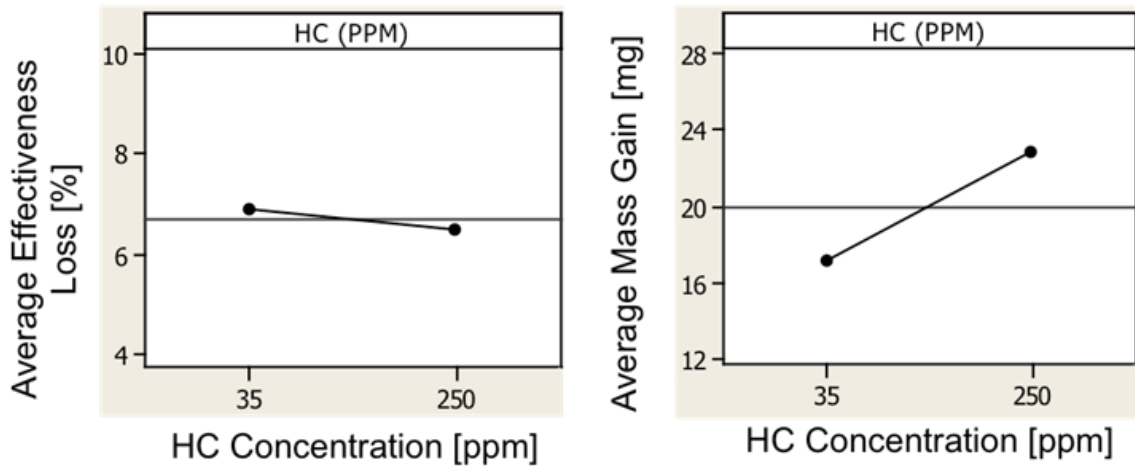


Figure 1.14: Effect of HC concentration on EGR cooler effectiveness loss and mass gain [12]

Previous work has suggested that an increase in deposit mass would lead to higher effectiveness loss (Figure 1.2, Figure 1.3). This study by Styles et al. contradicts that result and indicates a potential change in the deposit layer properties in order to improve EGR cooler effectiveness even as the deposit mass increases.

## 1.2 Deposits

As shown with previous work, oxidizing and filtering exhaust flow before the EGR heat exchanger appears to help prevent fouling. However, it is important to know the composition of the unfiltered flow and of the deposits found in the heat exchangers.

### 1.2.1 What are deposits

Lepperhoff et al. noted through elemental analysis of deposits that the main composition of deposits consist of organics such as carbon, hydrocarbons, oxygen, and nitrogen, inorganics like sulfur, and metals such as lead, barium and calcium [8].

Lepperhoff also noted that deposits have different structures at various temperatures. At temperatures below 200°C, dark material including soot, wet hydrocarbons, and tar-like components were visible. These deposits mainly consisted of low and high boiling hydrocarbons and soot typically found in lubricants and unburned fuel. At temperatures in-between 200 to 300°C, mostly dry, porous soot and tar-like materials were seen. The authors note that lacquer coatings in the deposits stem from lubricant derived deposition. At temperatures higher than 300°C, the deposit is lighter in color and thinner consisting mainly of inorganics stemming from the fuel and lubricant.

EGR coolers are typically operated around engine coolant temperature, around 90°C, although lower temperatures can be experienced for two-stage coolers, around 50°C, and during engine cold start/warm up. As deposits build up, the deposit-gas interface temperature increases due to the insulative properties of the layer. Exhaust gas temperatures vary according to engine load, but typical cooler out temperatures are around 120°C [5].

Hoard et al. cut a section of an EGR cooler and found significant caking in the passages (Figure 1.1). Particulate matter is expected from diesel exhaust and is typically in the range of 5-300 nm [13]. Upon further analysis, Hoard et al. determined a significant portion of the soot contained sulfates, likely due to the oxidation of fuel sulfur by a DOC.

While hydrocarbon emissions from diesel engines are typically fairly low, emissions levels can vary with fuels and can drastically increase for advanced low temperature combustions modes [1-4]. Thus, it is important to investigate the hydrocarbon composition of a deposit layer and determine its potential impact on EGR coolers. Hoard et al. performed a hydrocarbon extraction on a deposit layer and showed that the hydrocarbons mainly consisted of heavier carbon chains, typically found in lubricant, as shown in Figure 1.15 [6].

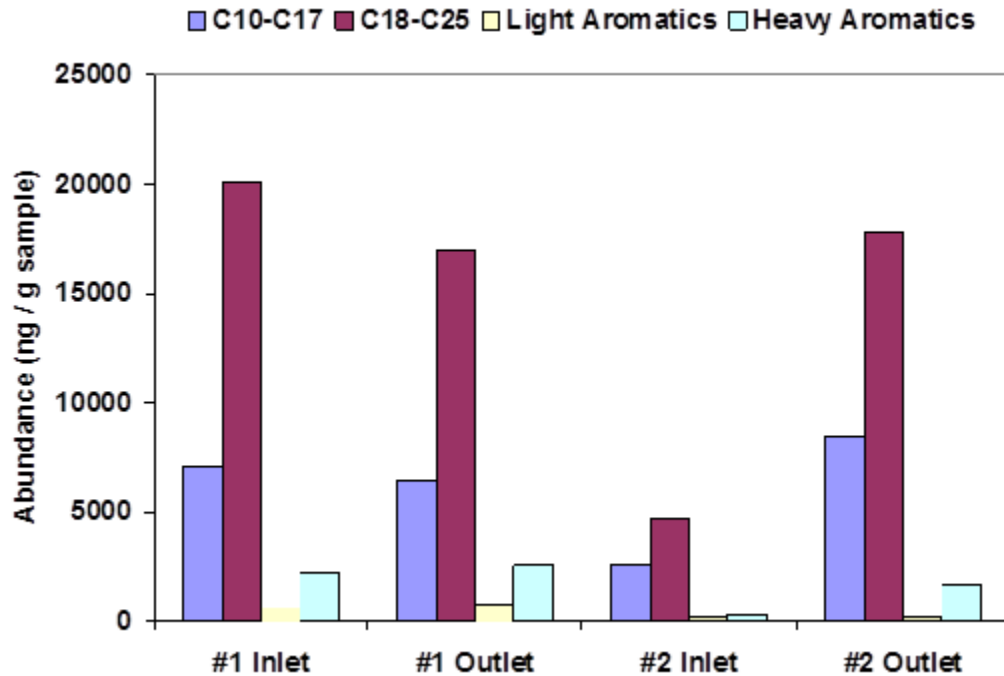


Figure 1.15: Hydrocarbon extraction from a Canadian market diesel fuel with ~400 ppm sulfur in a twin series EGR cooler configuration [6]

Sluder et al. [10] analyzed the deposits for hydrocarbons in three different cases: a heated tube, a catalyzed tube, and a cooled tube. Using a certification diesel fuel containing 300 ppm of sulfur, the baseline speciation results of the fuel are shown in Figure 1.16.



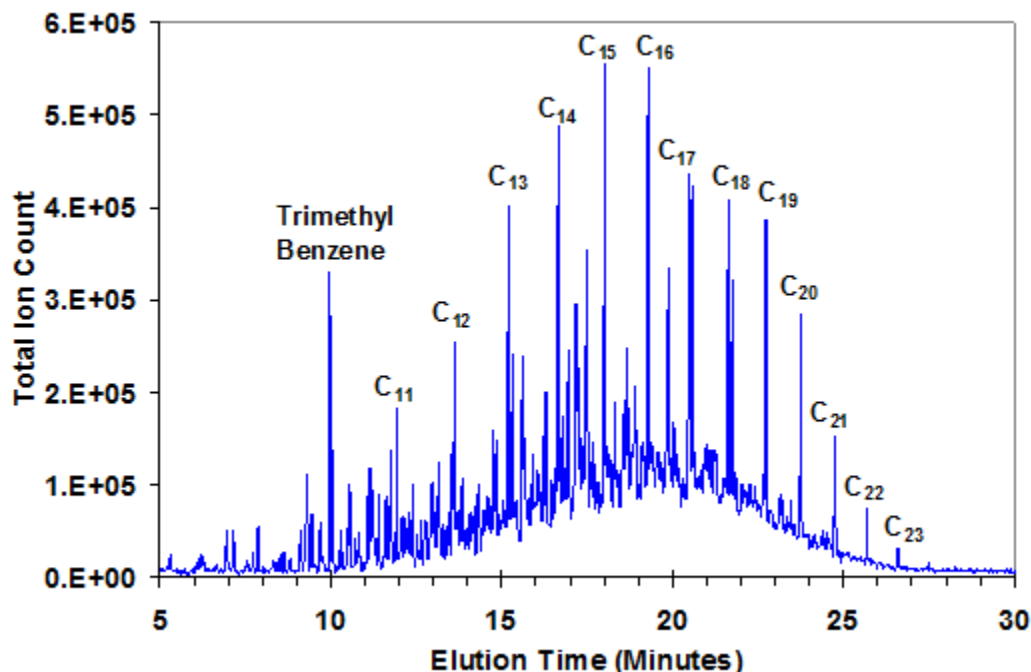


Figure 1.16: Speciation of certification diesel fuel with 300 ppm sulfur [10]

Speciation of the hydrocarbon deposits are shown in Figure 1.17. It can be seen that the heated tube, sufficiently hot enough to barely have deposition, had very little hydrocarbon condensation in the deposit layer. The catalyzed tube did not fully eliminate the hydrocarbons in the exhaust stream and resulted in heavier hydrocarbons condensing in the deposit layer. Finally, the cooled tubes showed the largest range of hydrocarbon species of the tubes, resembling more closely the diesel fuel speciation in Figure 1.16.

These results show that higher volatile compounds in un-catalyzed exhaust flow deposited onto the cooler walls. Figure 1.18 represents the vapor pressure curves of select alkanes and shows that if the temperature is low enough, gas phase hydrocarbon species will condense out of the gas phase onto the heat exchanger wall and deposit, adding mass and complexity to the properties of the deposit layer.

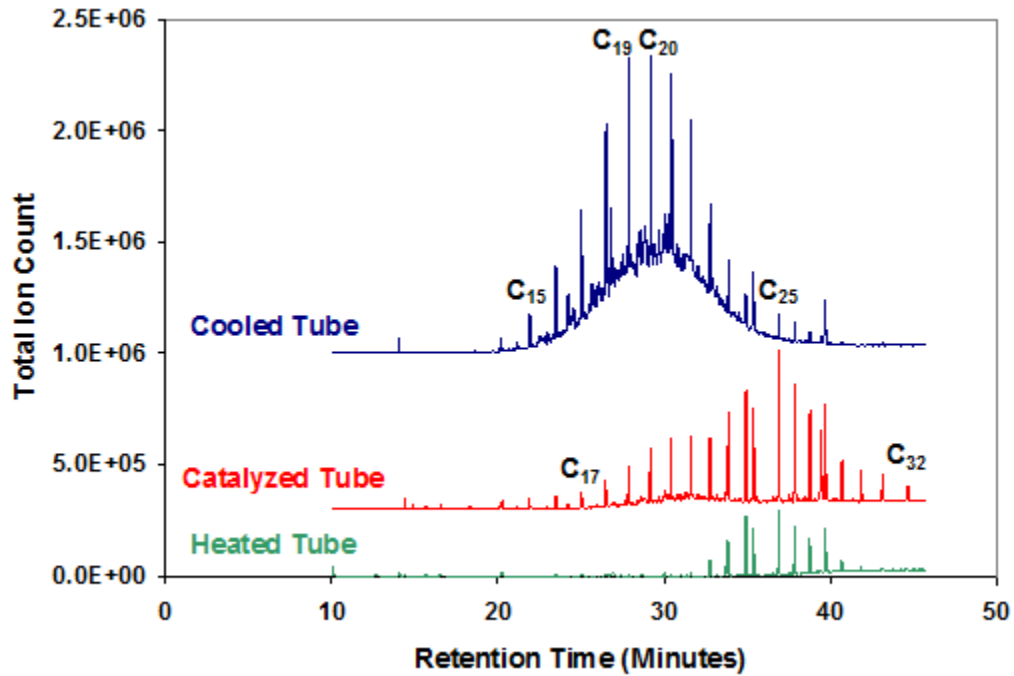


Figure 1.17: Hydrocarbon speciation of deposit layers found in heated, catalyzed, and cooled EGR tubes [10]

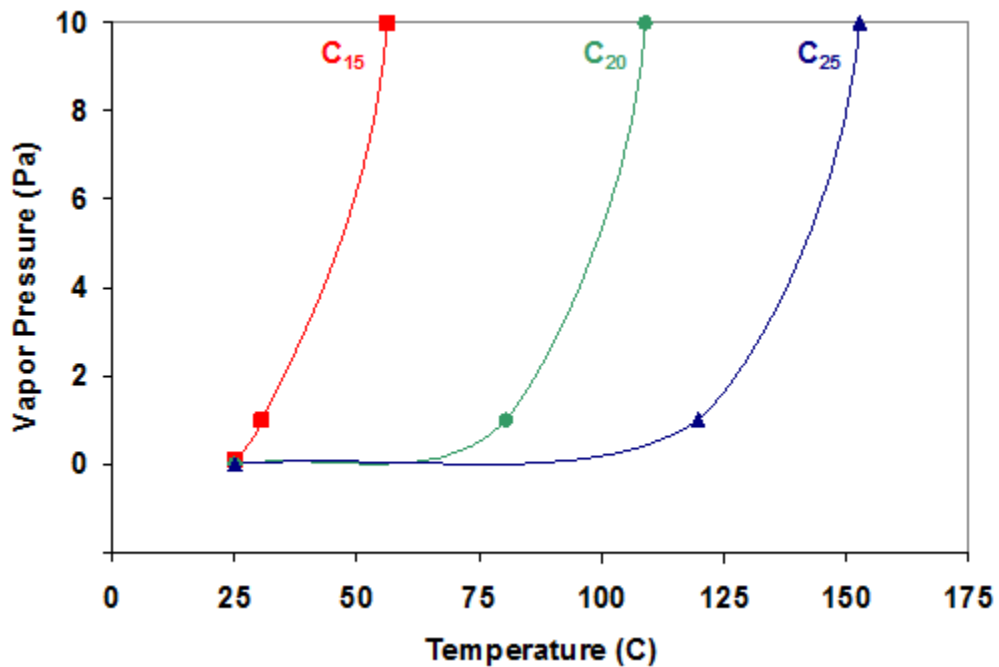


Figure 1.18: Vapor pressure for select alkane species [10]

Differences in deposit composition were verified when the mass fraction of the hydrocarbons in the deposit layer were analyzed in a later study by Sluder et al. [14].

Figure 1.19 shows that at initial exposures, the volatile fraction of deposit mass, including water, is almost 25% for ULSD (ultra-low sulfur diesel) and 55% for B20 (20% biodiesel, 80% ULSD). As the exposure time increases, the fraction seems to stabilize, perhaps due to the higher gas-deposit interface temperatures preventing further condensation. Since there is a change in the volatile fraction, there will surely be a change in the physical and thermal properties of the deposit layer as well.

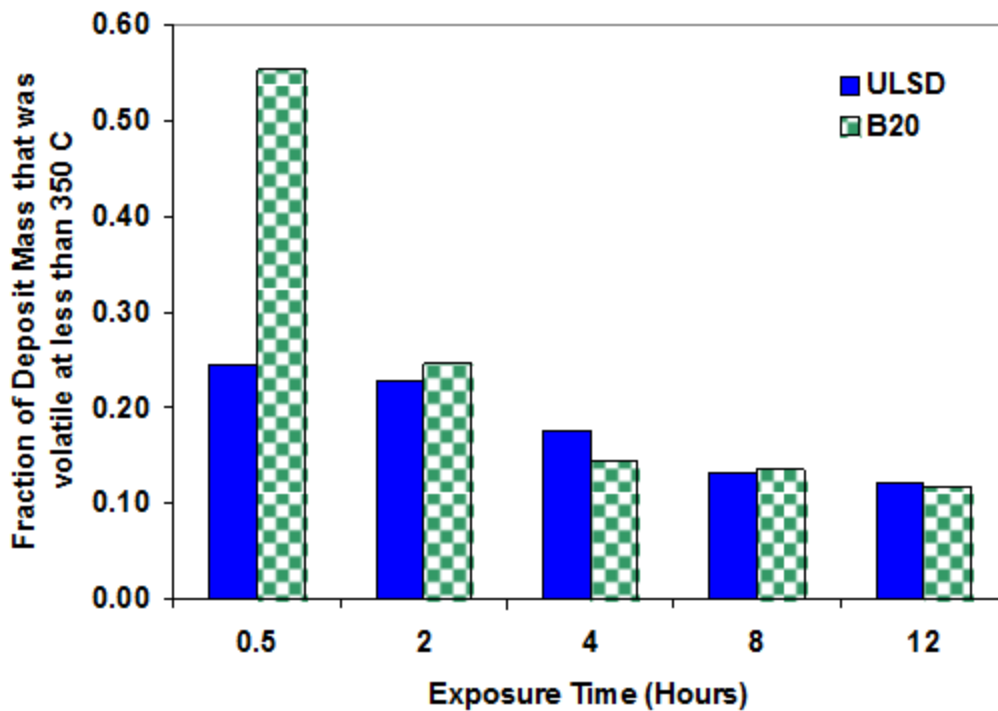


Figure 1.19: Volatile fraction of deposit mass for ULSD and 20% biodiesel [14]

### 1.2.2 Properties of deposits

Evidence of changing deposit properties has been seen through the composition analysis of deposit layers. Additional experimental evidence suggests a change in properties, as shown by Lepperhoff et al. Figure 1.20 shows that deposit thickness initially increases as deposition starts and stabilizes soon after. The deposit mass,

however, continues to increase with exposure time. These results suggest that perhaps deposit properties, such as density, change as a function of time.

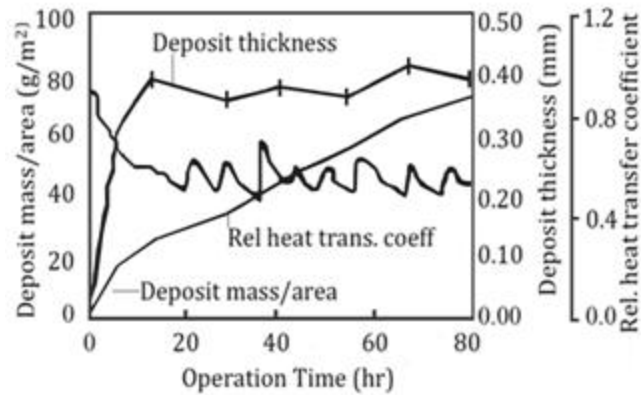


Figure 1.20: Evolution of deposit thickness, deposit mass/area, and relative heat transfer coefficient versus time, adapted from [8]

Sluder et al. also suggest a potential change in deposit layer properties in their studies. Cooler effectiveness loss was seen to asymptotically approach a steady state value (Figure 1.2) while mass gain continued to grow (Figure 1.3). The authors concluded that if thermal conductivity and deposit layer density were constant, the effectiveness loss would increase linearly with deposit mass. Since that is not observed, it is reasonable to assume the deposit properties changed at some point [7]. In addition, the authors concluded that differing fuel compositions (ULSD, 5% biodiesel, and 20% biodiesel) did not have a statistically significant impact on effectiveness loss.

Additional data suggesting a change in properties can be seen when Sluder et al. varied the heat exchanger coolant temperature [7]. The average effectiveness loss, Figure 1.21, was approximately equivalent for the three coolant conditions (90, 65, and 40°C) however the average total deposit mass was greater in the 40°C case. This was accompanied by a similar pressure differential across the tube as compared to the other coolant conditions (Figure 1.22). Thus, the authors concluded the additional mass gain was reflected in differences in density and not the thickness of the layer.

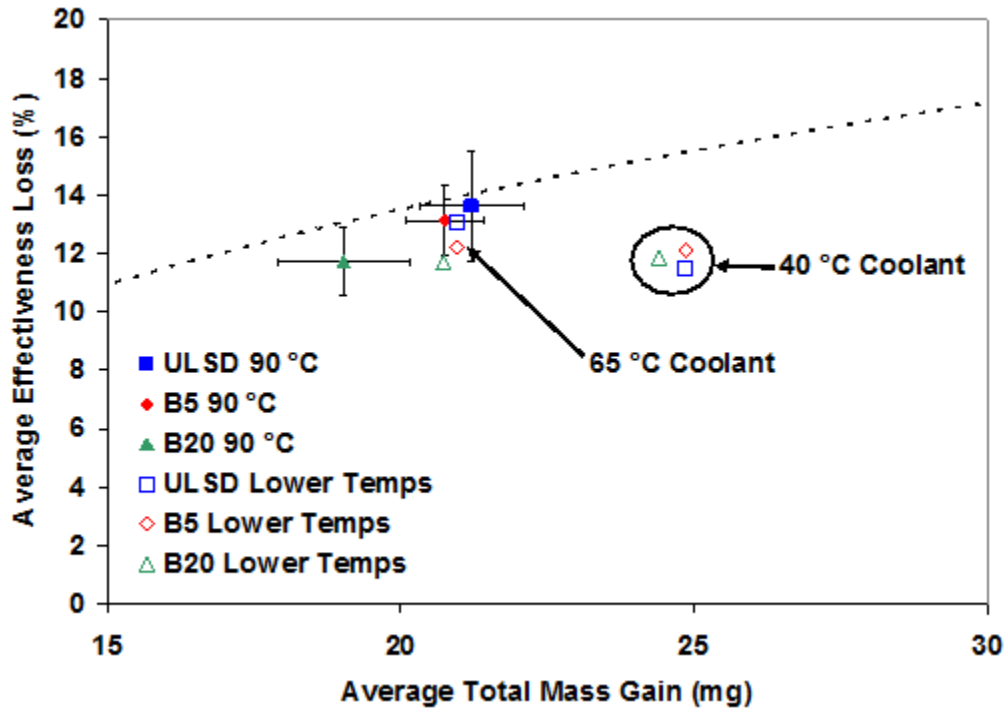


Figure 1.21: Average effectiveness loss of ULSD, 5% biodiesel, and 20% biodiesel at 90, 65, and 40°C coolant temperature [7]

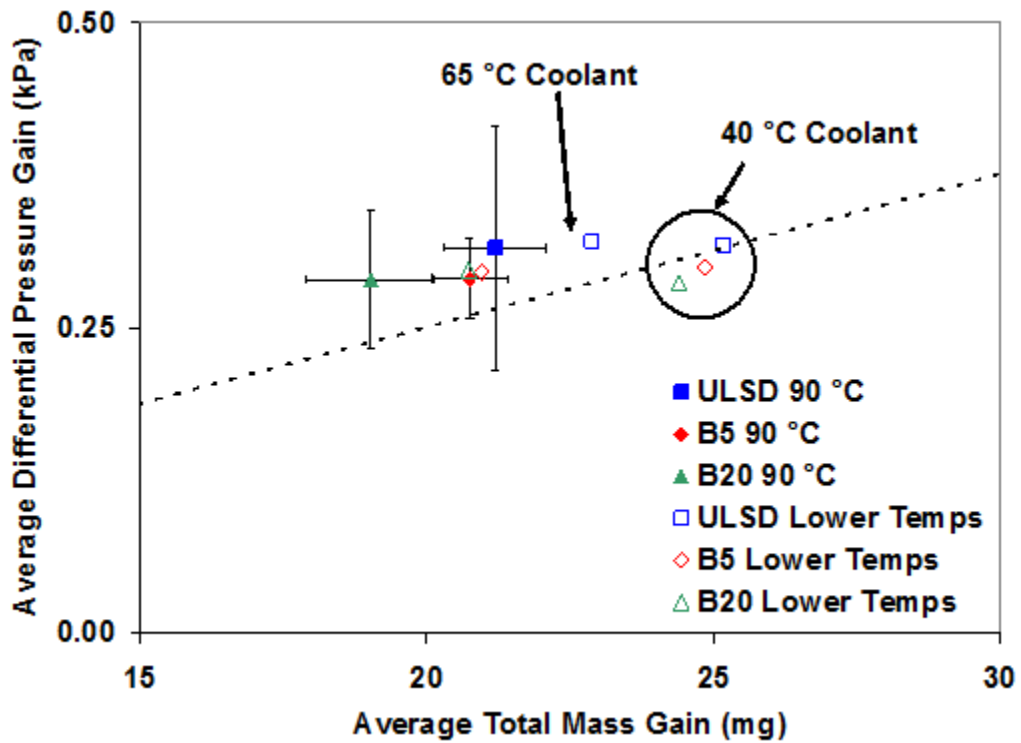


Figure 1.22: Average differential pressure across tubes for ULSD, 5% biodiesel, and 20% biodiesel at 90, 65, and 40°C coolant temperatures [7]

Another variable affecting deposit properties is engine-operating condition. Nishiwaki et al. demonstrated deposit thickness and thermal conductivity variations of combustion chamber deposits with engine operating condition. However, heat capacity was not seen to be affected [15]. Even though Nishiwaki et al. analyzed in-cylinder deposit properties, it is expected that these trends exist in the exhaust.

Cheng also noticed a change in the combustion chamber deposits as load increased [16]. As intake manifold pressure increased, and fuel increased accordingly to maintain constant fuel/air ratio, the deposit mass was recorded to decrease until an inflection point. Then, the deposit mass increased with manifold pressure. In addition, the composition of the deposits also changed and became darker as seen in Figure 1.23. These changes in the mass and appearance of the deposit could potentially lead to a change of the deposit properties.





















Manifold Pressure [kpa]	CCD #2	CCD #3	CCD #4	CCD #5	CCD avg
84.5	 0.18	 0.27	 0.35	 0.34	0.27
74	 0.13	 0.24	 0.28	 0.25	0.23
64	 0.19	 0.21	 0.32	 0.42	0.29
53.5	 0.36	 0.29	 0.35	 0.48	0.37
43.5	 0.37	 0.31	 0.42	 0.56	0.42

Figure 1.23: Variation of combustion chamber deposit mass with manifold pressure at constant fuel/air ratio, adapted from [16]

In an effort to quantify deposit properties, Lance et al. [17] measured the heat capacity, thermal diffusivity, and density of actual deposit in surrogate EGR tubes. During the heat capacity analysis, significant variations were observed in the initial data curve (Heating Run 1) compared to subsequent results as shown in Figure 1.24. The

authors cite cause of the atypical curve to the volatilization of water and hydrocarbons in the initial sample as temperature increased. They also acknowledge that perhaps not all of the hydrocarbons were removed due to the peak temperature reaching 430°C, possibly leaving heavier hydrocarbons in the sample. However, since the heating and cooling curves in Run 2 produced more repeatable and typical curves, the existence of additional hydrocarbons was determined to be minimal and Run 2 was used to establish the heat capacity of the deposit layer.

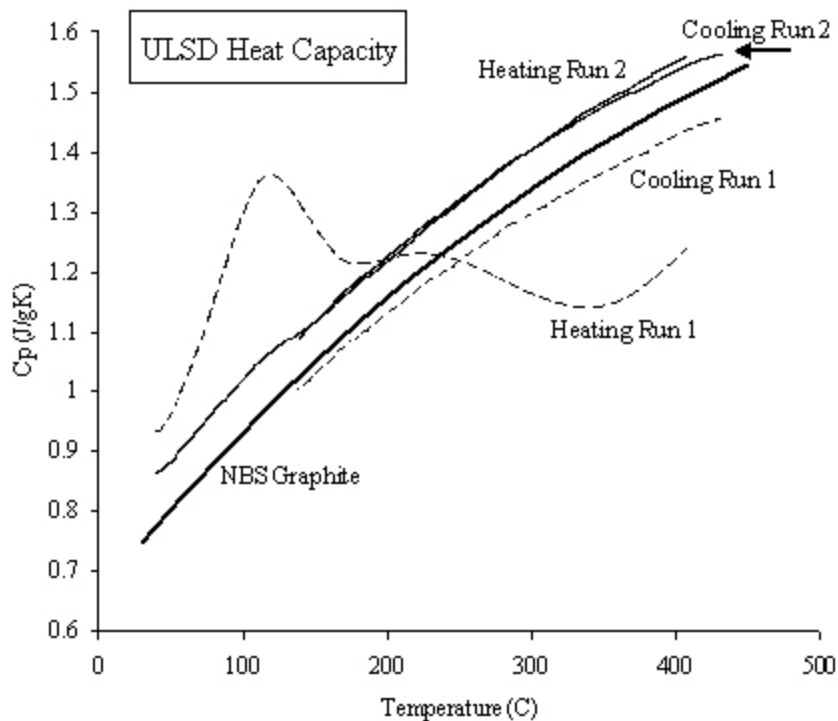


Figure 1.24: Volatilization of deposit sample during Heating Run 1 [17]

The authors also reported deposit layer thicknesses of 0.414 mm, 0.3725 mm, and 0.36 mm for ULSD, B5, and B20 respectively. The respective calculated densities were 0.0316, 0.0363, and 0.0379 g/cm<sup>3</sup>, averaging to 0.035g/cm<sup>3</sup>. The density measurements lead to a porosity calculation of ~98% assuming a primary soot particle density of 1.77 g/cm<sup>3</sup>. This measurement was performed ex-situ and included the volatile species. Changes in morphology have been seen in samples with time when left open to the atmosphere and the authors speculate that changes in water mass will cause deposit

density differences. The authors also note that large amounts of water and HC condensation can collapse the porous structure of the deposits and significantly increase the density.

The thermal diffusivity measurement consisted of a flash technique according to ASTM E1461. This technique applies a pulse of heat to the deposit side of a cut tube section and measures the temperature increase on the back of the metal tube. Diffusivity measurements and assumptions can be significantly affected if volatile species exist in the media. Lance et al. reported an averaged value of 0.013 cm<sup>2</sup>/s for ULSD, B5, and B20.

Using the previous measurements, Lance et al. calculated an average thermal conductivity of 0.041 W/mK for ULSD, B5, and B20 using Equation 1.1.

$$k = \rho C_p \alpha$$

Equation 1.1: Thermal conductivity calculation based on density, heat capacity, and thermal diffusivity

Where  $k$  is the thermal conductivity,  $\rho$  is the density,  $C_p$  is the heat capacity, and  $\alpha$  is the thermal diffusivity. The authors credit the low conductivity to the high porosity of the deposit layer. The porosity is mostly comprised of air, which has a thermal conductivity of 0.025 W/mK at 25°C, therefore the conductivity of a medium which is ~ 98% porous should be close to air [17].

In addition, deposit density variations have been reported by Storey et al. in Figure 1.25 [18]. The 20% biodiesel blend produced the most significant density variation at the start of exhaust exposure, likely due to the lower volatility of the biodiesel exhaust gas, and gradually settled down similar to the trend in Figure 1.19.



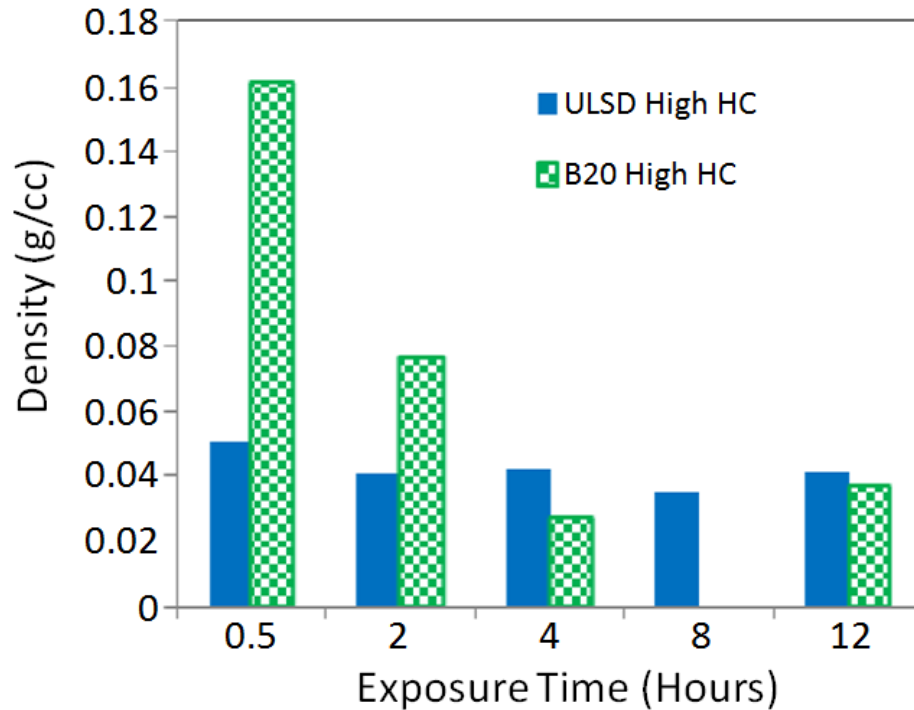


Figure 1.25: Deposit density measurements of ULSD and 20% biodiesel with increasing exposure time [18]

Lepperhoff et al. showed that the density of the deposit also varies in the radial direction (Figure 1.26). The density is seen to reach a maximum at the center of the deposit layer. The authors attribute this to diffusion and the balance between adsorption and evaporation creating differences in density in the radial direction.

These measurements coupled with differences in heat capacity and diffusivity can lead to a large uncertainty in calculated thermal conductivity, especially if volatile concentrations are seen to vary in time.

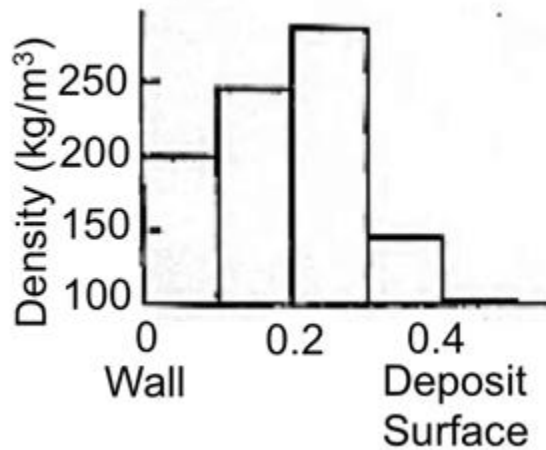


Figure 1.26: Deposit density variation from wall to deposit surface [8]

### 1.3 Deposition mechanisms

Numerous forces exist on the particles that can influence deposition. Thermophoresis, gravitational effects, inertial impaction, electrostatic forces, Brownian motion, diffusion, and condensation will be briefly discussed.

Thermophoretic deposition is accepted as the primary deposition method, exerting forces at least one order of magnitude larger than Brownian motion [19]. Thermophoresis is the result of unbalanced molecular interaction in a temperature gradient. The hotter side of the particle experiences more interactions with higher temperature molecules that force the particle towards the lower temperature side due to fewer interactions on the cooler side of the particle. In a heat exchanger, this would drive molecules from the hot mean flow path to the cooler heat exchanger wall.

Gravitational settling can also add to deposition and is due to differences in densities of particles and EGR gas. Particles in the exhaust stream are on the order of  $10^1 - 10^2$  nm and are highly dispersive. Their motion is only slightly influenced by gravitational forces thus they do not contribute much to deposition [20].

Inertial impaction can lead to deposition with heavier particles. Heavier particles cannot follow changes in the gas stream very easily and can be deposited on surfaces

with a change in flow direction. Typically, diesel exhaust particles are small enough to have minimal influence from inertial deposition [21].

Electrostatic forces stem from the static charge formed on particles from combustion [22] and an electrostatic field generated by friction between the EGR gas and wall flow channels. Typically water, some oxygenated hydrocarbons, and most of the compounds in engine exhaust ( $\text{CO}_2$ ,  $\text{N}_2$ ,  $\text{O}_2$ ) are non-polar. Electrostatic forces are not significant since most of the exhaust elements are non-polar and although 60-80% of particles are electrically charged, they are in equal numbers leaving the flow essentially neutral [20, 22]. In addition, a significant voltage is required to generate an electric field that will influence deposition [23].

Brownian motion could also contribute to deposition. Brownian motion is the force on a particle due to random actions from other neighboring particles

Diffusion and condensation leads to deposition through a concentration gradient and low temperatures. Diffusion velocity is proportional to the inverse of molecular weight and is present in a concentration gradient. Condensation occurs when the temperature at the heat exchanger surface is lower than the dew point of a species at a certain partial pressure. As species condense, it creates a locally lower gaseous concentration near the wall and builds a concentration gradient that results in diffusion [5].

The effect of pulsed flow on deposition is not well documented. The application of EGR coolers on engines will experience pulsed flow via the opening and closing of exhaust valves. This introduces hotter and higher-pressure gases into the engine exhaust headers and coolers. Lepperhoff et al. conducted a study on the effect of pressure wave amplitude on the separation efficiency, defined as radial particle flow to the wall of the pipe compared to total particle flow through the pipe [8]. The results showed that lower amplitude pressure waves increased the separation efficiency compared to high amplitude waves (Figure 1.27). This result indicates a larger tendency for particles to travel to the

pipe wall at low amplitudes. Lepperhoff et al. also determined the effect of Reynolds number on separation efficiency. The authors concluded that as Reynolds number increased, the low and high amplitude separation efficiency also increased until approximately a Re of 5000. This trend is due to the flow supporting thermophoresis under a Re of 5000 by transporting particles to the boundary layer. As  $Re > 5000$ , the boundary layer thickness reduces, the influence of thermophoretic forces is reduced due to higher flow rates and the particle concentration in the sub-layer is interrupted by bursts and downsweeps from the flow. The combined effects result in lower separation efficiencies.

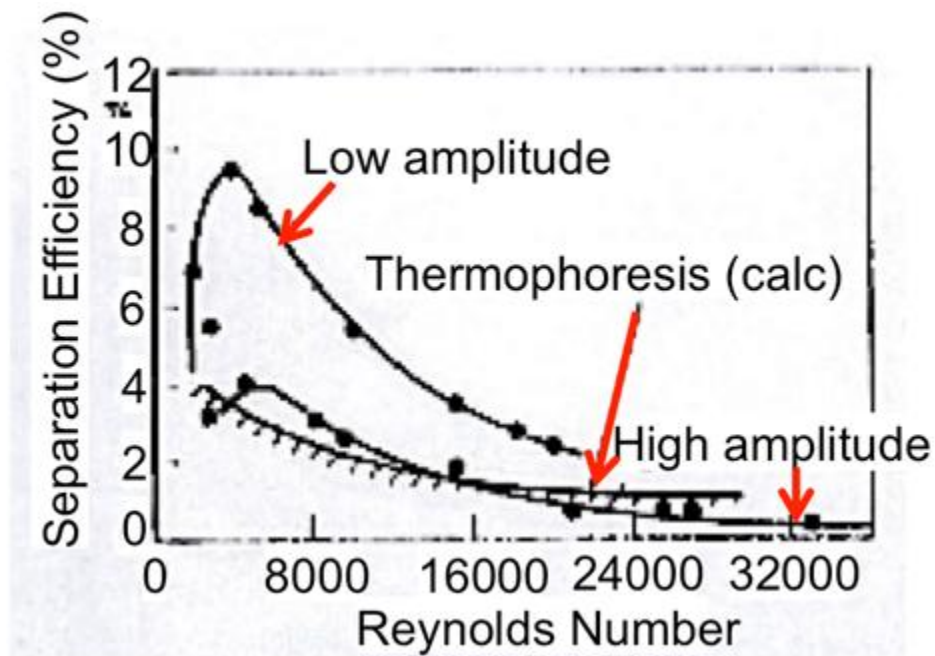


Figure 1.27: Effect of low amplitude and high amplitude pressure waves on radial particle flow [8]

#### 1.4 Stabilization and recovery

It can be seen through Figure 1.2, Figure 1.4, Figure 1.5, Figure 1.6, and Figure 1.7 that the cooler effectiveness and outlet temperature asymptotically reach a stabilized value. It should be noted, however, that the mass of the deposits continues to increase as shown in Figure 1.3 even with a stabilized cooler effectiveness (Figure 1.2). The

phenomenon is most likely indicative of a change in the properties of the deposit layer, such as the thermal conductivity or density. Figure 1.20 shows that as the deposit mass continues to increase with time, the thickness of the deposit layer stabilizes. These results suggest that perhaps both thermal and physical properties of the deposit change as a function of time.

Ismail et al. used a non-destructive neutron radiography technique to measure the thickness of the deposit layer along the length of the tube [24]. The authors reported that, for their exposure time of 5 hours, the inlet of the tube had a thicker layer and decreased along with tube length as shown in Figure 1.28. Also noted is the variation of thickness around 5-hour exposure. This wave-like appearance is speculated to be a result of shear stresses re-entraining some of the layer into the flow only to be deposited elsewhere in the tube.

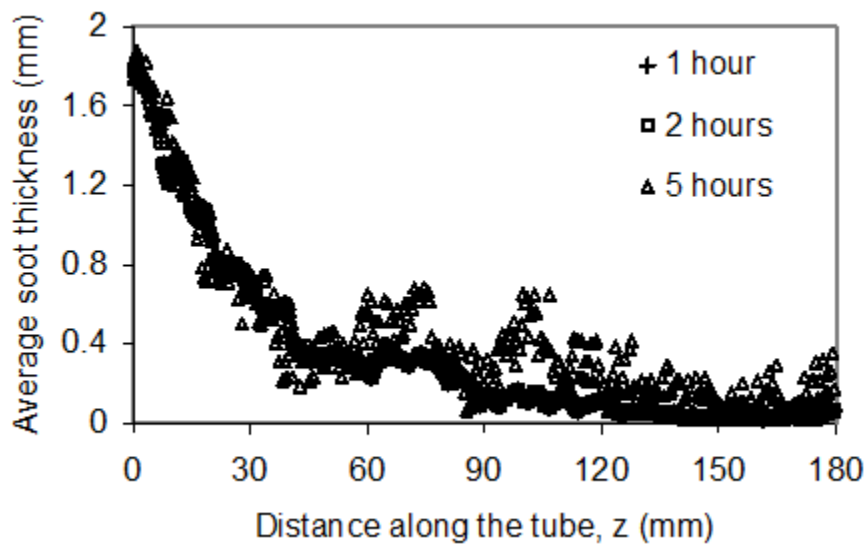


Figure 1.28: Deposit thickness variation along tube length [24]

However, Stolz et al. reported only a 0.1 to 0.2 mm thick deposit layer, with no variation between the inlet and the outlet [25]. This may result from the 200-hour exposure the cooler experienced. At a lengthy exposure interval, it can be argued that as a

deposit layer builds, the insulative tendencies of the deposits build as well. If the layer were thicker and therefore hotter at the inlet of the tube, the deposit would travel further down the tube to where the layer is thinner and deposit there, where a larger temperature difference exists. This would, in effect, stabilize the deposit thickness at the inlet of the tube. Stabilization would progress to other sections of the tube as deposit thickness increases and the temperature difference between the exhaust gas and the deposit surface decreases with time.

Removal mechanisms have not been directly published but studies have mentioned a recovery, defined as a sudden increase in effectiveness, during certain conditions. Stolz et al. claim that typical driving conditions are sufficient for a self-cleaning process caused by abrasive high gas velocities. This claim was supported by citing field experience of more than one year operational time and more than 200,000 km resulting in no clogging of tubes. Real evidence was not provided.

This result contradicts work from Sluder et al. Fouled heat exchanger tubes were thermally desorbed of volatiles and subjected to controlled airflow rates with an EEPS particle counter at the outlet of the tube. Results indicate that removal of deposit does not occur until very high gas flow velocities (~42 m/s) are achieved, as shown in Figure 1.29. The authors conclude that shear-based velocity removal is not a primary stabilization mechanism.

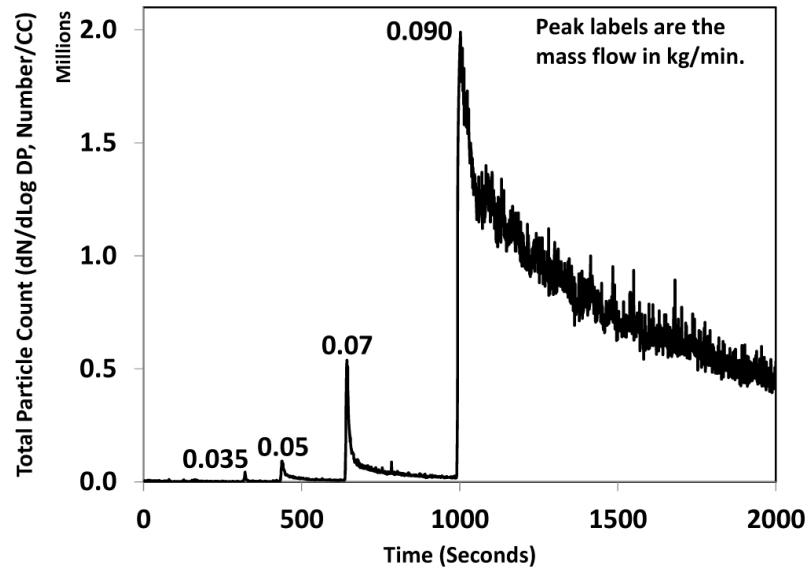


Figure 1.29: Deposit removal resulting from increasing gas velocity [26]

Bravo et al. attempted to simulate a de-fouling strategy where they imposed a deceleration of the engine [27]. The idea was to force clean gas through the fouled surface and remove the layer. The results were not favorable and the effectiveness was seen to return quickly back to the previous pre-de-fouling value.

Interestingly, Andrews et al. reported particulate storage and blow out in their experiments with after treatment devices [28]. The authors confirmed the removal was dependent on the preconditioning of the exhaust system. Particulate blow out was seen across the first silencer, located just after the catalyst, when preconditioned with an idle case (to build a particulate layer) and run from a cold start to high load. At the same time, deposition in the second silencer, located just upstream of the tailpipe, was observed. In another case, cold start to high speed at idle precondition, however, deposition was noted for the first silencer and blow out for the second silencer. The trends become more confusing when a high speed preconditioning, to remove particulate, is considered. Deposit build up was seen by both silencers in the cold start to high power case and blow out was seen in the cold start to high speed case. The results are inconclusive and a removal mechanism was not identified.

Styles et al. attempted to replicate a removal mechanism by developing a coefficient based on drag to bond force ratio [12]. The criterion for removal required the kinetic energy of the deposit layer molecules to exceed the bonding Van der Waals energy. When implemented with their deposition model, the degradation in effectiveness matched well with experimental data (Figure 1.30). However, when deposition was turned off by means of an inline DPF, the removal rate in the model was too strong and deviated from experimental data. The model predicted a large recovery in effectiveness and a significantly lower mass when compared to experimental data. The experiment did not experience effectiveness recovery; the change in effectiveness is due to a change in the pressure and temperature of the gas due to the DPF and not to deposit removal. If a physical removal mechanism does exist, it seems to be a complicated phenomenon that provides limited recovery.

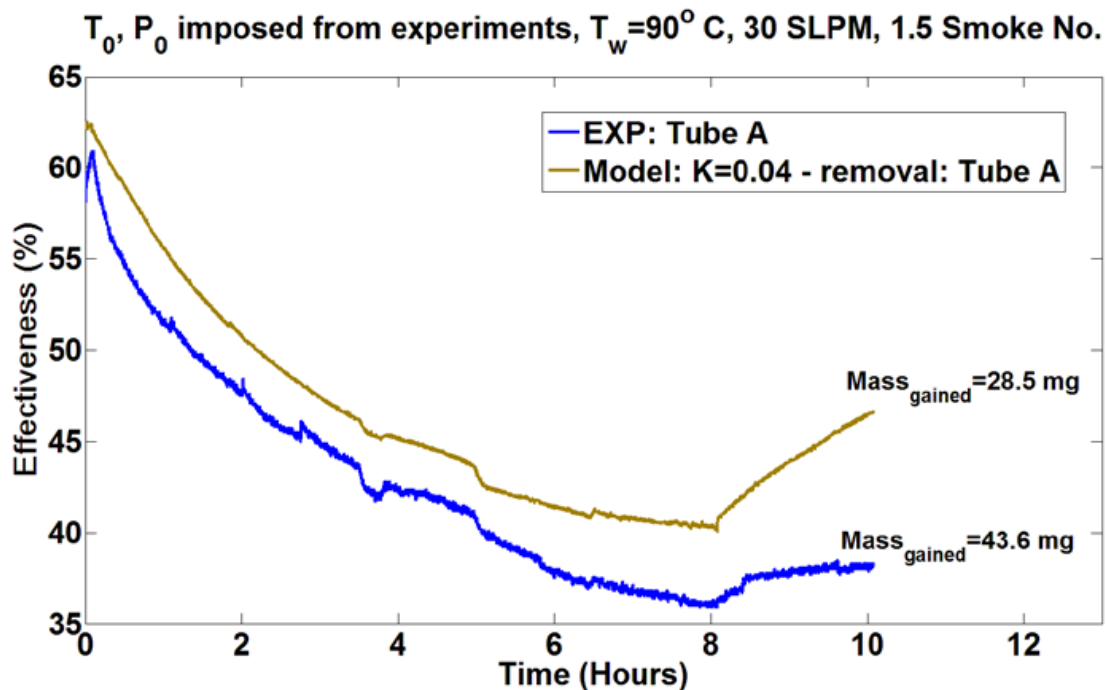


Figure 1.30: Comparison of removal mechanism in model to experimental data [12]

Abarham suggested potential removal mechanisms consisting of blow out, flaking, cracking, evaporation or oxidation, and wash out [29]. Blow out is dependent on



the shear stresses exhibited by the gas flow to overcome the bonding force of the deposits. Flaking may occur when the deposits lose adhesion to the surface and may be subject to removal. Cracking occurs if the deposit hardens with time and is exposed to thermal or other stresses. Evaporation or oxidation can cause removal by removing some of the volatile components in the deposit layer. Wash out occurs with condensation of water, hydrocarbon, or any other component that can cause a liquid film. This could reduce the adhesive force of the deposit layer and cause removal.

## 1.5 Models

Teng et al. [20] developed a fouling model considering thermophoretic deposition and a removal mechanism. The authors used the thermophoretic drift velocity to develop a relation for the thermophoretic coefficient using the following equation:

$$V_{th} = -K_{th}x \left(\frac{\nu}{T}\right) x \nabla T$$

Where  $\nu$  is the kinematic viscosity of EGR,  $T$  is the EGR temperature,  $\nabla T$  is the temperature gradient between the gas and the surface, and  $K_{th}$  is the thermophoretic coefficient. The relation was developed using a differential length in an EGR cooler and considering that the deposition of soot on the wall is equal to the rate of change of the soot particle concentration  $C$  over a distance  $dx$ . Then a temperature was determined by considering the heat transfer to the cooler wall over a length  $dx$ , which is equal to the change in EGR enthalpy. After a few more correlations were applied (for a full description, see [20]), a relation of  $K_{th}$  was determined.

The authors then consider the change of mass with time as

$$\frac{dm}{dt} = \dot{m}_d - \dot{m}_r$$

Where  $d$  represents deposition and  $r$  represents removal. The authors claim the top most layer of the deposit layer is highly porous and as such exhibits low density and low

Van der Waals forces. Thus, the authors claim a removal mechanism is present from high shear stresses from the exhaust flow. After introducing a fouling factor, the authors then introduce tunable constants  $K_1$  and  $K_2$  that find their way into a final form of the fouling factor ( $R_f$ ) for a stabilized cooler:

$$R_f = \dot{R}_f x \left[ 1 - \exp\left(-\frac{K_2 \rho U^2}{\rho_d} t\right) \right]$$

$$\dot{R}_t = \frac{K_1 C_s}{K_2 k_d U} x \left\{ 1 - \left[ \frac{T_w}{T_0} + \left(1 - \frac{T_w}{T_0}\right) x \exp\left(-4St \frac{L}{D}\right) \right]^{Pr K_{th}} \right\}$$

$K_1$  and  $K_2$  are described as a correction factor and a parameter characterizing the dispersion of soot particles removed from the deposits. The model loses physical meaning with the introduction of these parameters but produced reasonable predictions of heat exchanger fouling over relatively short exposures. Using some of the physical insights from their modeling efforts, the authors highlighted the EGR inlet temperature, soot particle concentration, and EGR mass flow rate as key parameters influencing EGR cooler fouling.

Abarham et al. developed an analytical solution to model thermophoretic deposition of particles in a cooled tube [11]. Their approach involved solving the energy equations for bulk gas flow and applying mass conservation of particles in turbulent pipe flow to predict pipe diameter as a function of time and deposited mass. A number of simplifying assumptions were required to approximate and linearize the ODE and added slight error into the solution, as shown in Figure 1.31. At the end of a simulated 3-hour exposure, the error in pipe diameter prediction between the two solutions was 2.1%. However, due to an axial independent assumption required to solve the analytical equations, the deposit mass estimation was 40% higher in the analytical case than the numerical solution.

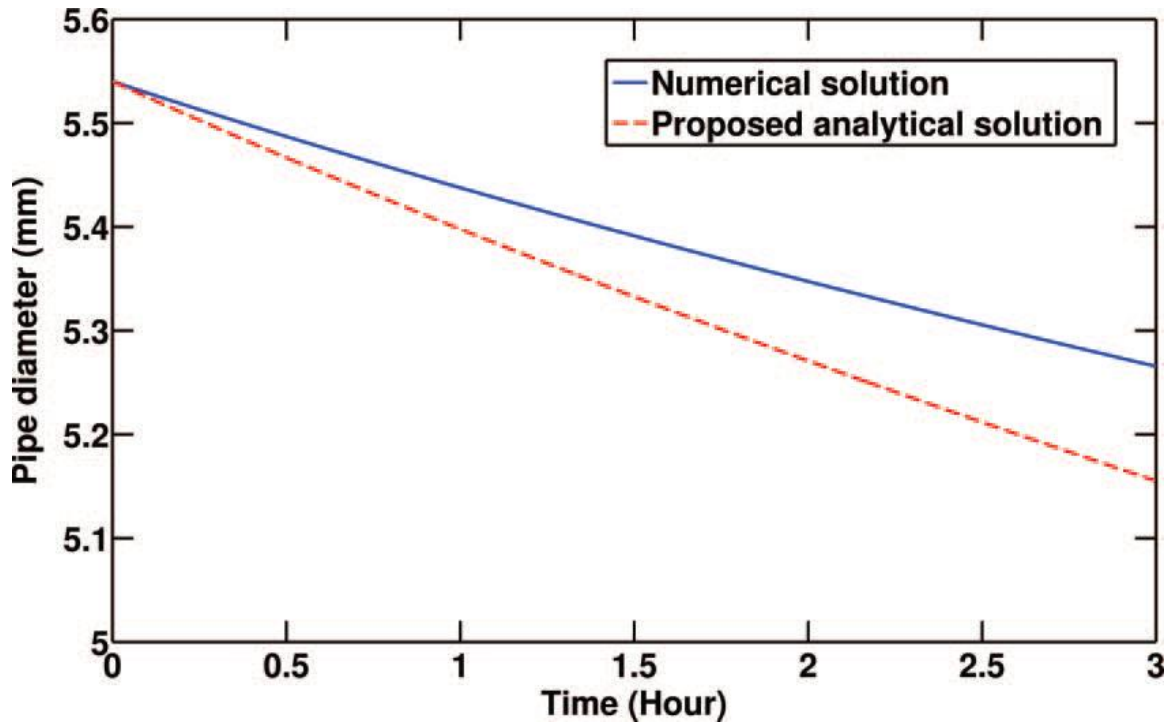


Figure 1.31: Numerical versus analytical prediction of pipe diameter [11]

It is noted that Abarham et al. used constant deposit layer properties derived from Lance et al. [17]. In addition, the gas properties were calculated and held constant for the average temperature between the inlet and wall temperatures. These assumptions can also add error in the pipe diameter and deposit mass estimations.

Abarham furthered their deposition modeling efforts by developing a 1-D model as well as an axi-symmetric CFD model [29]. These newer routines are not restricted to a uniform deposit layer along the length of the tube and allow for variations in deposit layer thickness as a function of local thermophoretic forces. Additionally, bulk gas temperature is now a function of heat transfer to the walls and deposit layer with gas properties varying with bulk temperature. The deposit layer thermal conductivity was varied with the average temperature of the gas-deposit interface and coolant temperatures in the 1-D simulation, and the local cell temperature in the axi-symmetric CFD model. Deposit conductivity was also varied according to porosity of the layer, as described by Ciro et al. [30]:

$$k_d = (1 - \varphi)^{1.5}k_{Graphite} + \varphi^{0.25}k_{EGR}|_T$$

$$k_{Graphite} = 13.0839 - 0.03495 \times T + 3.82 \times 10^{-5}T^2 - 1.48 \times 10^{-8}T^3$$

Where  $k_d$  is the thermal conductivity of the deposit,  $k_{Graphite}$  is the thermal conductivity of graphite,  $k_{EGR}$  is the thermal conductivity of EGR, and  $\varphi$  is the porosity of the deposit layer.

Figure 1.32 shows the numerical predictions compared with the experiment. It can be seen that the initial slope in the experiment and final effectiveness values differ from the model prediction. This can be due to variations in the composition of the deposit layer (HC build up, density variations, thermal conductivity differences). As mentioned previously, density of the deposit layer is seen to vary with exposure time as well as in the radial direction of a tube. The same applies for condensed hydrocarbons. Since thermal conductivity is in part a function of porosity and composition of the deposit layer, it is expected that the conductivity will change as well.

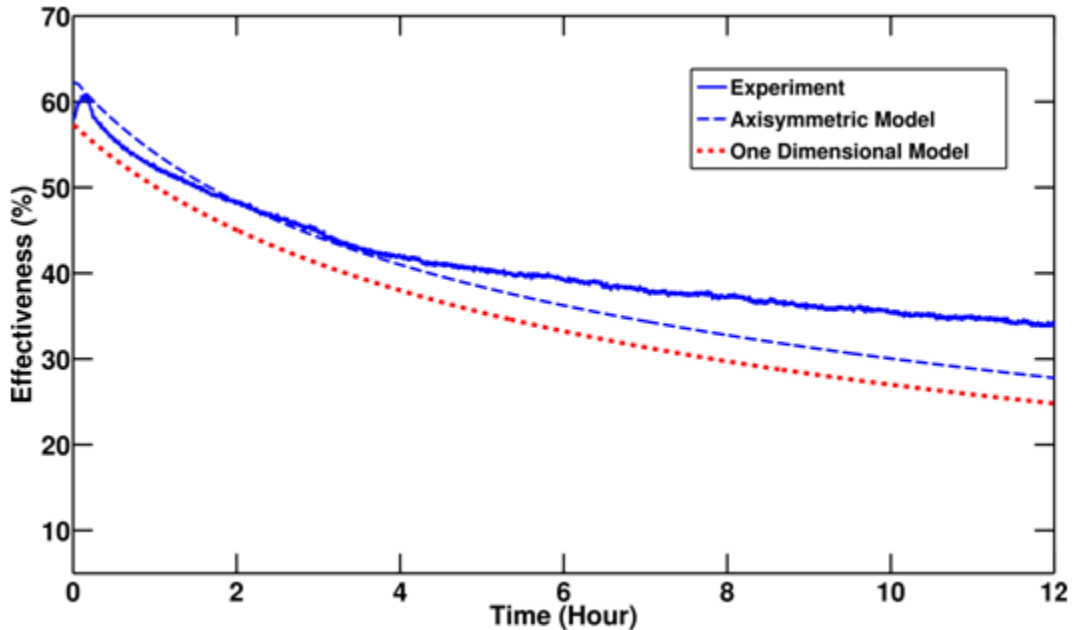


Figure 1.32: Predicted and actual effectiveness versus time [29]

Figure 1.33 is the result of a partial rank correlation (PRCC) of parameters that affect the deposit mass. It can be seen that the thermal conductivity and density of the deposit layer are insignificant in affecting the deposit mass, whereas the inlet temperature, inlet pressure, particulate concentration, and mass flow rate all have significant effects. A positive correlation value means that an increase in that parameter will increase the deposit mass and a negative value means an increase in the parameter will decrease the deposit mass.

Figure 1.34 shows that the PRCC ranks more significantly the effect of thermal conductivity and deposit density on effectiveness reduction. This means that as thermal conductivity and density are increased, a decrease in the effectiveness reduction, or an increase in effectiveness, can be expected. The same applies for inlet pressure. Increasing the inlet temperature, particulate concentration, and mass flow rate have the effect of depositing more mass on the tube surfaces and increasing the effectiveness reduction, or reducing effectiveness. Of these parameters, only the deposit density and conductivity are properties of the layer and must be assumed.

Abarham also noted the significant impact of small changes in porosity on the deposit layer thermal conductivity (Figure 1.35) [29]. In addition, Abarham noted the dependence of deposit conductivity on temperature. This figure really highlights the importance of deposit properties on thermal conductivity and can greatly affect heat exchanger effectiveness.

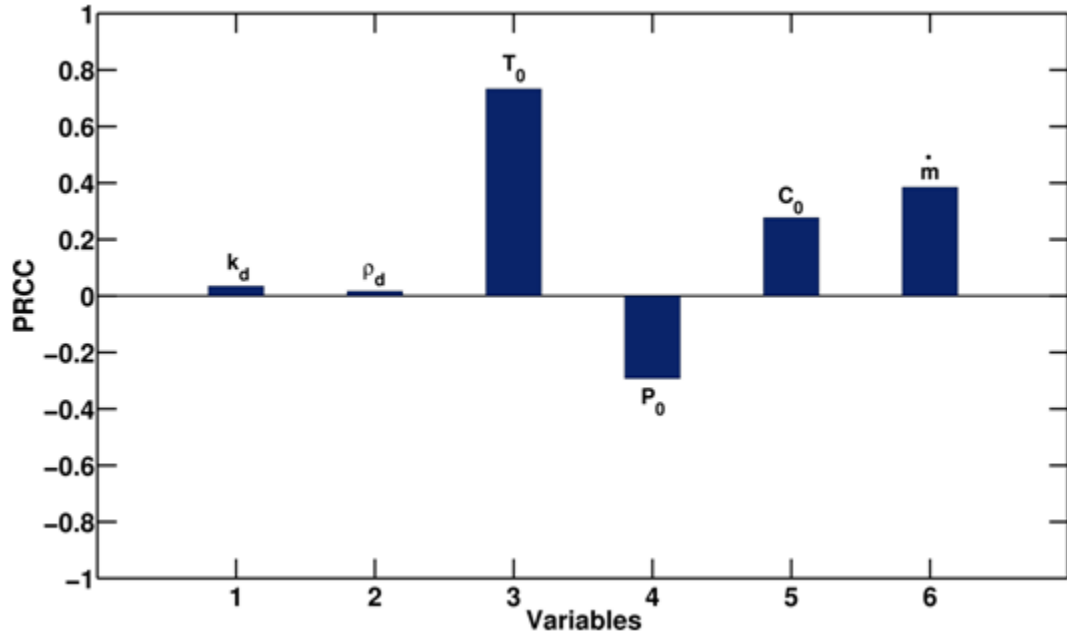


Figure 1.33: PRCC values for parameters influencing deposit mass gain [29]

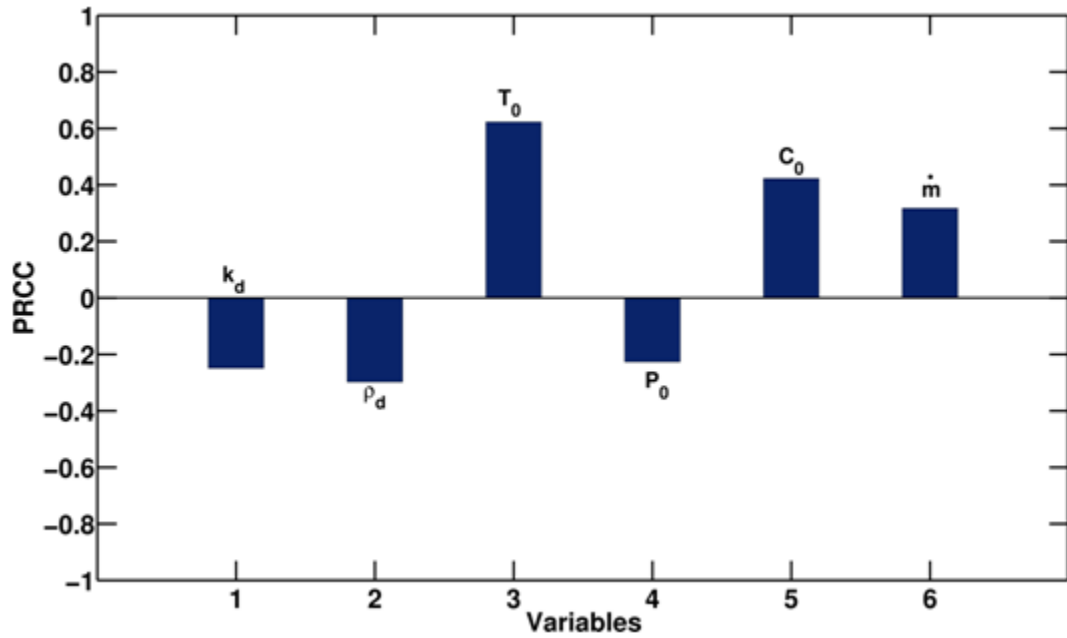


Figure 1.34: PRCC values of parameter influence on heat transfer reduction [29]

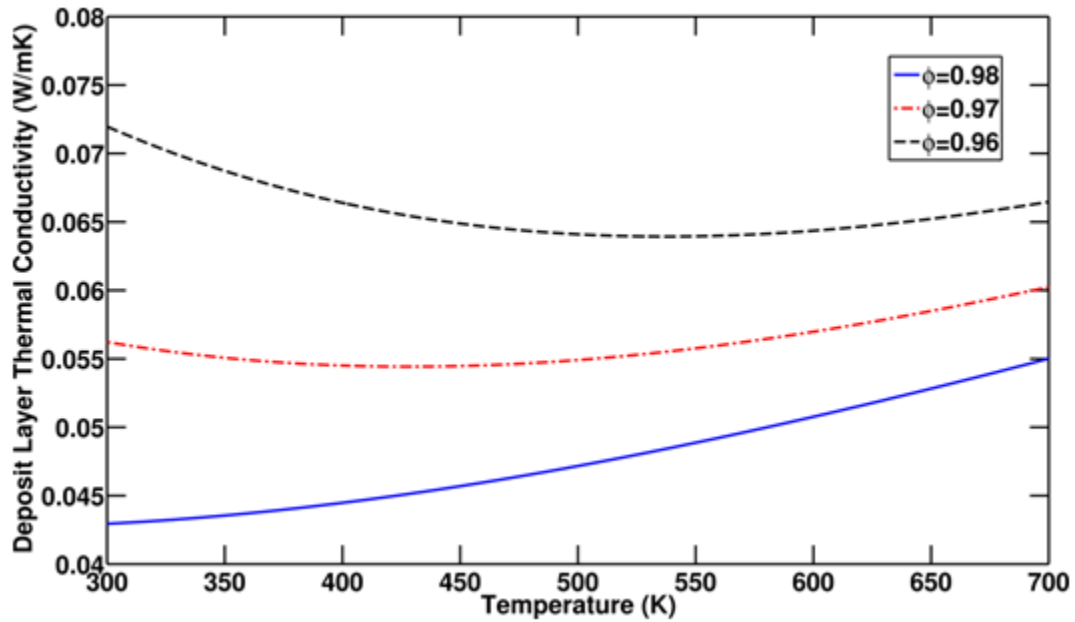


Figure 1.35: Effect of porosity and surface temperature on deposit layer thermal conductivity [29]

It is evident that significant effort has been spent on understanding the effect of particles and volatiles on the effectiveness of heat exchangers. Models have been developed to predict the performance of these heat exchangers however require physical insights into deposit properties to produce accurate results. Properties of deposit layers have been analyzed with ex-situ techniques and while these deposit property analyses produce a good representation of thermal conductivity, they do not necessarily represent accurate measurements of the deposit in-situ. Volatile species in the layer can change the thermal conductivity of the layer and the heat transfer characteristics of the EGR cooler; thus deposit properties must be measured in-situ.

The purpose of this thesis is to introduce a novel measurement methodology to determine the in-situ thermal properties of a deposit layer in a research oriented EGR heat exchanger. In addition, investigations into key parameters for deposit layer removal are also presented. The organization of this thesis is as follows: discussed first is the measurement principle, followed by a description of the equipment employed to make the required measurements, followed by results, and finally conclusions and future work.

## 1.6 References

- [1] Chang, D. Y. and Gerpen, J. H. V., "Determination of Particulate and Unburned Hydrocarbon Emissions from Diesel Engines Fueled with Biodiesel," *SAE International*, 1998.
- [2] Janssen, A., Muether, M., Pischinger, S., Kolbeck, A., Lamping, M., and Koerfer, T., "Tailor-Made Fuels for Future Advanced Diesel Combustion Engines," *SAE International*, 2009.
- [3] Knothe, G., Sharp, C. A., and Ryan Iii, T. W., "Exhaust emissions of biodiesel, petrodiesel, neat methyl esters, and alkanes in a new technology engine," *Energy and Fuels*, vol. 20, no. 1, pp. 403-408, 2006.
- [4] Northrop, W. F., Bohac, S. V., and Assanis, D. N., "Premixed Low Temperature Combustion of Biodiesel and Blends in a High Speed Compression Ignition Engine," *SAE International*, 2009.
- [5] Hoard, J., Abarham, M., Styles, D., Giuliano, J. M., Sluder, C. S., and Storey, J. M. E., "Diesel EGR Cooler Fouling," *SAE International*, 2008.
- [6] Hoard, J., Giuliano, J., Styles, D., Sluder, S., Storey, J., Lewis, S., Strzelec, A., and Lance, M., "EGR Catalyst for Cooler Fouling Reduction," in *DOE Diesel Engine-Efficiency and Emissions Reduction*, Detroit, MI, 2007.
- [7] Sluder, C. S. and Storey, J. M. E., "EGR Cooler Performance and Degradation: Effects of Biodiesel Blends," *SAE International*, 2008.
- [8] Lepperhoff, G. and Houben, M., "Mechanisms of Deposit Formation in Internal Combustion Engines and Heat Exchangers," 1993.
- [9] Zhan, R., Eakle, S. T., Miller, J. W., and Anthony, J. W., "EGR System Fouling Control," *SAE Int. J. Engines*, vol. 1, no. 1, pp. 59-64, 2008.
- [10] Sluder, C. S., Storey, J. M. E., Lewis, S. A., Styles, D., Giuliano, J., and Hoard, J. W., "Hydrocarbons and Particulate Matter in EGR Cooler Deposits: Effects of Gas



- Flow Rate, Coolant Temperature, and Oxidation Catalyst," *SAE Int. J. Engines*, vol. 1, no. 1, pp. 1196-1204, 2008.
- [11] Abarham, M., Hoard, J. W., Assanis, D., Styles, D., Sluder, C. S., and Storey, J. M. E., "An analytical study of thermophoretic particulate deposition in turbulent pipe flows," *Aerosol Science and Technology*, vol. 44, pp. 785-795, 2010.
- [12] Styles, D., Curtis, E., Ramesh, N., Hoard, J., Assanis, D., Abarham, M., Sluder, S., Storey, J., and Lance, M., "Factors Impacting EGR Cooler Fouling - Main Effects and Interactions," in *16th Directions in Engine-Efficiency and Emission Research Conference*, Detroit, MI, 2010.
- [13] Salvi, A. A., Assanis, D., and Filipi, Z., "Impact of Physical and Chemical Properties of Alternative Fuels on Combustion, Gaseous Emissions, and Particulate Matter during Steady and Transient Engine Operation," *Energy & Fuels*, vol. 26, no. 7, pp. 4231-4241, 2012.
- [14] Sluder, C. S., Storey, J. M. E., and Youngquist, A., "ULSD and B20 Hydrocarbon Impacts on EGR Cooler Performance and Degradation," *SAE International*, 2009.
- [15] Nishiwaki, K. and Hafnan, M., "The Determination of Thermal Properties of Engine Combustion Chamber Deposits," 2000.
- [16] Cheng, S.-w. S., "The Impacts of Engine Operating Conditions and Fuel Compositions on the Formation of Combustion Chamber Deposits," *SAE International*, 2000.
- [17] Lance, M. J., Sluder, C. S., Wang, H., and Storey, J. M. E., "Direct Measurement of EGR Cooler Deposit Thermal Properties for Improved Understanding of Cooler Fouling," *SAE International*, 2009.
- [18] Storey, J. M. E., Sluder, C. S., Lance, M. J., Styles, D., and Simko, S., "Exhaust Gas Recirculation Cooler Fouling in Diesel Applications: Fundamental Studies, Deposit Properties and Microstructure," in *International Conference on Heat Exchanger Fouling and Cleaning IX*, Crete, Greece, 2011.

- [19] Abarham, M., Hoard, J., Assanis, D., Styles, D., Curtis, E., and Ramesh, N., "Review of Soot Deposition and Removal Mechanisms in EGR Coolers," *SAE Int. J. Fuels Lubr.*, vol. 3, no. 1, pp. 690-704.
- [20] Teng, H. and Regner, G., "Particulate Fouling in EGR Coolers," *SAE Int. J. Commer. Veh.*, vol. 2, no. 2, pp. 154-163, 2009.
- [21] Epstein, N., "Elements of particle deposition onto nonporous solid surfaces parallel to suspension flows," *Experimental Thermal and Fluid Science*, vol. 14, no. 4, pp. 323-334, 1997.
- [22] Maricq, M. M., "On the electrical charge of motor vehicle exhaust particles," *Journal of Aerosol Science*, vol. 37, no. 7, pp. 858-874, 2006.
- [23] dela Cruz, E., Chang, J. S., Berezin, A. A., Ewing, D., Cotton, J. S., and Bardeleben, M., "Electrical effect of soot depositions in a co-axial wire pipe flow," *Journal of Electrostatics*, vol. 67, no. 2-3, pp. 128-132, 2009.
- [24] Ismail, B., Ewing, D., Cotton, J. S., and Chang, J.-S., "Characterization of the Soot Deposition Profiles in Diesel Engine Exhaust Gas Recirculation (EGR) Cooling Devices Using a Digital Neutron Radiography Imaging Technique," 2004.
- [25] Stolz, A., Fleischer, K., Knecht, W., Nies, J., and Ströhle, R., "Development of EGR Coolers for Truck and Passenger Car Application," 2001.
- [26] Sluder, C. S., Storey, J., Lance, M. J., and Barone, T., "Removal of EGR Cooler Deposit Material by Flow-Induced Shear," *SAE Int. J. Engines*, vol. 6, no. 2, pp. 999-1008, 2013.
- [27] Bravo, Y., Moreno, F., and Longo, O., "Improved Characterization of Fouling in Cooled EGR Systems," 2007.
- [28] Andrews, G. E., Clarke, A. G., Rojas, N. Y., Sale, T., and Gregory, D., "The Transient Storage and Blow-Out of Diesel Particulate In Practical Exhaust Systems," 2001.

- [29] Abarham, M., "Investigation of Nano-Particulate Transport in Non-Isothermal Turbulent Internal Flows," in *Mechanical Engineering*. vol. Ph.D. Ann Arbor: University of Michigan, 2011.
- [30] Ciro, W. D., Eddings, E. G., and Sarofim, A. F., "Experimental and numerical investigations of transient soot buildup on a cylindrical container immersed in a jet fuel pool fire," *Combustion Science and Technology*, vol. 178, no. 12, pp. 2199-2218, 2006.

## CHAPTER 2

### MEASUREMENT PRINCIPLE AND EXPERIMENTAL EQUIPMENT

In order to determine the thermal conductivity of a deposit layer in-situ, a number of deposit layer measurements are required and are performed by various pieces of experimental equipment. This chapter will introduce the measurement principle employed to determine the thermal conductivity of a deposit layer, followed by a description of the experimental visualization rig, and corresponding measurement hardware.

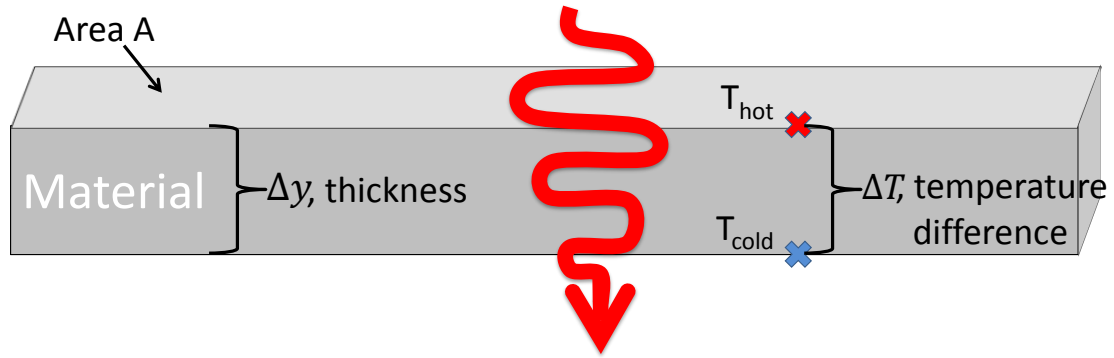
#### 2.1 Measurement Principle

As illustrated earlier, thermal conductivity of the deposit layer significantly affects the heat transfer characteristics of heat exchangers. To calculate thermal conductivity, the 1-D heat equation is employed and rearranged for conductivity [1]:

$$\dot{Q} = \frac{k \times A \times \Delta T}{\Delta y} \rightarrow k = \frac{\dot{Q} \times \Delta y}{A \times \Delta T}$$

Equation 2.1: 1-D heat conduction equation

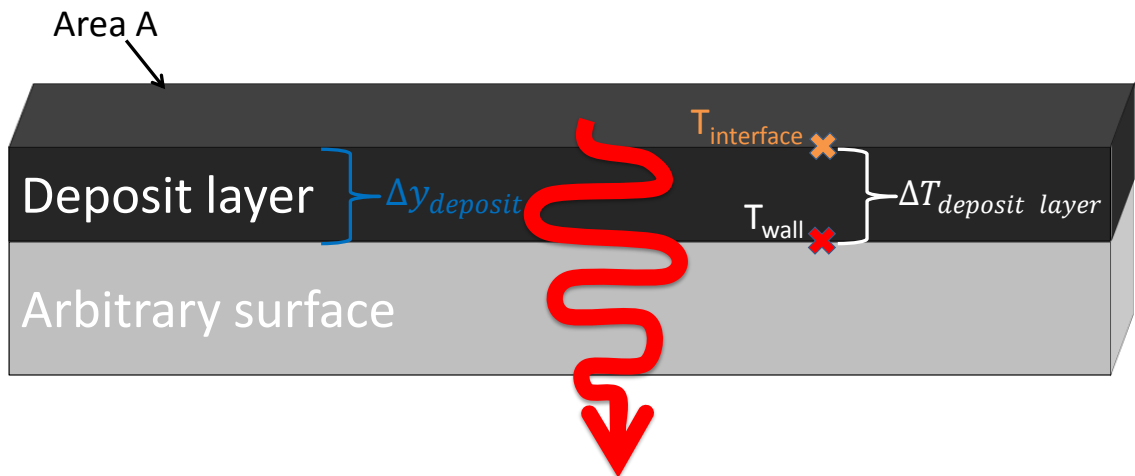
Where  $k$  is the thermal conductivity [W/mK],  $\dot{Q}$  is the heat transfer rate [W],  $A$  is the surface area of heat conduction [m<sup>2</sup>],  $\Delta y$  is the thickness of the material heat is flowing through [m], and  $\Delta T$  is the temperature difference of the surfaces of the material. Figure 2.1 shows a schematic of the relevant parameters in heat conduction.



Heat transfer rate,  $\dot{Q}$

Figure 2.1: Schematic of heat conduction

With the identified measurements, the conductivity of the material can be determined. This sample principle can be used to determine the conductivity of a deposit layer, however slight modifications are required. Expanding Figure 2.1 to encompass an arbitrary deposit layer developed on an arbitrary surface, as shown in Figure 2.2, specific measurements to calculate deposit conductivity are introduced.



Heat transfer rate,  $\dot{Q}$

Figure 2.2: Schematic of heat conduction through deposit layer with required measurements for thermal conductivity measurements

To calculate the deposit layer thermal conductivity, the heat transfer rate  $\dot{Q}$  through the layer is required. Various techniques for determining heat flux exist, however suffer from accuracy and precision errors; specifically differential temperature derived heat flux calculations based on Equation 2.1. In addition, differential temperature based

calculations can also suffer from the influence of convective heat transfer if the measuring thermocouple is exposed to the convective fluid. The thermocouple also generates a footprint and thermal resistance on the surface being measured thereby affecting the temperature and heat flux. Therefore, a heat flux probe that produces a self-generated voltage corresponding to the heat flux is selected for increased measurement confidence and is placed in direct contact with the deposit layer (Figure 2.3). To create heat transfer through the layer, a temperature potential is created with hot air/exhaust flow on the deposit side and coolant flow on the metal side. The  $T_{\text{wall}}$  temperature is measured by an embedded K-type thermocouple in the heat flux probe, the  $\Delta y_{\text{deposit}}$  is determined by the 3-D optical microscope, and the  $T_{\text{interface}}$  is determined by an infrared camera as shown in Figure 2.3. All measurements are performed on the heat flux probe to ensure consistency and accuracy of results.

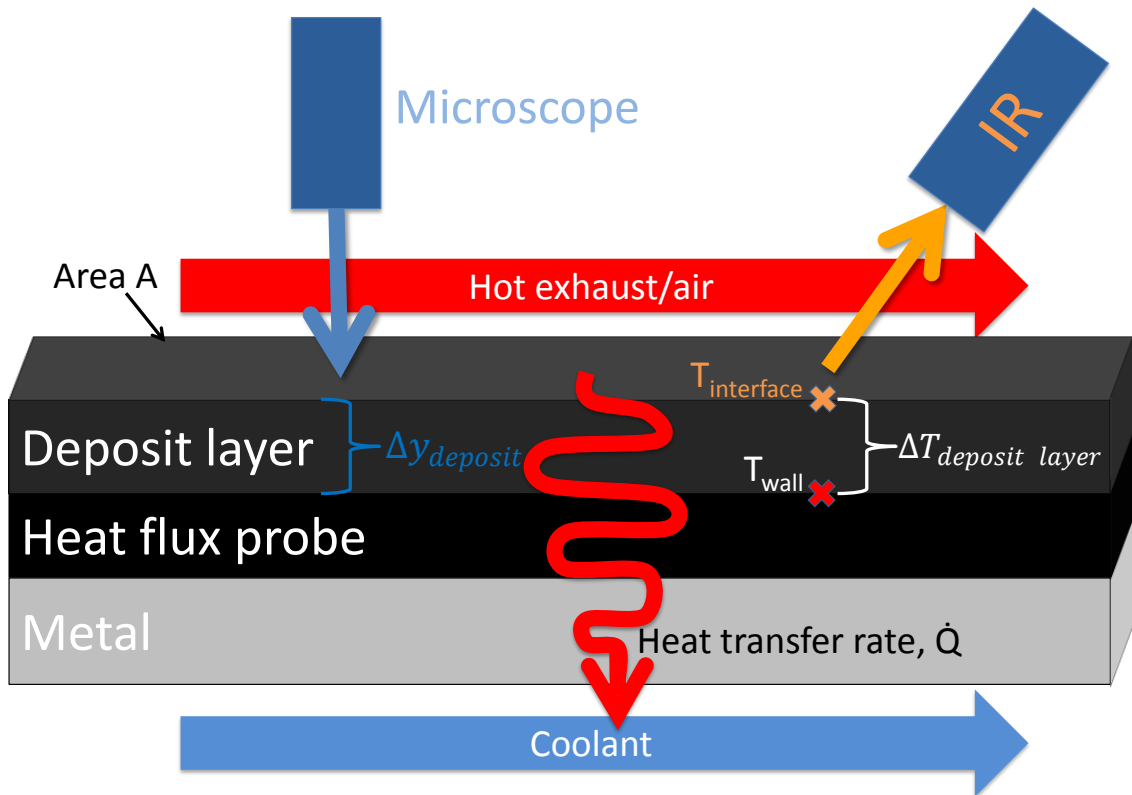


Figure 2.3: Schematic of heat conduction through deposit layer with required measurements and instruments

The final calculation for deposit layer thermal conductivity is as follows (Equation 2.2):

$$k_{deposit\ layer} = \frac{\dot{Q} \times \Delta y_{deposit}}{A_{deposit} \times (T_{interface} - T_{wall})}$$

Equation 2.2: Final form of deposit layer conductivity calculation

## 2.2 Experimental hardware

### 2.2.1 Visualization rig

In order for the experimental visualization rig to simulate an actual EGR cooler, it was designed to replicate similar EGR cooler Reynolds number flows while providing optical and infrared access for measurements. This rig is an evolution of the same test stand Abarham et al. have reported on previously [2, 3].

The simulated cooler utilizes a rectangular cross sectional flow area of dimensions 21.5x12x280 mm and is sized to experience anywhere from laminar, transition, and turbulent flows. The side opposite the optical window is a stainless steel specimen. The specimen is cooled by coolant flow and allows for thermophoretic deposition onto its 1 mm thick stainless steel surface and heat flux probe as shown in Figure 2.4. In addition to flowing exhaust gas, the rig can also flow hot air for heat flux analysis and characterization of deposit layer properties (Figure 2.5). This rig also allows for various temperature and pressure instrumentation above and below the stainless steel test specimen.





The coolant inlet and outlet are offset in height to prevent vapor lock and ensure consistent cooling. This approach prevents coolant from separating from the bottom-side of the stainless steel specimen resulting in un-cooled locations. The coolant passage area and volume are larger than the exhaust passage, as shown in Figure 2.6. This is to ensure sufficient cooling with a large thermal mass of coolant as well as to eliminate exhaust side specimen temperature gradients resulting from wall and coolant boundary layer effects.

A thin 1 mm test specimen was adopted due to its lower thermal inertia and to facilitate the 1-D heat transfer approximation through the heat flux probe. The assembled and exploded views of the visualization rig are provided in Figure 2.7.

The test rig takes an exhaust sample from the high-pressure exhaust loop on a diesel engine. The high-pressure exhaust drives the sample flow to the rig without the need for a sample pump. Flow is controlled with the use of production stepper EGR motors. Heated compressed air is used to warm up and cool down the fixture to prevent water condensation when exhaust gas is sampled and to also prevent the thermal stressing of optical components.

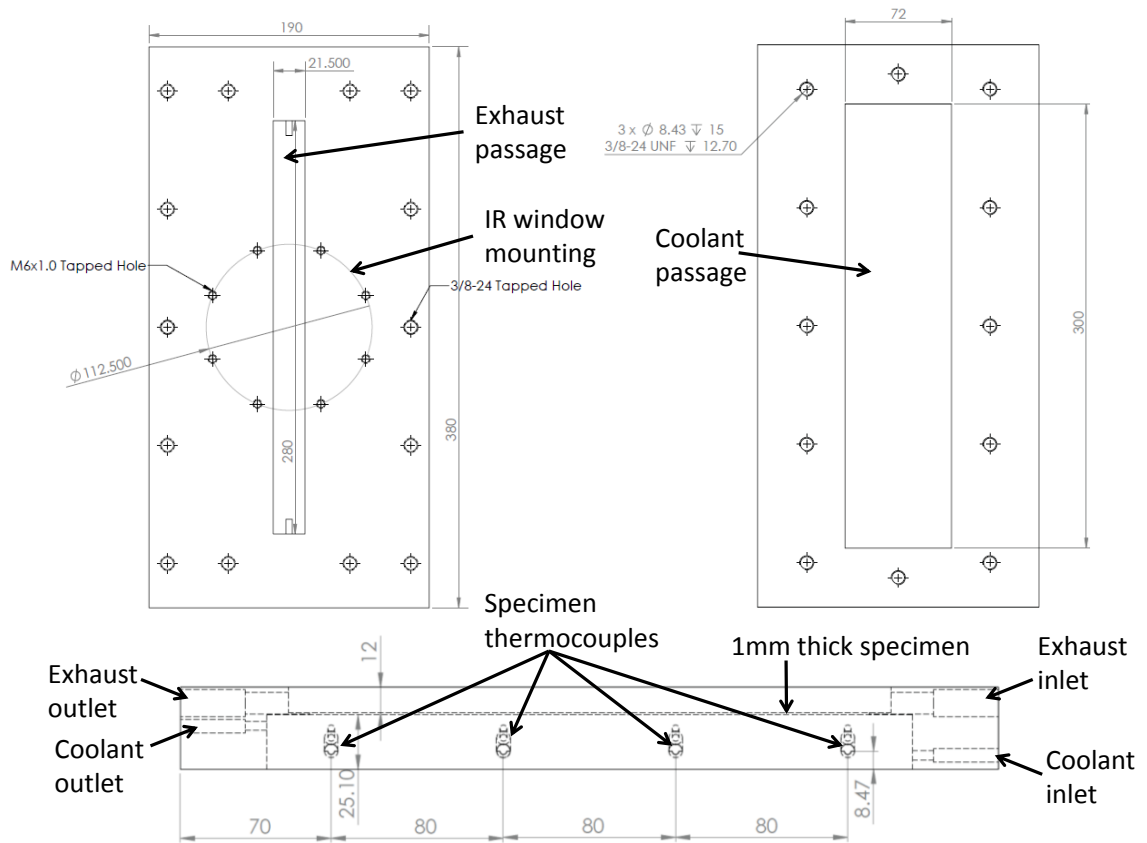


Figure 2.6: Visualization rig version 3 dimensional drawing

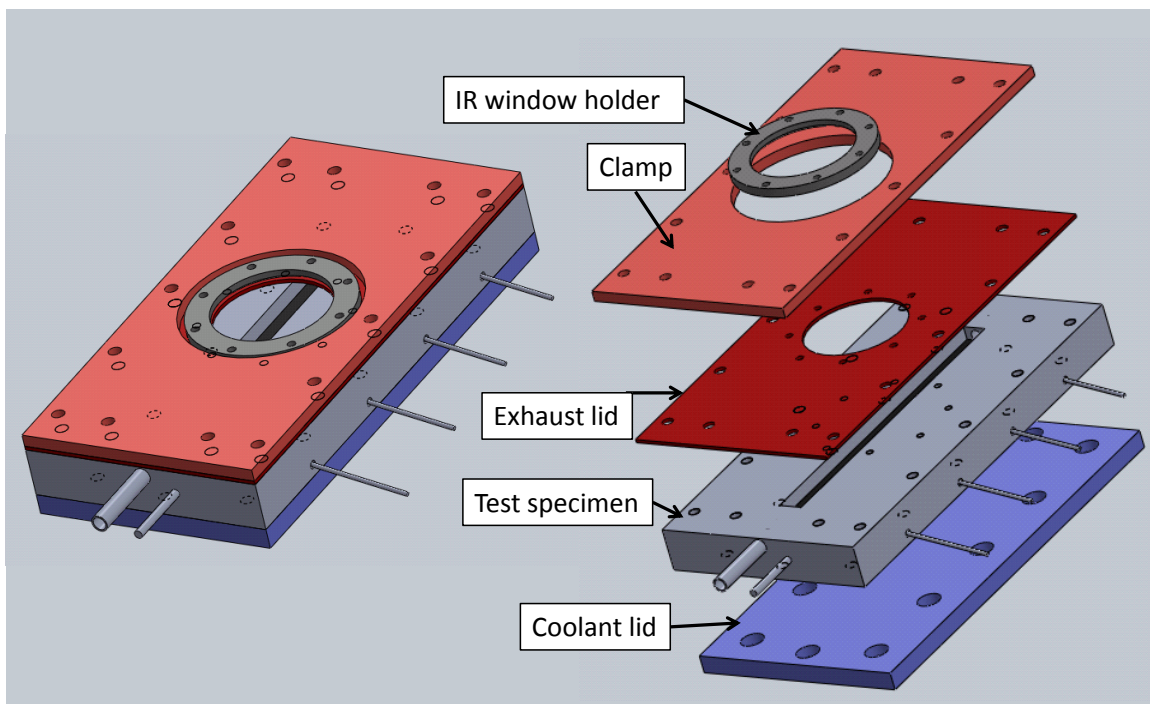


Figure 2.7: Assembled and exploded views of visualization rig version 3

### 2.2.2 Infrared camera

A FLIR SC600 7.5 – 13  $\mu\text{m}$  long-range infrared camera is employed to measure the deposit layer surface temperature. The camera measures from 0 – 650°C  $\pm$  2°C or 2% of reading. The camera is capable of performing time-lapse imaging as well as video recording.

The long-range wavelength was selected for a number of reasons. Primarily, the radiation detected by the camera will need to travel through an environment high in CO<sub>2</sub> and H<sub>2</sub>O concentration resulting from combustion. The long-wave spectrum, as shown in Figure 2.8 from 7.5 – 13  $\mu\text{m}$ , indicates maximum transmittance attenuation resulting from these two molecules. This allows for robust infrared measurement in an environment of exhaust gas without additional, expensive wavelength filters.

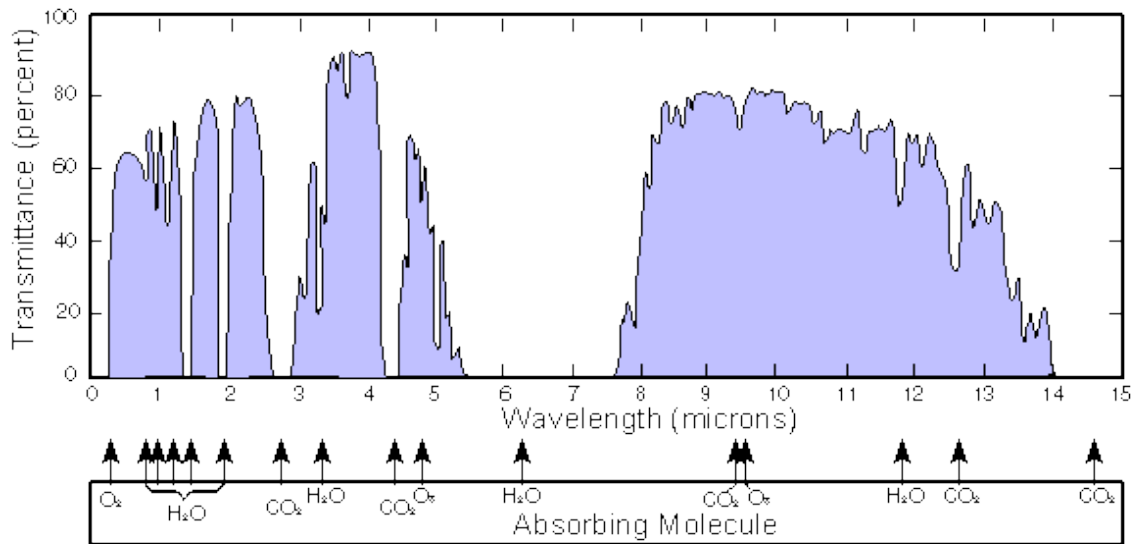


Figure 2.8: Molecular attenuation in the infrared spectrum[4]

Data acquisition and post processing of the infrared images is handled by the FLIR ExaminIR® software. This software also allows for user specified emissivity, ambient temperature, and ambient humidity corrections as well as incorporation of external optic transmissivity and temperature.

### Infrared thermography

The use of infrared thermography for temperature determination has been utilized in various fields ranging from academic research, industrial safety, and even national security. One of the main advantages of infrared technology is its non-intrusive principle, allowing for temperature observation from a distance and without disturbing the measurement object. For these reasons, infrared thermography was selected to measure the surface temperature of a deposit layer in order to determine the thermal properties of the layer.

For typical materials, incident wavelength specific radiation can be absorbed, reflected, or transmitted. The sum of these parts is always equal to 1:

$$\alpha_{\lambda} + \rho_{\lambda} + \tau_{\lambda} = 1$$

Equation 2.3: Absorptance, reflectance, and transmittance

Where  $\alpha$  is the absorptance,  $\rho$  is the reflectance, and  $\tau$  is the transmittance. Kirchhoff's law states that spectral absorptance and spectral emittance are equal at a specified wavelength and temperature. Emissivity is a value between 0 and 1 and is the ratio of radiated power from an object compared to a blackbody at the same wavelength and temperature:

$$\varepsilon_{\lambda} = \frac{W_{\lambda,object}}{W_{\lambda,blackbody}}$$

The emissivity of an object is a critical property for infrared thermography as it determines how much radiation is emitted from the object. For an opaque object and substituting emittance for absorptance, Equation 2.3 becomes:

$$\varepsilon_{\lambda} + \rho_{\lambda} = 1$$

According to the Stefan-Boltzmann formula, the total power radiated from a blackbody is related to the fourth power of its temperature:

$$W_b = \sigma T^4$$

Equation 2.4: Stefan-Boltzmann formula for a blackbody

Where  $W_b$  is the radiated power,  $\sigma$  is the Stefan-Boltzmann constant ( $5.67E-8$   $W/m^2K^4$ ), and  $T$  is the blackbody temperature. For a greybody, the formula becomes

$$W_b = \epsilon\sigma T^4$$

Equation 2.5: Stefan-Boltzmann formula for a greybody

Measurement of an object temperature is not as simple as pointing an infrared camera at it and recording. The total radiation received by the camera is affected by other parameters, such as ambient reflections, atmospheric filtration/emission, and external optics as well as object emission and transmission (illustrated in Figure 2.9).

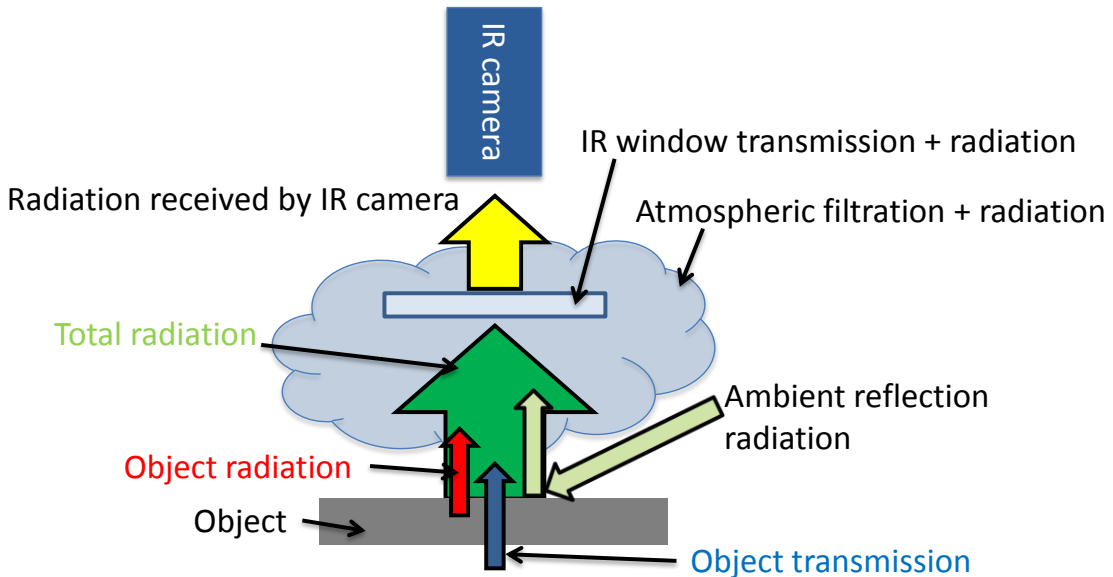


Figure 2.9: Total radiation received by infrared camera

Ambient reflections may stem from hot/cold sources in the environment. The radiation from these sources may be reflected off of the object and appear as radiation from the object, thus altering the perceived object temperature.

Object transmission may result from partial translucence of the target object in the infrared spectrum. Imagine a thin plastic bag held up to the light. Light can still transmit through the plastic bag however the bag is still opaque enough to be seen. This is the same concept but applied to the infrared spectrum.

Atmospheric and infrared window filtration occurs due to molecules in the material absorbing incident radiation. This serves to reduce the transmission of incident radiation from the target object to the infrared detector. The absorbing material also becomes a radiant emitter if the transmittance is less than 1 and contributes to the total radiation received by the infrared detector.

Summing up all of the sources and filters of infrared radiation, and assuming an opaque object and minimal reflections from the infrared window, the total radiation received by the infrared camera is:

$$W_{Total} = \varepsilon \times \tau_{Atmosphere} \times \tau_{IR\ window} \times W_{Object} + (1 - \varepsilon) \times \tau_{Atmosphere} \times \tau_{IR\ window} \times W_{Ambient\ reflections} + (1 - \tau_{Atmosphere}) \times \tau_{IR\ window} \times W_{Atmosphere} + (1 - \tau_{IR\ window}) \times W_{IR\ window}$$

Equation 2.6: Total radiation received by the infrared camera

Where  $\varepsilon$  is the emissivity of the object,  $\tau_{Atmosphere}$  is the transmission through the atmosphere,  $\tau_{IR\ window}$  is the transmission through the infrared window,  $W_{Object}$  [W/m<sup>2</sup>] is the radiated power from the object,  $W_{Ambient\ reflections}$  [W/m<sup>2</sup>] is the radiated power from ambient reflections,  $W_{Atmosphere}$  [W/m<sup>2</sup>] is the radiated power from the atmosphere,  $W_{IR\ window}$  [W/m<sup>2</sup>] is the radiated power from the infrared window, and  $W_{Total}$  [W/m<sup>2</sup>] is the total radiated power received by the infrared camera.

In order to determine  $W_{Object}$  and the target temperature, a few parameters are required:

1. Emissivity of the target – covered in Chapter 3
2. Atmospheric transmission – determined by
  - a. Atmospheric temperature
  - b. Atmospheric humidity
  - c. Distance through atmosphere
  - d. Composition of atmosphere
3. Infrared window transmission – covered in Chapter 3
4. Infrared window temperature
5. Ambient reflection temperature

Most of these parameters can be measured with sensors. The infrared window transmission and emissivity of the target will need to be determined and are discussed in Chapter 3.

The radiation is received by an array of microbolometer sensors in the infrared camera. The change in temperature of the sensors from the incident radiation corresponds to a change in the sensor's electrical resistance. The resistance is measured and processed into a temperature and, in combination with the rest of the array, generates a thermal image. The combination of all of these measurements allow for the successful measurement of the object temperature.

### 2.2.3 Infrared and optically transmissible window

Both visual and infrared measurements of the deposit layer are required and formed the basis of window requirements. The window will be subjected to high temperature and high pressure, adding to the list of considerations. In addition, infrared windows act to filter infrared signals thus a high transmissivity window is required for optimal measurements.

While only a handful of window materials satisfy the requirements ( $\text{CaF}_2$ ,  $\text{BaF}_2$ , Sapphire, KRS-5), the Fluke FLK-100-CLKT window was selected due to its use in highly volatile environments, such as high voltage inspection, and its compatibility with long-wave infrared. A list of specifications is listed in Table 2.1.

The window mount was modified from factory to promote a more robust and secure mounting. Additional periphery mounting holes in the aluminum holder were added to evenly distribute clamping loads. The window was secured to the holder using RTV epoxy, creating a seal between the flow in the test specimen and the environment as shown in Figure 2.10. The RTV provides soft mounting and accommodates for the thermal expansion of the window. This mounting also allows for the Al window housing, instead of the infrared window, to absorb the clamping loads through carbon based gaskets and increases the robustness of the apparatus.

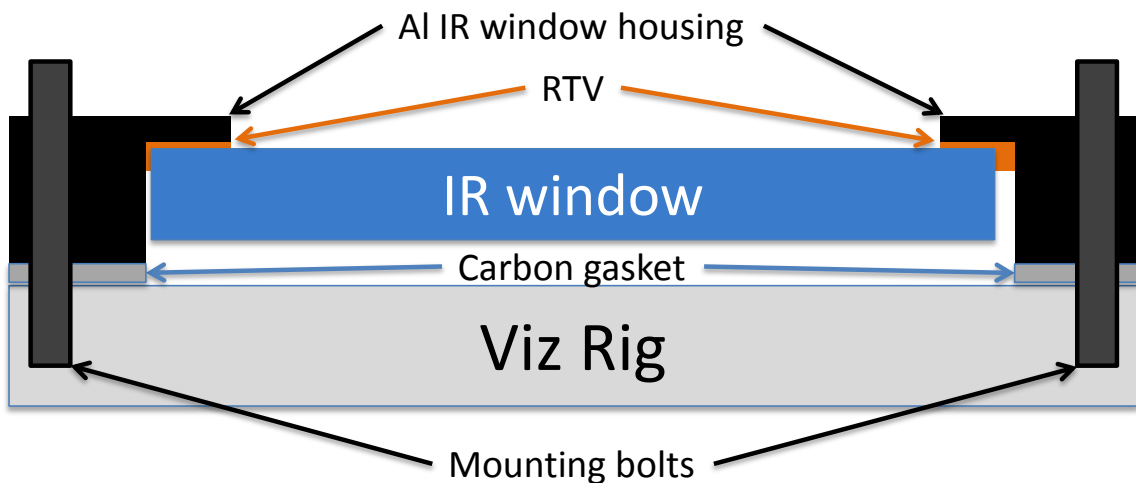


Figure 2.10: Infrared window mounting



Table 2.1: Infrared window specifications

Crystal insert diameter [mm]	100
Viewing aperture diameter [mm]	89
Thickness [mm]	4
Maximum operating temperature [C]	1400
Shortwave IR capable	Yes
Midwave IR capable	Yes
Longwave IR capable	Yes

The transmissivity and window composition are of proprietary nature, however an overall transmissivity of the window was determined to be 0.85 and is discussed in Chapter 3.

#### 2.2.4 Microscope

A Keyence VH-Z50L microscope provides optical imaging and thickness measurement of the deposit layer. The microscope is capable of 50-500x magnification and enables thickness readings via a 3-D measurement algorithm. The user specifies the upper and lower focal bound of the desired image and the microscope traverses the interval in prescribed steps. At each step, an image is taken and after the process is finished, a fully focused 3-D image is produced with corresponding height data. Essential to these measurements is deposit surface lighting, which is provided by a fiber optic light.

The microscope is also capable of high-resolution time-lapse imaging and video recording.

#### 2.2.5 Heat flux probe

Accurate measurement of heat flux is essential to determine thermal conductivity. The probes constitute a large thermal resistance and to minimize their thermal effects, the probes were epoxied onto the exhaust side of the stainless steel channel in the visualization rig. The thin stainless steel metal provides minimal thermal resistance and

acts as a thermal sink for the probe. This configuration allows thermophoresis to build a deposit layer on top of the heat flux probes and allows for the direct measurement of various deposit properties.

Two probes of similar dimensions (13x25x2 mm) were installed in-line with the flow. The first probe serves to develop and maintain stabilized flow and eliminate leading edge flow effects while the second probe serves as the main measurement location (Figure 2.11, Figure 2.12). An embedded K type thermocouple measures the temperature between the interface of the probe and bottom of the deposit layer.



Figure 2.11: Heat flux probe installation schematic



Figure 2.12: Actual heat flux probe installation

All wires were routed out of the fixture through a downstream side port as noted in Figure 2.12. The side port was sealed from the environment with an epoxy sealed tube through which the wires exited. To ensure thermal longevity of the wires, a thin coating of high temperature RTV was applied to the wires and used to secure the wires to the stainless steel channel. Properties of the probe are found in Table 2.2.

Table 2.2: Concept Engineering heat flux probe properties

Model	FM-060-K
Dimensions	13mm x 25mm x 2mm
Thermal conductivity	0.311 W/mK
Heat flux range	12600 W/m <sup>2</sup>
Temperature range	-50 to 150 °C
Emissivity	0.94
Sensitivity	~140 (W/m <sup>2</sup> )/mV

### 2.2.6 Diesel engine

Experimental work was conducted on a production Ford 6.4L V-8 with specifications shown in Table 2.3 and is pictured in Figure 2.13. This engine utilizes two liquid cooled high pressure EGR coolers in combination with high pressure common rail fuel injection, sequential turbo charging with high-pressure VGT, an intake throttle, and a DOC/DPF after-treatment system to satisfy 2007 emissions regulations. The high-pressure common rail fuel delivery system is capable of producing 2000 bar injection pressure and up to 6 injection events per combustion cycle, allowing for advanced combustion strategies. Full ECU access is available, allowing for manual control over injection quantity and timing and various other parameters. A thermal image of the engine at idle conditions is shown in Figure 2.14. The white/yellow color indicates hot exhaust flow from the exhaust headers to the turbo turbine. A sample of exhaust from the right bank of the engine is routed to the on-board EGR cooler identified in the image.

Table 2.3: Diesel engine specifications

Manufacturer	International
Cylinders	8, V configuration
Displacement [L]	6.4
Rated power [kW]	261 @3000 RPM
Peak torque [Nm]	881 @2000RPM
Bore [mm]	98.2
Stroke [mm]	105
Connecting rod length [mm]	176
Wrist pin offset [mm]	0
Compression ratio	17.5
Aspiration	Sequential turbo charging
Piston geometry	Bowl-in-piston
Valves per cylinder	4
Fuel injection system	High pressure common rail
Injector location	Centrally located
Injector holes	6
Cone angle [deg]	154
Injector hole diameter [mm]	0.191
EGR system	Dual sequential high pressure liquid cooled EGR coolers with upstream DOC



Figure 2.13: 6.4L diesel engine

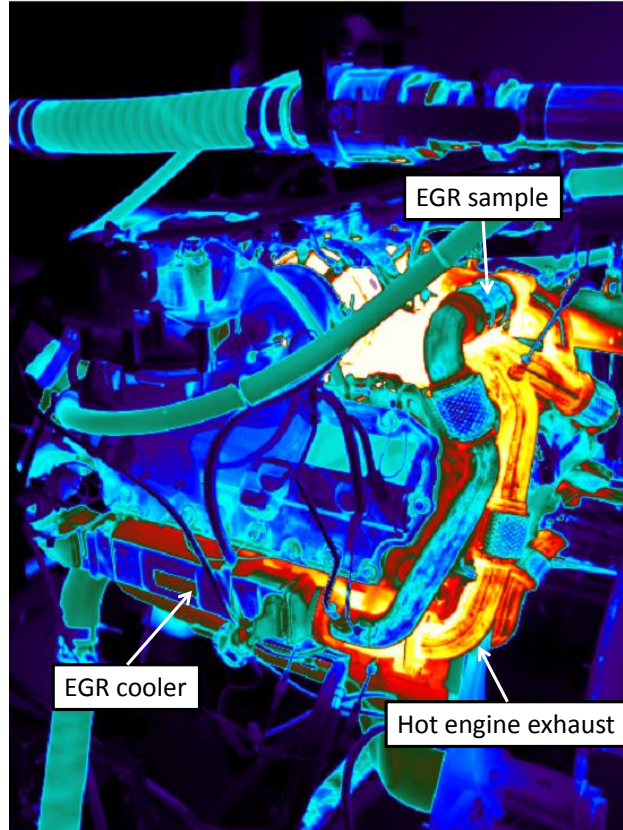


Figure 2.14: Thermal image of diesel engine highlighting exhaust gas flow path and on-board EGR cooler

### 2.2.7 Gaseous emissions analyzer

An AVL SESAM FTIR is utilized to measure gaseous components from the engine exhaust, and is pictured in Figure 2.15. The FTIR component of this analyzer can measure a variety of components due to its broad spectrum IR source measuring multiple compounds. Species concentrations are calculated by comparing IR absorption at certain frequencies with a reference spectrum and applying Lambert-Beer's law.

A CO<sub>2</sub> analyzer is also equipped for EGR rate calculation. An EGR sample is taken from the intake of the engine, filtered, and then passed through heated exhaust lines to a CO<sub>2</sub> analyzer. Then, a non-dispersive infrared analyzer (NDIR) measures the absorption of IR at a certain frequency correlated to CO<sub>2</sub> (2.5 – 8 μm) to determine the concentration of CO<sub>2</sub>.

A paramagnetic oxygen analyzer is equipped on the SESAM as well. The analyzer uses the fact that oxygen is the only exhaust gas compound that is strongly paramagnetic to measure its concentration. As the concentration of oxygen in the analyzer, which is surrounded by a non-uniform magnetic field, changes, a rotational force is imparted on a suspended test body. The voltage required to keep the test body from rotating is proportional to the oxygen concentration of the sample.

In addition, the analyzer also contains a flame ionization detector, FID, to analyze the total hydrocarbon emissions from the exhaust of the engine. The FID determines the mass of carbon in the sample and converts it into a hydrocarbon mass by assuming a specific carbon to hydrogen ratio. The FID measures the ions released from combustion on a burner fueled by a mixture of hydrogen and helium. The sample hydrocarbon laden exhaust flow is premixed with the hydrogen and increases the ion count, which can be correlated to the concentration of hydrocarbons.



Figure 2.15: AVL SESAM emissions analyzer

### 2.2.8 Particulate analyzers

Critical to particulate fouling studies, these instruments analyze the concentration of particulates with different principles and subsequently produce different insights.

#### Cambustion Differential Mobility Spectrometer

The Cambustion Differential Mobility Spectrometer (DMS500) measures exhaust particulate matter in the range of 5 to 1000 nm, and is pictured in Figure 2.16. The instrument inducts sample exhaust flow and filters particles over 1000 nm via a cyclone separator and is mixed with dilution air. The flow is then passed through a corona discharge where a charge is applied on the incoming particles. The flow then travels down a classifier column with a high voltage electrode in the center. The particles get deflected towards the walls of the classifier column according to their charge/drag ratio and deposit their charge on highly sensitive current pickups. Particles with a high charge/low drag ratio are deflected more and detected earlier in the classifier column and vice versa. A schematic of the classifier column is shown in Figure 2.17:



Figure 2.16: Cambustion differential mobility spectrometer (DMS500)

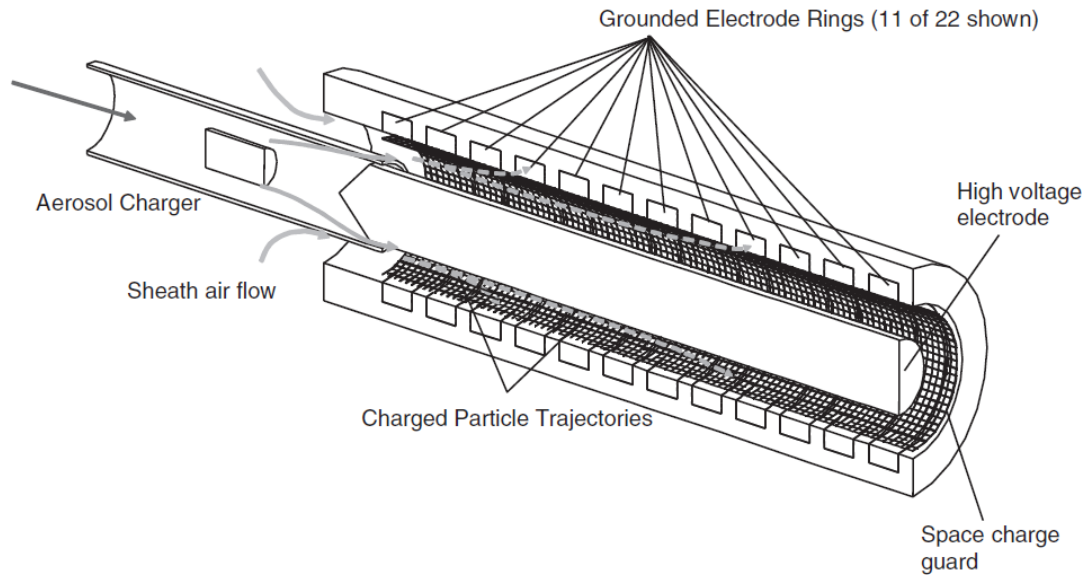


Figure 2.17: DMS500 classifier column schematic [5]

#### AVL 415S smoke meter

An AVL 415S variable smoke meter was also employed to provide steady state smoke value, and is pictured in Figure 2.18. The smoke meter operates using the principles of optics and measures “paper blackening” to determine the corresponding smoke value. The smoke meter draws a known volume of exhaust through a filter paper and measures remitted light produced by a lamp using a photodiode. The current of the photodiode is then converted into voltage and correlated to paper blackening (PB) according to:

$$PB = 10 \cdot \left( \frac{U_{GV} - U_{BV}}{U_{WV} - U_{BV}} \right)$$

Equation 2.7: Paper blackening correlation

Where  $U_{GV}$  is the output voltage of the reflectometer head produced by the sample filter paper,  $U_{BV}$  is the output voltage of the reflectometer head when the filter paper is completely blackened, and  $U_{WV}$  is the output voltage of the reflectometer head when the filter paper is clean. ISO 10054 is then used to convert paper blackening into a



filter smoke number using the PB value and sample volume. To convert to mass concentration, the manufacturer suggested the following correlation [6]:

$$\text{Soot Conc.} \left( \frac{\text{mg}}{\text{m}^3} \right) = \frac{1}{0.405} \cdot 4.95 \cdot \text{FSN} \cdot e^{0.38 \cdot \text{FSN}}$$

Equation 2.8: Manufacturer suggested soot mass correlation

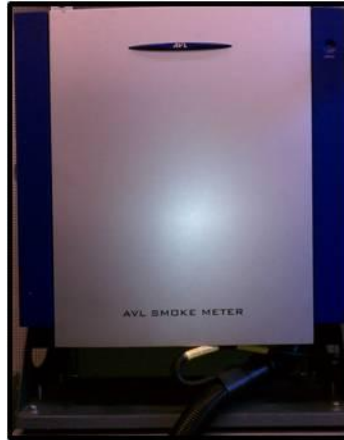


Figure 2.18: AVL 415S variable smoke meter

## 2.3 References

- [1] Incropera, F. and DeWitt, D., Fundamentals of Heat and Mass Transfer, 5th ed.: John Wiley & Sons, Inc, 2002.
- [2] Abarham, M., Chafekar, T., Salvi, A., Hoard, J. W., Styles, D., Scott Sluder, C., and Assanis, D., "In-situ visualization of exhaust soot particle deposition and removal in channel flows," Chemical Engineering Science, vol. 87, no. 0, pp. 359-370, 2013.
- [3] Abarham, M., Chafekar, T., Hoard, J., Styles, D., and Assanis, D., "A Visualization Test Setup for Investigation of Water-Deposit Interaction in a Surrogate Rectangular Cooler Exposed to Diesel Exhaust Flow," SAE International, 2012.
- [4] [http://www.absoluteastronomy.com/topics/Atmospheric\\_window](http://www.absoluteastronomy.com/topics/Atmospheric_window). Accessed July 22, 2013.
- [5] Symonds, J., Reavell, K., Olfert, J., Campbell, B., and Swift, S., "Diesel soot mass calculation in real-time with a differential mobility spectrometer," Journal of Aerosol Science, vol. 1, no. 38, pp. 52-68, 2006.
- [6] Christian, V. R., Knopf, F., Jaschek, A., and Schindler, W., "Eine neue Meßmethodik der Bosch-Zahl mit erhöhter Empfindlichkeit," Motortechnische Zeitschrift 54, pp. 16-22, 1993.

## **CHAPTER 3**

### **EXPERIMENTAL IN-SITU METHODOLOGY**

As noted in Chapter 2, numerous factors affect the total radiation received by the infrared camera ultimately influencing the measured temperature of the target. This chapter describes the methodology for determining the reflected ambient temperatures and the emissivity of deposit layers as well as the effect of the infrared window and IR camera angle on measured temperature. In addition, deposit layer transparency is also discussed.

#### **3.1 Reflected temperature**

Temperature reflections from the ambient can serve to influence the measured target temperature and need to be accounted for. In order to do so, a highly reflective piece of aluminum foil is crumpled up and straightened out and placed on top of the target (Figure 3.1). The crumpled foil acts as a diffuse reflector and the reflected temperature can be determined by measuring the aluminum foil temperature at an emissivity of 1 as shown in Figure 3.2. This is the same procedure that FLIR recommends for reflected temperature determination.

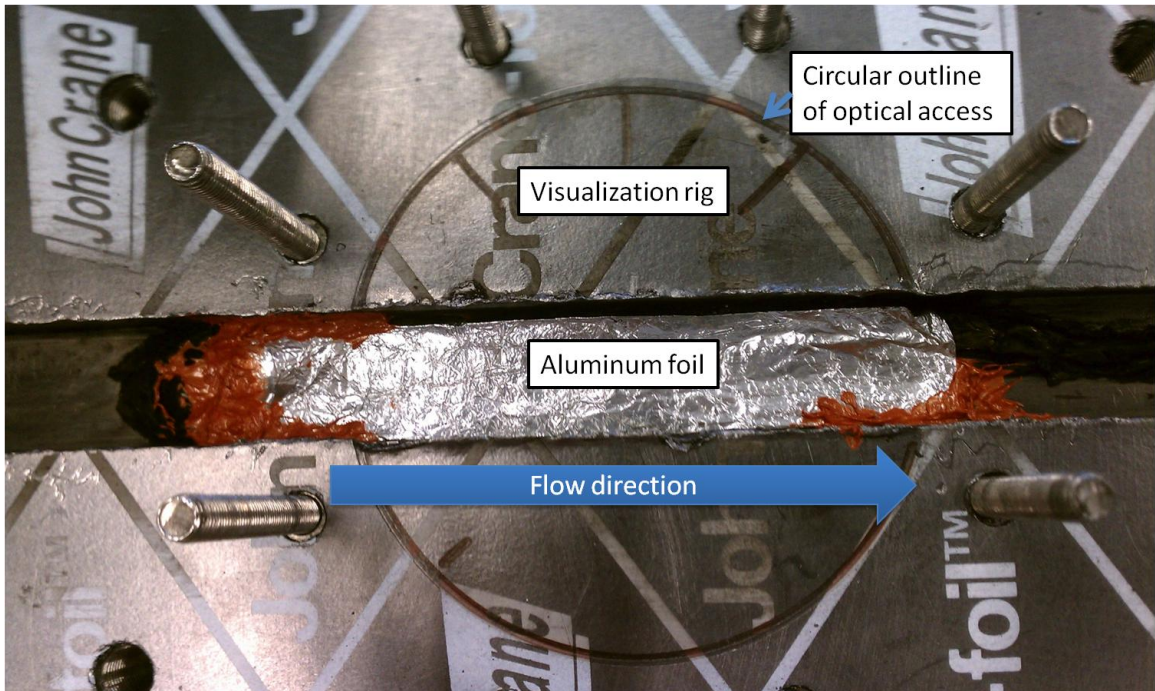


Figure 3.1: Crumpled aluminum foil for reflection temperature

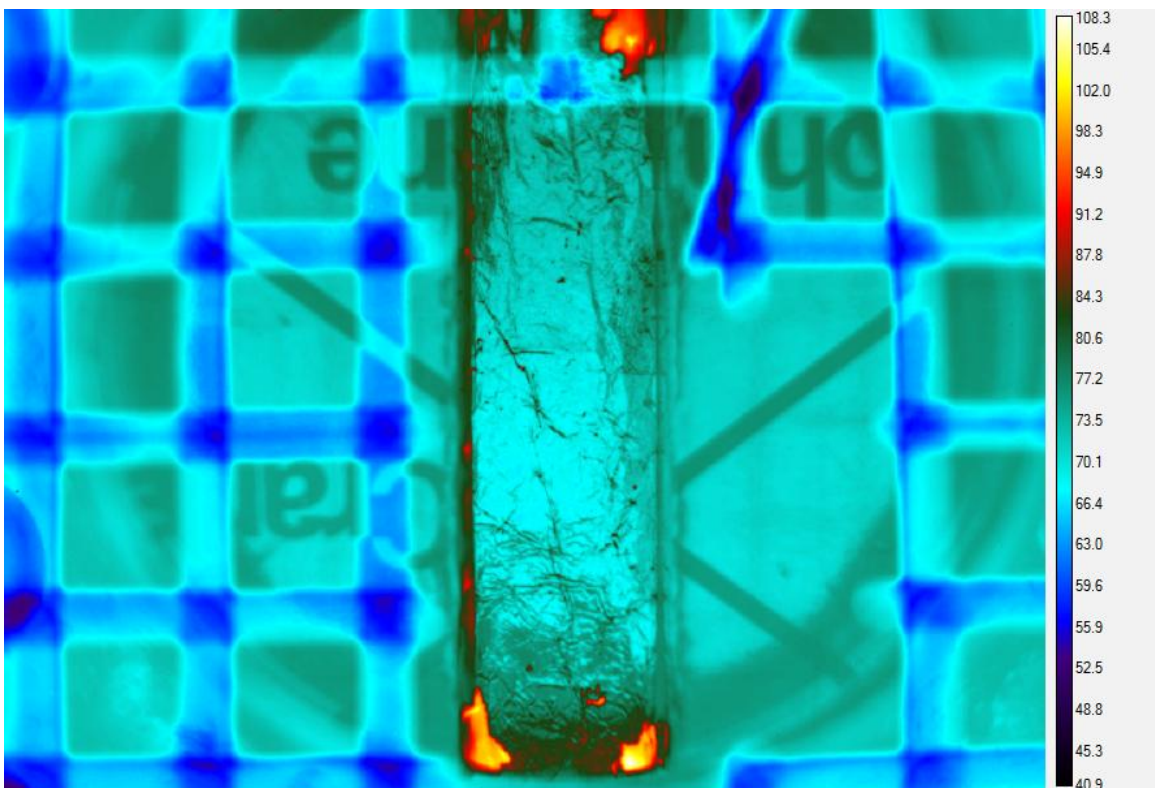


Figure 3.2: Aluminum foil experiment for infrared reflected temperature

The reflected temperatures for varying inlet air flow rates at 200°C are shown in Figure 3.3 for two locations: heat flux probe 1, heat flux probe 2.

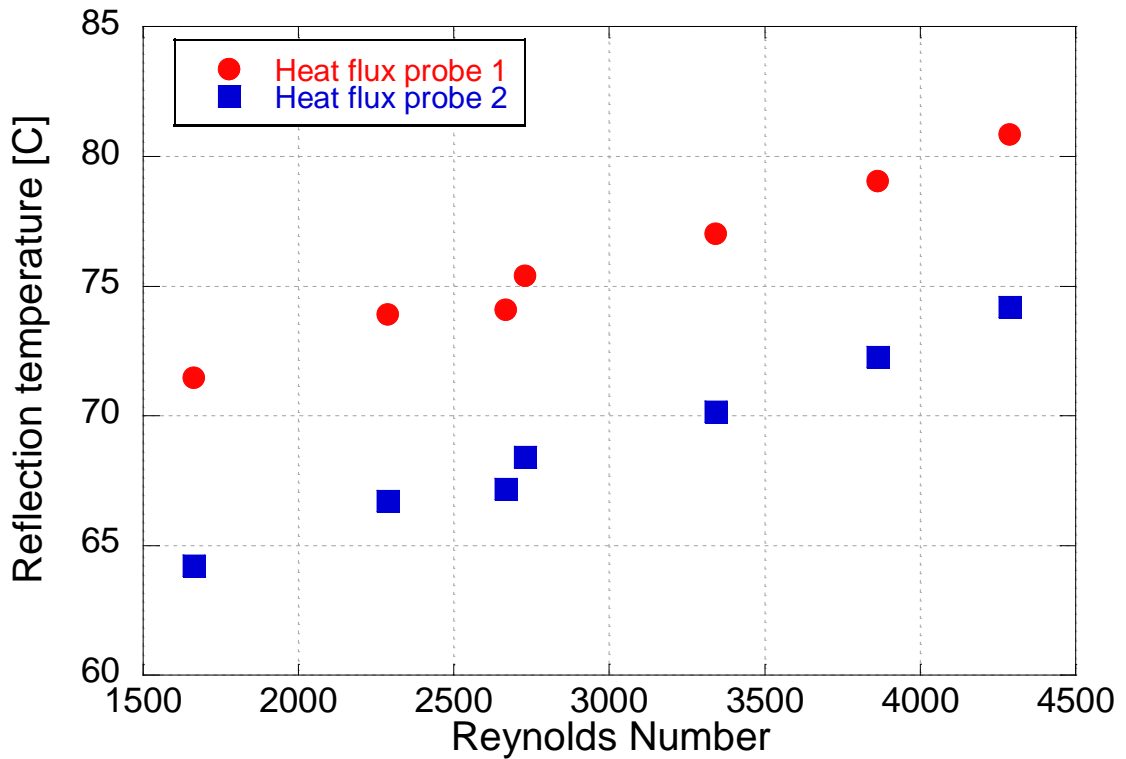


Figure 3.3: Reflection temperature versus Reynolds number

### 3.2 Deposit layer emissivity

To determine the appropriate radiation from the target deposit layer for temperature calculation, the emissivity of the layer must be accounted for. Since this is the first application of infrared thermography to deposit layers, the emissivity must be measured. The emissivity of a target can be measured if the object is heated to a known temperature, as measured by a thermocouple for example, and its temperature measured by an infrared camera. The emissivity of the target can then be adjusted in the infrared software to match the measured infrared temperature to that of the known temperature.

However, complications arise from using a thermocouple to measure the temperature of a thin porous structure. To facilitate this measurement, an isothermal experiment was designed and conducted.

### 3.2.1 Isothermal experiment

The idea behind an isothermal experiment is to heat the deposit layer sufficiently to produce a strong infrared measurement while minimizing the net heat transfer through the thickness of the deposit, thereby equalizing the temperature through the layer. Isothermal conditions can be achieved by flowing similar temperature air and coolant into the fixture and allowing for steady state conditions to develop, as shown in the schematic in Figure 3.4. Since the two fluids are of similar temperature, the net heat transfer between them is roughly zero and the temperature of the deposit layer can be assumed to be that of the surrounding air and is easily measured with a standard thermocouple.

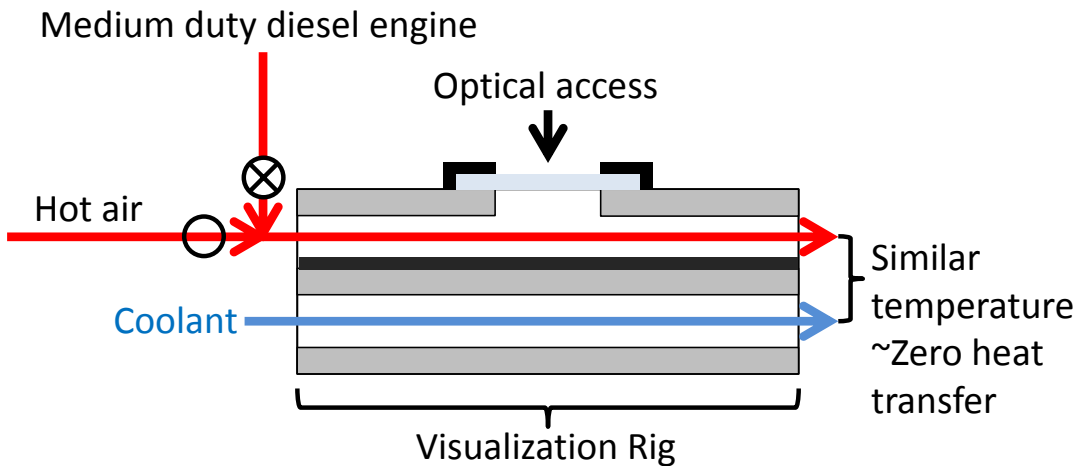


Figure 3.4: Isothermal experiment schematic

The emissivity of the target deposit layer is then adjusted to match the measured infrared deposit temperature and the measured air temperature. The resulting emissivity of the deposit layer was determined to be 1 and is illustrated by the uniform color corresponding to the same air temperature in Figure 3.5. This is an expected result since the layer is primarily soot based and the emissivity of soot is 0.95 [1]. This is a convenient result as an emissivity of 1 cancels out the effect of reflected temperatures (Equation 2.6).

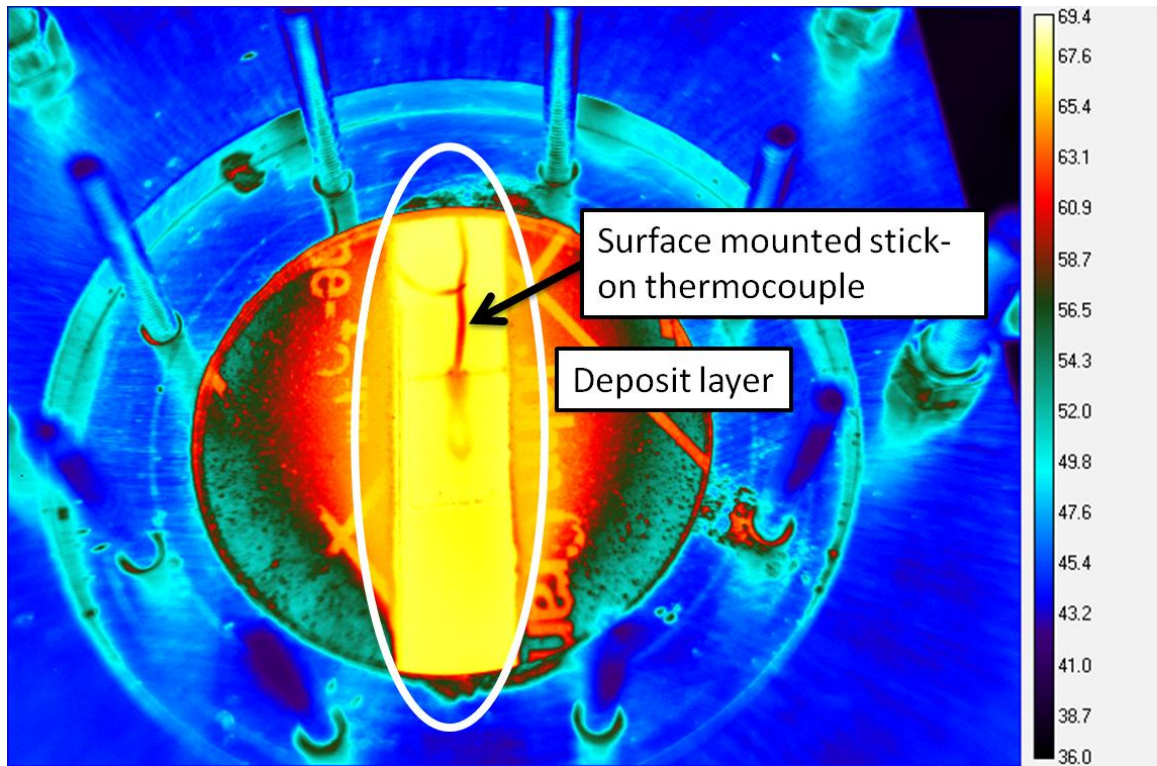


Figure 3.5: Emissivity of deposit layer

To highlight the importance of emissivity on measured surface temperature, consider Figure 3.6. The deposit layer and stainless steel appear to be drastically different temperatures (deposit layer  $\sim 57^{\circ}\text{C}$ , stainless steel  $\sim 37^{\circ}\text{C}$ ), however they are in-fact the same temperature. The apparent difference is due to the difference in material emissivity, where the deposit layer is 1 and the stainless steel can vary between 0.17 and 0.90 depending on temperature, composition, and oxidation [2].

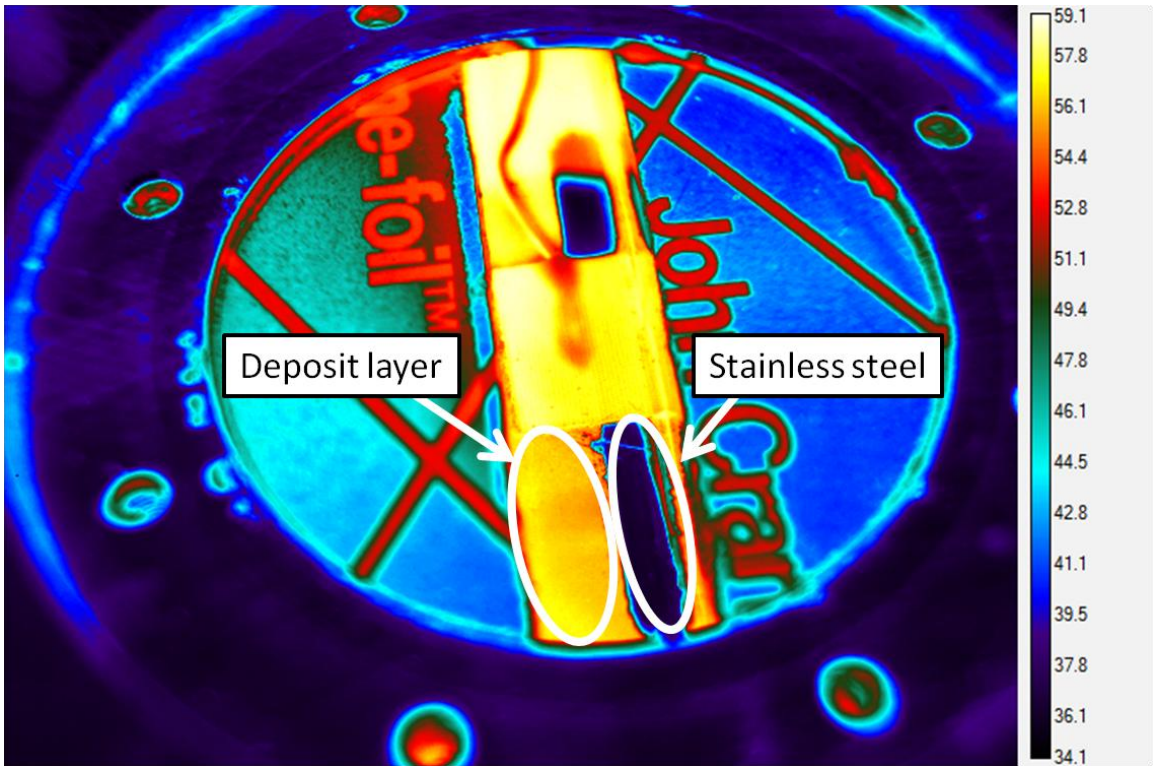


Figure 3.6: Emissivity differences between deposit layer and stainless steel

### 3.3 Infrared window

#### 3.3.1 Transmissivity

Another factor affecting the total radiation received by the infrared camera is the presence of an infrared and optically transparent window. This window is required to create a seal between the visualization rig and the environment and allows for thermal and optical analysis of the layer at elevated temperatures and pressures. The window, however, filters part of the emitted deposit radiation and also emits its own depending on window temperature.

The filtration effect can be observed in Figure 3.7, Figure 3.8, and Figure 3.9. Figure 3.7 shows an infrared image of the deposit layer in the absence of an infrared window. When one window is added in-between the deposit layer and the infrared camera, Figure 3.8, the temperature of the deposit layer appears to decrease. The apparent



decrease in temperature is further amplified with the addition of a second infrared window as shown in Figure 3.9. This effect is due to the transmissivity of the infrared window.

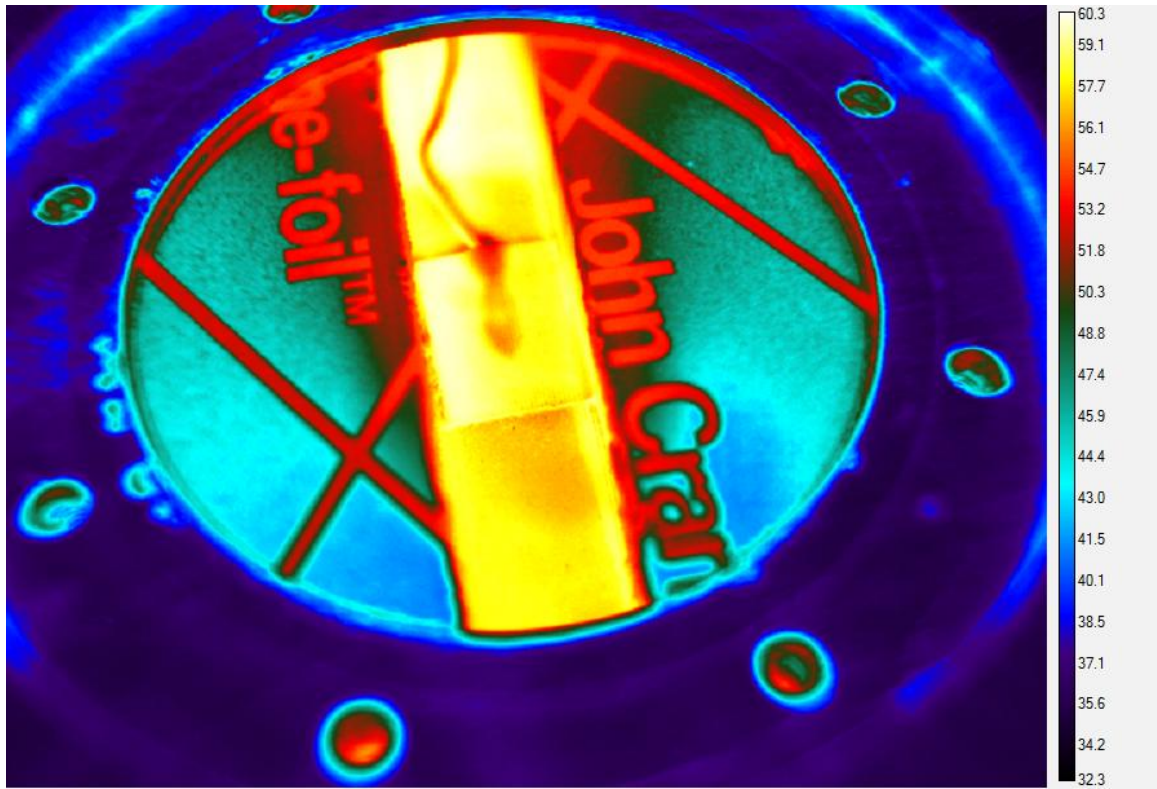


Figure 3.7: Infrared image of deposit layer in absence of infrared window

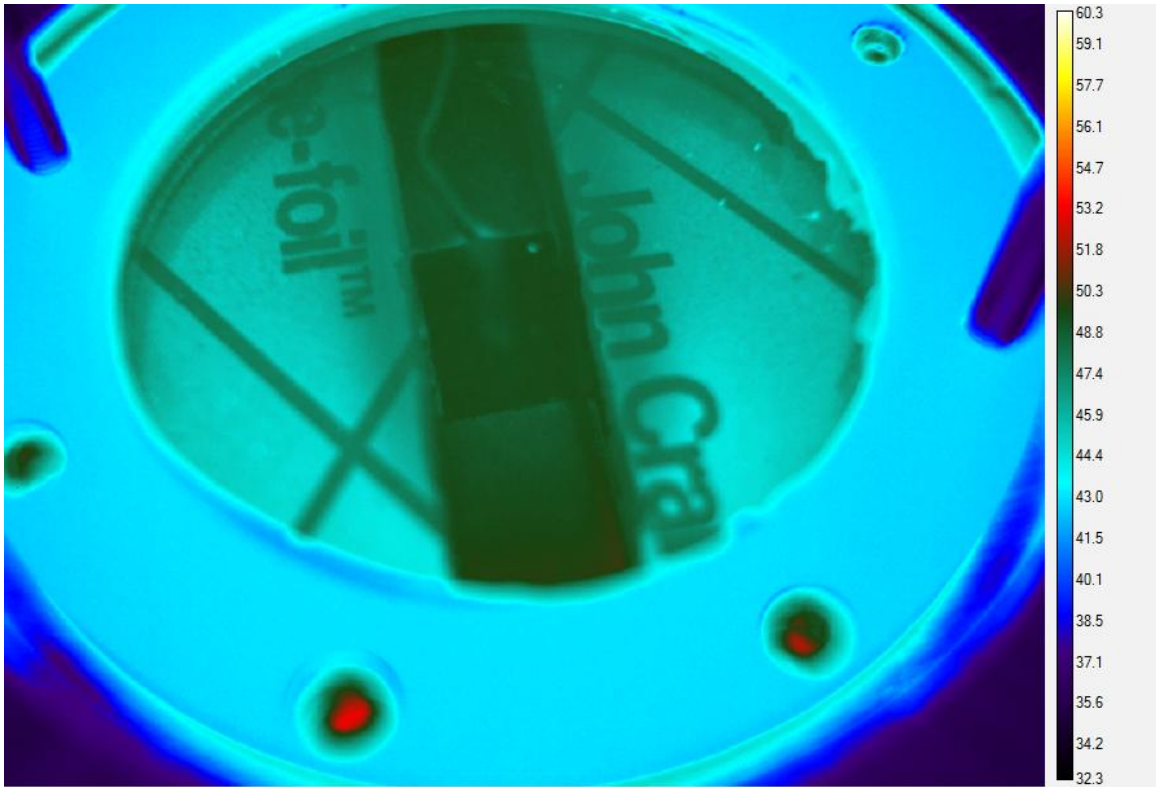


Figure 3.8: Infrared image of deposit layer with one infrared window in line of sight

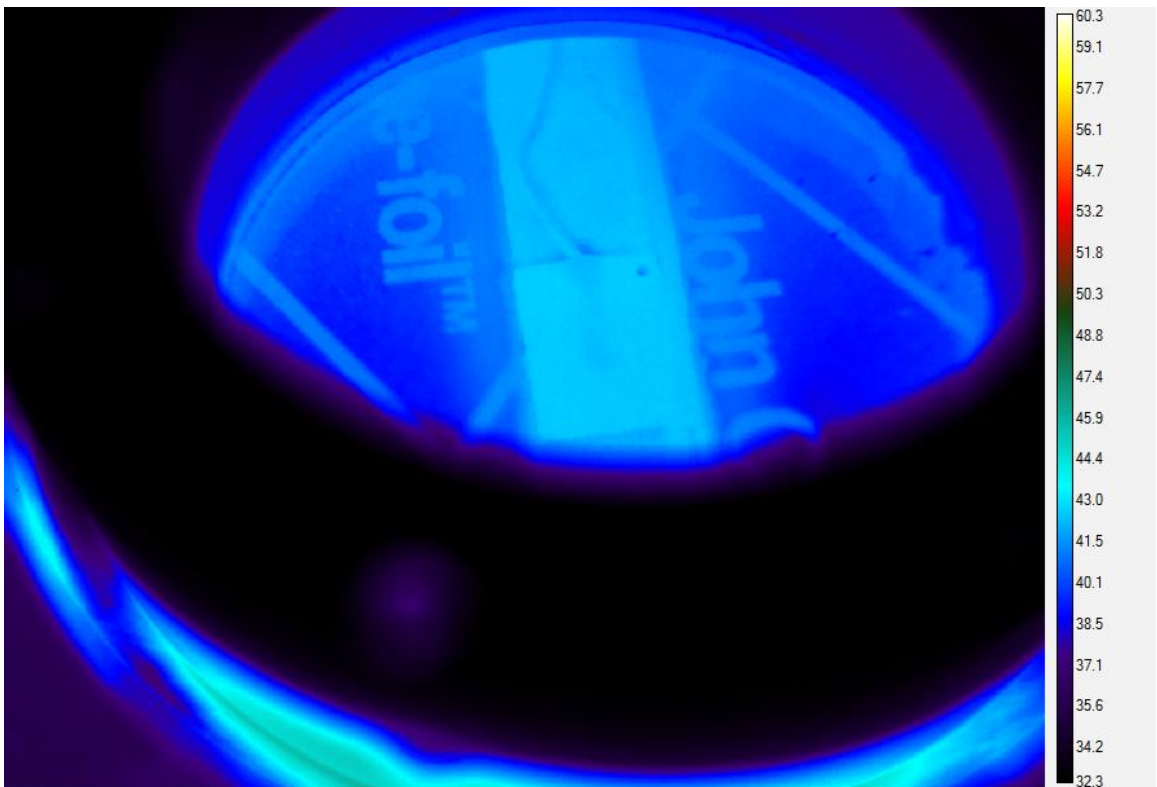


Figure 3.9: Infrared image of deposit layer with two infrared windows in line of sight

To determine the transmissivity of the infrared window, an object of known emissivity and temperature is measured with an infrared camera with the infrared window placed in-between. The temperature of the infrared window must also be measured. The transmissivity of the window, while adjusting for the window temperature, can then be adjusted under the External Optics section in the Object Parameters in the ExaminIR software (Figure 3.10) to match the measured temperature of the object at a known temperature. This procedure can be accomplished by utilizing the aforementioned isothermal experiment in conjunction with a thermocouple measuring the window temperature. The transmissivity of the window was determined to be 0.85.

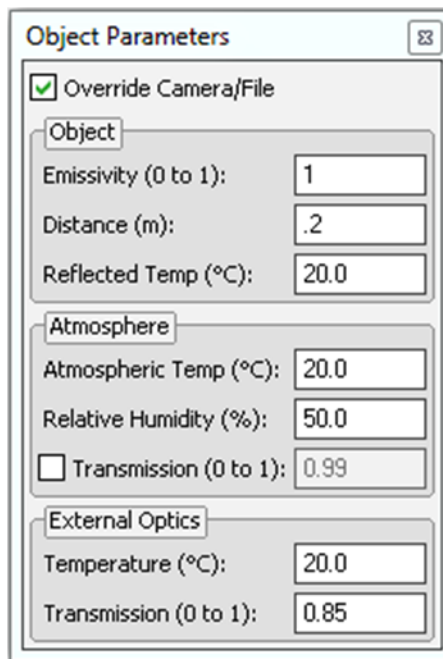


Figure 3.10: ExaminIR object parameters

### 3.3.2 Infrared camera angle

The angle at which the infrared camera looks through the infrared window can also affect temperature measurement. As the camera moves from perpendicular to parallel to the window, the path length of the infrared radiation through the window increases. To determine the significance of this effect, an experiment varying the

effective infrared camera angle relative to the infrared window is employed (schematic in Figure 3.11). The results show a diminished window transmissivity as camera angle increases from perpendicular to parallel, as shown in Figure 3.12 for a two-window configuration. As can be seen, a steep drop off in measurement is observed for angles greater than 45 degrees. For best temperature results, measurements should be performed with the infrared camera perpendicular to the infrared window.

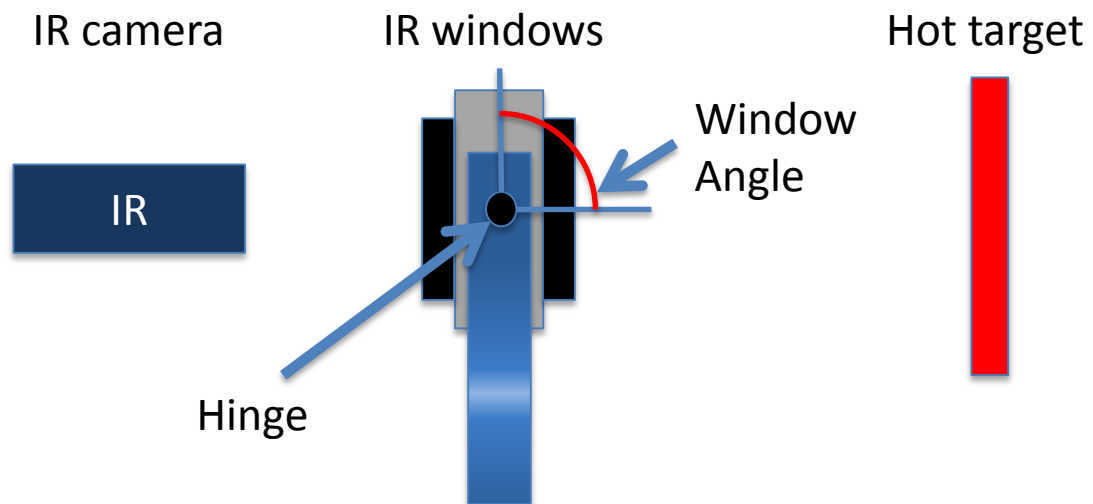


Figure 3.11: Infrared camera angle schematic

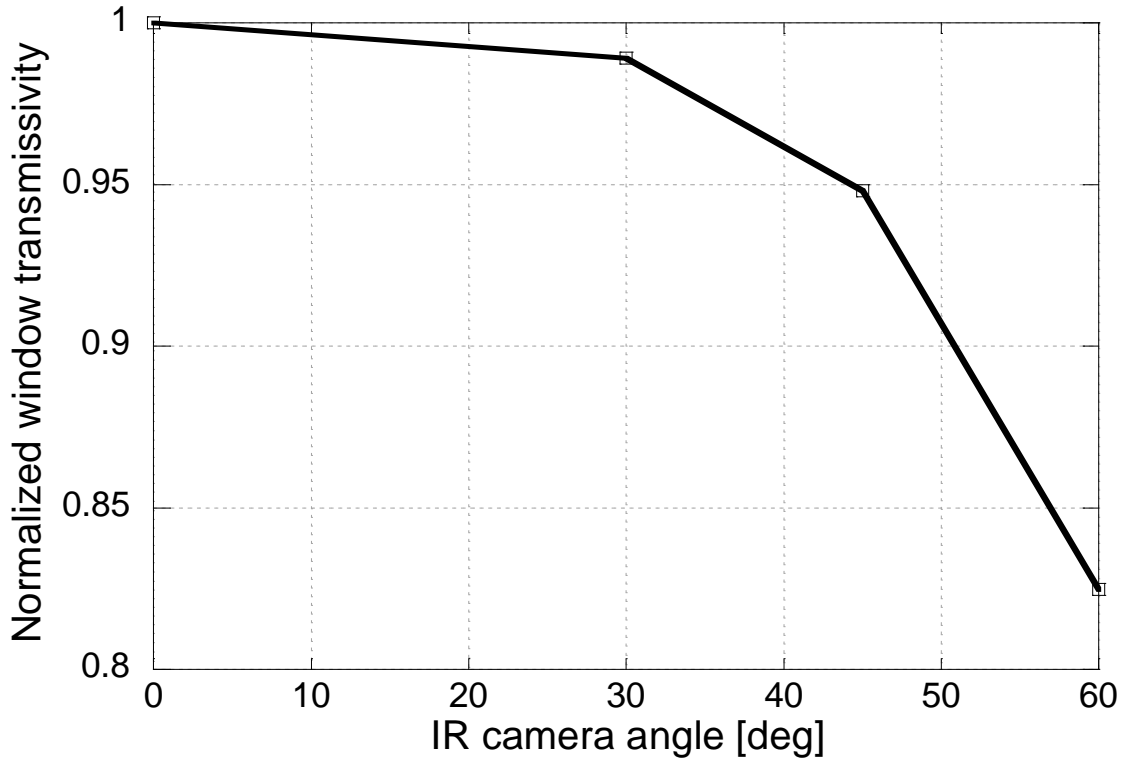


Figure 3.12: Infrared window transmissivity as a function of infrared camera angle for a two-window setup

### 3.4 Deposit layer transparency

Infrared radiation can also transmit through the target source, resulting in contamination of the target temperature by the temperature of the object behind the target. Transparency is perhaps easier to understand through Figure 3.13. A thin soot layer developed during a deposition event is pictured on top of a reflective carbon gasket, on the left side of the channel. The presence of the thin layer is noted by the darkness gradient from the edge of the channel towards the circumferential edge. A section of the thin layer is removed at the bottom of the left edge to highlight its presence. The letters “ne-foil” are clearly seen underneath the deposit layer and refer to the gasket manufacturer John Crane and the product Crane-foil™. On the opposing side of the channel, powdered charcoal was applied on top of the same gasket. However, it is noted that the gasket material is not visible underneath the charcoal.

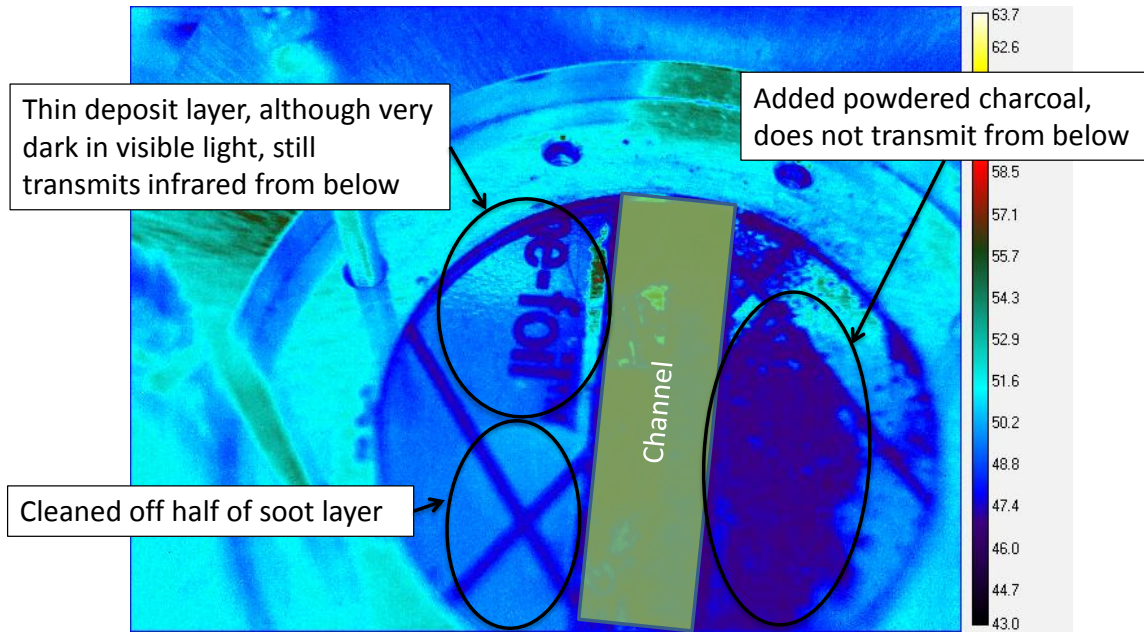


Figure 3.13: Transparency of deposit layer compared to powdered charcoal

The difference in the two cases and layer transparency is attributed to the high porosity and thinness of the deposit layer. Deposit porosity has been estimated to be as high as 98% [3] and when coupled with a thin layer, the structure of the layer can allow for transmission of infrared radiation. To illustrate this, consider Figure 3.14. With a clean surface, the radiation received by the infrared camera is solely from the stainless steel surface of the channel in the rig. As the layer builds in thickness, lesser amounts of stainless steel radiation permeates through the deposit thickness (as noted by the fewer and thinner blue arrows) while deposit radiation is increased. After a certain layer thickness, the radiation from the stainless steel surface ceases to transmit through the deposit and only the radiation from the deposit will be received by the camera, as indicated by the thick black arrows.

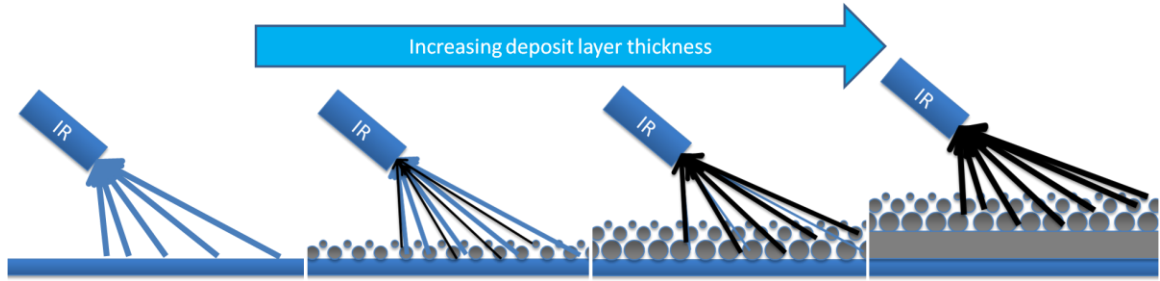


Figure 3.14: Evolution of deposit layer transparency with increasing layer thickness

Transparency can be further described by reflection. When a heat source is present in the surrounding environment, but not heating the deposit layer, reflections of the source can be seen in the layer. Since the deposit emissivity was determined to be  $\sim 1$ , the deposit itself cannot cause a reflection. Therefore, the reflections are due to transmission through the layer, reflection from the stainless steel surface, back through the layer and finally into the infrared camera. This scenario is depicted in Figure 3.15.

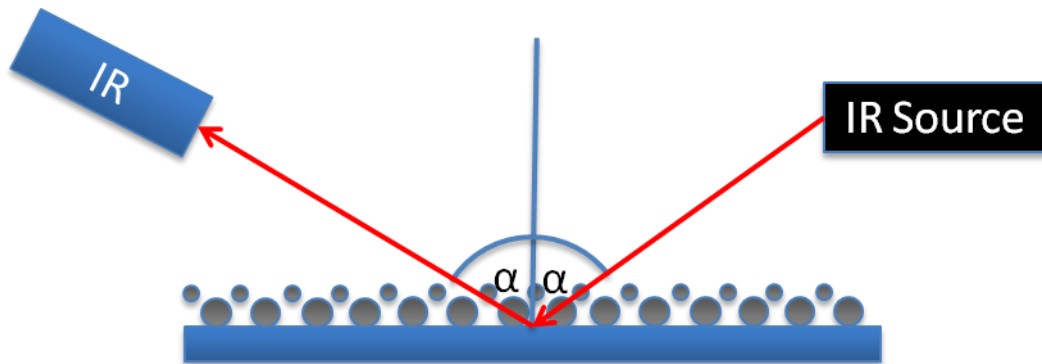


Figure 3.15: Schematic of reflection through thin deposit layer

Reflections are also noticed experimentally. A 5 hour, 104 micron deposit layer was developed and investigated for reflections. Reflections from an infrared source are seen at the inlet and outlet of the channel, shown in Figure 3.16. However, reflection is not noticed on top of contact stick-on thermocouple. This phenomenon is attributed to the porosity of the deposit layer and does not occur on the stick-on thermocouple since it is made from a solid material.

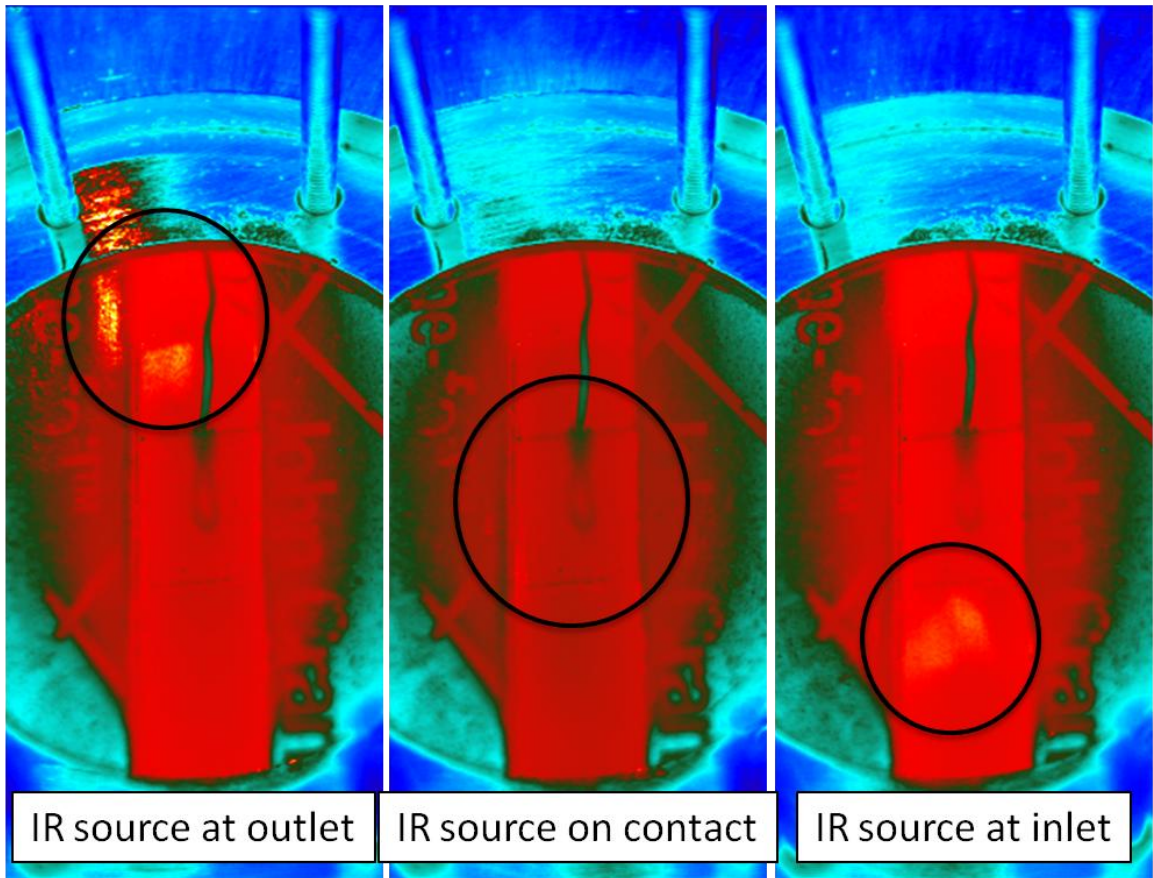


Figure 3.16: Experimental evidence of reflection through deposit layer but not on contact thermocouple

Insights into reflections can be developed by considering the deposit layer as a coating on top of a stainless steel substrate, as shown in Figure 3.17 where  $L$  is the coating thickness,  $n_1$  is the coating index of refraction,  $n_2$  is the substrate index of refraction,  $\rho_1$  is the coating reflectivity, and  $\rho_2$  is the substrate reflectivity. It can be seen in Figure 3.18 that increasing the product of coating absorptivity  $a_1$  and coating thickness  $L$  results in lower reflections. This is also demonstrated experimentally as strong reflections are seen with a clean substrate (Time 0 min), but as deposition continues the reflections subside (Figure 3.19).

In addition, decreasing the index of refraction of the coating will also reduce reflections. Finally, a reduction in the reflectivity of the substrate will also reduce reflections.



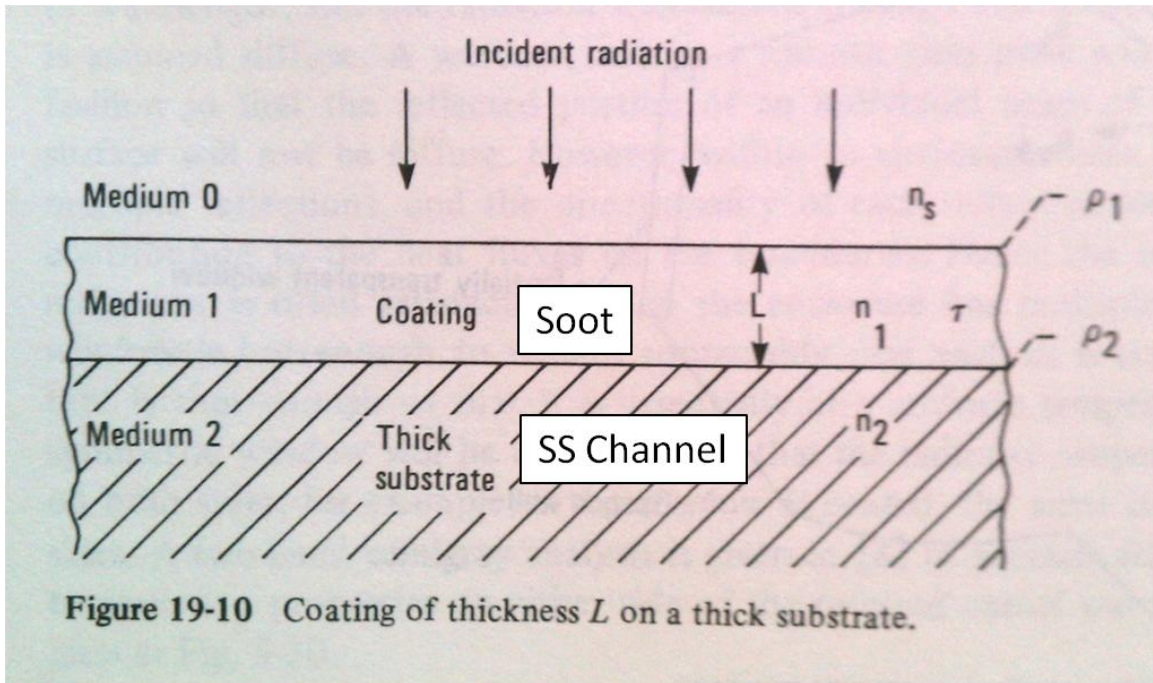


Figure 3.17: Schematic of reflection coating [1]

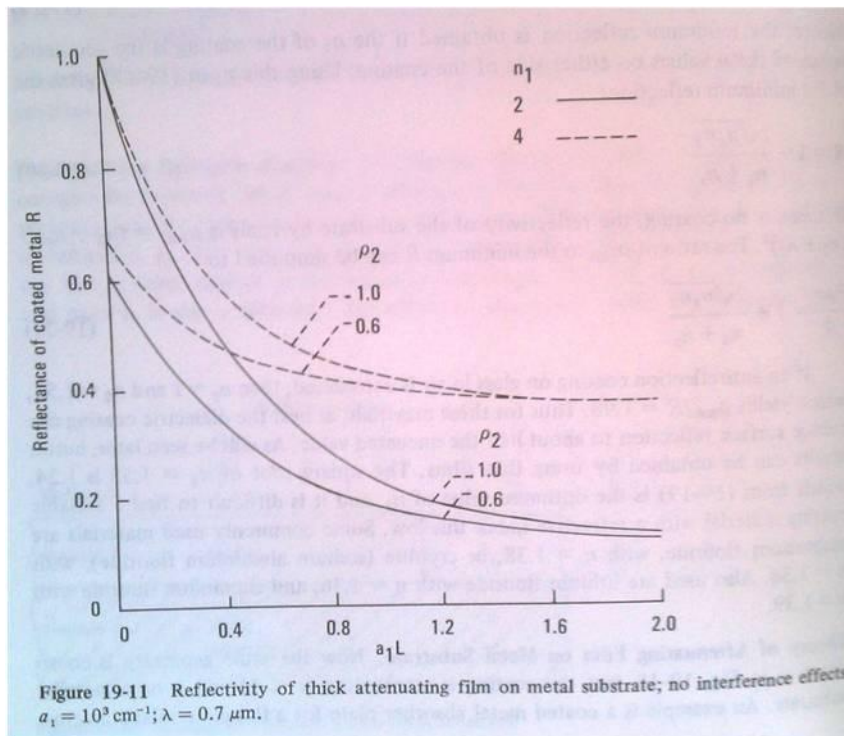


Figure 3.18: Effect of coating properties on substrate reflection [1]

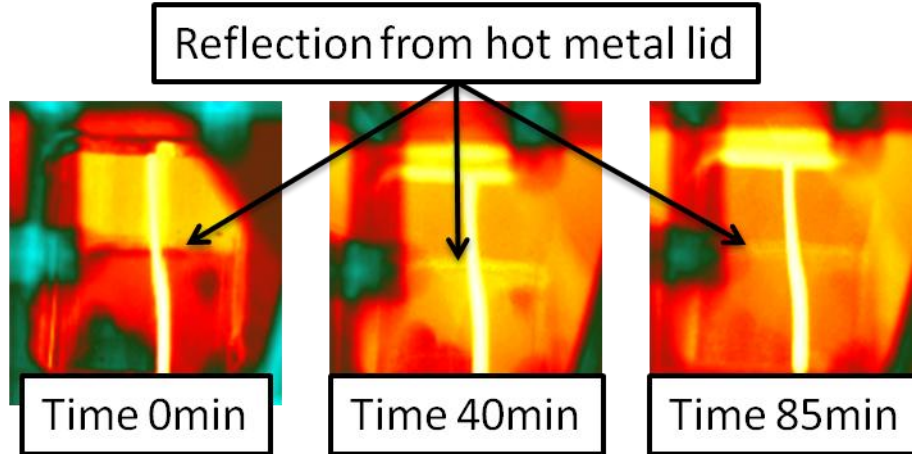


Figure 3.19: Evolution of reflection with increasing deposition

To understand the experimental limitations of layer transparency, high emissivity paint was applied to the clean surface of stainless steel channel as shown in Figure 3.20. A young 3 hour, roughly 60 micron thick deposit layer was then built on top of it. Figure 3.21 shows that the high emissivity paint is still seen through the layer. However, as deposition continued to 6 hours and the thickness of the layer increased to approximately 140 microns, the surface paint was no longer observable as shown in Figure 3.22.

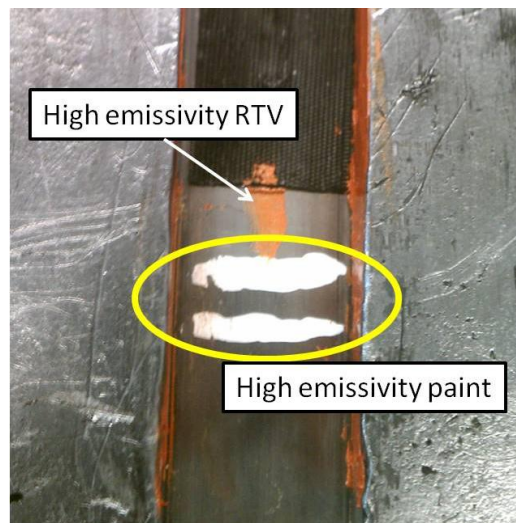


Figure 3.20: High emissivity paint applied across channel width in addition to a small strip of RTV along channel length

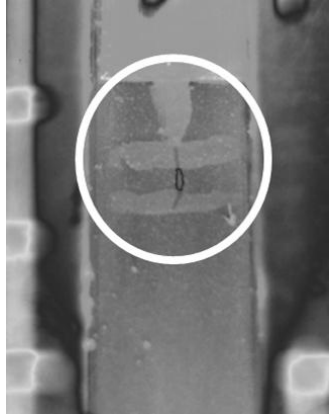


Figure 3.21: Infrared image of transmission of high emissivity paint through 60 micron thick deposit layer

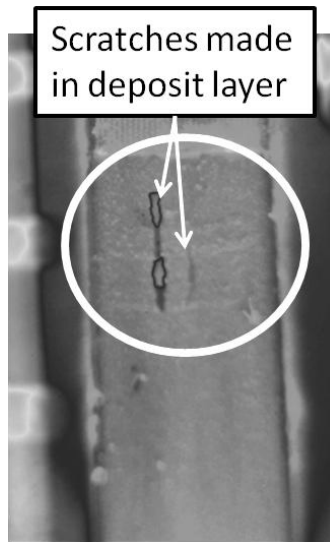


Figure 3.22: Infrared image of negligible transmission of high emissivity paint through 140 micron thick deposit layer

Incorporating these findings to produce reliable measurements results in requiring the deposit layer to be of sufficient thickness (roughly 140 microns) to minimize reflections and performing these measurements on the less reflective heat flux probes of high emissivity, as described in Chapter 2.

### 3.5 References

- [1] Siegel, R. and Howell, J., *Thermal Radiation Heat Transfer*, 2nd ed. Washington: Hemisphere Publishing Corporation, 1981.
- [2] Incropera, F. and DeWitt, D., *Fundamentals of Heat and Mass Transfer*, 5th ed.: John Wiley & Sons, Inc, 2002.
- [3] Lance, M. J., Sluder, C. S., Wang, H., and Storey, J. M. E., "Direct Measurement of EGR Cooler Deposit Thermal Properties for Improved Understanding of Cooler Fouling," *SAE International*, 2009.

## **CHAPTER 4**

### **DEPOSIT LAYER EVOLUTION ON STAINLESS STEEL SUBSTRATE**

Using the equipment described in Chapter 2, the evolution of deposit characteristics is measured over a 24-hour period in 3-hour intervals. Insights into deposit properties in the absence of heat flux measurements are presented in this chapter.

#### **4.1 Experimental conditions**

A 24-hour deposition in 3-hour intervals was conducted at steady state engine conditions. The visualization rig was warmed up using hot compressed air while flowing warm coolant to ensure steady state conditions. The engine was warmed up to a coolant temperature of 90°C and maintained at that condition until engine BMEP stabilized. A post-injection was utilized to boost the filter smoke number in order to accelerate deposit layer build-up. Ultra-low sulfur diesel was used as the fuel. The engine and visualization rig conditions are listed in Table 4.1:

Table 4.1: Engine and visualization rig conditions

Engine RPM [RPM]	1200
Engine BMEP [bar]	7.5
Post injection quantity [mg/stk]	2
Post injection timing [CAD aTDC]	30
Filter smoke number, w/o post injection [FSN]	0.4
Filter smoke number, w/ post injection [FSN]	1.5
Visualization rig inlet temperature [C]	210
Visualization rig pressure [kPa]	155
Effective rig coolant temperature [C]	85
Exhaust flow rate [kg/hr]	5

#### 4.1.1 Engine conditions

Engine conditions are presented in this section and the impact of using a post-injection is quantified in terms of engine fueling rate, air fuel ratio (A/F ratio), and engine combustion. The conventional condition represents the same operating engine speed and load (matched BMEP) however without a post-injection.

##### Fueling rate

The total fueling rate for the engine increased for the post-injection compared to the conventional case at matched load conditions and is shown in Figure 4.1. The increase is due to combustion inefficiencies associated with a retarded post-injection, requiring additional fuelling in order to maintain similar load. This, however, is accompanied with a reduction in fuel quantity for the main injection event and is required to match engine conditions to the conventional case as the post-injection contributes to the net engine load.

### Air/fuel ratio

The post-injection led to a decrease in A/F ratio from 20.2 for conventional to 19.1 as measured by the laminar flow element (LFE) and coriolis fuel flow meter and is shown in Figure 4.2. The richer, yet still lean, exhaust causes lower exhaust O<sub>2</sub> concentrations than the conventional condition.

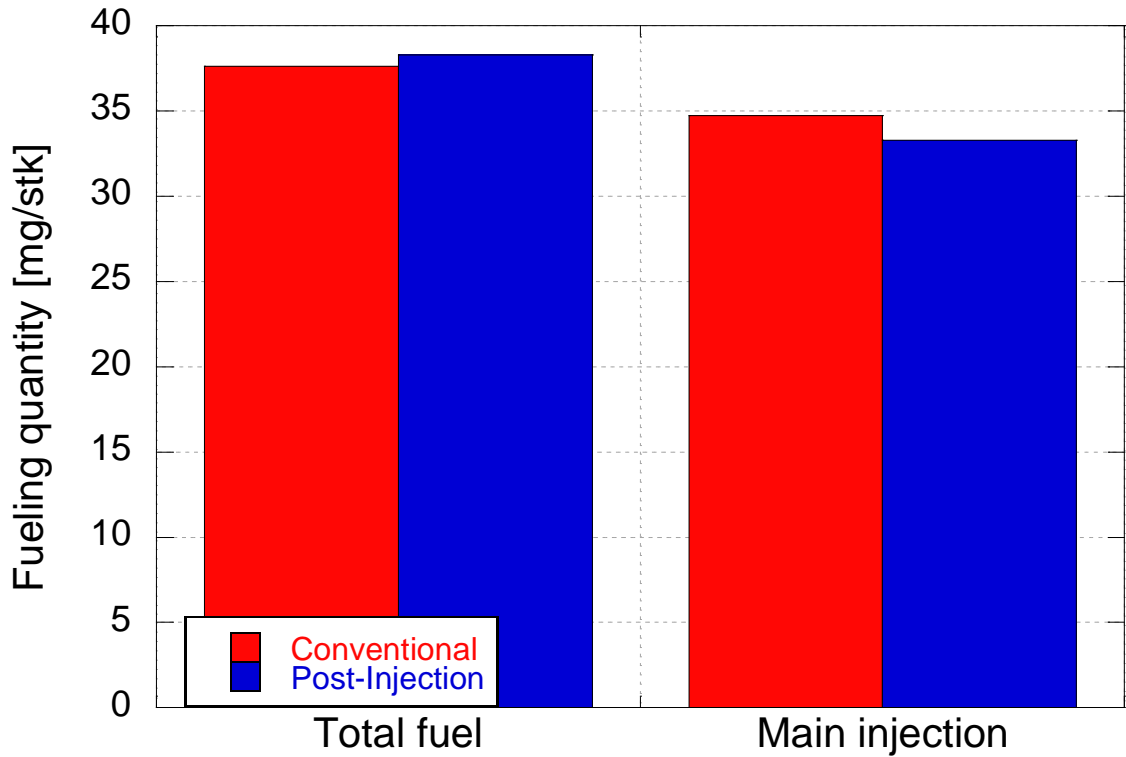


Figure 4.1: Fueling quantity at conventional and post-injection conditions

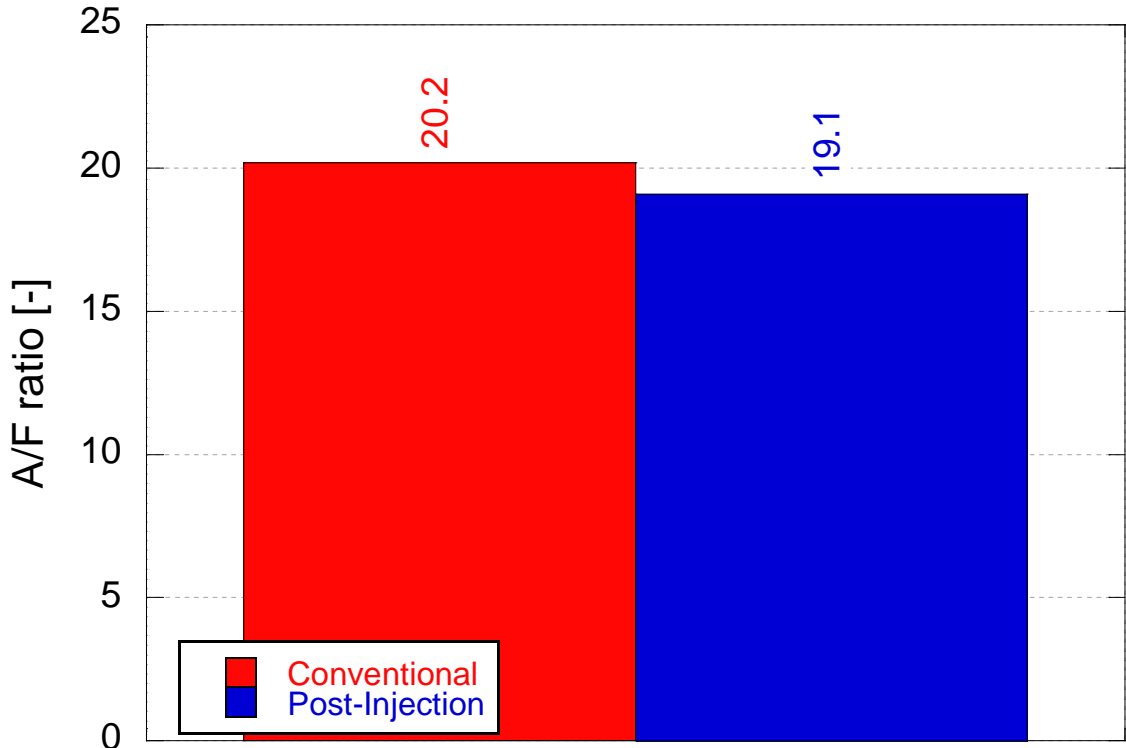


Figure 4.2: A/F ratio for conventional and post-injection engine conditions

### Combustion

The University of Michigan Heat Release (UMHR) code was used to analyze raw cylinder pressure traces from the engine. Coupled with information about engine fueling and airflow rate, the UMHR code enables combustion analysis.

Rates of heat release (ROHR) for the conventional and post-injection case are shown in Figure 4.3. Slight variations were seen at the start of combustion (-13 crank angle degrees), the pre-mixed burn (-4 crank angle degrees), and main heat release event during the diffusion burn (starting at -1 crank angle degree). Integrating the ROHR curve generated the cumulative heat release (HR) shown in Figure 4.4. The post-injection case exhibited a delayed main heat release event with a lower peak output. This is due to the lower main fuelling rate required to match loads with the conventional case in the presence of a post-injection. The post-injection heat release is apparent around 32 degrees aTDC.



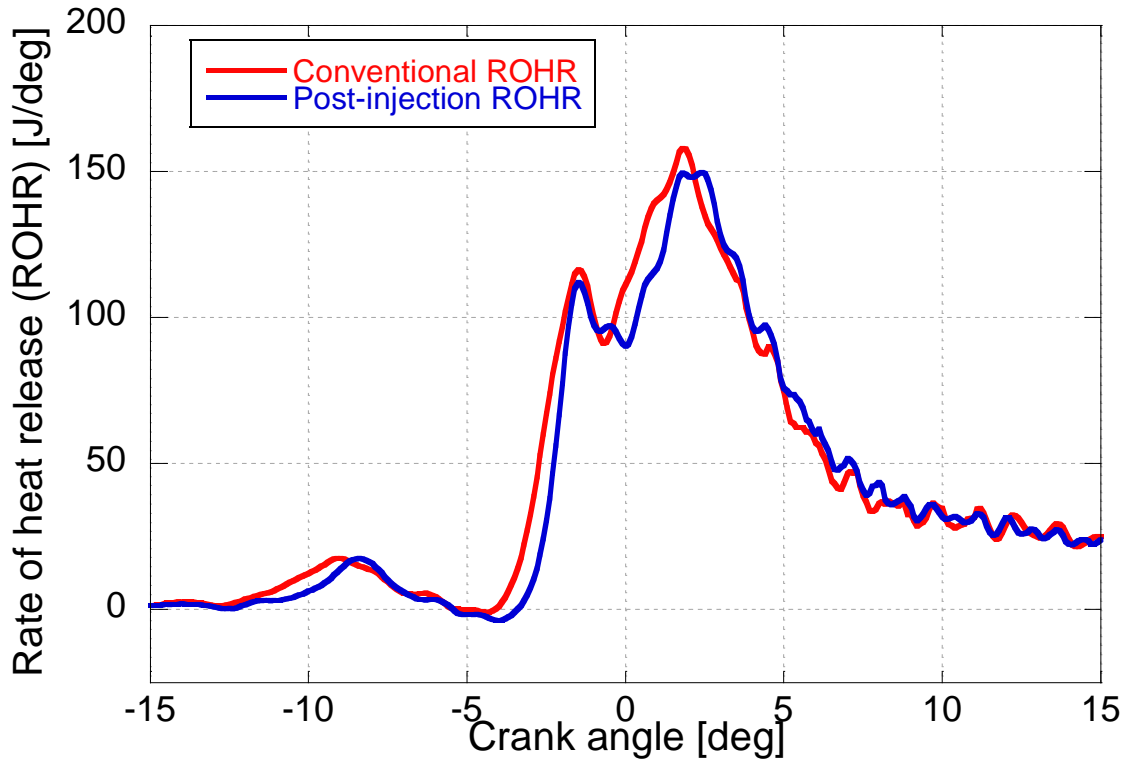


Figure 4.3: Rate of heat release during combustion for the conventional and post-injection engine condition

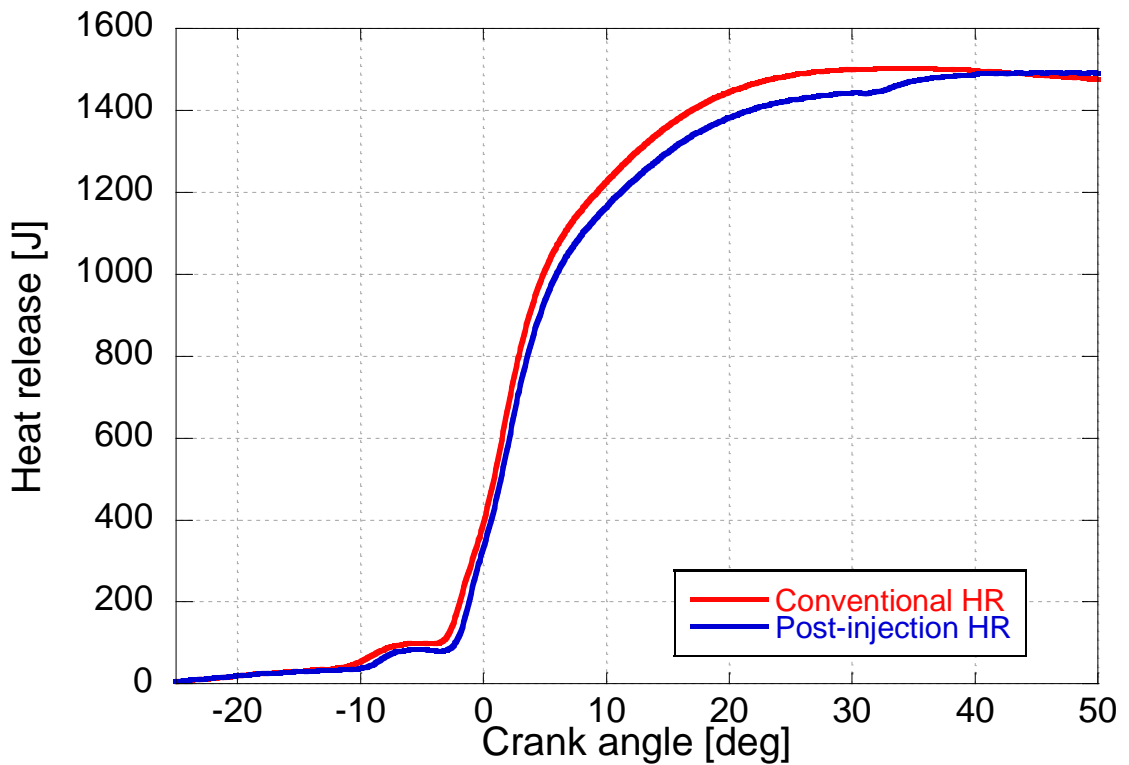


Figure 4.4: Cumulative heat release for the conventional and post-injection engine condition

The overall combined effect of the changes in combustion can be represented by the 50% mass fraction burn location (MFB50) and the 10 – 90% mass fraction burn duration. The MFB50 for the conventional case was 2.45 degrees aTDC, while the MFB50 for the post-injection was 3.08 degrees aTDC. The slightly delayed MFB50 of the post-injection resulted in a decrease in engine efficiency, hence the increased fuelling rate compared to the conventional case.

The 10 – 90% MFB duration for the conventional condition was 17.02 degrees while the 10 – 90% MFB for the post-injection was 18.96 degrees. The post-injection combustion was slightly slower than the conventional case, due to the delayed start of combustion and addition of a post-injection late into the expansion stroke. The slower combustion further reduced the engine efficiency. The slower combustion coupled with the late combustion from the post-injection resulted in a significant increase in the filter smoke number discussed later.

#### 4.1.2 Exhaust gas composition

##### Gaseous emissions

The AVL SESAM emissions analyzer measured the gaseous compounds emitted from the engine and they are presented here. As in Section 4.1.1, the impact of using a post-injection is addressed in terms of gaseous emissions. The conventional condition represents the same operating engine speed and load (matched BMEP) however without a post-injection. Idle is the fully warmed up natural engine idle condition.

Figure 4.5 shows the levels of H<sub>2</sub>O, CO<sub>2</sub>, O<sub>2</sub>, the EGR rate, and CO<sub>2</sub> EGR for conventional, post-injection, and idle engine conditions. The addition of a post-injection increased the H<sub>2</sub>O, CO<sub>2</sub>, EGR rate, and CO<sub>2</sub> EGR levels while decreasing O<sub>2</sub>. The increased emissions are due to the increased fueling rate, as noted in Figure 4.1, required to match engine conditions with a late post-injection. The increased fuel consumption

increased  $\text{H}_2\text{O}$  and  $\text{CO}_2$ . The decrease in  $\text{O}_2$  is also a by-product of the late post-injection requiring more fuel to maintain similar conventional BMEP levels.

Figure 4.6 shows the levels for  $\text{NO}_x$ ,  $\text{CO}$ ,  $\text{THC}$  on a C3 basis for conventional, post-injection, and idle engine conditions.  $\text{CO}$  and  $\text{THC}$  increased while  $\text{NO}_x$  decreased for the post-injection condition.  $\text{CO}$  and  $\text{THC}$  stem from incomplete combustion and are increased due to the post-injection introducing fuel late into the combustion cycle, resulting in partially oxidized HC compounds.  $\text{NO}_x$  decreased due to reduction in the main fueling event, resulting in reduced peak cylinder temperatures and decreased the thermally dependent  $\text{NO}_x$  formation rate. The compositional breakup of  $\text{NO}_x$  into  $\text{NO}$  and  $\text{NO}_2$  for the conventional and post-injection conditions is not seen to vary significantly as shown in Figure 4.7.

The reduction of exhaust  $\text{O}_2$  and increase in  $\text{THC}$  results in a decrease in the A/F ratio, as calculated from the laminar flow element (LFE) and the fuel flow meter, from 20.2 for conventional to 19.1 (Figure 4.2) for post-injection. This corresponds to a decrease in lambda from 2 to 1.89 as measured by the emissions analyzer and is shown in Figure 4.8.

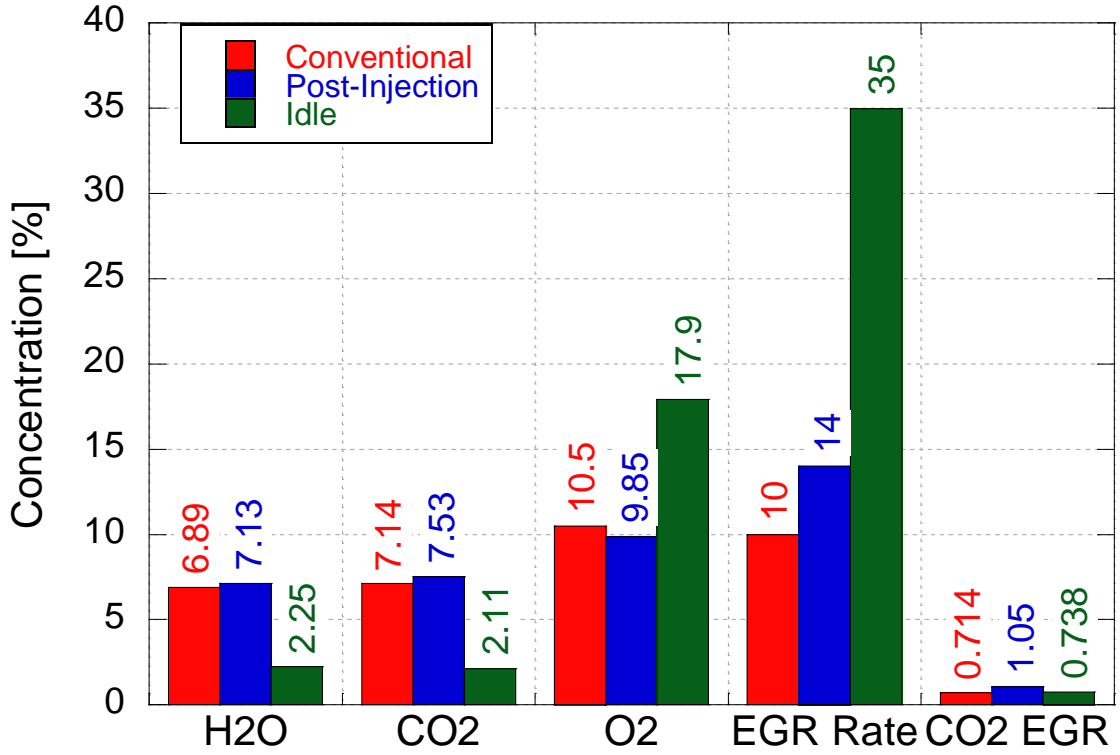


Figure 4.5: Emissions levels for H<sub>2</sub>O, CO<sub>2</sub>, O<sub>2</sub>, EGR rate, and CO<sub>2</sub> EGR for conventional, post-injection, and idle engine conditions

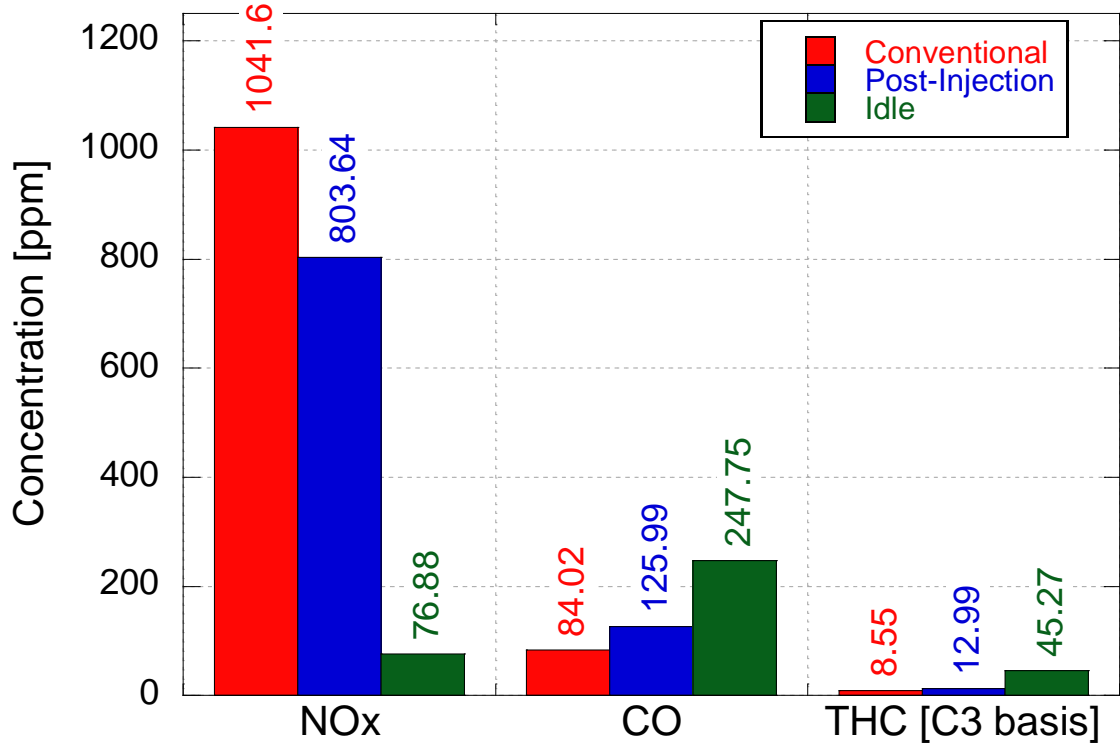


Figure 4.6: Emissions levels for NO<sub>x</sub>, CO, and THC for conventional, post-injection, and idle engine conditions

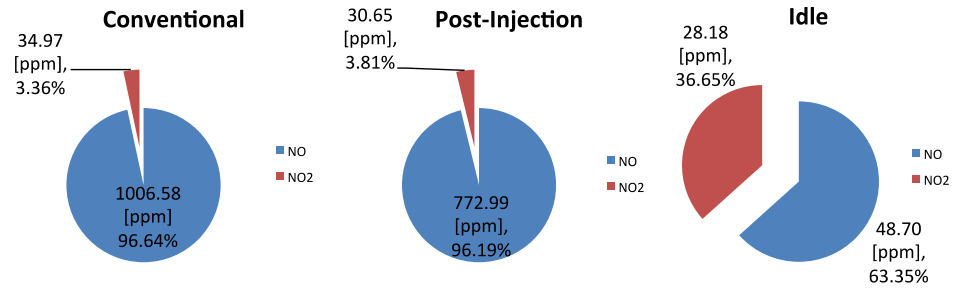


Figure 4.7: NOx break-up for conventional, post-injection, and idle engine conditions

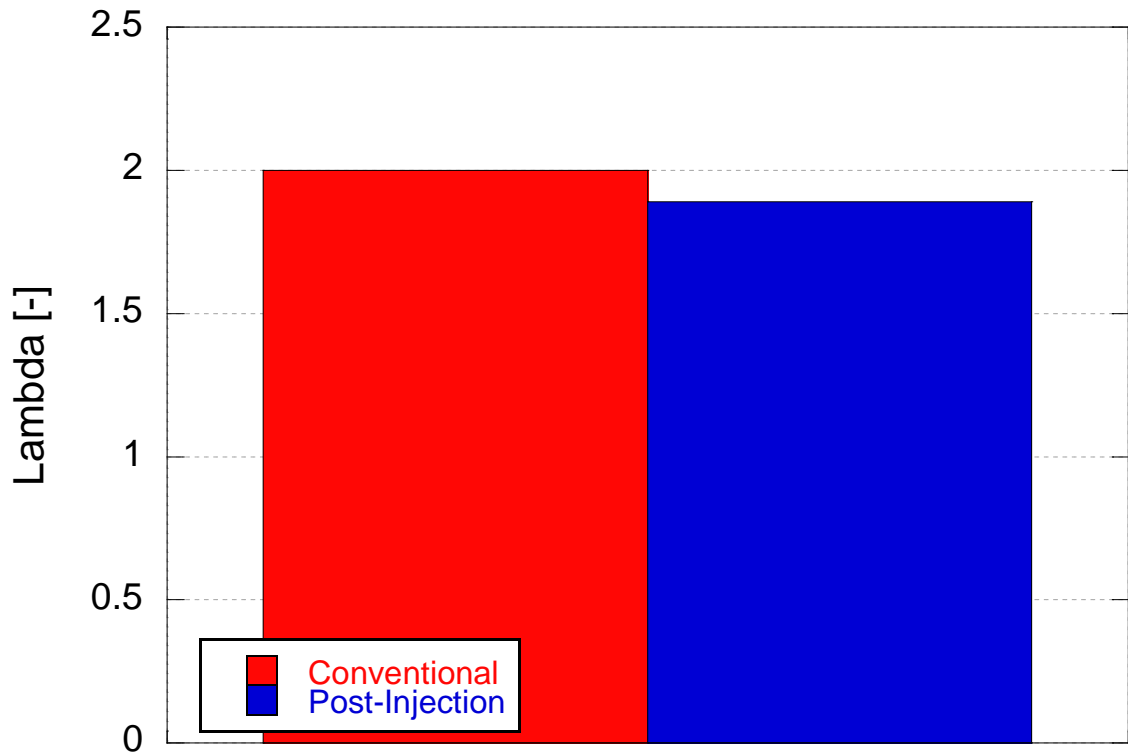


Figure 4.8: Lambda values measured from the SESAM for conventional and post-injection conditions

### Particulate emissions

Using the AVL 415S, the filter smoke number (FSN) for conventional and post-injection conditions is shown in Figure 4.9. The addition of the post-injection considerably increased the FSN allowing for more rapid deposit layer development in the visualization rig.

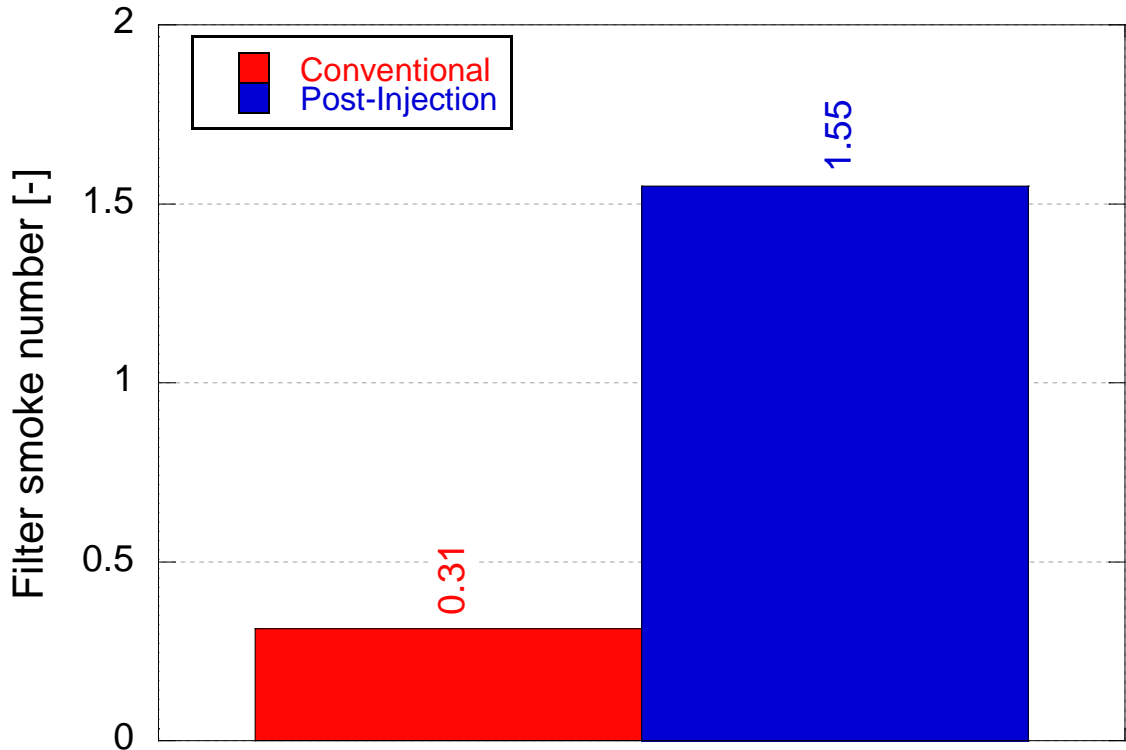


Figure 4.9: Filter smoke number for conventional and post-injection conditions

The Combustion differential mobility spectrometer (DMS500) was also utilized to quantify the particle size distribution of exhaust particulates entering and exiting the rig. The DMS500 was used in conjunction with a Dekati diluter operating at a dilution ratio of 4.3:1, using heated gaseous N<sub>2</sub> as the diluent (schematic in Figure 4.10). While the 24-hour deposition discussed later is performed with an inlet temperature of 210°C, the inlet temperature for the particle profiles was performed at 280°C. All sampling tubes were maintained at 190°C. The diluter temperature was 52°C for the inlet sampling point and 61°C for the outlet. A total (sample plus dilution) flow rate of about 11 slpm was achieved.

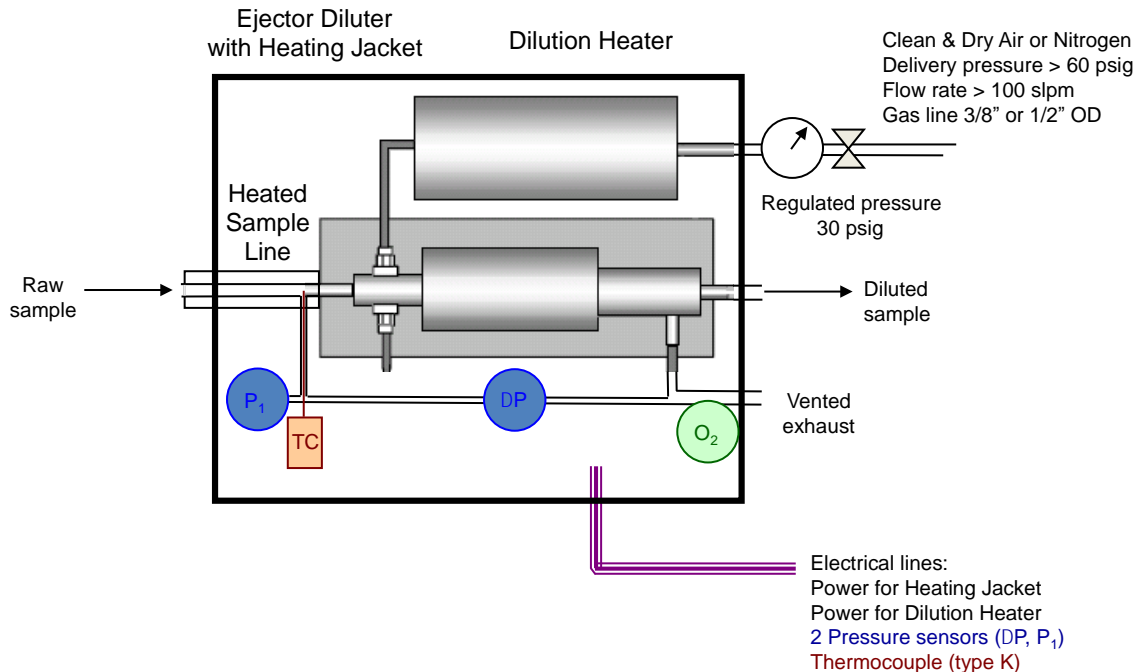


Figure 4.10: Diluter schematic, courtesy of Joe Szente, Ford Motor Company

Figure 4.11 shows a clear decrease in the number of particles between the inlet and outlet of an initially clean channel. This is expected since deposition is occurring in the fixture, reducing the number of particles at the outlet. As fouling continues over time and deposition decreases and stabilizes, the difference between the number of particles in the outlet and inlet is expected to reduce.

Due to the high sooting conditions, a dominant accumulation mode profile was present resulting in larger count median diameters (CMD) as shown in Figure 4.12. The CMD indicates the particle diameter at which half the total number of particles is larger and half are smaller. The larger outlet CMD suggests that smaller diameter particles were more likely to deposit in the fixture than larger ones. Previous analysis suggests this should not be the case [1], however could be explained by volatile condensation and drop out in the fixture thus removing the smaller end particle sizes.

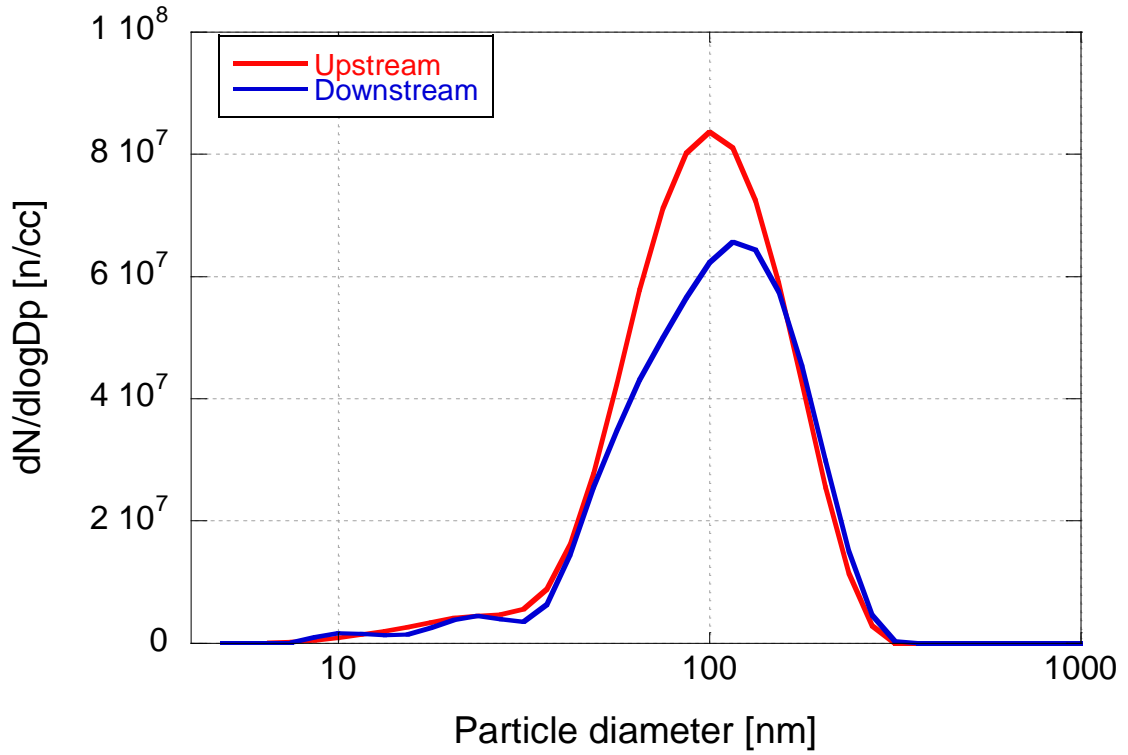


Figure 4.11: DMS particle profiles upstream and downstream of visualization rig

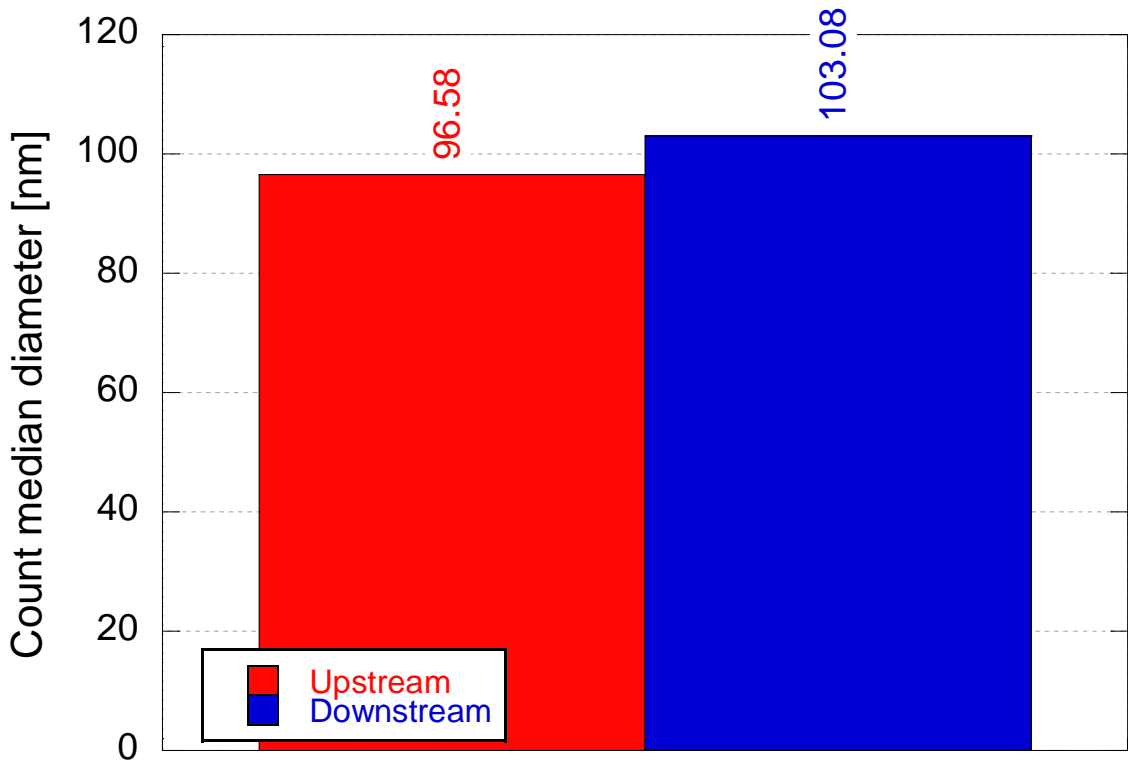


Figure 4.12: Count median diameter size for upstream and downstream rig locations, as measured by the DMS



## 4.2 24-hour deposition experimental results

### 4.2.1 Deposit layer thickness

Using the optical microscope, the deposit layer thickness was recorded over the 24-hour interval and is shown in Figure 4.13. Contrary to other research, the deposit growth was determined to be linear with time instead of asymptotic.

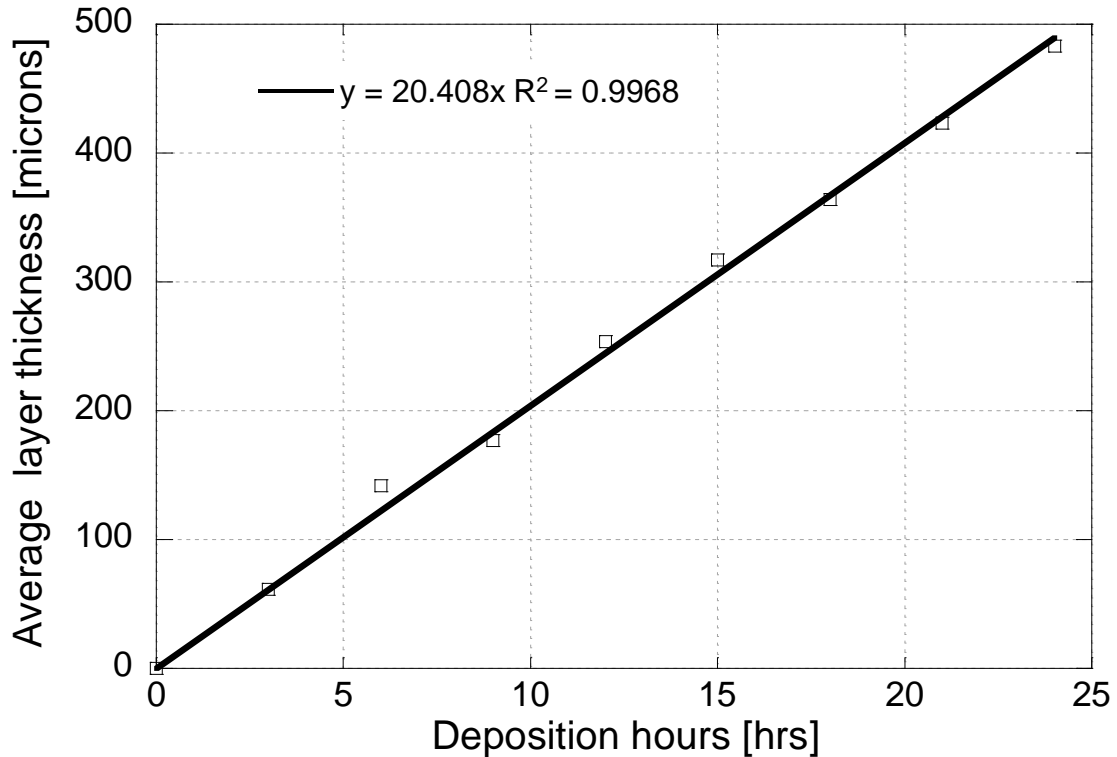


Figure 4.13: 24 hour deposit thickness evolution on stainless steel substrate

A possible explanation for the linear increase of deposit thickness is related to the large cross sectional flow area of the visualization rig. The large hydraulic diameter creates a reduced convective heat transfer coefficient between the deposit layer and exhaust gas, reducing heat transfer thus consequently reducing deposit growth and delaying asymptotic deposit growth.

The large flow area potentially reduces the effect of radiative temperature reinforcement as seen with smaller flow area and is illustrated in Figure 4.14. The

reinforcement acts to increase the deposit layer temperature, reducing the thermophoretic deposition rate and slows deposit thickness growth. The reduction of radiative reinforcement produces lower deposit temperatures resulting in high thermophoretic deposition velocities.

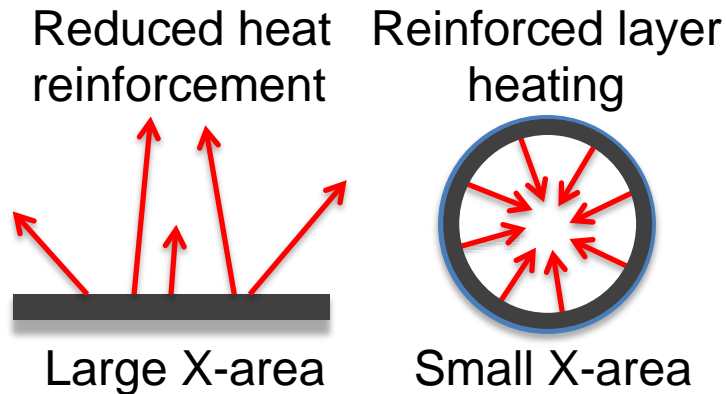


Figure 4.14: Schematic of radiative layer heating in large and small cross sectional areas

Another potentially significant effect is the impact of deposition on gas velocity. As a deposit layer forms, the cross sectional area available for gas flow decreases. For a constant mass flow rate, this is accompanied with an increase in gas velocity. An increase in gas velocity reduces the residence time of the hot gas in the heat exchanger, reducing the time available for thermophoretic forces to drive particles to the cold walls. This results in a decrease in deposition. An increase in gas velocity can also create deposit shearing, potentially removing some of the deposit and causing a decrease in deposit growth. These effects are more significant for a small cross sectional area, as the effect of a deposit layer has a larger impact on the area than on a large cross sectional area. As an example, consider a 500 micron thick layer. The cross sectional area reduction due to deposit build on a 4 mm inner diameter (clean) tube is 44% whereas for the visualization rig (21.5 x 12 mm clean), it is 6.4%. These area reductions translate directly to velocity increases for a constant mass flow rate. It is evident that velocity increase is not significant in the visualization rig and could delay signs of velocity based removal and stabilization.

To verify the impact of cross sectional area, the deposition model developed by Abarham et al. was utilized with two flow channel configurations: a 22 mm wide channel and a 6 mm wide channel [2]. The results in Figure 4.15 show a linear increase in deposit growth for the wider channel as opposed to non-linear growth for a narrower width with all other conditions kept constant. These results support experimental evidence.

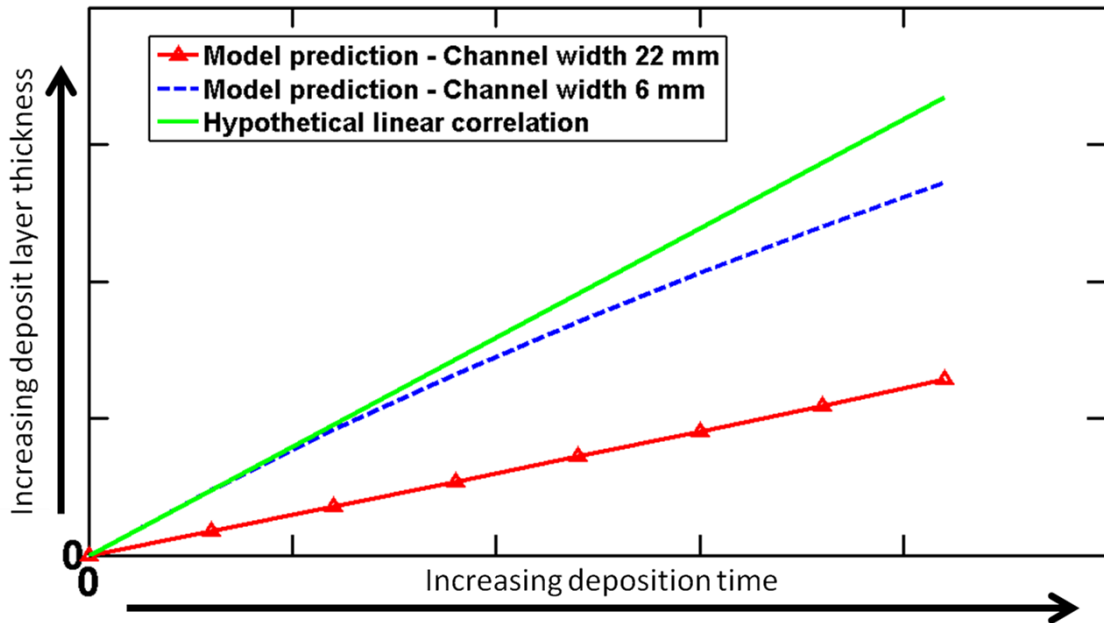


Figure 4.15: Model prediction of deposit thickness for 22 mm and 6 mm wide channels

It is hypothesized that if deposition continued for a longer period of time, asymptotic behavior would be seen when the deposit thickness reached a sufficient thickness.

#### 4.2.2 Deposit layer topography and surface area

Optical images of the surface of the deposit layer show highly topographical features, as shown in Figure 4.16. This result is contrary to the usual modeling assumptions of a flat layer. The increased topography increases the surface area of the layer and may lead to increased convective heat transfer from the gas to the deposit

surface. This could potentially be a significant aspect for fouling prediction. Therefore, it is useful to calculate the surface area of the deposit layer.

The 3-D optical microscope images are exported as csv files and imported into MATLAB. A routine was developed to discretize the x, y components with their associated height components in the z-direction into three-dimensional triangles. The cross product between the three-dimensional vectors of the triangle yields the surface area of the triangle. This is performed for the entire set of x, y coordinates of the deposit image and summed to determine an overall surface area. A new metric is introduced, the surface area ratio, and is simply the ratio of the calculated deposit surface area over a corresponding flat surface area of similar x, y dimensions. The MATLAB code used to process microscope images and calculate the surface area is given in Appendix A.1.

Surface area ratio was calculated for the 24-hour deposition interval and is shown in Figure 4.17. The surface area ratio increased minimally at thinner deposits and significantly with thicker deposits. The increase is a result of additional and magnified surface layer topography created by deposition on top of large particle deposits. Large particles in the exhaust stream and presence in the heat exchanger were recorded by Hoard et al. [3].

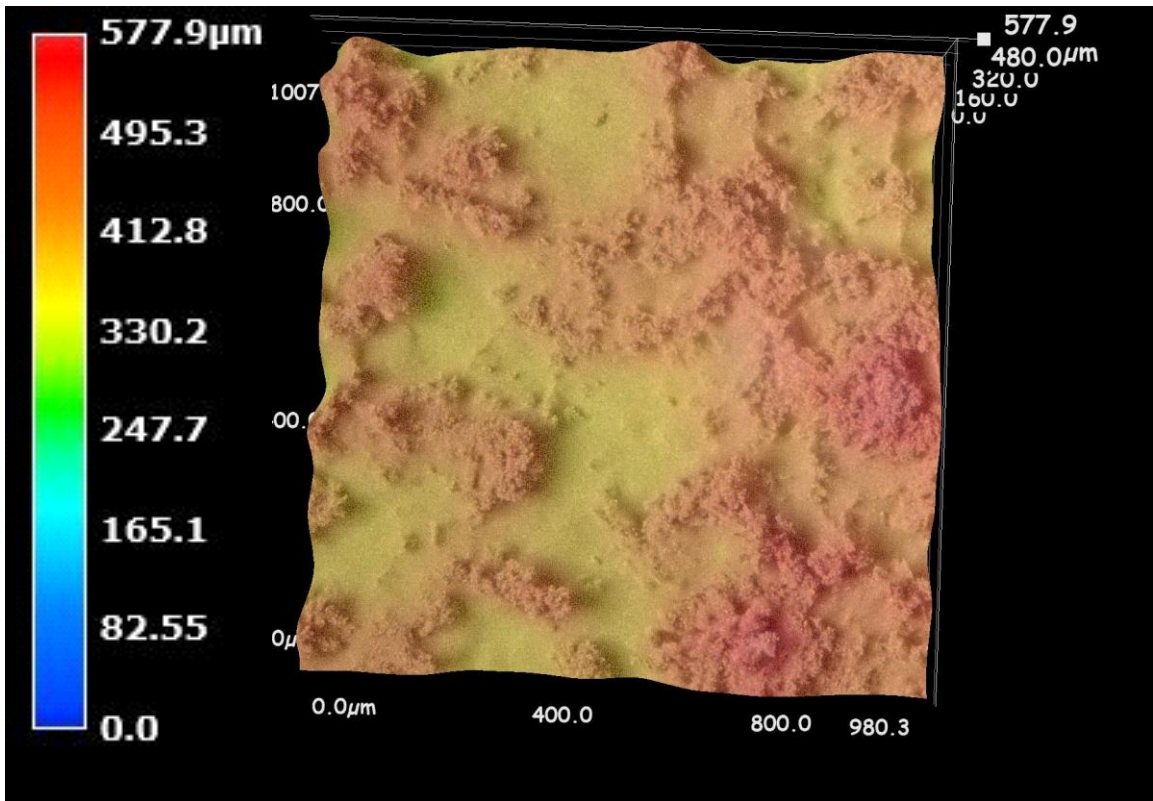


Figure 4.16: Topographical features on the deposit layer

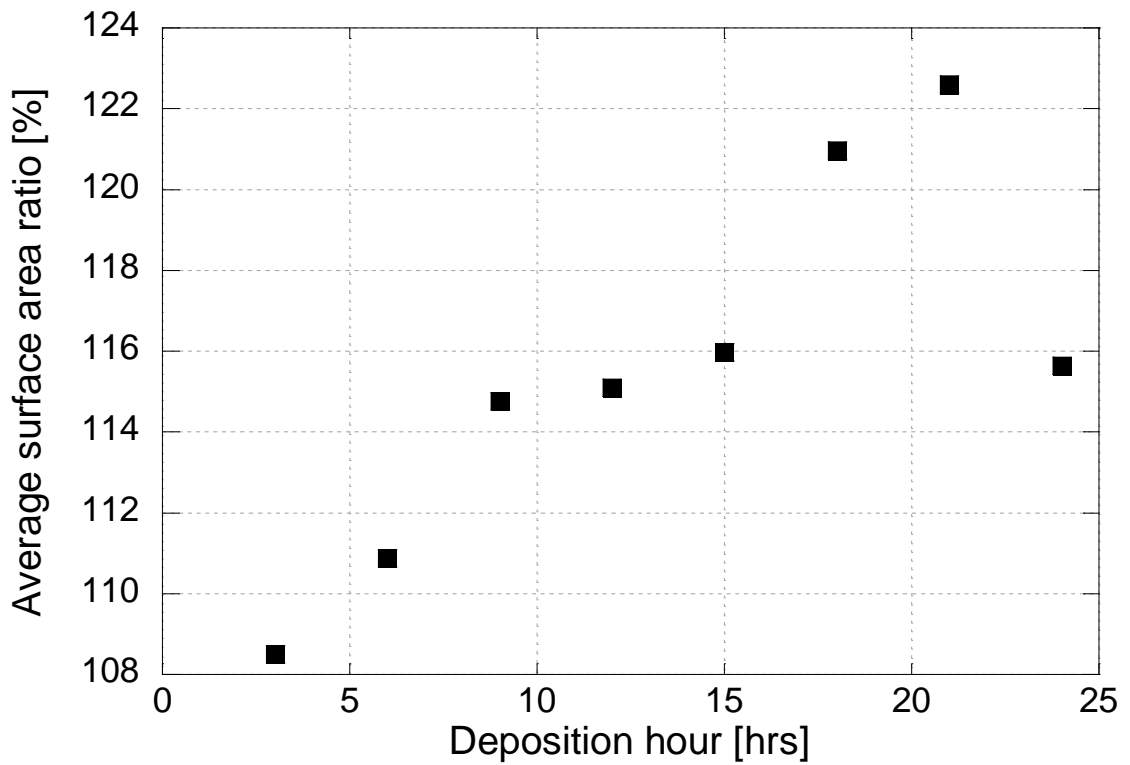


Figure 4.17: Average surface area ratio with increasing deposit layer thickness

The increased surface area serves to improve heat transfer from the gas just as radiator fins serve to increase heat transfer. It is the area exposed to the flow that transfers heat from the gas flow, and subsequently that heat is transferred via conduction to the coolant.

A convective heat transfer correlation shows that a potential increase of 20% on the surface area directly increases the convective heat transfer by 20%.

$$(1.2 \times Q) = h(1.2 \times A)(T_{gas} - T_{deposit})$$

Equation 4.1: Convective heat transfer correlation from gas to deposit surface

Where  $Q$  is the total heat transfer rate,  $h$  is the convective heat transfer coefficient,  $T_{gas}$  is the temperature of the gas, and  $T_{deposit}$  is the temperature of the deposit. If the area increased by 20%, the total heat transfer rate would be increased by 20%, assuming the difference in temperature is unaffected. Relating this to the energy of the airflow into the tube (Equation 4.2) suggests a 20% increase in the difference in temperature between the inlet and the outlet of the tube as the specific heat  $C_p$  and mass flow rate  $\dot{m}$  do not change.

$$\dot{m}C_p(1.2 \times (T_{gas\ tube\ inlet} - T_{gas\ tube\ outlet})) = h(1.2 \times A)(T_{gas} - T_{deposit})$$

Equation 4.2: Energy of flow related to convective heat transfer

This potentially yields a 20% increase in the effectiveness of a smooth tube, since the 20% increase in the difference in gas temperature between the inlet and outlet of the tube is reflected in the numerator of effectiveness  $\varepsilon$ :

$$\varepsilon_{rough\ surface} = \frac{1.2 \times (T_{gas\ inlet} - T_{gas\ outlet})}{T_{gas\ inlet} - T_{coolant}} = (1.2 \times \varepsilon_{smooth\ surface})$$

Equation 4.3: Potential impact of increased surface area on heat exchanger effectiveness

Roughness is also associated with an impact on the convective heat transfer coefficient. As the roughness of a tube increases, the friction factor also increases as noted by [4]. The friction factor is directly linked to the Nusselt number (Equation 4.4) and consequently, the convective heat transfer coefficient (Equation 4.5). Thus, an increase in the roughness of the layer will act to increase the convective heat transfer coefficient, improving heat transfer from the gas to the deposit surface.

$$Nusselt = \frac{\left( \left( \frac{friction\_factor}{8} \right) \times Re \right) \times Pr}{1.07 + 12.7 \times (friction\_factor^{0.5}) * \left( Pr^{\frac{2}{3}} - 1 \right)}$$

Equation 4.4: Dependence of Nusselt number on friction factor, for  $Re > 2300$  Petukhov relation [4]

$$h_{convective} = \frac{Nusselt * Conductivity_{air}}{Hydraulic\ diameter}$$

Equation 4.5: Dependence of convection heat transfer coefficient on Nusselt number [4]

Currently, relations for friction factors are determined for smooth tubes only and are only a function of Reynolds number. As surface roughness is unaccounted for, the assumed friction factor is lower than in actuality and may lead to erroneous heat transfer coefficients and effectiveness prediction.

Utilizing a modified 1-D model from Abarham [2], the effect of surface area on heat exchanger effectiveness was determined. Conditions from the 24-hour layer were input to the model, but with 100% and 120% surface ratios and an assumed thermal conductivity of 0.041 W/mK. Figure 4.18 shows that the increased surface area reduced the gas temperature more for the same thickness deposit layer than the flat surface area condition. This resulted in an increase in heat exchanger effectiveness from 13.34% to 15.75%, an increase of 18%. This value is close to the calculated increase of 20% identified in Equation 4.3.

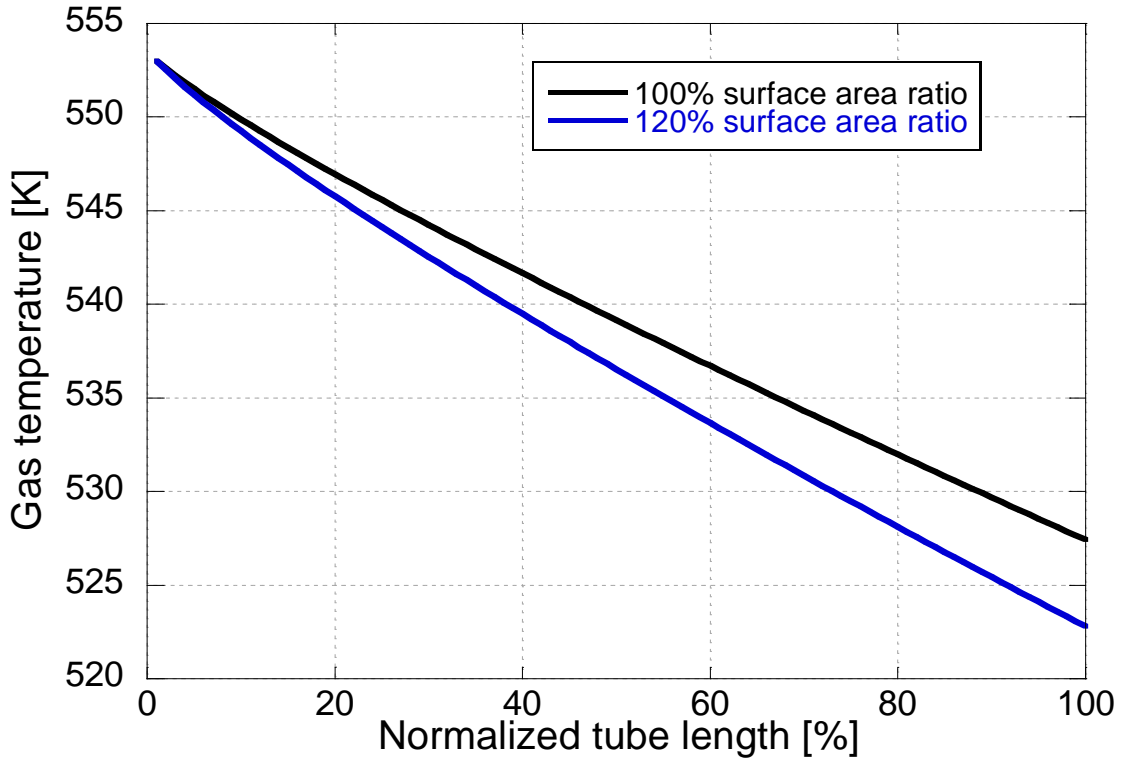


Figure 4.18: Model results for the impact of 100% compared to 120% surface area ratio on gas temperature for a 483 micron thick layer

The effect of surface area ratio for varying thickness on heat exchanger effectiveness was investigated using the modified 1-D model. Figure 4.19 shows that as layer thickness increased, the heat exchanger effectiveness decreased as expected. The thicker layer provides increased insulation and prevents heat from being rejected from the gas flow, thus decreasing the heat exchanger effectiveness.

The increase in surface area appears to linearly affect the heat exchanger effectiveness. This effect can be seen through Equation 4.3 as the effectiveness of the heat exchanger is directly linked to the heat exchange area. At first glance, the influence of surface area on overall effectiveness appears to decrease with increasing thickness, as noted by the decreasing slope of effectiveness with surface area for increasing layer thickness. This is due to the increasing insulating effect of thicker layers reducing the overall effectiveness. The percent increase of heat exchanger effectiveness remains



similar to the increase in deposit surface area ratio and tends to increase with increasing thickness as shown in Figure 4.20.

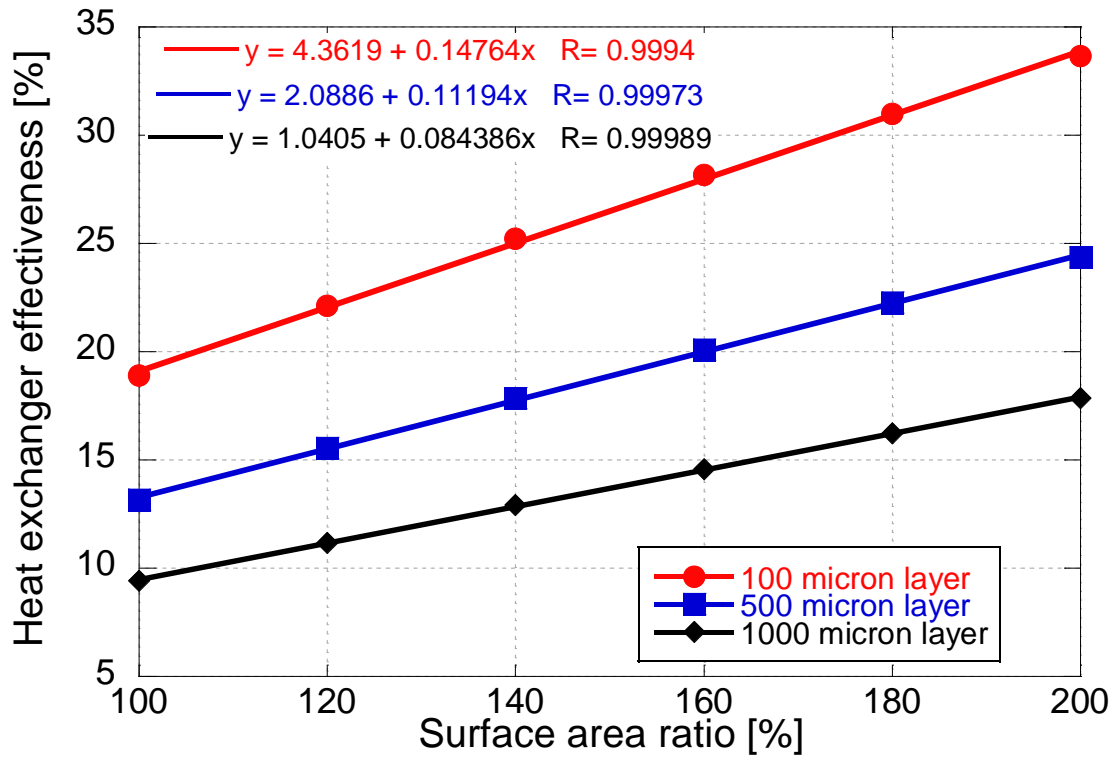


Figure 4.19: Effect of surface area ratio on heat exchanger effectiveness for varying thicknesses

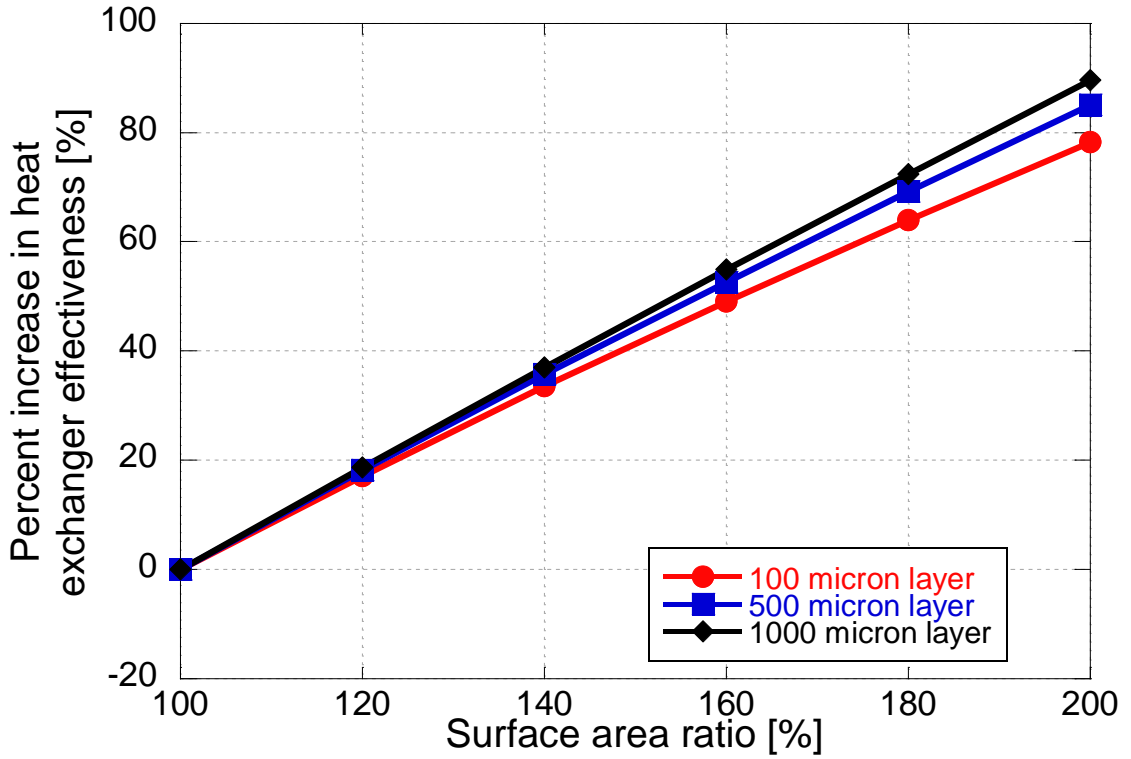


Figure 4.20: Percent increase in heat exchanger effectiveness as a function of surface area ratio for varying thicknesses

#### 4.2.3 Infrared surface temperature

Deposit layer interface surface temperatures were also measured over the 24-hour interval. Hot compressed air was flown through the fixture at various flow rates and temperatures, as described in Table 4.2. Only the results from hours 9-24 are shown.

Table 4.2: Interface surface temperature experiment, compressed air conditions

	Air flow rate [kg/hr]	Inlet air temperature [C]	Reynolds number
Point 1	4.56	200	2711
Point 2	4.56	202	2698
Point 3	4.55	204	2687
Point 4	5.64	206	3316
Point 5	6.47	206	3812
Point 6	7.23	202	4280
Point 7	3.9	202	2312
Point 8	2.77	198	1649
Point 9	4.88	208	2862

The evolution of surface temperature for Point 6 is visually shown in Figure 4.21. As deposit thickness increased, the apparent surface temperature also increased. This trend is expected since the deposit acts as an insulative coating preventing heat transfer from the gas into the coolant. Therefore, as deposit thickness increases, the total insulation of the layer increases; consequently reducing the heat flux from the gas and increasing the gas temperature. This effect can be further realized by observing the scratches made in the deposit surface for thickness measurements. As fresh scratches are filled in with new deposits, the thinner layer resulted in a lower surface temperature in subsequent hot air experiments. As these scratches developed thicker deposit layers, their surface temperatures approached the undisturbed layer. A prime example of this is highlighted in the north-south scratches seen in the 9-hour layer. As these scratches filled in with additional deposits, their appearance starts to disappear until they are barely noticeable in hour 24. In the visible spectrum, aged scratches are barely visible.

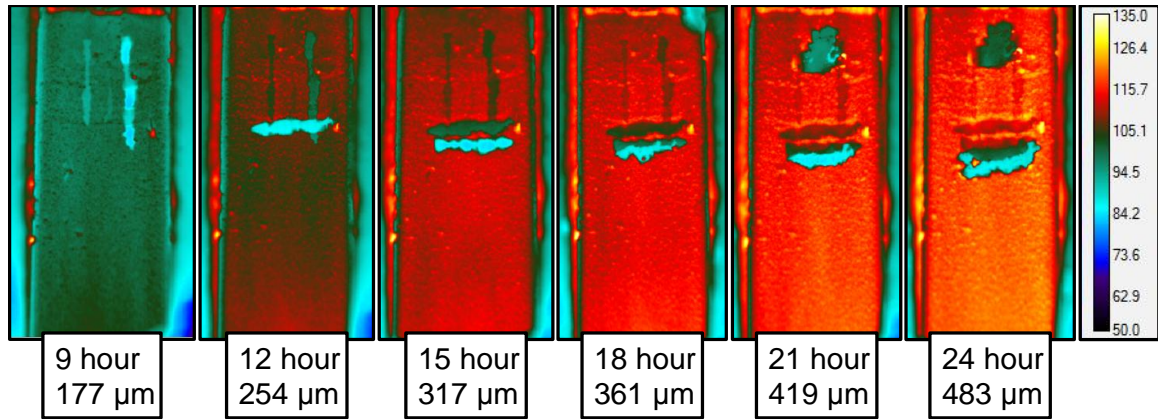


Figure 4.21: Infrared surface temperature evolution with deposit thickness for Point 6

Figure 4.22 tracks the infrared surface temperature over a range of Reynolds numbers for constant thicknesses. For a constant thickness, as Reynolds number increased the surface temperature also increased. The higher Reynolds number flow decreased the residence time of the gas in the channel and reduced the time for heat exchange between the gas and the coolant. This created a hotter gas temperature as shown in the figure and is an expected trend. However, the increase in surface temperature with Reynolds number is non-linear; a trend that is not expected and might suggest a change in the thermal properties of the layer.

Surface temperature increased with deposit thickness as mentioned earlier. To understand the relationship between surface temperature and deposit thickness, the data from Figure 4.22 is re-plotted for constant Reynolds number and varying deposit thickness in Figure 4.23 for select Reynolds numbers. As deposit thickness increased, the surface temperature was seen to increase however did so non-linearly. 1-D modeling analysis does show an asymptotic increase in interface temperature with Reynolds number, however shows a more linear increase with deposit thickness (Figure 4.24).

Abarham's studies indicate that as the porosity of the deposit layer changes, the thermal conductivity of that layer is also expected to change, as shown in Figure 4.25 [2]. As porosity decreases, the deposit conductivity is driven less by the conductivity of the surrounding air and more by the assumed graphite structure of the deposit layer. The

inflection point in the conductivity is due a trade-off between the decreasing thermal conductivity of graphite and increasing thermal conductivity of air with temperature and is a function of porosity. The non-linear behavior of surface temperature with deposit thickness may suggest a change in the thermal properties of the deposit layer or a possible densification of the layer as thickness increases.

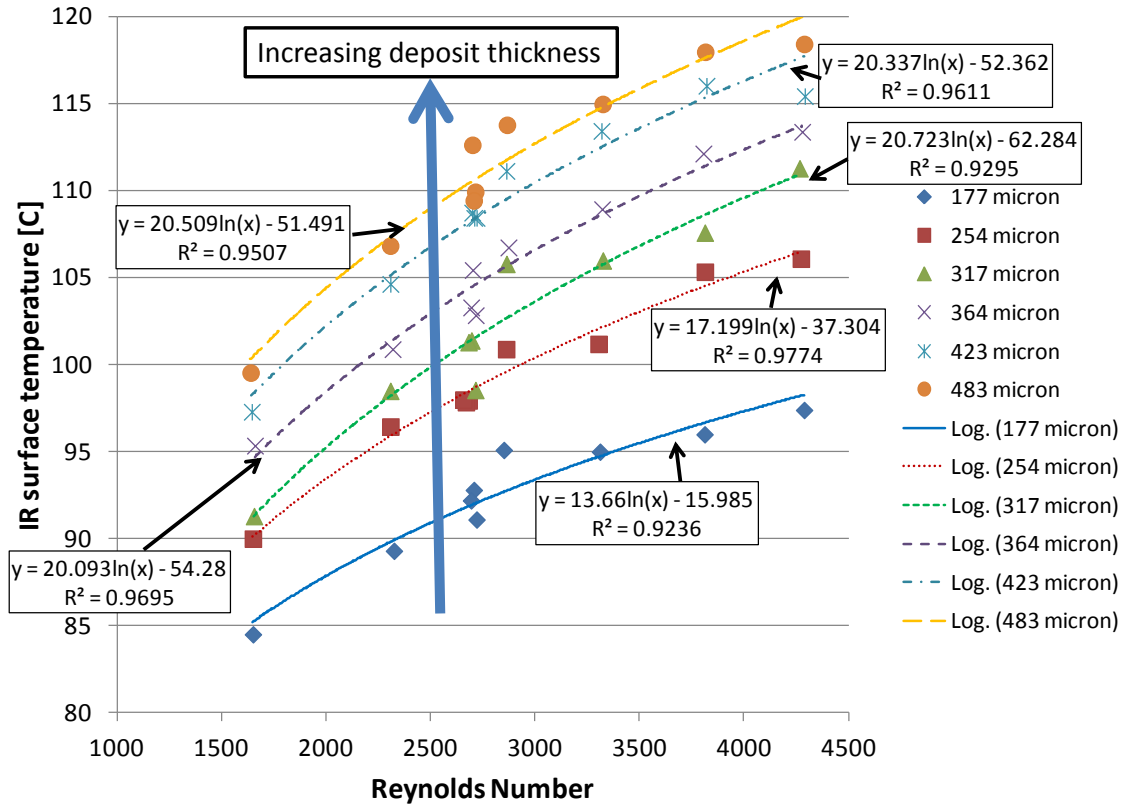


Figure 4.22: Interface deposit surface temperature as a function of varying Reynolds number for constant deposit thickness

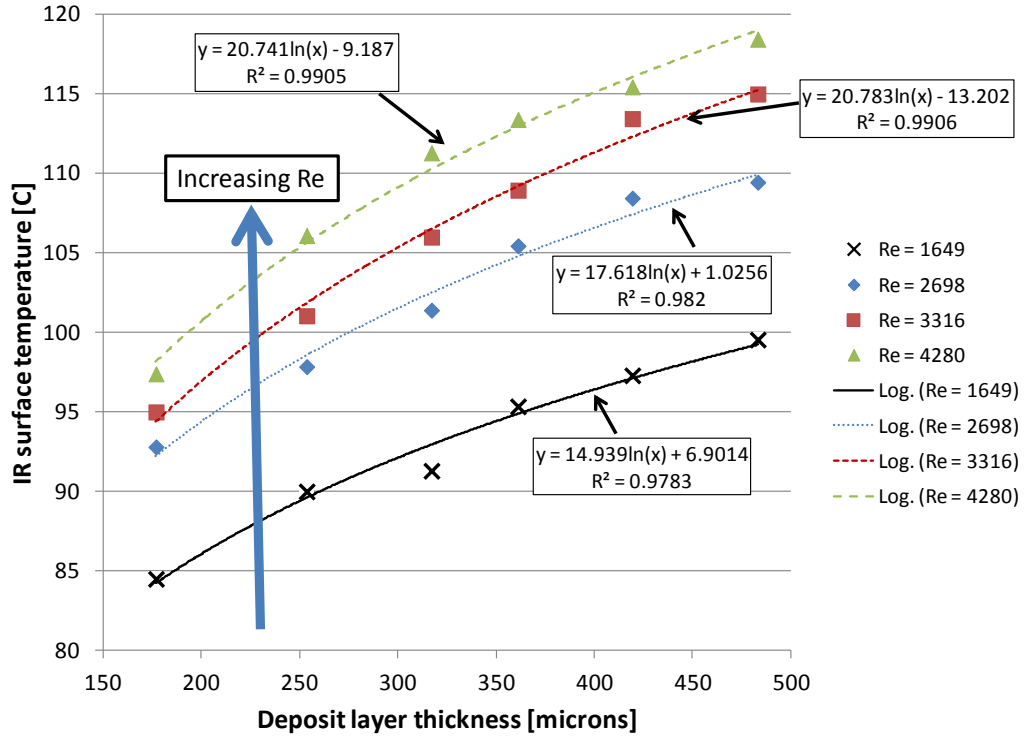


Figure 4.23: Interface deposit surface temperature evolution with layer thickness for constant Reynolds number

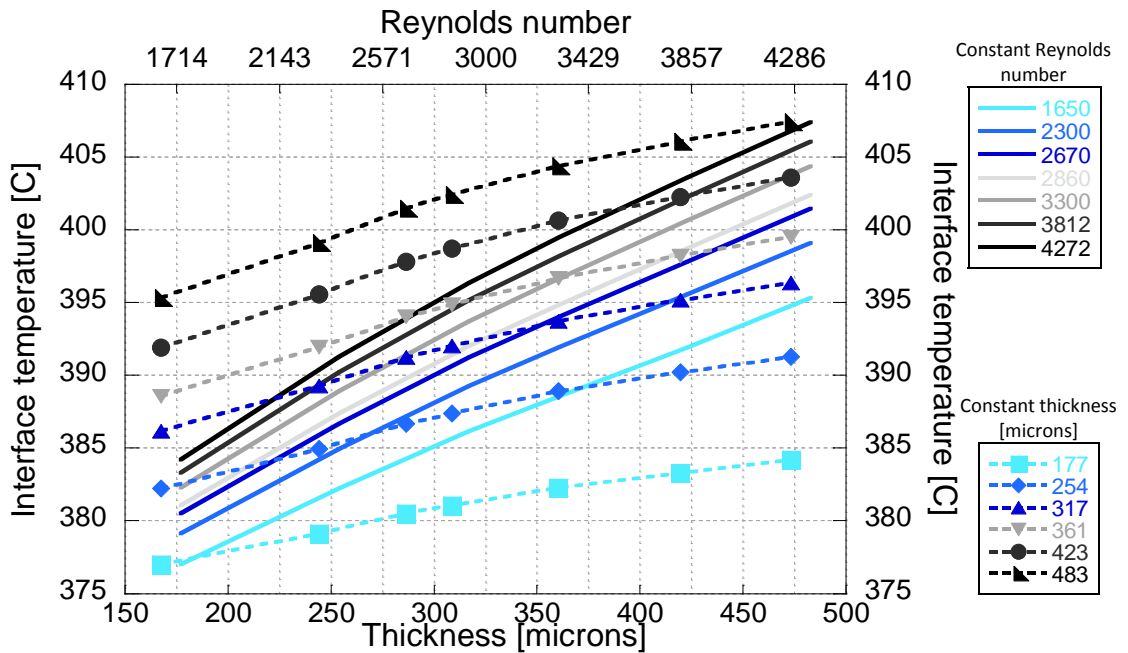


Figure 4.24: 1-D model estimates of surface temperature (both y-axes) for constant Reynolds number, varying thickness (solid lines without markers, corresponding to bottom x-axis) and constant thickness, varying Reynolds number (dashed lines with solid markers, corresponding to the top x-axis)

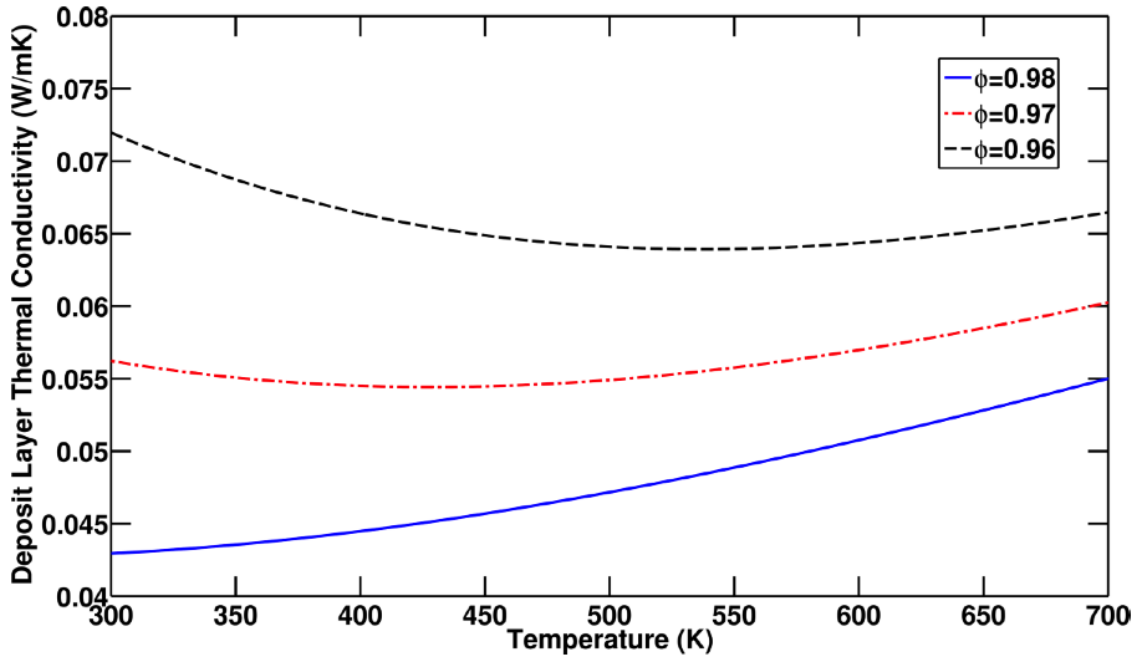


Figure 4.25: Calculated deposit conductivity as a function of temperature and layer porosity [2]

The topography mentioned in Section 4.2.2 is not noticed significantly in the infrared images of the surface and highlights the potential for temperature data to be washed out by the spatial resolution of the infrared optics. To evaluate this concern, a close-up infrared lens was acquired from FLIR that can resolve up to 50 microns spatially (specifications in Table A.1 in the Appendix). The close-up image in Figure 4.26 shows that the peaks of the deposit layer are hotter than the surroundings. The maximum temperature difference between the hottest and coolest was measured to be 10°C, 7°C between the hottest and the mean temperature, and 2°C between the coolest and the mean temperature. These results show that the majority of the surface layer is cooler than the peaks and justifies the use of the mean temperature as a representative surface temperature.

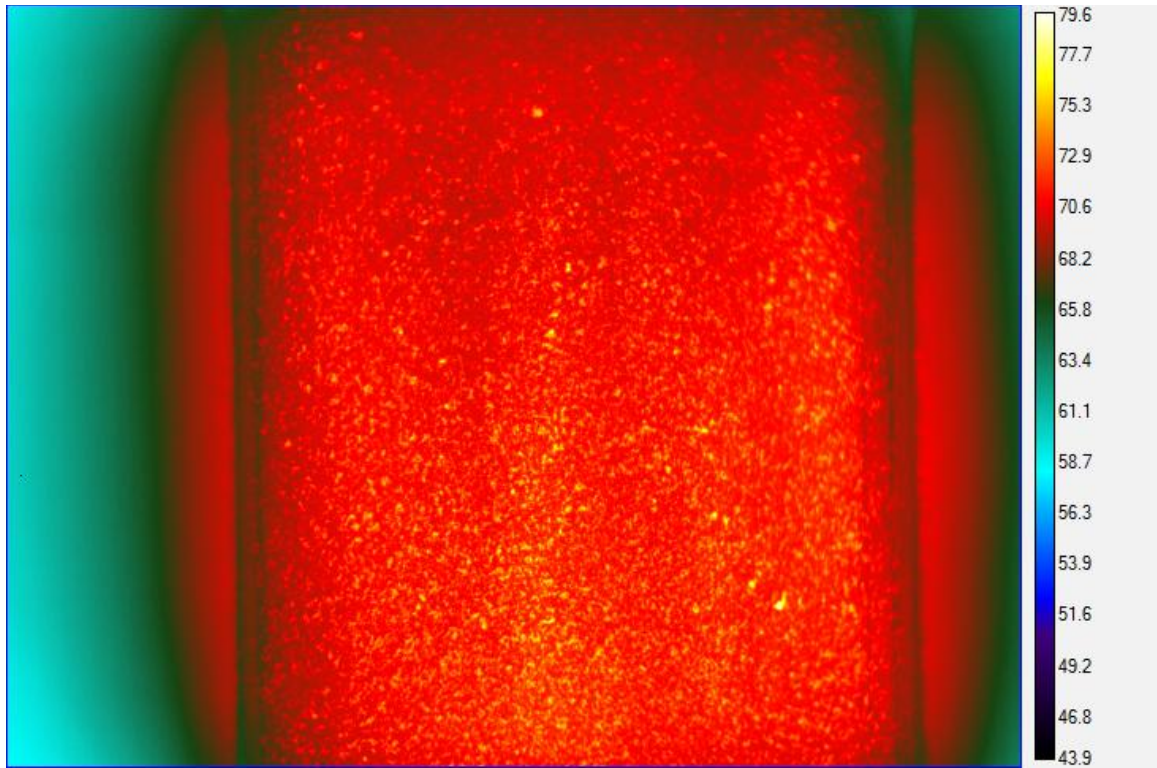


Figure 4.26: Close up of 3-hour deposit layer, 5.6 kg/hr at 202°C air flow rate

### 4.3 Conclusions

Initial investigations into carbon based nano-particulate deposit layers were conducted over a 24-hour deposition event. Measurements were performed every three hours and utilized an optical microscope to measure deposit thickness and surface area and an infrared camera to measure deposit surface interface temperature as a function of layer thickness and Reynolds number.

Deposit thickness increased linearly with deposition time and is contrary to previous research. The large cross sectional area of the visualization rig reduced the convective heat transfer coefficient from the gas to the deposit surface, thereby keeping the surface temperature low and thermophoresis high. Modeling work supported the experimental results and also shows asymptotic thickness growth for smaller hydraulic diameters.



Deposit surface area was also seen to increase with deposition thickness. The increased surface area may serve to increase heat transfer from the gas to the deposit layer, and subsequently into the coolant. The increase in area is not currently accommodated for in modeling approaches and could be significant in estimating heat exchanger effectiveness.

Deposit surface temperature increased with increased Reynolds number flows and deposit thickness. The increased Reynolds number flows reduced the residence time of the gas in the rig, decreasing the heat transfer from the gas to the coolant thus increasing the gas, and therefore deposit, temperature. As the deposit layer thickness increased, the total insulation of the layer increased, decreasing the heat transfer from the gas to the coolant. The decreased heat transfer from the gas resulted in increased gas and deposit surface temperature. The increase in surface temperature with Reynolds number and deposit thickness is expected; however the increase is non-linear and may suggest a change in deposit thermal properties or density. To investigate these differences in deposit properties, heat flux sensors are installed in the fixture to enable thermal conductivity calculations and results are presented in the next chapter.

#### 4.4 References

- [1] Warey, A., Balestrino, S., Szymkowicz, P., and Malayeri, M. R., "A one-dimensional model for particulate deposition and hydrocarbon condensation in exhaust gas recirculation coolers," *Aerosol Science and Technology*, vol. 46, no. 2, pp. 198-213.
- [2] Abarham, M., "Investigation of Nano-Particulate Transport in Non-Isothermal Turbulent Internal Flows," in *Mechanical Engineering*. vol. Ph.D. Ann Arbor: University of Michigan, 2011.
- [3] Hoard, J., Chafekar, T., Abarham, M., Schwader, R., Uplegger, S., and Styles, D., "Large particles in modern diesel engine exhaust," in *ASME 2012 Internal combustion engine division spring technical conference (ICES 2012)*, Torino, Italy, 2012.
- [4] Incropera, F. and DeWitt, D., *Fundamentals of Heat and Mass Transfer*, 5th ed.: John Wiley & Sons, Inc, 2002.

## CHAPTER 5

### IN-SITU DEPOSIT LAYER PROPERTIES

An additional 24-hour deposition was performed on the visualization rig with heat flux probes mounted on the exhaust side of the stainless steel specimen as mentioned in Chapter 2. The addition of the heat flux probes, in combination with measurements from the optical and infrared cameras, allowed for the calculation of the in-situ thermal conductivity of the deposit layer as a function of time and exhaust composition. This chapter will serve as experimental validation of the novel measurement technique described in Chapter 2.

The experimental conditions and exhaust gas composition were the same as mentioned in Chapter 5, except that the inlet exhaust temperature was increased to 280°C

#### 5.1 24-hour deposition experimental results

Measurements were performed on both heat flux probes; with heat flux probe 1 (HF1) being upstream and heat flux probe 2 (HF2) downstream. Results will be presented for both and in 6-hour increments; however hour 12 will be omitted due to equipment failure.

##### 5.1.1 Deposition

The heat flux probes are equipped with an embedded K-type thermocouple on the exhaust side of the probe. This temperature location measures the wall side temperature

of the deposit layer and enables the measurement of the change in temperature across the thickness of a deposit layer. As a measure of their accuracy, Figure 5.1 shows the temperature measurements of the probes during the first deposition event, hours 0-6. The fixture is initially warmed up with hot air during the “Warm-up” (until ~5000 seconds), then switched to engine exhaust for the “Deposition”. The probe temperatures were similar through the warm up and first part of the deposition. As deposit built up, the probe temperatures deviated and the downstream probe measured a hotter temperature than the upstream probe. This is due to the buildup of a deposit layer starting at the inlet of the fixture and progressing downstream. The insulative property of the layer kept the exhaust temperature hotter as it moved through the fixture. As the layer continued to build, the gas temperature on probe 2 increased due to a lower rejection of heat at upstream locations.

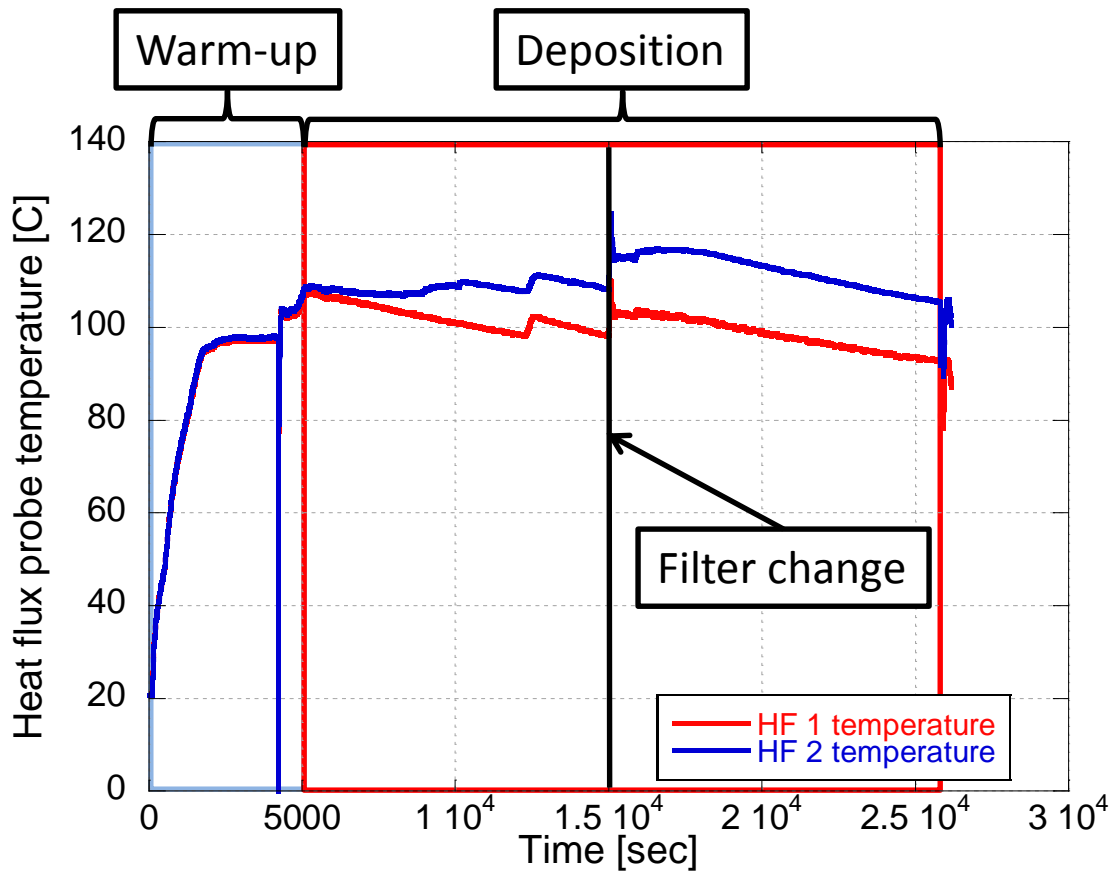


Figure 5.1: Heat flux probe temperatures during live deposition

The periodic cycling of the temperature is due to a thermostatic coolant heater. This problem was resolved in subsequent deposition events with the use of a heat tape, thus providing a constant inlet temperature. The sudden increase in temperature in the middle of the deposition event ( $\sim 1.5 \times 10^4$  seconds) is due to the replacement of an in-line 1" x 7" heated exhaust filter. The filter is installed downstream of the rig and is used to capture particles upstream of the mass flow meter. This filter becomes clogged with particles, increasing the pressure in the rig and decreasing the gas flow rate. The filter is replaced every 3 hours to maintain sufficient gas flow rates.

#### 5.1.2 Deposit layer thickness

As a deposit layer is built and measured on top of the heat flux probes, instead of the stainless steel substrate as in Chapter 4, it is important to capture the effects of the additional probe thermal resistance on deposit growth. Figure 5.2 shows that probe 1 has a thicker deposit build than that of probe 2. This is an expected trend since probe 1 is upstream and is subjected to hotter gas flows and therefore higher thermophoretic forces. Contrary to the results presented in Chapter 4, the deposit thickness deviated from a linear growth pattern and is highlighted with the presence of linear extrapolations based on the initial 0-6 hour deposit growth rate. The differences are attributed to the additional thermal resistance of the heat flux probes. The surface of the probes, the side exposed to the hot exhaust gases, have increased surface temperatures compared to the bare stainless steel substrate. This is due to an increased thermal resistance from the probes' low thermal conductivity (0.311 W/mK compared to 14.6 W/mK for stainless steel), and resulted in non-linear deposit growth from reduced thermophoretic forces.

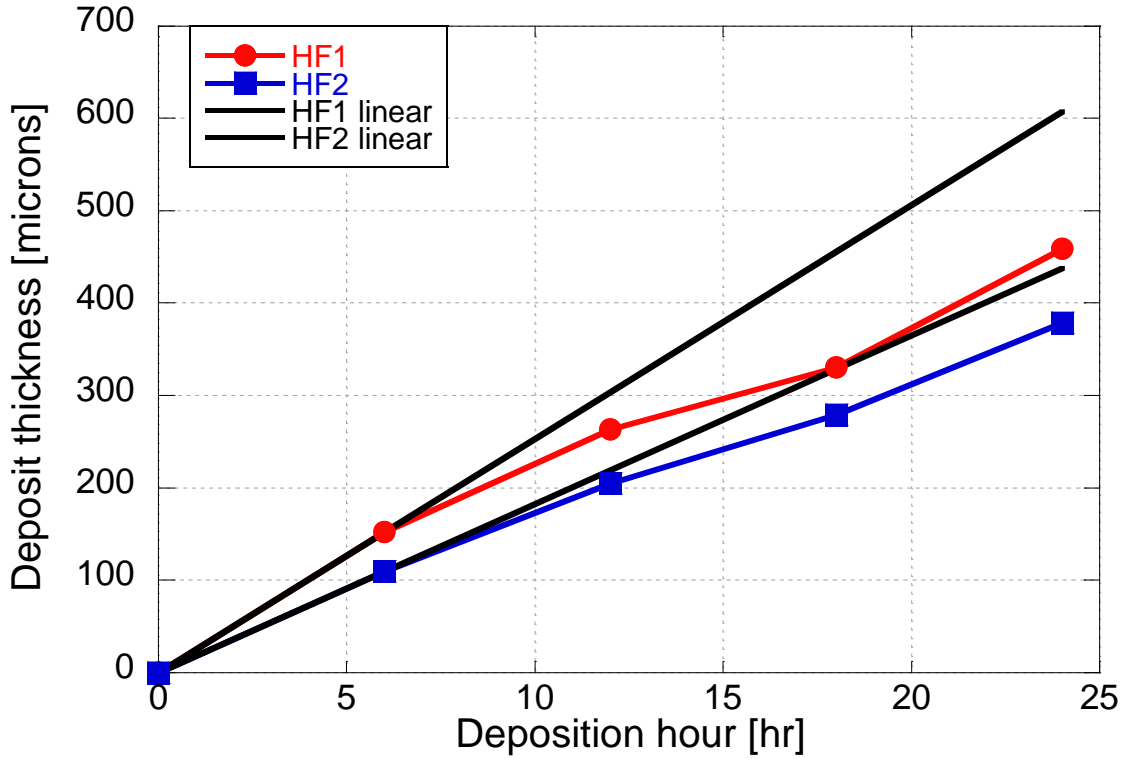


Figure 5.2: Deposit layer growth on heat flux probe 1 and 2 with linear extrapolation

### 5.1.3 Deposit surface area

Deposit surface area increased with increasing deposit thickness. Surface area appears to increase more for the downstream probe, probe 2, than the upstream probe 1. This phenomenon may be due to flow differences between the two locations. The upstream location produces a leading edge to the flow, changing the boundary layer development across the probe. This effect may produce slight shearing across the peaks of the deposit on probe 1 and reduce the surface area relative to probe 2.

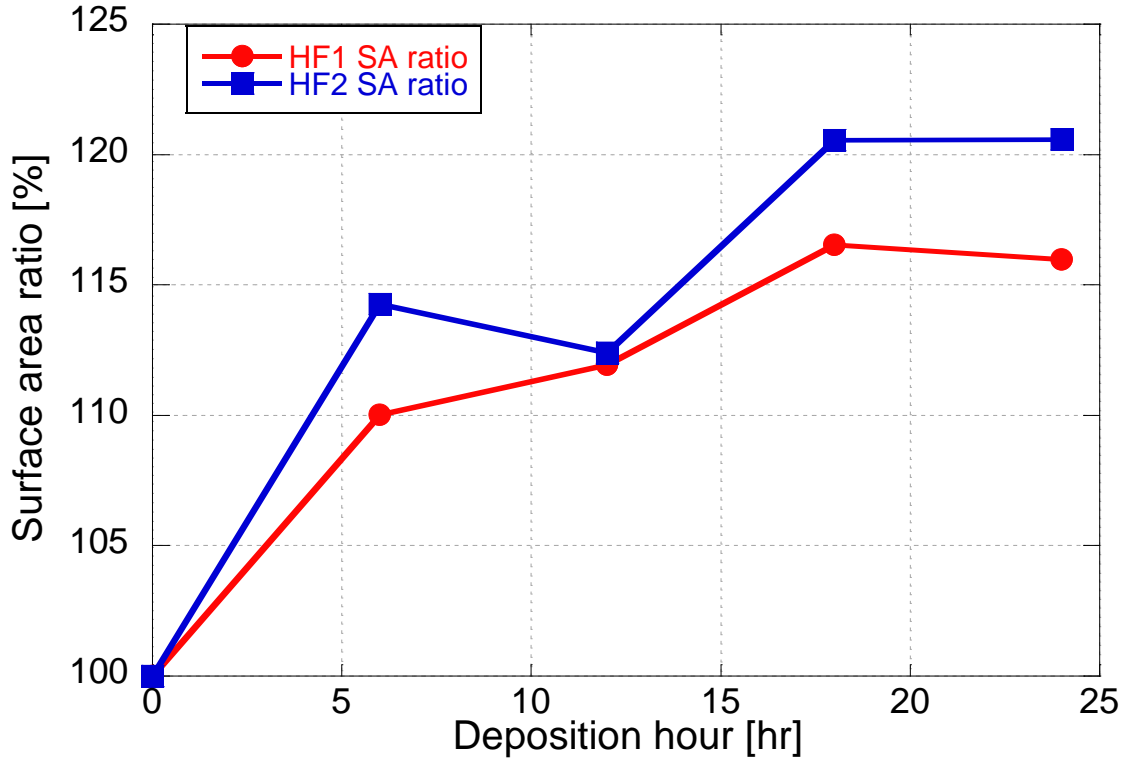


Figure 5.3: Deposit surface area ratio for probes 1 and 2

#### 5.1.4 Deposit temperature

Conditions for measuring the surface temperature changed from Chapter 4. Hot airflow flowed through the fixture at the conditions described in Table A.2 in the Appendix. The purpose of the hot air in these experiments is to generate heat transfer through the deposit layer while being measured by the heat flux probe in order to calculate deposit thermal conductivity. The airflow rate is varied to change the Reynolds number of the flow while maintaining an inlet temperature of 200°C.

Figure 5.4 illustrates the infrared surface temperature for constant thickness and varying Reynolds number. The trends are similar to those in Chapter 4. As Reynolds number increased, the hotter thermal mass flow rate and decreased residence time in the heat exchanger increased the air temperature. Surface temperatures for probe 2 were lower than for probe 1 due to a thinner deposit layer, heat transfer across probe 1, and hotter surface temperatures on probe 1 due to leading edge effects.

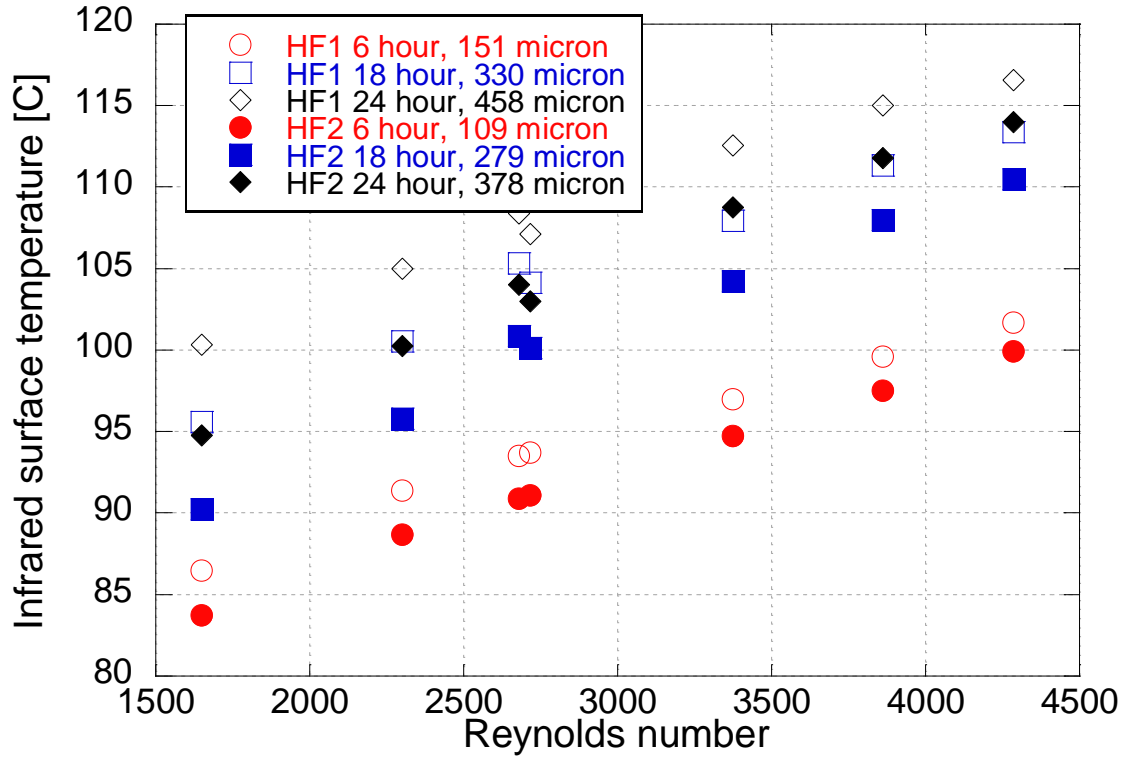


Figure 5.4: Infrared surface temperature of deposit layers on heat flux probes 1 and 2

Figure 5.5 re-plots the data for constant Reynolds number and highlights that as deposit thickness increased, the infrared interface temperature also increased. The increased temperature is due to the increased insulation provided by the deposit layer; however the increase in temperature is non-linear with thickness.



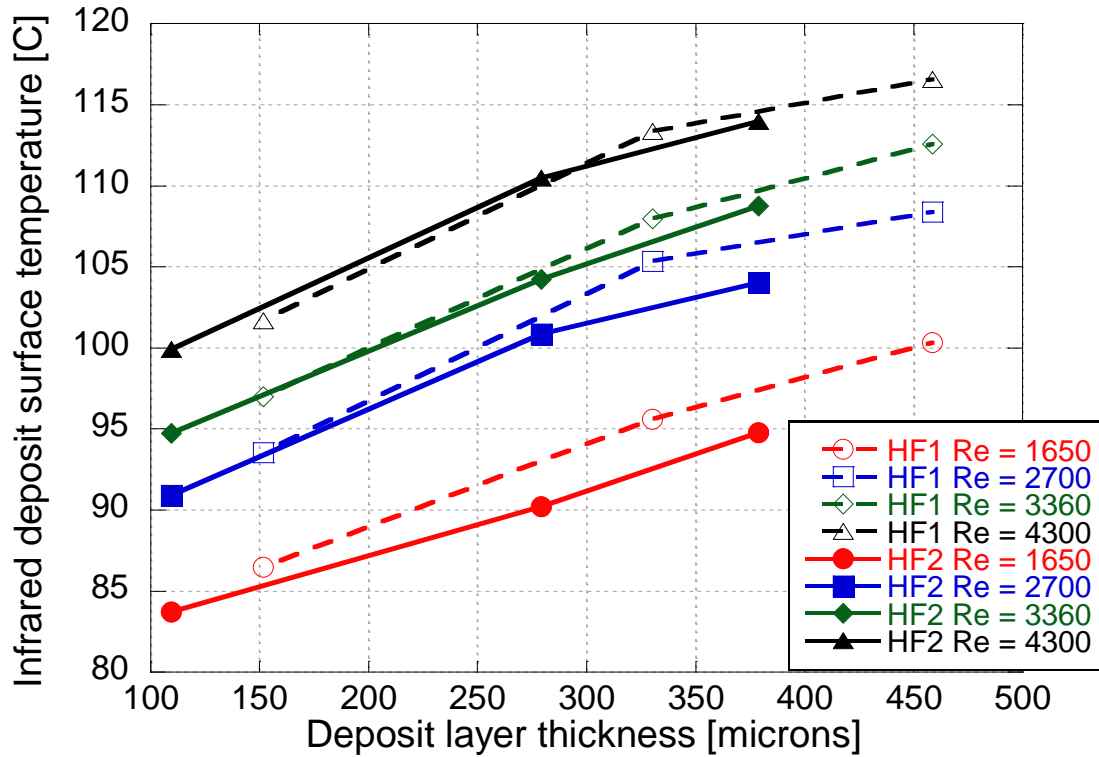


Figure 5.5: Infrared surface temperature versus deposit thickness

The temperature difference across the thickness of the deposit for constant thickness and varying Reynolds number is shown in Figure 5.6. Just as in the case for the surface temperature, the delta T through the thickness of the deposit layer increased with Reynolds number. Once again, this is due to a hotter thermal mass flow rate creating a hotter gas temperature.

The temperature gradient across the deposit layer increased as thickness increased, as shown in Figure 5.7. This trend is expected as the insulation effect of the deposit increases with thickness.

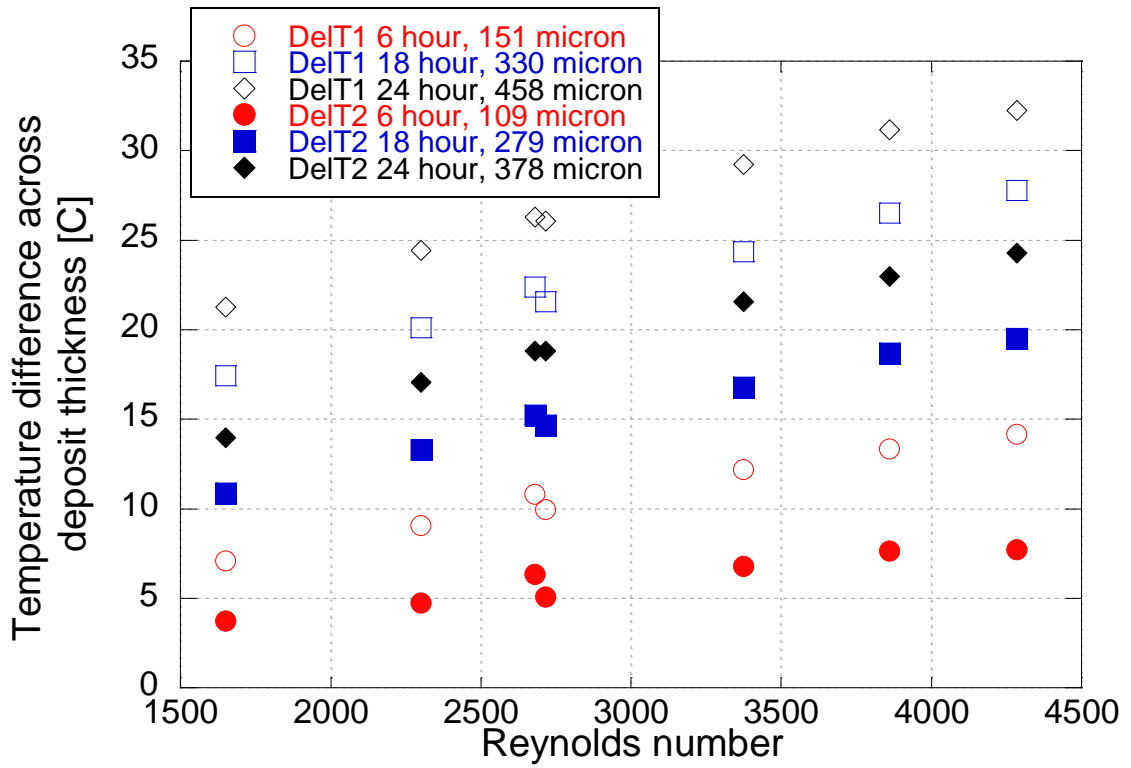


Figure 5.6: Temperature difference across deposit thickness as a function of Reynolds number

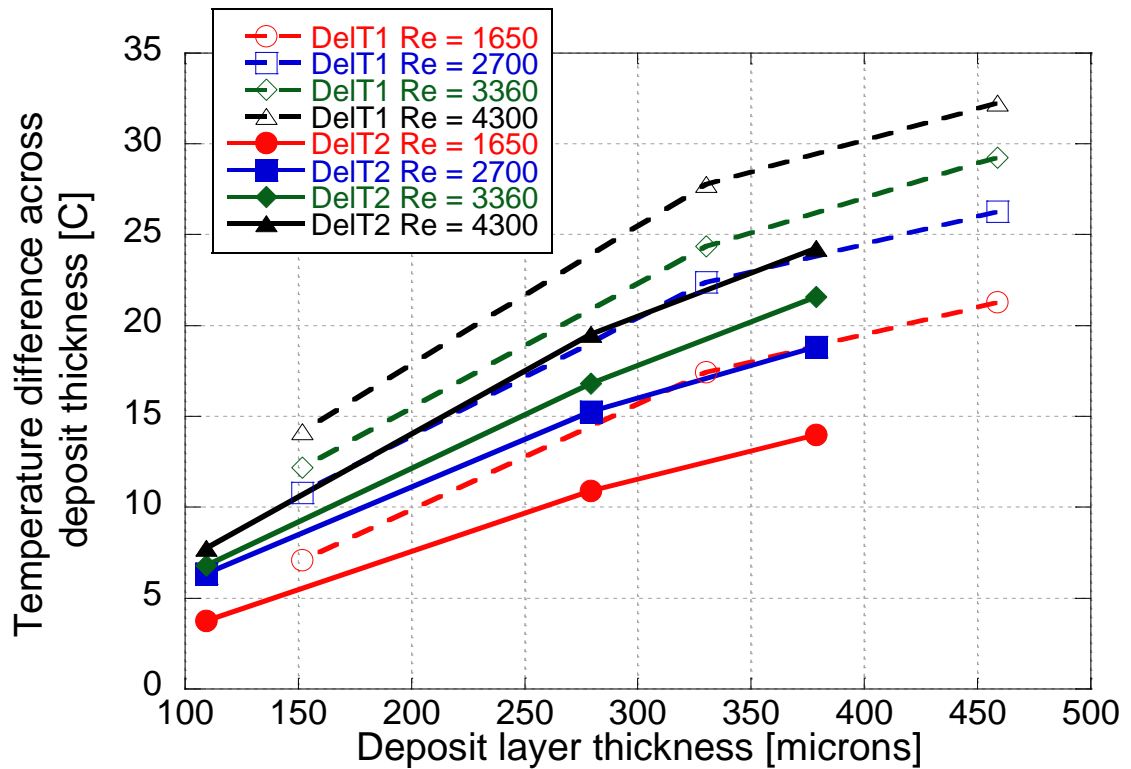


Figure 5.7: Temperature difference across deposit thickness as a function of deposit thickness

### 5.1.5 Heat flux

For a fixed thickness, heat flux increased with increasing Reynolds number flows and is shown in Figure 5.8. The increase in air temperature with increasing Reynolds number created a larger temperature difference between the air and the coolant resulting in increased heat flux through the deposit layer. As deposit thickness increased with deposition, the heat flux through the layer decreased. Heat flux differed significantly between the two probes for a young, thin layer. As deposition continued and the deposit thickness on the probes increased, the difference in heat flux between the two probes decreased. This trend is due to the increase in deposit thickness acting as increased insulation; reducing heat flux through the layer. At early exposures, the deposit thickness on the upstream probe, probe 1, is sufficiently thin to allow for a high heat flux. The increased heat flux on probe 1 reduced the temperature of the flowing gas and reduced the downstream probe, probe 2, heat flux. As probe 1 developed a thicker layer, the heat flux through the layer decreased and the gas flow remained hotter due to lower heat rejection. The hotter gas caused probe 2 to measure increased heat flux, however heat flux is also decreased due to a thicker deposit layer. The combination of these two effects caused a decrease in heat flux with deposition, as well as decreased the difference in heat flux between the two probes.

Reduced heat flux as a function of deposit thickness is illustrated in Figure 5.9 for both probes. This effect increases the outlet temperature of EGR coolers and can lead to problems with emissions and combustion control.

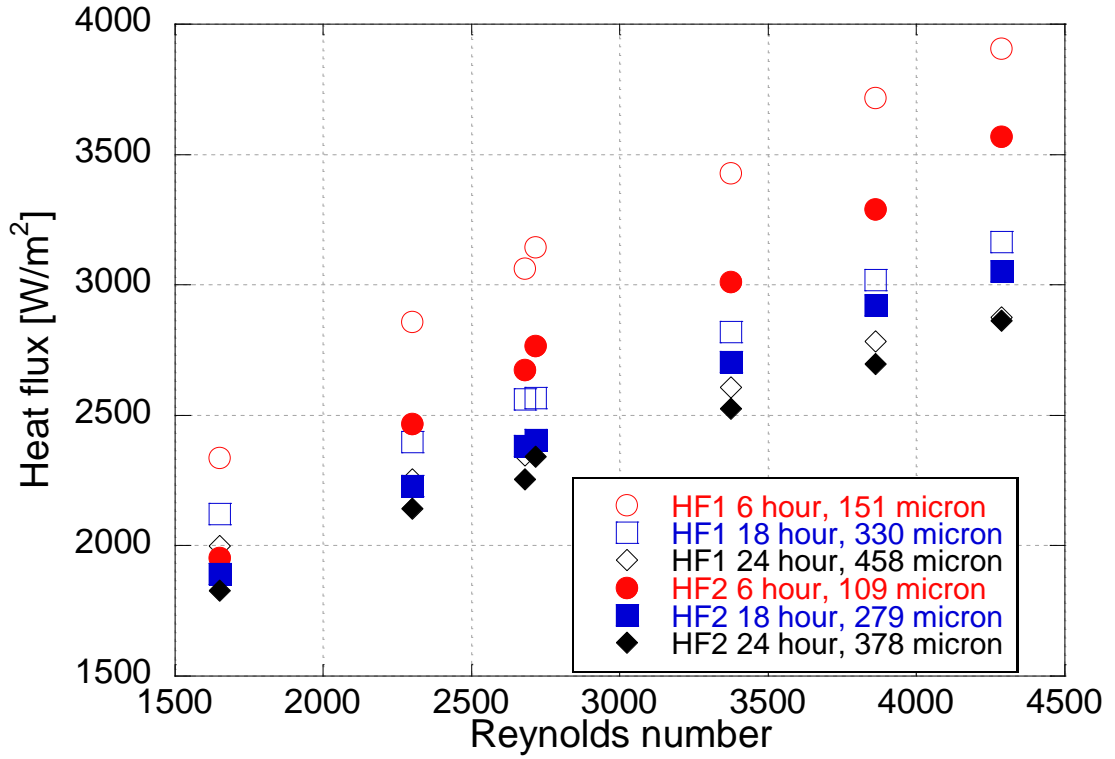


Figure 5.8: Heat flux for constant thickness and varying Reynolds number

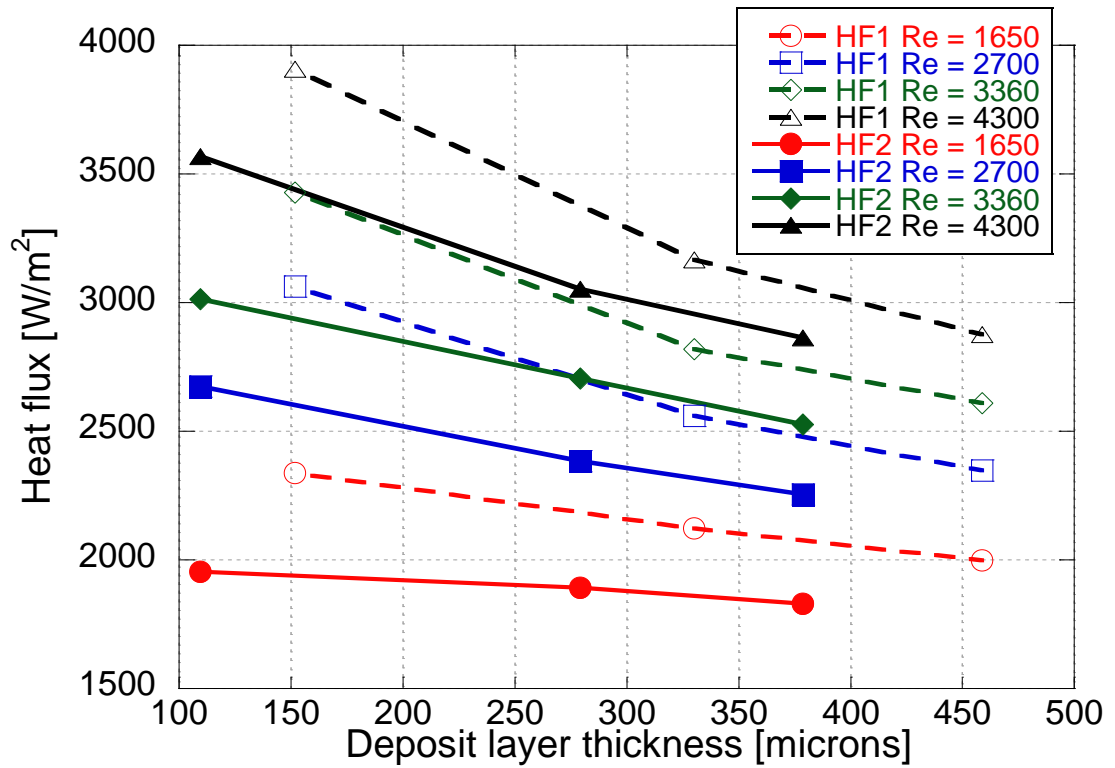


Figure 5.9: Heat flux for fixed Reynolds number and varying thickness

### 5.1.6 Thermal conductivity

Utilizing the previously discussed measurements, the thermal conductivity as a function of deposit thickness and Reynolds number was calculated. Figure 5.10 shows the thermal conductivity for a fixed thickness and varying Reynolds number. The conductivity of the downstream probe, probe 2, was slightly higher than that of probe 1. This is due to the slightly elevated surface temperatures on probe 1 due to leading edge effects. The thinner boundary layer on the leading edge allowed for hotter gases to influence the deposit surface, and increased the apparent insulative properties of the deposit. This resulted in a lower calculated conductivity.

Deposit thickness does not appear to have a significant impact on the deposit thermal conductivity, as noted from the fairly similar conductivity values for various thicknesses. This result suggests that densification does not occur with deposition; otherwise layer porosity would decrease and result in a higher thermal conductivity (Figure 5.11). The only exception was at the thin 6-hour layer developed on probe 2. The higher and somewhat erratic behavior of the conductivity was due to high measurement uncertainty resulting from the small temperature gradient across the deposit thickness. Measurement uncertainty is discussed in Chapter 8.

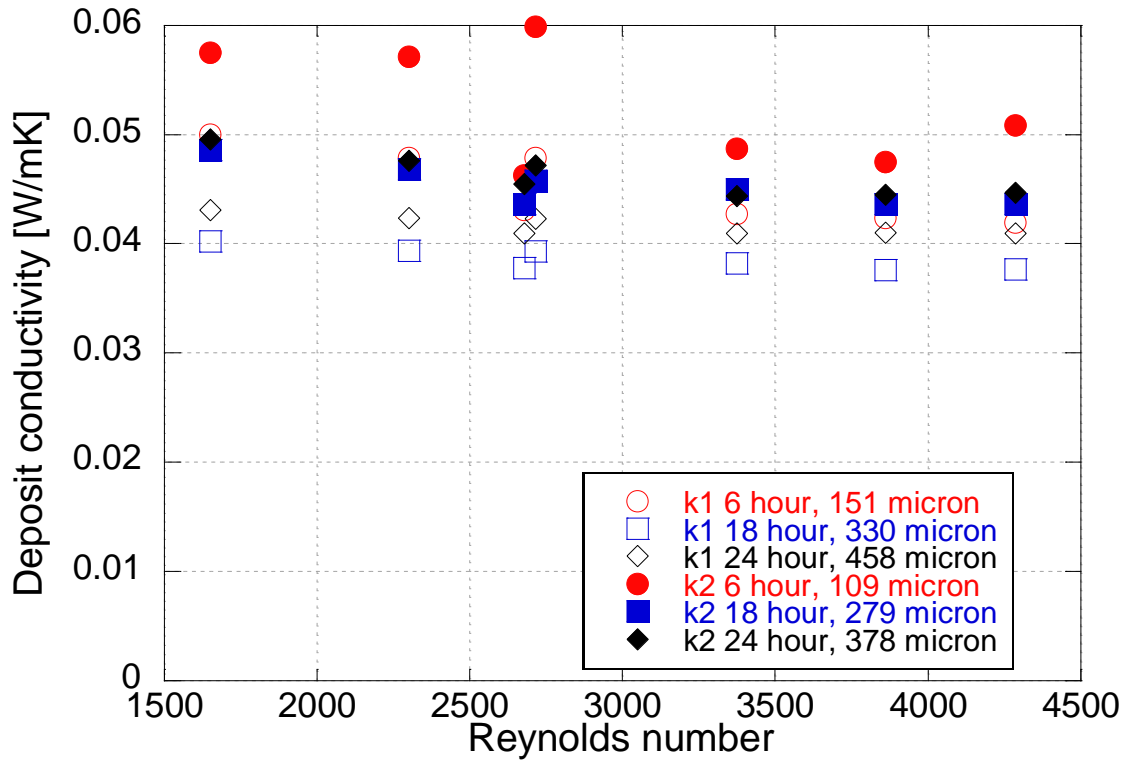


Figure 5.10: Deposit conductivity for constant thickness as a function of Reynolds number

Layer thermal conductivity does appear to be related to Reynolds number. As Reynolds number decreased, the conductivity increased. According to modeling estimates, the thermal conductivity of the layer is non-linear with temperature as shown in Figure 5.11 [1]. As surface temperature increases greater than 300K, the apparent thermal conductivity of the layer is dominated by that of the assumed graphite structure and decreases with temperature. However, as temperature increases past a certain point, the conductivity of the exhaust gas increases and dominates the trend. The temperature and severity of the inflection depends on layer porosity.

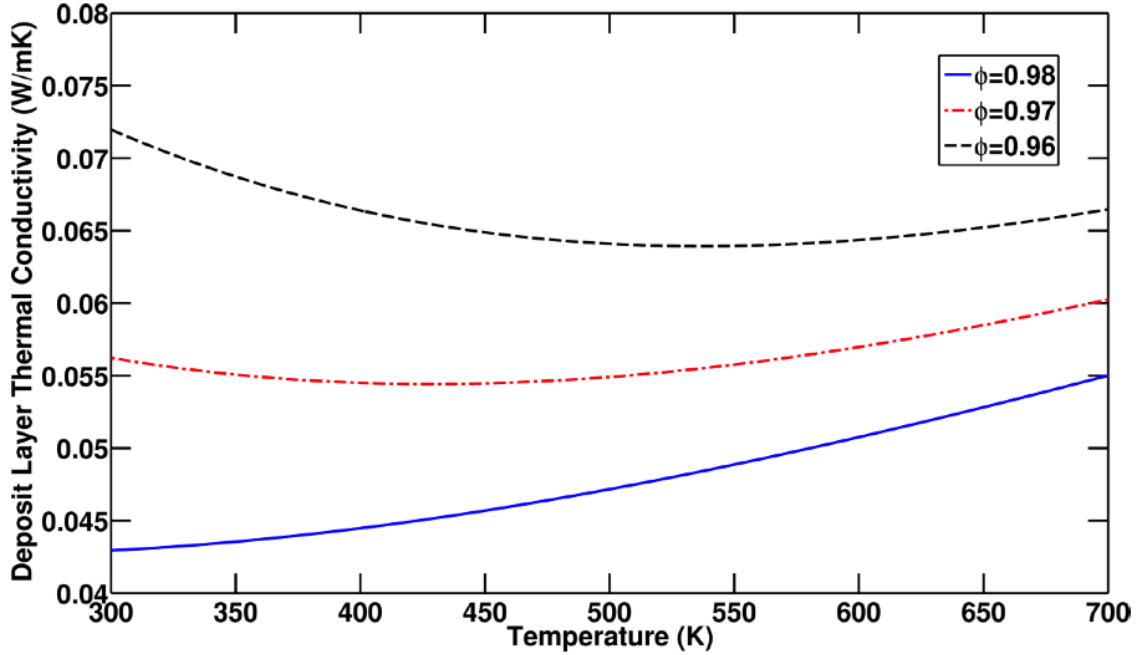


Figure 5.11: Estimated deposit conductivity as a function of porosity and temperature [1]

The deposit conductivity can be estimated for a porous layer in an air environment by extending the work of [1, 2]. Instead of assuming the pores are filled with exhaust as Abarham did [1], the pores are assumed to be filled with air and the porous deposit conductivity is estimated by approximating the solid structure as graphite and using the following correlations:

$$k_{air} = 6.37E - 5 \times T + 0.00813 \text{ [W/mK]}$$

$$k_{graphite} = 13.0839 - 0.03495 \times T + 3.82E - 5 \times T^2 - 1.48E - 8 \times T^3 \text{ [W/mK]} \text{ [1]}$$

$$k_{estimated\ deposit} = (1 - porosity)^{1.5} \times k_{graphite} + porosity^{0.25} \times k_{air} \text{ [W/mK]} \text{ [2]}$$

Equation 5.1: Estimated thermal conductivity of a porous deposit layer in air

The conductivity of air was linearized over a range from 300 to 750K using the thermal conductivity values of air found in [3]. The estimated deposit conductivity for an environment in air for various porosities is shown in Figure 5.12.

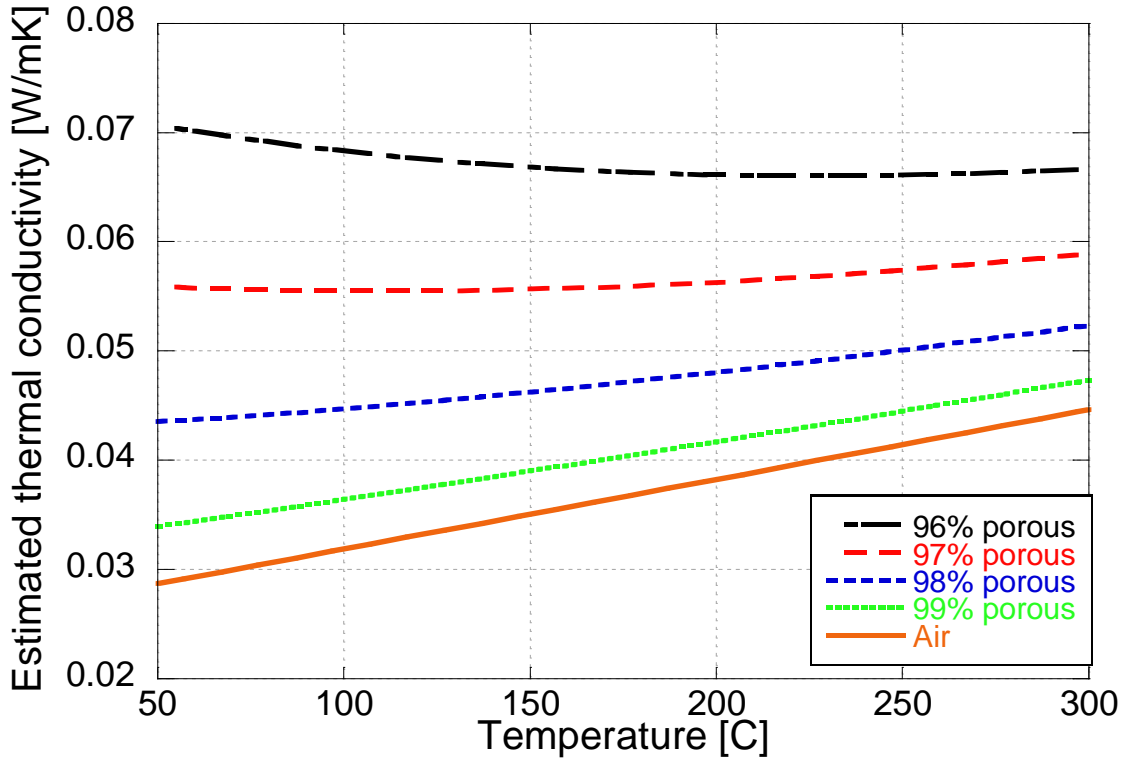


Figure 5.12: Estimated deposit thermal conductivity in air as a function of temperature and porosity

Figure 5.13 and Figure 5.14 plot deposit conductivity as a function of infrared surface temperature for probe 1 and probe 2 respectively. The influence of temperature on conductivity seems apparent, with lower surface temperatures exhibiting higher thermal conductivities. The thermal conductivity of air is also plotted as a function of temperature and serves as the minimum of the deposit conductivity. The increased deposit conductivity at lower surface temperatures could be due to increased measurement uncertainty stemming from the thin deposit layer at the 6-hour interval. To address this concern, a sweep of lower Reynolds number flows resulting in lower surface temperatures was conducted on the 18-hour layer.

Figure 5.15 illustrates the influence of surface temperature on deposit conductivity for an 18-hour layer on probes 1 and 2. The inlet flow rate was reduced to as low as 0.98 kg/hr while still maintaining an inlet temperature of 200°C (conditions listed



in Table A.3 in the Appendix). Conductivity was determined to increase as the deposit surface temperature decreased.

Combining the experimental conductivity with the estimated conductivity suggests a deposit porosity of approximately 98%. This value is similar to that reported in literature. Discrepancies exist as surface temperature decreased and experimental conductivity increased whereas the 98% porosity conductivity continues to decrease. The increase in conductivity with decreasing surface temperature resembles the lower porosity trend such as that of 96% shown in Figure 5.12, however with differing thermal conductivity values. The discrepancy may be due to the presence of volatiles in the deposit or with the assumption of a graphite deposit structure.

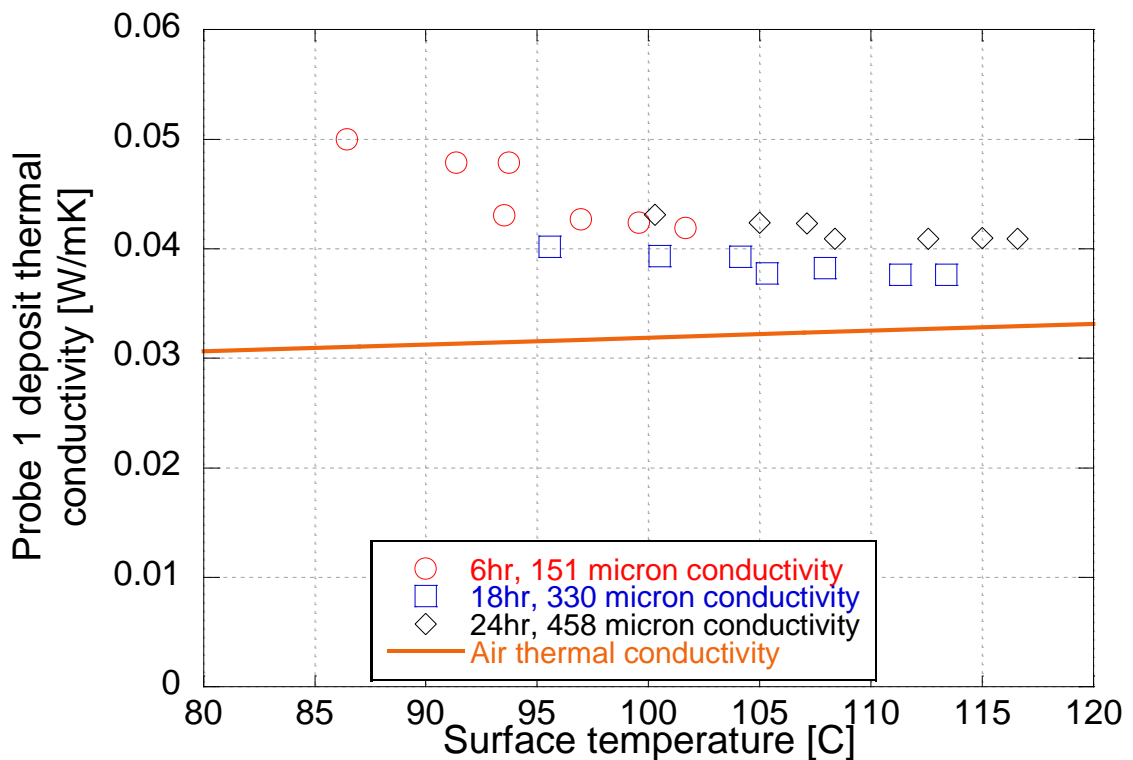


Figure 5.13: Probe 1 deposit conductivity as a function of probe 1 infrared surface temperature

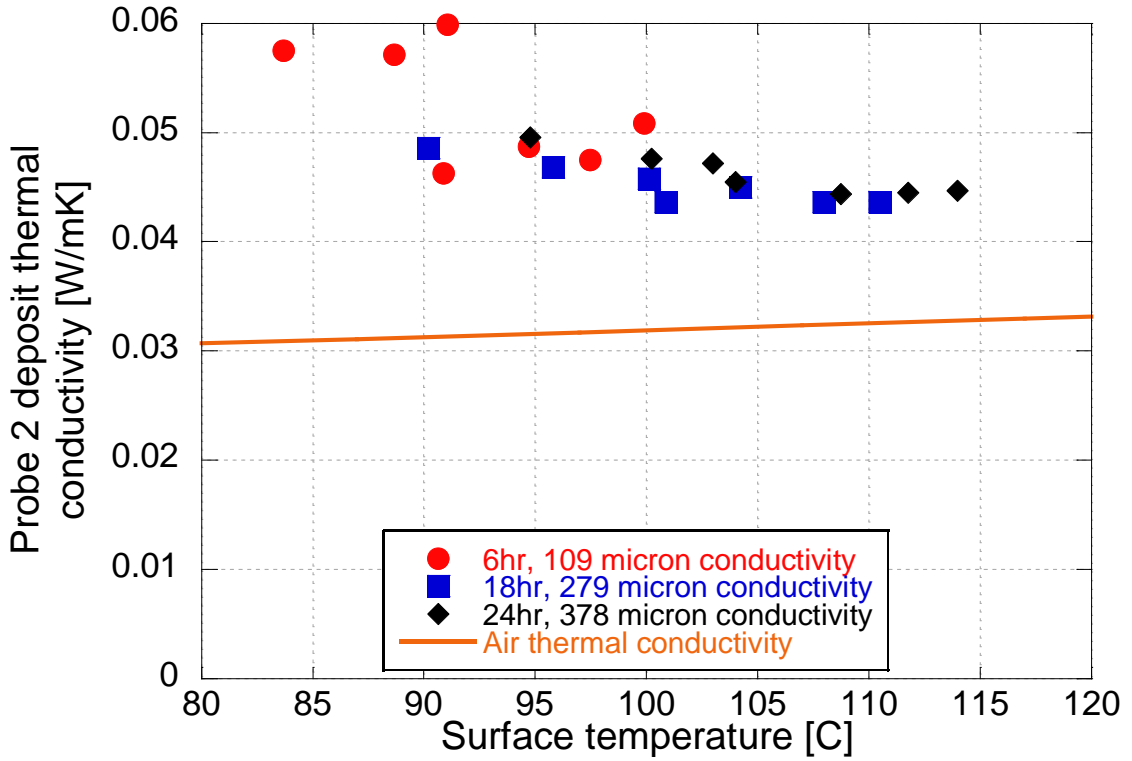


Figure 5.14: Probe 2 deposit conductivity as a function of probe 2 infrared surface temperature

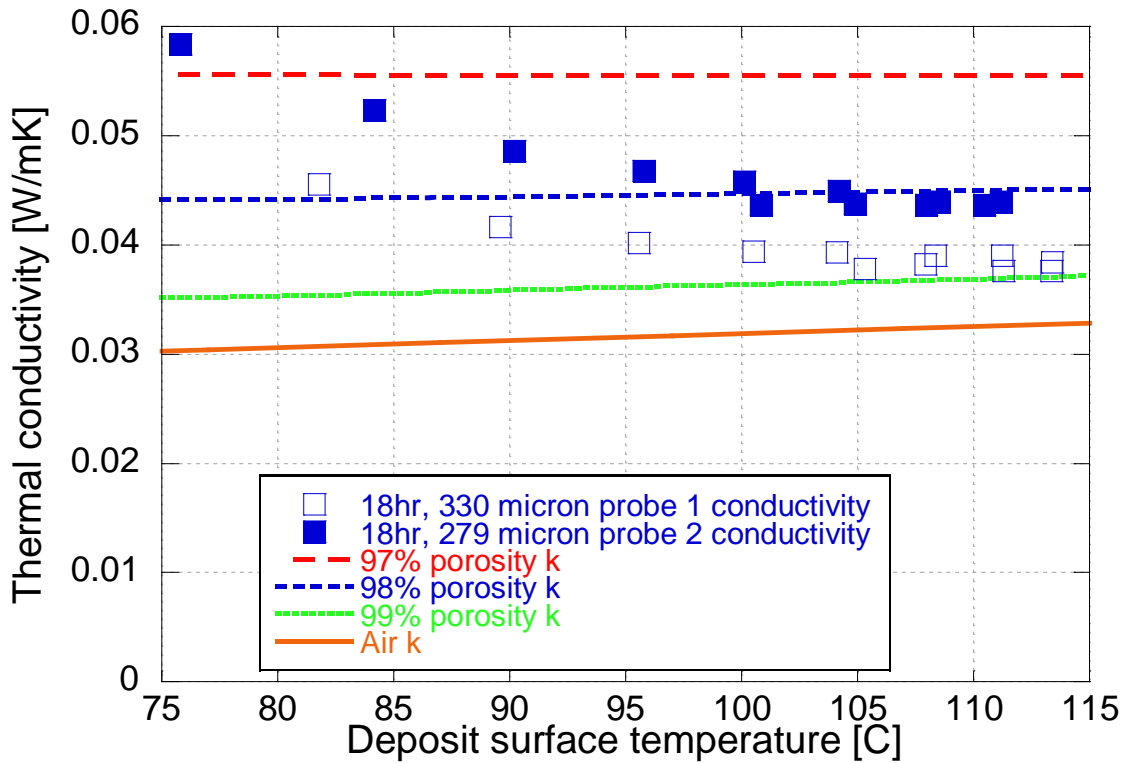


Figure 5.15: 18-hour layer conductivity for low surface temperature with estimated thermal conductivity at 98% porosity as a function of deposit surface temperature

### 5.1.7 Thermal resistance

Dividing the thermal conductivity with the layer thickness, the thermal resistance of the deposit was determined. The resistance is best approximated as growing linearly with deposit growth over the entire Reynolds number range, as shown in Figure 5.16 for heat flux probe 1 and Figure 5.17 for heat flux probe 2. The fit is forced through the origin because at zero layer thickness, zero thermal resistance from the layer is present. The slope of the linear fit generates an “average” thermal conductivity of the deposit, seen to be 0.041 W/mK for probe 1 and 0.046 W/mK for probe 2. Comparing these values to those reported by Lance et al. [4] of 0.032, 0.034, and 0.057 for an average of 0.041 W/mK shows that the in-situ value is slightly more conductive.

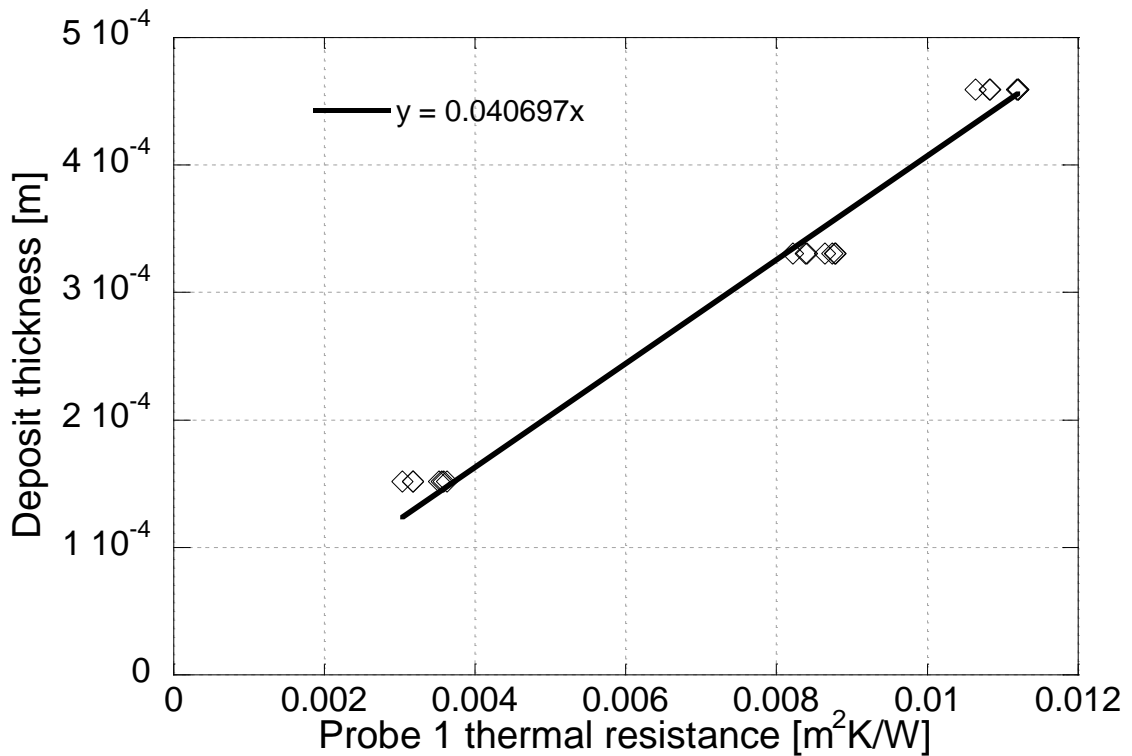


Figure 5.16: Thermal resistance of deposit layer on heat flux probe 1

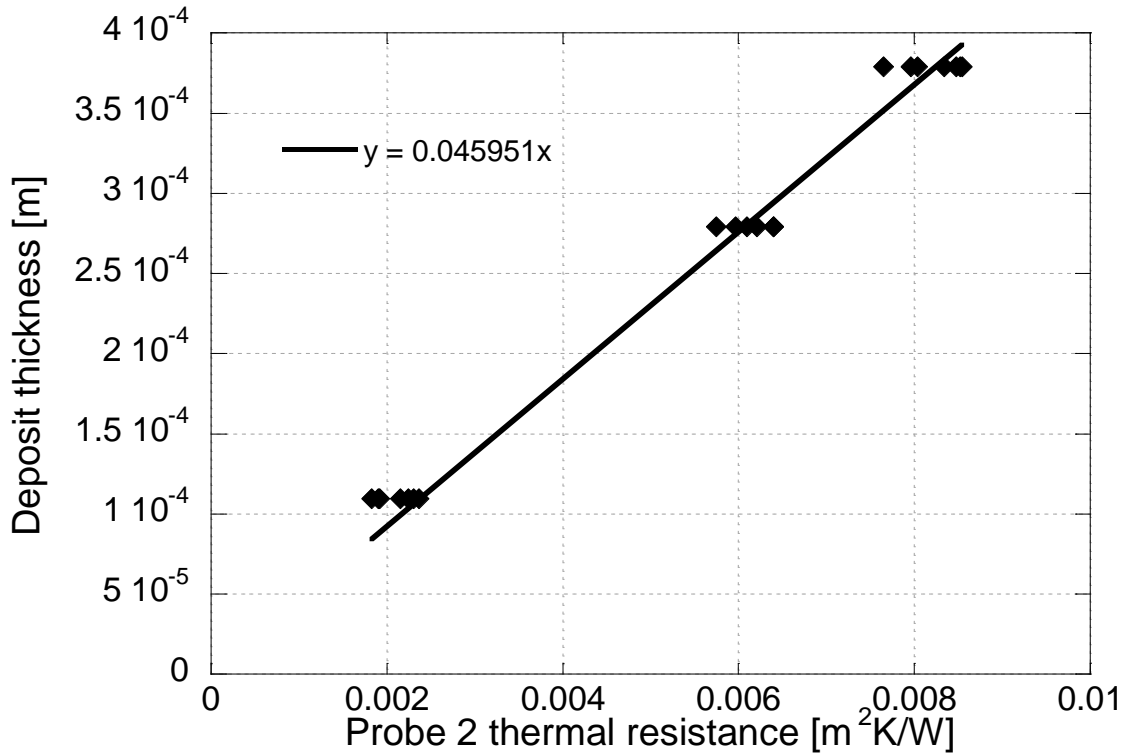


Figure 5.17: Thermal resistance of deposit layer on heat flux probe 2

Utilizing the 1-D model from Abarham [1], the impact of the differing conductivities on heat exchanger effectiveness was determined. Assuming the same thickness layer at the same inlet conditions, the conductivity was varied from 0.035, 0.041, and 0.046 W/mK. Increasing the conductivity from 0.035 to 0.041 W/mK resulted in a 5.5% increase in effectiveness, while 0.046 W/mK produced a 9.4% increase compared to 0.035 W/mK.

## 5.2 Conclusions

Heat flux probes were added to the visualization rig and enabled conductivity calculations. A 24-hour layer in increments of 6 hours was developed on top of two heat flux probes, one upstream and one downstream. Thickness, layer temperature, and heat flux were measured on the probes and utilized for thermal conductivity calculations.

Deposit thickness was measured to be thicker on the upstream probe. The hotter gas temperatures increased the thermophoretic deposition velocities and resulted in increased deposit thicknesses. The deposit growth was seen to deviate from the linear growth pattern seen in Chapter 4 due to deposit build up on different substrates. The heat flux probes increase the thermal resistance between the deposit layer and the coolant, and result in hotter deposit surface temperatures as compared to bare stainless steel. The increased surface temperatures reduced the thermophoretic driving potential and created the non-linear growth pattern.

Layer temperature also increased with Reynolds number and deposit thickness. As the Reynolds number of the gas flow increased, the thermal mass flux also increased, increasing the layer temperature. Due to the insulative properties of the deposit, as deposit thickness increased so did the total insulation of the layer. This resulted in increased layer temperatures with deposit thickness.

Heat flux decreased with deposit thickness and is due to the insulative properties of the deposit layer. As the deposit thickness increased, the total insulation of the layer increased as well and reduced heat transfer from the gas to the coolant.

During early deposition intervals and thin deposit layers, the differences in heat flux between the upstream and downstream probe were significant. Due to the thin deposit layer, significant heat transfer occurred on the upstream probe, lowering the gas temperature and reducing the heat flux through the downstream probe. As deposition continued, however, the difference in heat flux between the two probes decreased. This, again, is due to the increased insulation of the thicker deposit layer. In addition to lowering overall heat flux, the lower heat rejection maintained a hotter gas temperature on the downstream probe and increased the measured heat flux. The combination of a thicker layer reducing the overall heat flux and hotter gas temperatures increasing heat flux resulted in a decreasing heat flux with deposit thickness with decreasing differences between the upstream and downstream probe.

Deposit layer conductivity did not change with deposit thickness and deposition time. Conductivity did, however, change with surface temperature. As surface temperature decreased, thermal conductivity increased. This is due to a trade-off between the reducing thermal conductivity of the solid deposit layer structure and the increasing thermal conductivity of air with increasing temperature. At lower temperatures, the thermal conductivity trends of the solid structure are dominant however at hotter temperatures, the thermal conductivity of air is dominant.

### 5.3 References

- [1] Abarham, M., "Investigation of Nano-Particulate Transport in Non-Isothermal Turbulent Internal Flows," in *Mechanical Engineering*. vol. Ph.D. Ann Arbor: University of Michigan, 2011.
  
- [2] Ciro, W. D., Eddings, E. G., and Sarofim, A. F., "Experimental and numerical investigations of transient soot buildup on a cylindrical container immersed in a jet fuel pool fire," *Combustion Science and Technology*, vol. 178, no. 12, pp. 2199-2218, 2006.
  
- [3] Incropera, F. and DeWitt, D., *Fundamentals of Heat and Mass Transfer*, 5th ed.: John Wiley & Sons, Inc, 2002.
  
- [4] Lance, M. J., Sluder, C. S., Wang, H., and Storey, J. M. E., "Direct Measurement of EGR Cooler Deposit Thermal Properties for Improved Understanding of Cooler Fouling," SAE International, 2009.

## CHAPTER 6

### EFFECT OF VOLATILES ON DEPOSIT LAYER PROPERTIES

After the 24-hour layer was developed and analyzed, a bake-out was performed on the layer to remove low-end volatiles and determine their effect on deposit properties. Two bake-out events were performed: bake 1 and bake 2. Bake 1 occurred at 120°C at 8 kg/hr (~10.1 m/s) and bake 2 occurred at 150°C at 6 kg/hr (~9.4 m/s) with hot airflow as the carrier gas. Oxidation of the deposit is not expected due to the high oxidation temperature of carbon (~500°C). In case the volatiles are biased towards the coolant side of the deposit thickness, the fixture was drained of coolant to ensure thorough, uniform heating and volatile removal throughout the deposit thickness.

The deposit thermal properties were determined with the technique outlined in Chapter 2. In addition, thermo-gravimetric analysis (TGA) was performed on samples from the 24-hour deposit prior to the bake-out (referred to as pre-bake), after bake 1 (referred to as bake 1), and after bake 2 (referred to as bake 2). The TGA results quantify the volatile composition of the deposit layer and will be used to determine the amount of volatile removal during the bake-out events.

After the volatile analysis on the 24-hour layer was completed, an additional 6-hour deposition was performed to generate a 30-hour layer, albeit with two bake-out events at the 24-hour interval. The 30-hour layer was also subjected to a bake-out event and followed similar trends to the 24-hour and will not be reported. At the conclusion of



the 30-hour analysis, isopropyl alcohol was added to collapse the deposit layer and additional layer analysis was performed.

Real EGR heat exchangers are exposed to varying levels of volatiles and this chapter attempts to quantify the effect of these volatiles on deposit thermal properties. Opportunities to exploit the properties of the volatiles and deposit structure to recover fouled heat exchanger effectiveness are investigated.

## 6.1 Volatile removal results

### 6.1.1 Deposit thickness and surface area

Deposit thickness and surface area was measured after each bake-out and is summarized in Table 6.1. The layer was measured to be thinner and smoother than the pre-bake layer.

Table 6.1: Thickness and surface area ratio pre- and post-bake

Condition	HF1 thickness [ $\mu\text{m}$ ]	HF1 SA ratio [%]	HF2 thickness [ $\mu\text{m}$ ]	HF2 SA ratio [%]
24hr pre-bake	459	116	379	120
24hr bake 1	407	109	346	112
24hr bake 2	366	109	320	112

These measurements are supported by visual evidence as the pre-bake layer, shown in Figure 6.1 and Figure 6.2, is much more dendritic and delicate compared to the post-bake layer surfaces shown in Figure 6.3 and Figure 6.4. Images are shown at the same location on heat flux probe 2.

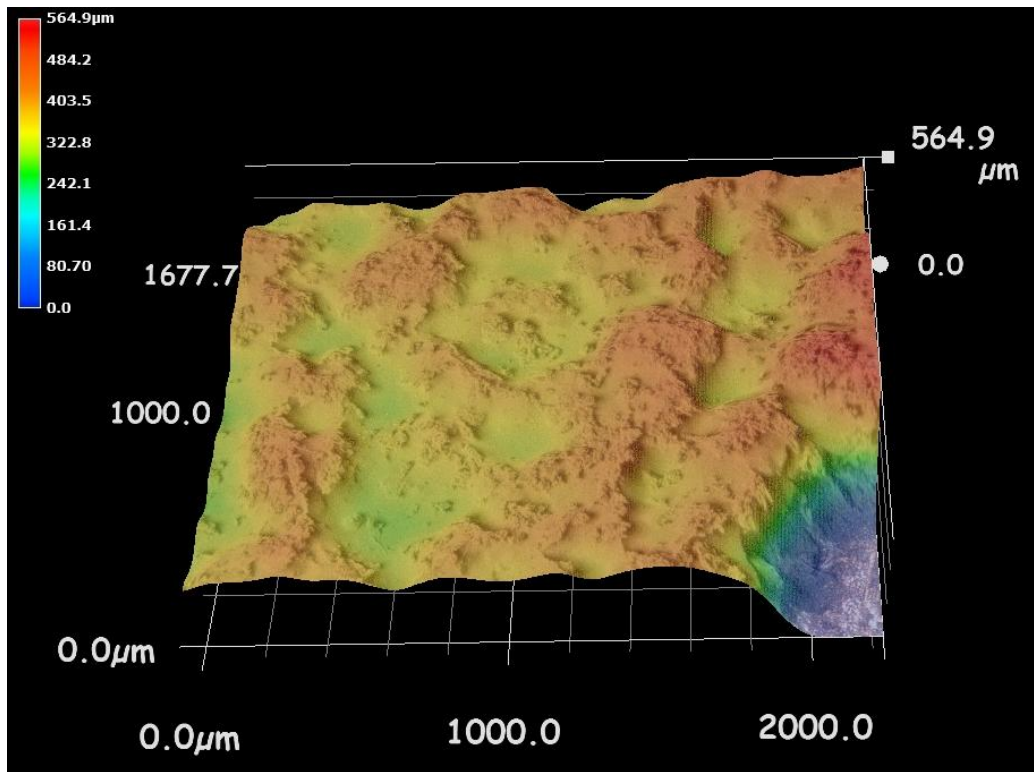


Figure 6.1: 24hr pre-bake layer, 150x magnification

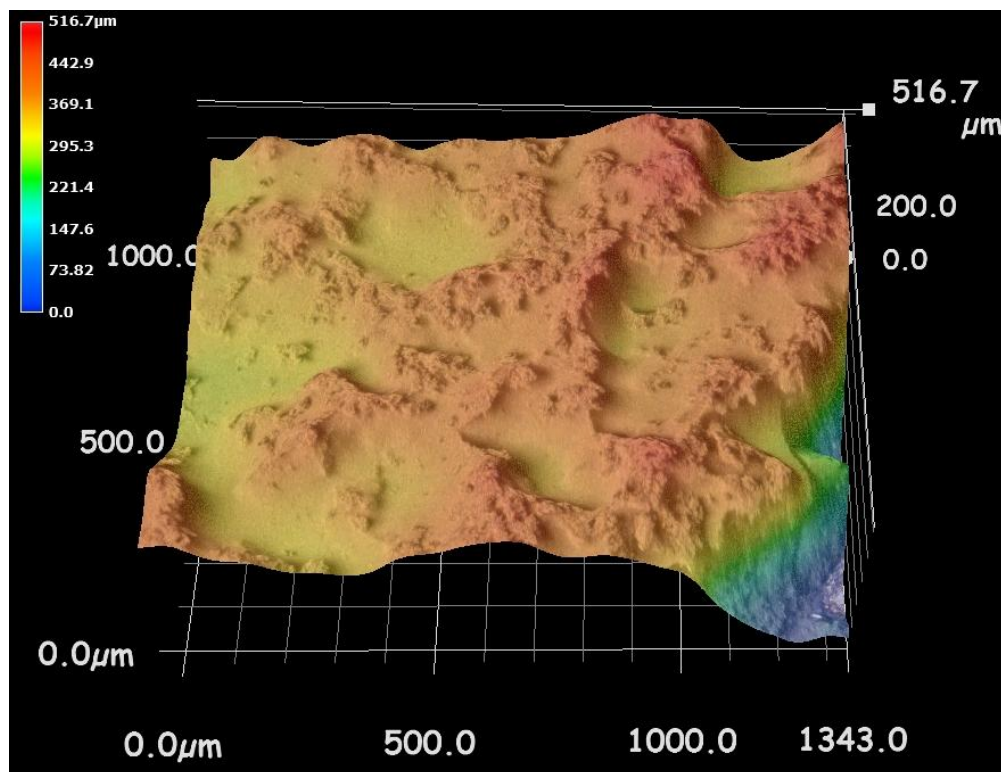


Figure 6.2: 24hr pre-bake layer, 250x magnification

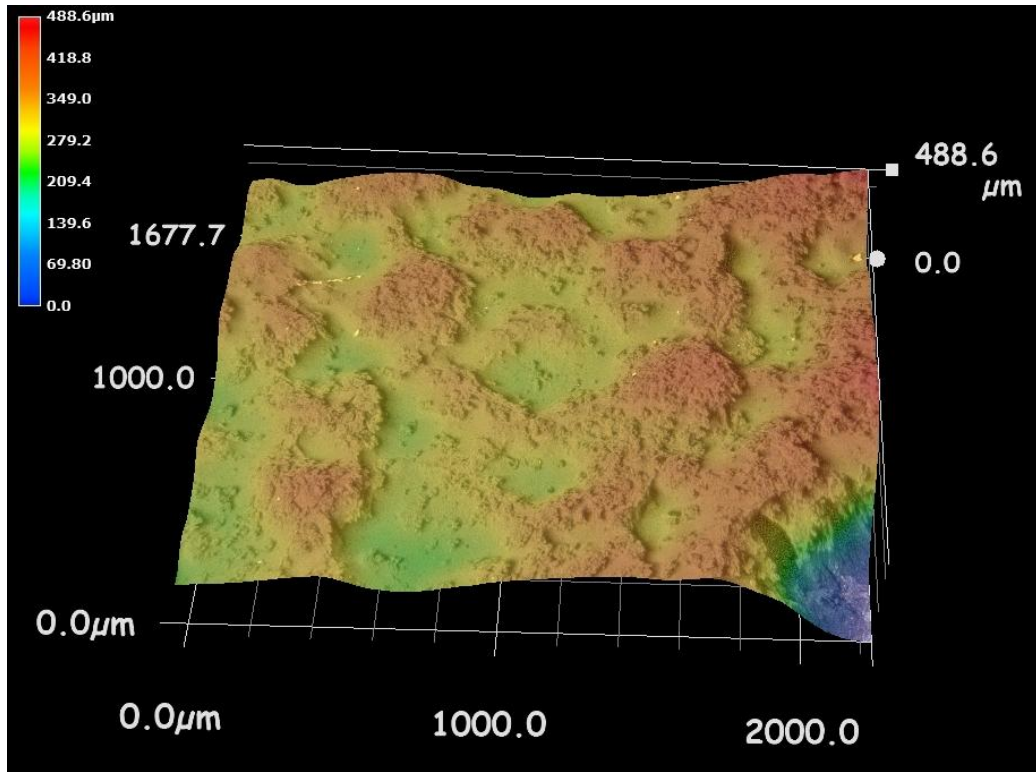


Figure 6.3: 24hr bake-out layer, 150x magnification

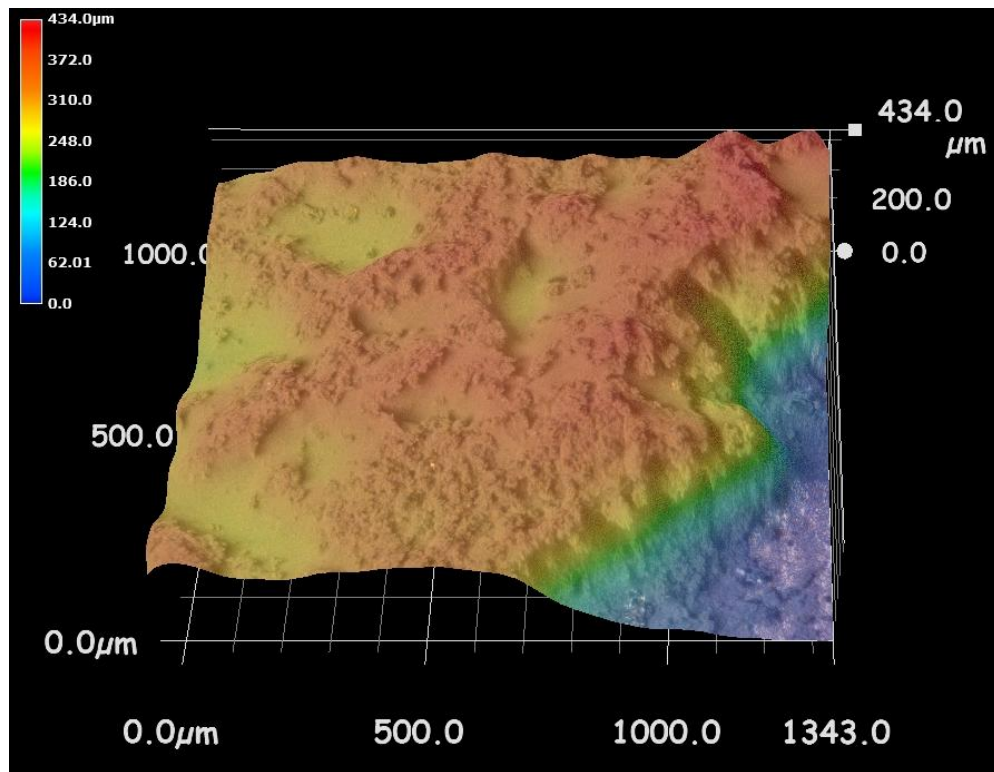


Figure 6.4: 24hr bake-out layer, 250x magnification

During bake 1, slight particle motion of the layer surface was noticed by time-lapse microscope images. The presence of tiny deposit clumps in Figure 6.3 and Figure 6.4 is the result of gas velocity shear removing the peaks of the deposit dendrites and relocating them elsewhere on the deposit. While velocity shear may contribute slightly to layer thickness reduction, it is not expected to be significant. Sluder et al. [1] determined that velocities greater than 40 m/s were required to achieve removal and since the velocity during bake 1 was ~10.1 m/s, minimal disruption to the layer is expected.

During bake 2, no noticeable particle movement occurred however a reduction in layer thickness was still observed. This coupled with the fact that surface area ratio remained constant leads to the conclusion that removal did not occur. Therefore, the hypothesis that the deposit layer thickness reduction was a result of layer compaction is presented. The compaction of the layer could be due to the settling of the deposit layer into a lower porosity structure, facilitated by a higher kinetic energy of the layer due to increased temperatures.

To investigate any further changes in the layer, thermal measurements were conducted.

#### 6.1.2 Thermal measurements

The infrared surface temperatures for the 24hr pre-bake, bake 1, and bake 2 are shown in Figure 6.5 for heat flux probe 1 and Figure 6.6 for heat flux probe 2. As Reynolds number increased, the deposit surface temperature also increased due to an increase in thermal heat flux. After each bake-out, the surface temperature tended to decrease. However, after bake 2, the infrared surface temperature increased more strongly as a function of Reynolds number.

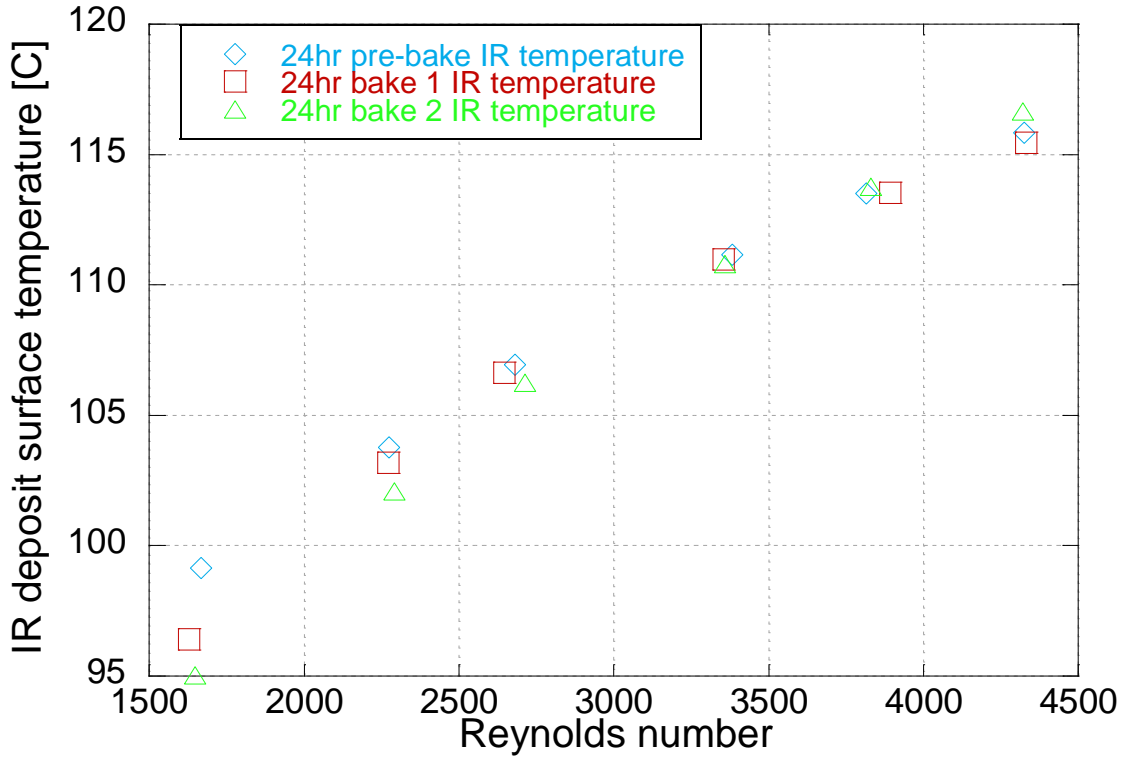


Figure 6.5: Deposit surface temperature for 24hr pre-bake and post-bake layers on heat flux probe 1

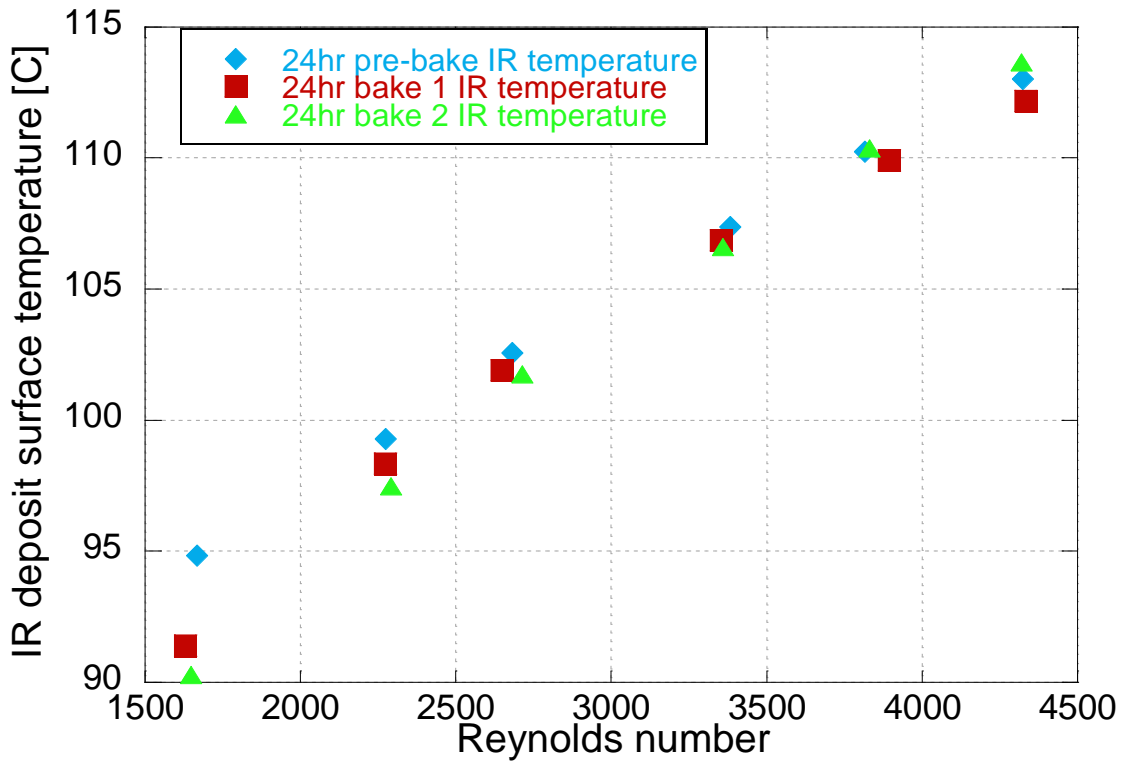


Figure 6.6: Deposit surface temperature for 24hr pre-baked and post-bake layers on heat flux probe 2

Similar trends exist for the temperature differential across the deposit layer thickness, as shown in Figure 6.7 for probe 1 and Figure 6.8 for probe 2. Larger changes are seen on the upstream probe, probe 1, and are likely due to hotter temperatures experienced during the bake-out events causing a change in the deposit composition in addition to slightly increased velocity shear from leading edge effects.

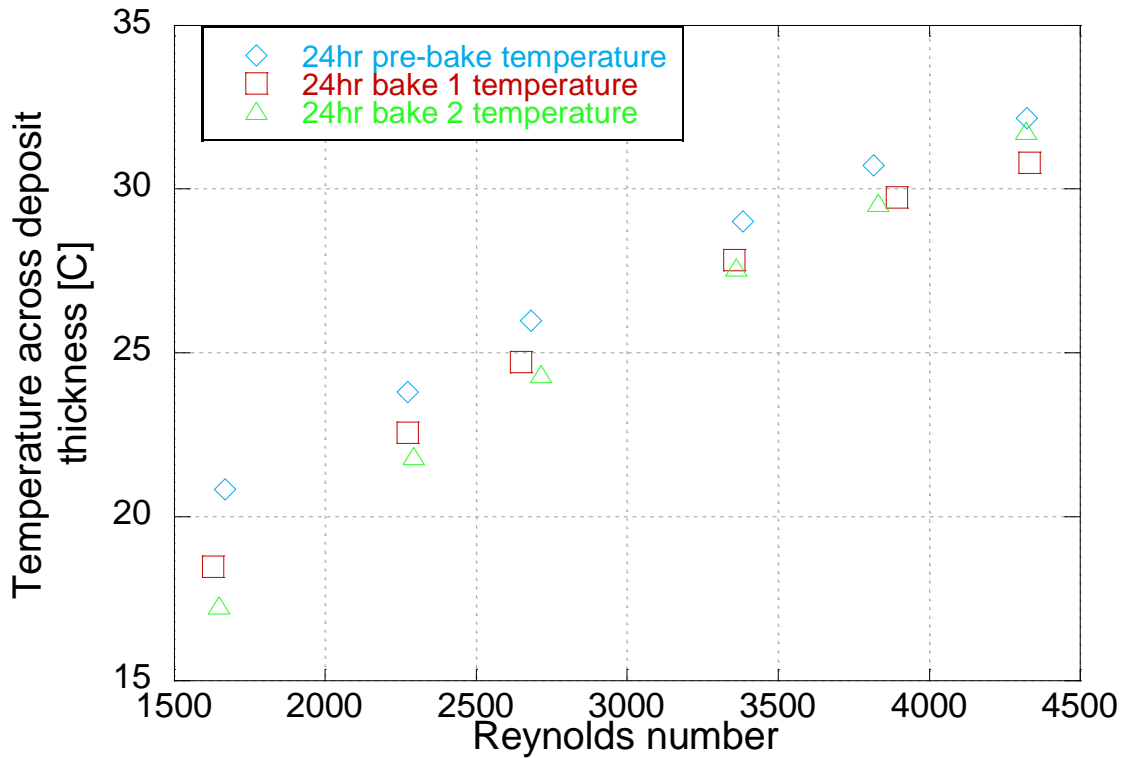


Figure 6.7: Temperature across deposit layer thickness for 24hr pre-bake and post-bake layers on heat flux probe 1

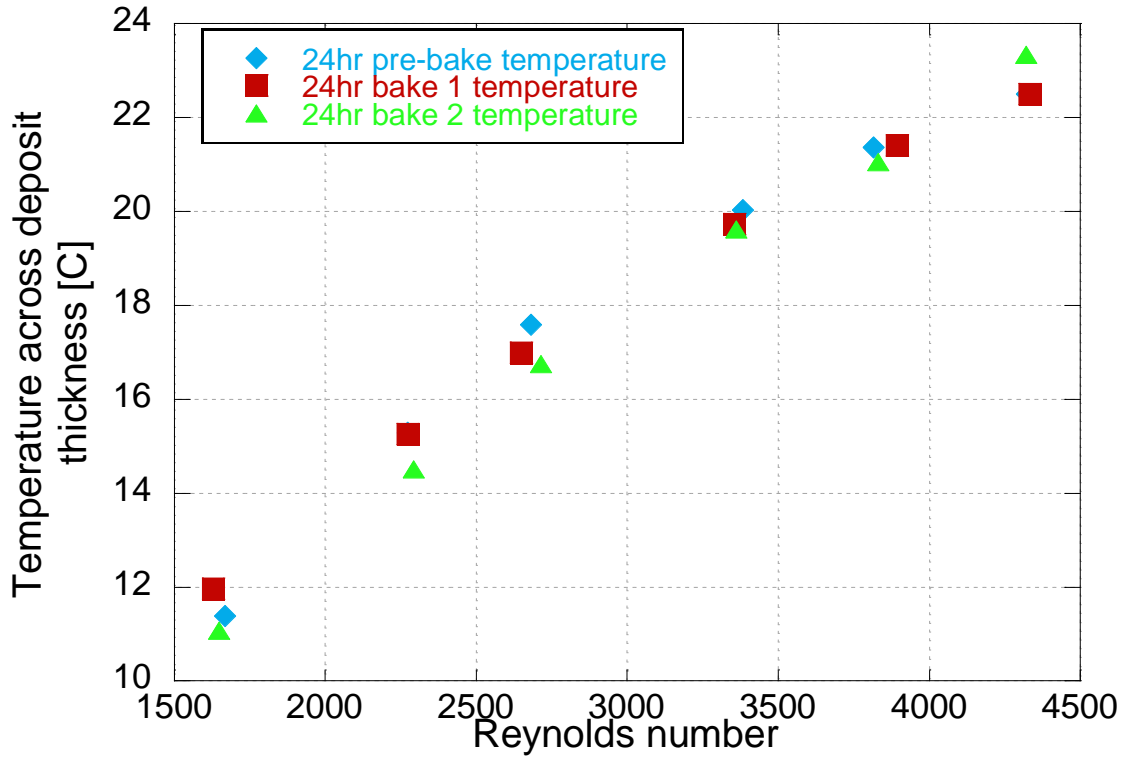


Figure 6.8: Temperature across deposit layer thickness for 24hr pre-bake and post-bake layers on heat flux probe 2

Measurements from both probes indicated a strong surface temperature and temperature across deposit thickness dependence on Reynolds number for bake 2. This may be due to hotter deposit temperatures achieved during bake 2, thus changing the deposit characteristics. To verify this, heat flux measurements were also performed.

### 6.1.3 Heat flux

Heat flux is shown for probe 1 in Figure 6.9 and probe 2 in Figure 6.10. Both probe measurements indicated an increase in heat flux through the layer with subsequent bake out events. In addition, heat flux increased with increasing Reynolds number due to a higher mass flow rate of hot air.

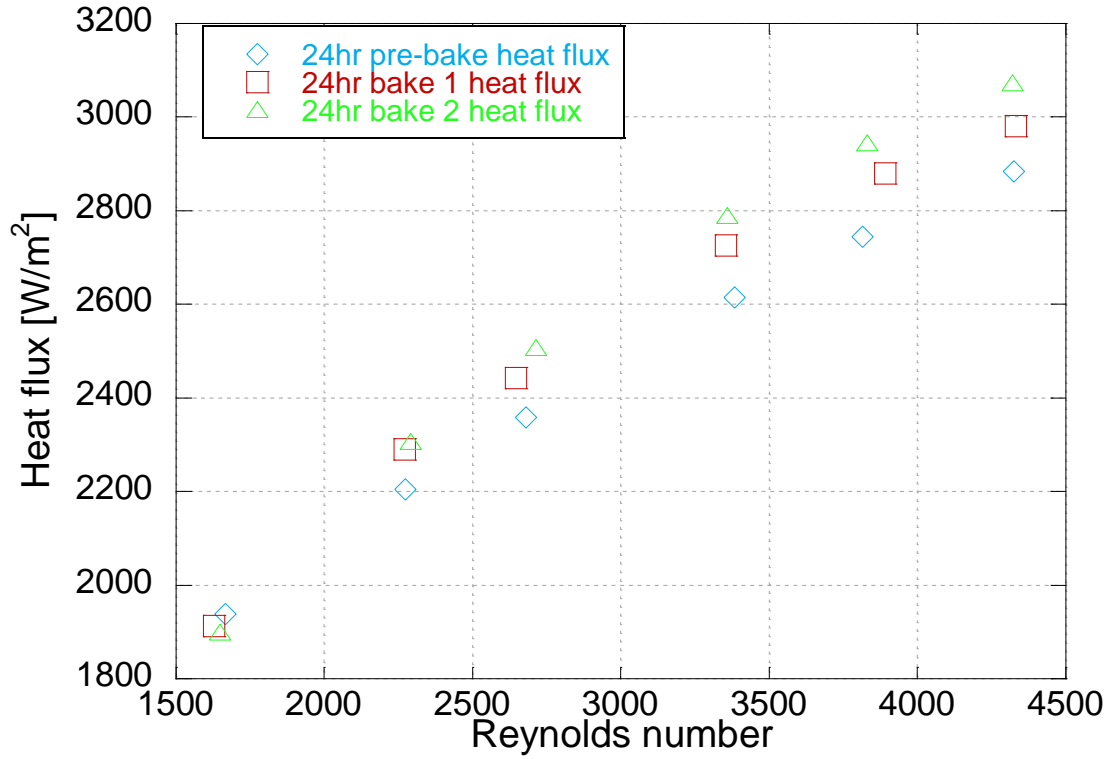


Figure 6.9: Heat flux through 24hr pre-bake, bake 1, and bake 2 layers for heat flux probe 1

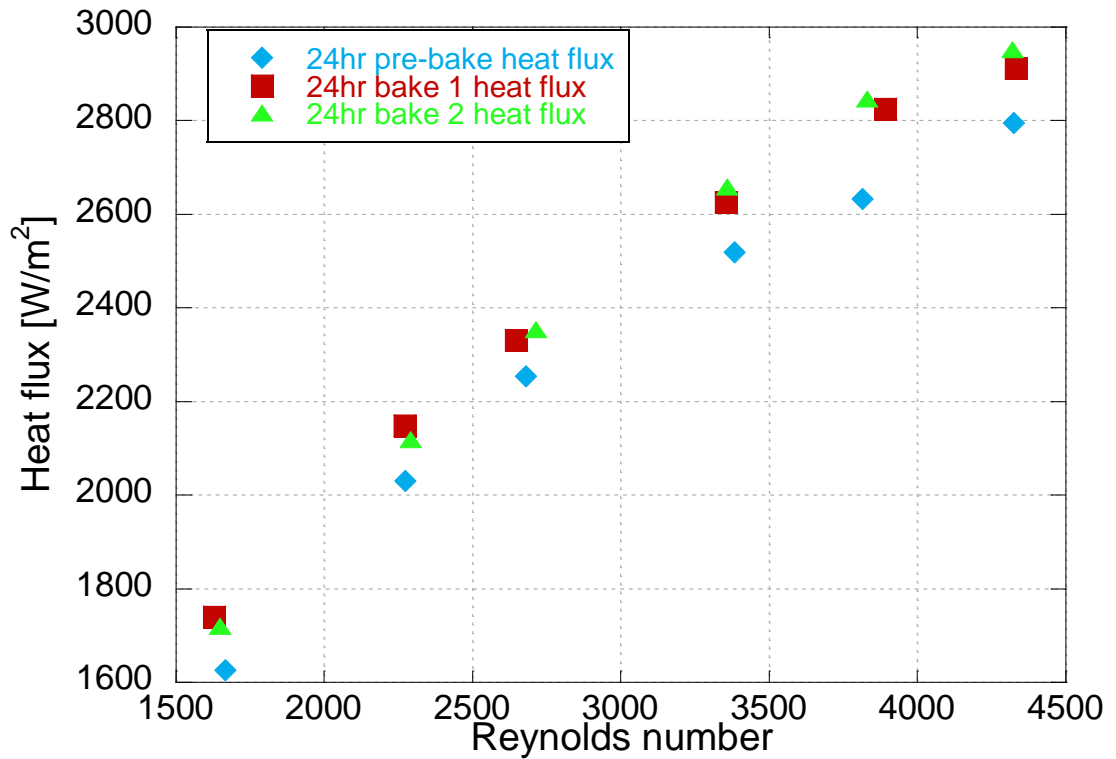


Figure 6.10: Heat flux through 24hr pre-bake, bake 1, and bake 2 layers for heat flux probe 2



Due to a significant portion of the fixture being exposed to the ambient environment, the effectiveness of the rig cannot be measured as a result of ambient heat loss. However, the increase in heat flux with bake-out events infers an increase in the effectiveness of the heat exchanger since more of the heat is transferred from the gas to the coolant.

The increase in heat flux may stem from a thinning of the deposit layer or a change in the thermal properties of the deposit layer. As illustrated in Chapter 5, Figure 5.9, heat flux decreased as deposit thickness increased. This is due to total insulation of the deposit increasing with thickness. If the increase in heat flux is solely due to the shrinking of the deposit layer, the relative change in thickness should relate to the relative change in heat flux. Table 6.2 and Table 6.3 summarize changes in thickness and heat flux relative to the 24hr pre-bake condition for probes 1 and 2 respectively. It is evident that the changes in thickness are greater than the changes in heat flux, thus the increase in heat flux is not solely from the reduction in thickness.

Table 6.2: Layer thickness reduction for bake-out events relative to 24hr pre-bake

Condition	HF1 thickness reduction [%]	HF2 thickness reduction [%]
24hr bake 1	11.3	8.7
24hr bake 2	20.2	15.5

Table 6.3: Heat flux increase for bake-out events relative to 24hr pre-bake

Re	HF1 bake 1 [%]	HF1 bake 2 [%]	HF2 bake 1 [%]	HF2 bake 2 [%]
2699	3.6	6.3	3.4	4.4
3362	4.9	7.3	4.2	5.6
3860	4.9	7.3	7.3	8.1
4284	3.3	6.5	4.2	5.6
2270	3.9	4.6	5.8	4.4
1650	-1.3	-1.9	7	5.8

It can be argued that the reduction in surface area from 24hr pre-bake to bake 1 may play a factor in the measured heat flux. To investigate this, thickness and heat flux

from bake 2 will be compared to bake 1 since the surface area ratio was unaffected between these conditions. Table 6.4 and Table 6.5 present the relative thickness reduction and heat flux increase for 24hr bake 2 relative to 24hr bake 1. The analysis shows the same trend: the thickness reduction is greater than the heat flux increase. These results suggest a possible change in the deposit layer properties and can be investigated by calculating the thermal conductivity.

Table 6.4: Layer thickness reduction for 24hr bake 2 relative to bake 1

Condition	HF1 thickness reduction [%]	HF2 thickness reduction [%]
24hr bake 2	10	7.5

Table 6.5: Heat flux increase for 24hr bake 2 relative to bake 1

Re	HF1 bake 2 [%]	HF2 bake 2 [%]
2699	2.7	1.0
3362	2.4	1.3
3860	2.3	0.8
4284	3.1	1.4
2270	0.7	-1.4
1650	-0.6	-1.1

#### 6.1.4 Deposit thermal conductivity

Combining the previous measurements with Equation 2.2 yields the thermal conductivity of the layer. Figure 6.11 and Figure 6.12 are the thermal conductivities for probe 1 and probe 2, respectively, as a function of Reynolds number for the 24hr pre-bake, bake 1, and bake 2 events. Both calculations indicated a reduction in the thermal conductivity of the deposit with subsequent bake-out events. In addition, the behavior of conductivity changed for the bake-out events and continually decreased with increasing Reynolds number.

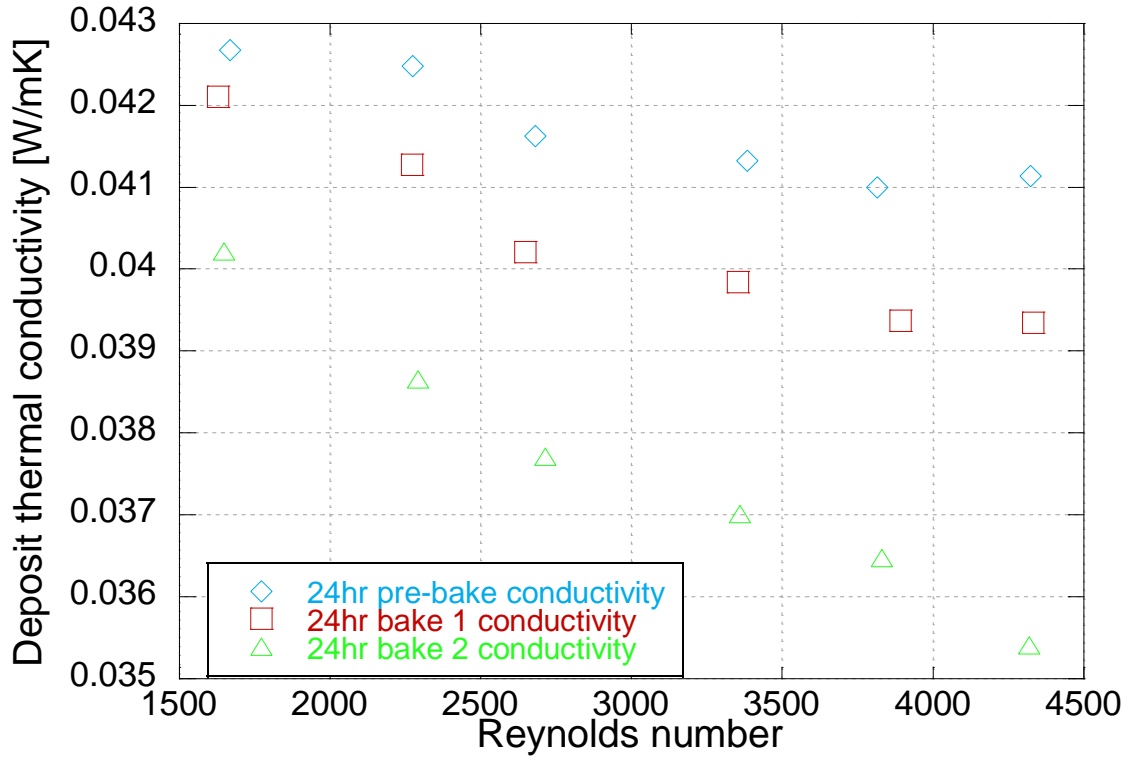


Figure 6.11: Deposit conductivity as a function of Reynolds number for heat flux probe 1

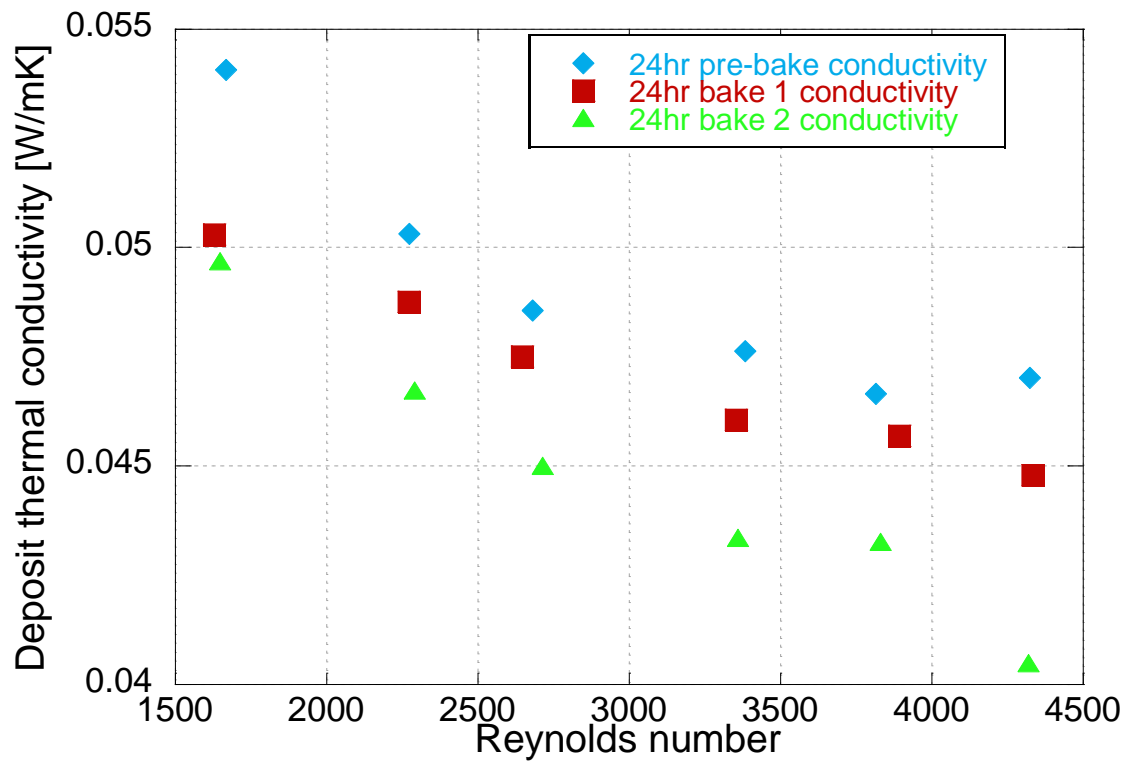


Figure 6.12: Deposit conductivity as a function of Reynolds number for heat flux probe 2

Interpreting from the thermal conductivity modeling work, if the layer porosity decreased as a result of the bake-out events, the thermal conductivity is expected to increase (Figure 6.13). This is not reflected in the experimental results. However, Figure 6.13 shows that as porosity decreases, the inflection point of decreasing and increasing conductivity trends of the graphite and air layer becomes more apparent and moves to higher temperatures. This is a trend that is seen in the experimental data, shown in Figure 6.14 for probe 1 and Figure 6.15 for probe 2, as noted by the continuous decrease of thermal conductivity after the bake-out events. It is hypothesized that if the surface temperature increased further, an inflection point would be noticed and conductivity would start to increase.

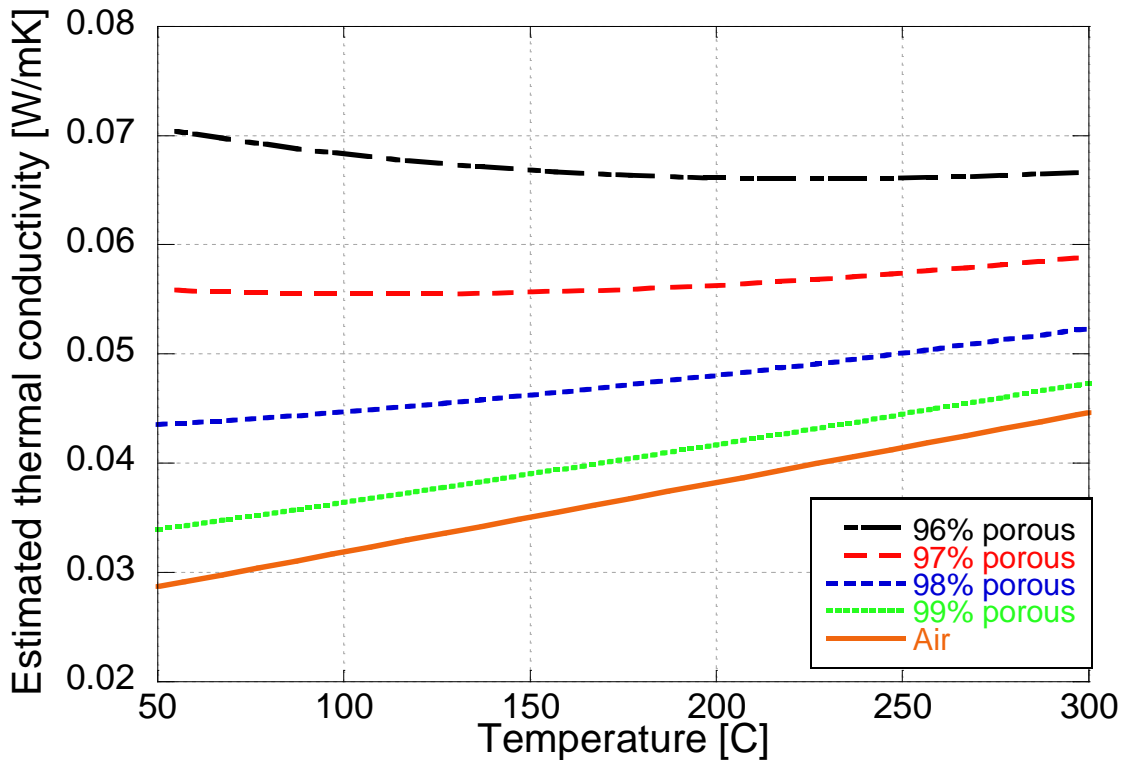


Figure 6.13: Estimated deposit conductivity as a function of porosity and temperature

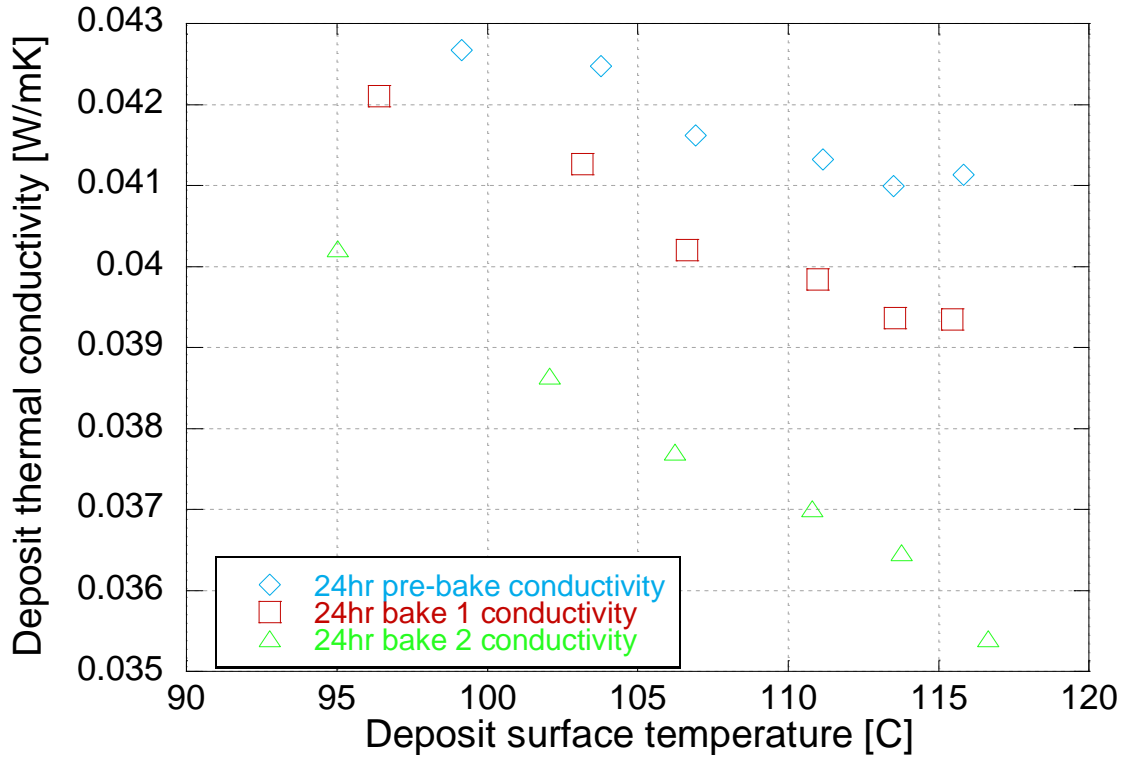


Figure 6.14: Deposit conductivity as a function of deposit surface temperature on heat flux probe 1

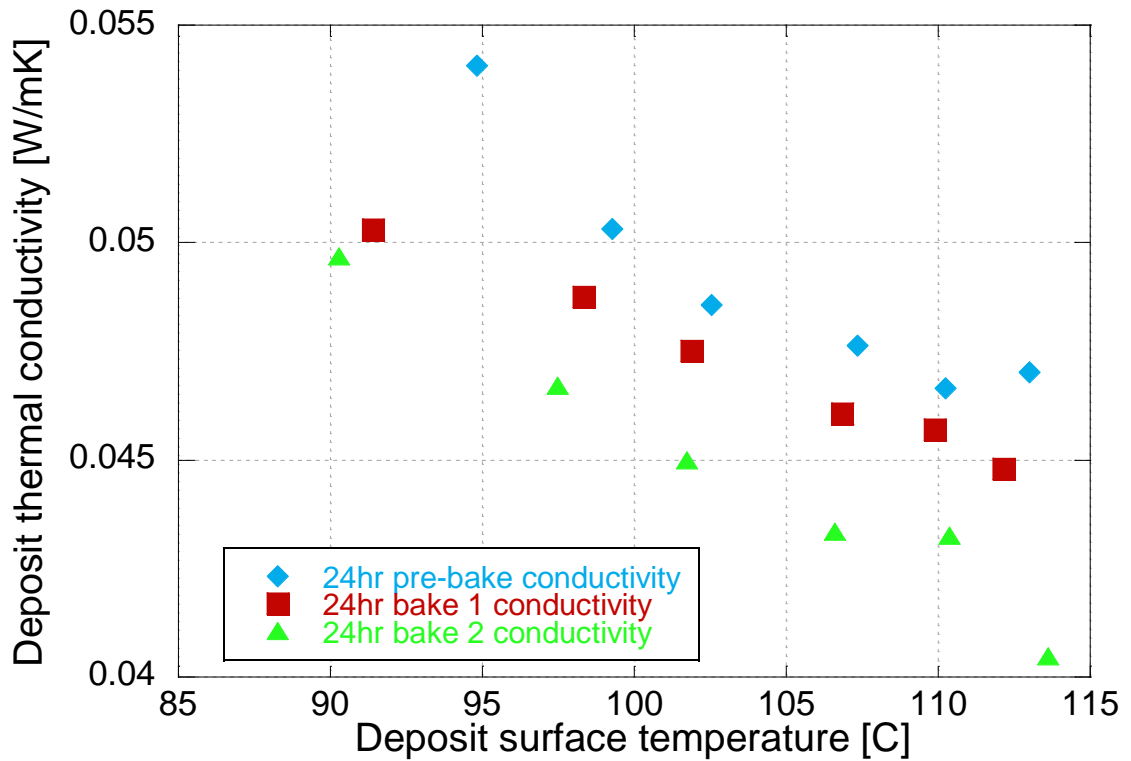


Figure 6.15: Deposit conductivity as a function of deposit surface temperature for heat flux probe 2

The lower conductivity trend may be explained by TGA as shown in Figure 6.16. The TGA results showed a low-end volatile fraction in the pre-bake sample that does not exist for the post-bake. The pre-bake sample consisted of 6.5% volatiles up to 350°C while the post-bake sample had 4%. Therefore, 2.5% of the volatile mass was removed during the bake-out event.

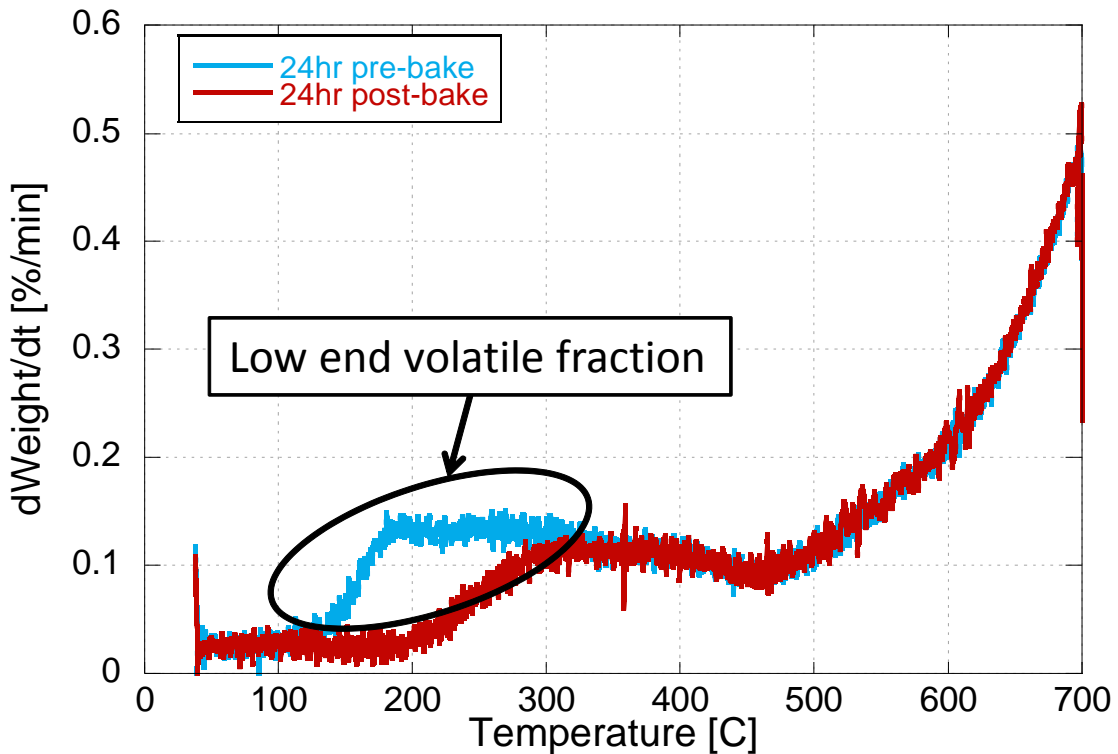


Figure 6.16: TGA on 24hr pre-bake and post-bake layers

The bake-out event may in-fact reduce the porosity of the layer, creating a thinner deposit however the increase in conductivity could be negated by the drier composition of the layer. This would explain the experimental trends observed.

Even with a lower calculated thermal conductivity, the heat flux through the layer increased with subsequent bake-out events. This is due to the thinning of the deposit layer as a thinner layer is less insulative overall; allowing for increased heat transfer. This result implies an increase in heat exchanger effectiveness and therefore constitutes a mild recovery event. These results are further verified with the modified 1-D model from

Abarham. A thinner and less thermally conductive layer (bake 2 layer) resulted in a more or less equivalent heat exchanger effectiveness of 16.73% compared to the 16.46% of the thicker, pre-bake layer.

## **6.2 Addition of volatiles**

### **6.2.1 Layer collapse**

In an effort to determine the impact of significant volatile addition to the deposit layer, isopropyl alcohol was added directly to the surface of the deposit. Where as previously the deposit was seen to be hydrophobic [2], the alcohol was immediately absorbed into the deposit. The absorption of the alcohol collapsed the structure of the deposit layer, resulting in a very thin and presumably dense layer. Figure 6.17 shows a time-lapse sequence of images that captures the introduction of the isopropyl alcohol, subsequent collapse of the layer, and alcohol evaporation.

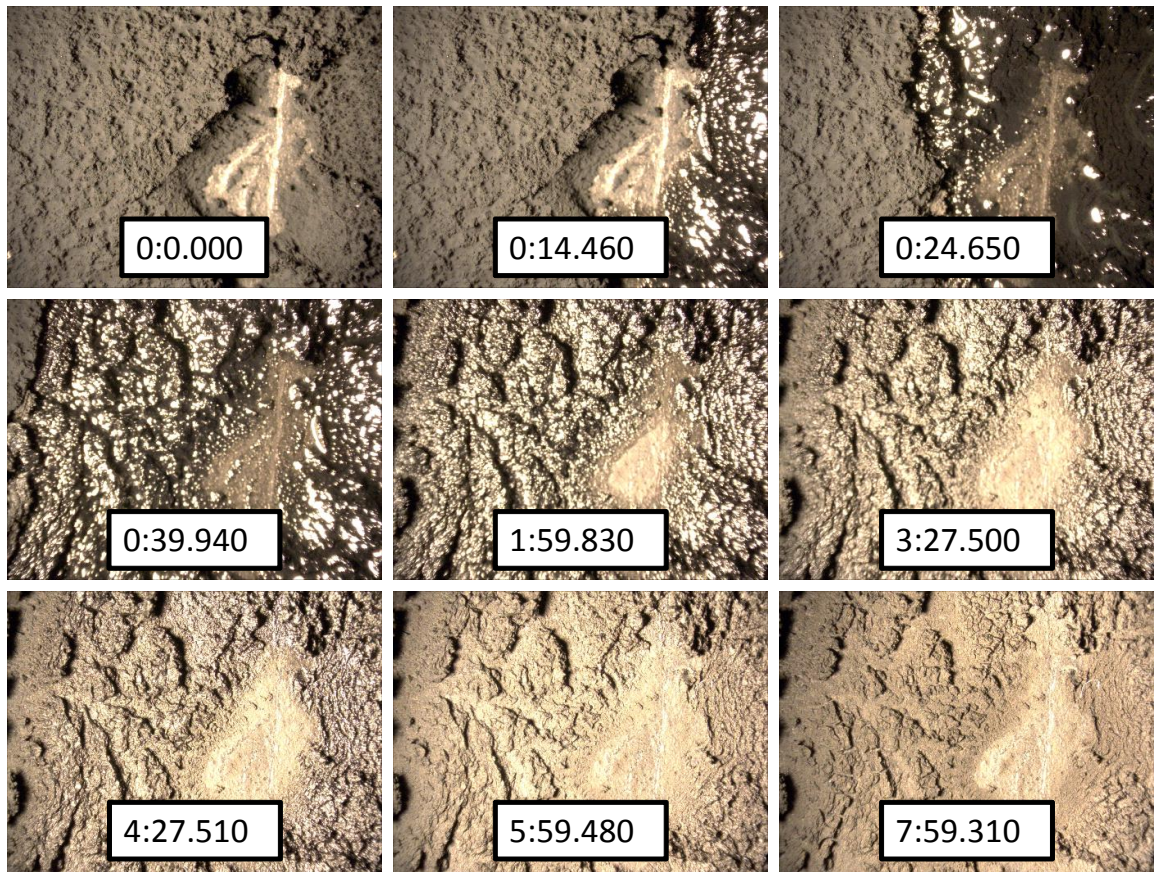


Figure 6.17: Time-lapse images of isopropyl alcohol addition to deposit layer on heat flux probe 2 (time interval is listed as min:sec.msec)

After the alcohol evaporated, evidence of layer mud-cracking was apparent. These mud-cracks have been reported previously [3] and have been primarily observed at the inlet of EGR cooler tubes where the inlet gas flow is hottest. Observations from the alcohol evaporation process suggest mud-cracks are formed by the surface tension of the alcohol, contracting and pulling the layer apart. The deposit contracting and forming mud-cracks is best shown in the sequence images in Figure 6.18, Figure 6.19, Figure 6.20, and Figure 6.21 which are shown for the layer on heat flux probe 1. This helps explain why mud-cracks are seen near the inlet of EGR cooler tubes since the hot exhaust gases evaporate volatiles in the deposit layer, causing the layer to dry out and contract resulting in mud-cracks. Of course, this is dependent on the volatile composition and concentration in the layer.





Figure 6.18: Image of deposit layer just after alcohol-induced collapse (time interval is listed as min:sec.msec)



Figure 6.19: Image of contracted deposit layer (time interval is listed as min:sec.msec)



Figure 6.20: Image of a further contracted deposit layer and at the onset of mud-cracking (time interval is listed as min:sec.msec)



Figure 6.21: Image of contracted and mud-cracked deposit layer (time interval is listed as min:sec.msec)

Due to the highly irregular surface, the deposit thickness cannot be reliably measured. Best estimates for the thickness are shown in Table 6.6. Thicknesses before the collapse were 468 and 393 microns for HF1 and HF2 respectively. Assuming a completely solid collapsed layer, the collapsed thicknesses suggest an estimated 88% and 93% porous layer for HF1 and HF2. These estimates are similar to the porosity estimates made by Lance et al. [4].

Table 6.6: Deposit thickness and surface area ratio for collapsed layer

	Heat flux probe 1	Heat flux probe 2
Thickness [ $\mu\text{m}$ ]	54	29
Surface area ratio [%]	111	104

### 6.2.2 Heat flux analysis

Due to the thin nature of the deposit, layer thermal conductivity could not be calculated due to overlapping measurement errors. Heat flux, however, was measured and is shown in Figure 6.22. Heat flux for the post-IPA collapse is significantly higher than the porous, pre-IPA layer. The thin collapsed layer does not provide a significant thermal resistance to heat transfer due to its limited thickness and increases the heat flux through the layer. In addition, the collapsed layer is much less porous than the pre-IPA layer and therefore is a better thermal conductor. Due to an overlap in measurement error, the conductivity of the collapsed layer could not be determined. However, assuming the collapsed layer is primarily solid carbon, the conductivity is around 1.6 W/mK [5]. Compared to the conductivity mentioned in Chapter 5 of 0.046 W/mK, the increased conductivity also increases the heat transfer through the layer due to a lower thermal resistance.

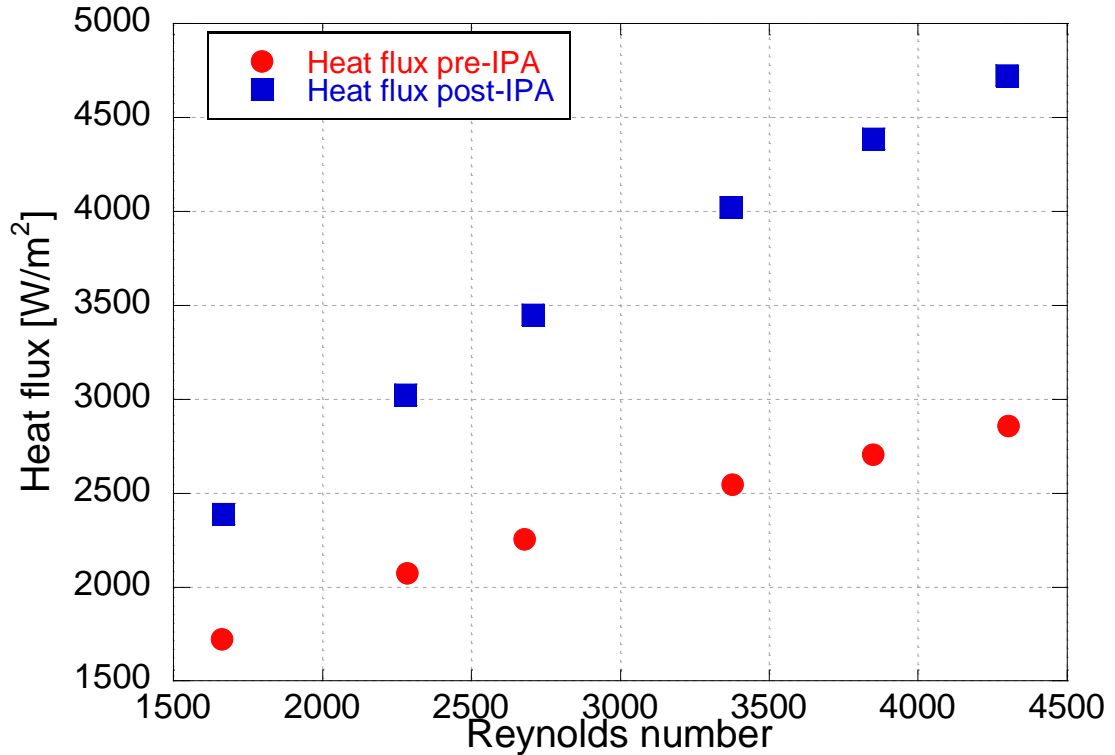


Figure 6.22: Heat flux measurements on heat flux probe 2 for pre- and post-IPA alcohol collapse

### 6.2.3 Infrared surface temperature

The significantly decreased layer porosity is further verified by surface thermal measurements. In undisturbed porous layers, the flow of hot air over the deposit surface created transient temperature fluctuations and is shown frame-by-frame at 25 Hz in Figure 6.23 for a 6-hour layer, Figure 6.24 for a 24-hour layer, and Figure 6.25 the collapsed layer. Airflow is shown flowing from the bottom to the top of the image for the 7.24 kg/hr, 200°C inlet condition corresponding to a Reynolds number of ~4300. In the collapsed layer, however, these transient temperature fluctuations were not observed and very steady temperatures were recorded. The reduction in temperature fluctuations are also quantitatively seen by an order of magnitude reduction in the standard deviation of measured surface temperature, shown in Table 6.7. Leading edge effects from the hot airflow on heat flux probe 1 are also apparent in the figures.

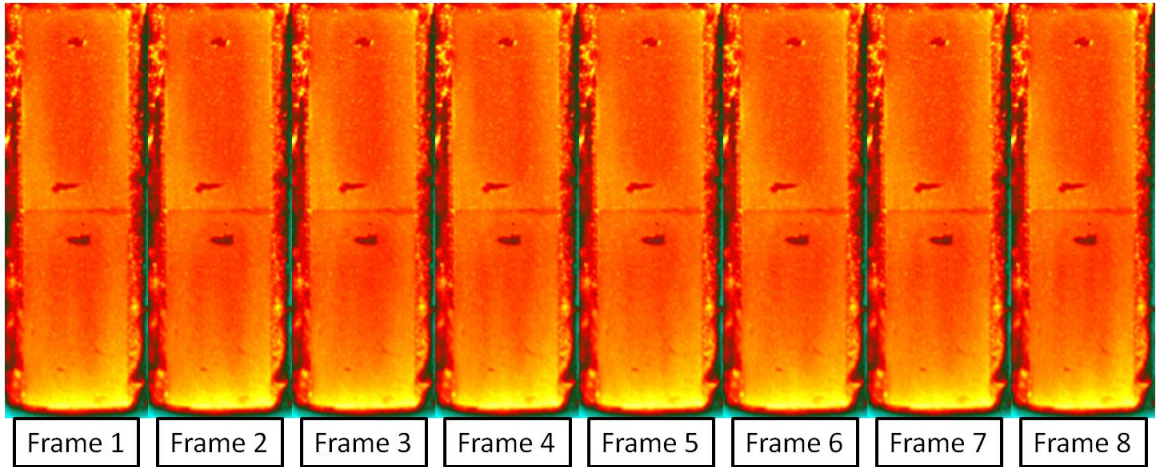


Figure 6.23: Frame-by-frame variations of surface temperature on 6-hour deposit layer.  
Imaged at 25 Hz

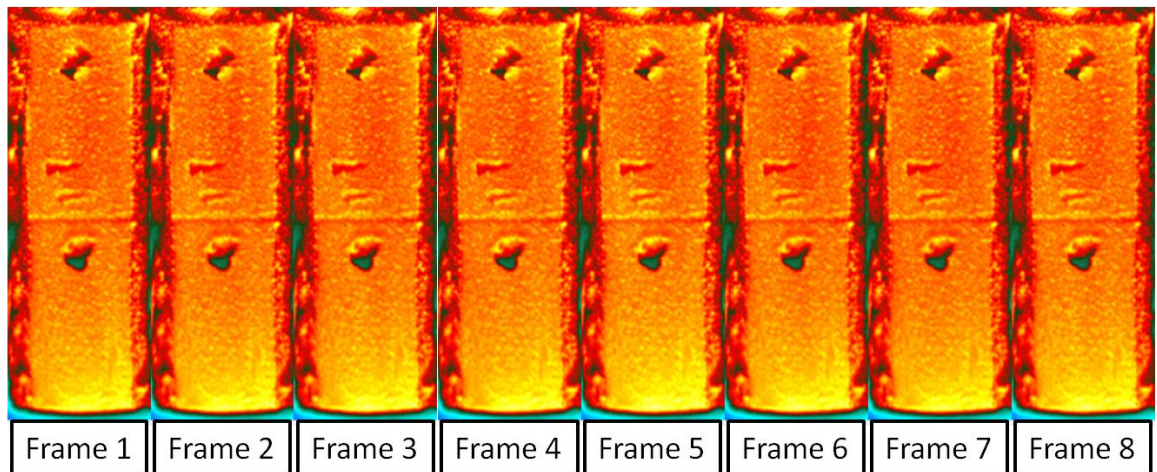


Figure 6.24: Frame-by-frame variations of surface temperature of 24-hour deposit layer.  
Imaged at 25 Hz

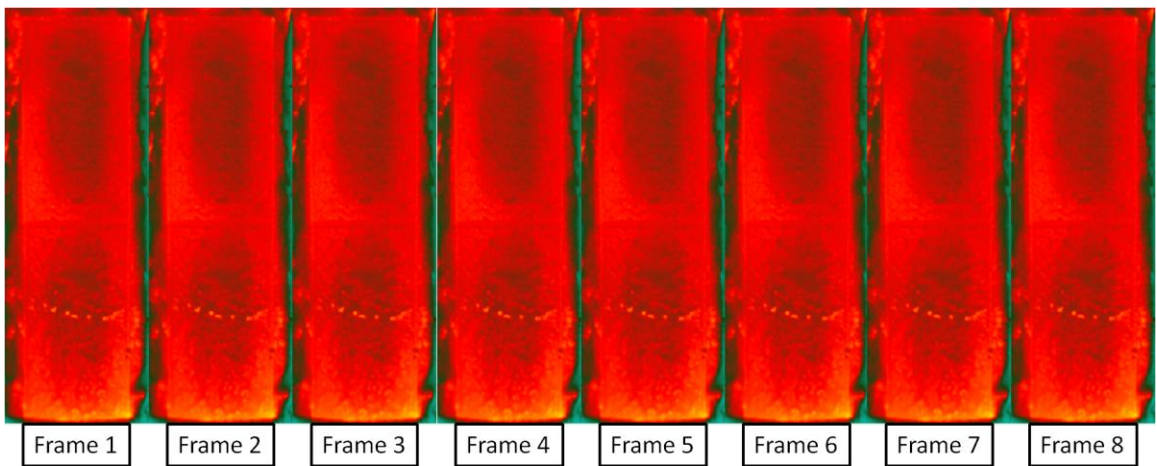


Figure 6.25: Frame-by-frame negligible variations in surface temperature on 30-hour collapsed layer. Imaged at 25 Hz

Table 6.7: Standard deviation of measured surface temperature

	Standard deviation of surface temperature on HF1 [C]	Standard deviation of surface temperature on HF2 [C]
6-hour layer	0.158	0.112
24-hour layer	0.229	0.173
Collapsed 30-hour layer	0.048	0.022

The variation of surface temperature in the porous layer suggests penetration of airflow into the layer resulting in porous flow. A cartoon of this effect is shown in Figure 6.26. The potential effect of porous flow is an increase in heat transfer surface area, in addition to the surface area increase measured by the optical microscope. Porous flow could increase the measured heat flux through the deposit layer resulting in an apparent increase in deposit thermal conductivity. However, the in-situ methodology is still relevant to determining the apparent thermal conductivity of the deposit because the deposit layer is also porous in actual EGR cooler applications. Therefore, it is appropriate to report the apparent thermal conductivity resulting from layer porosity, surface area, and volatiles due to their in-situ presence in EGR cooler applications.

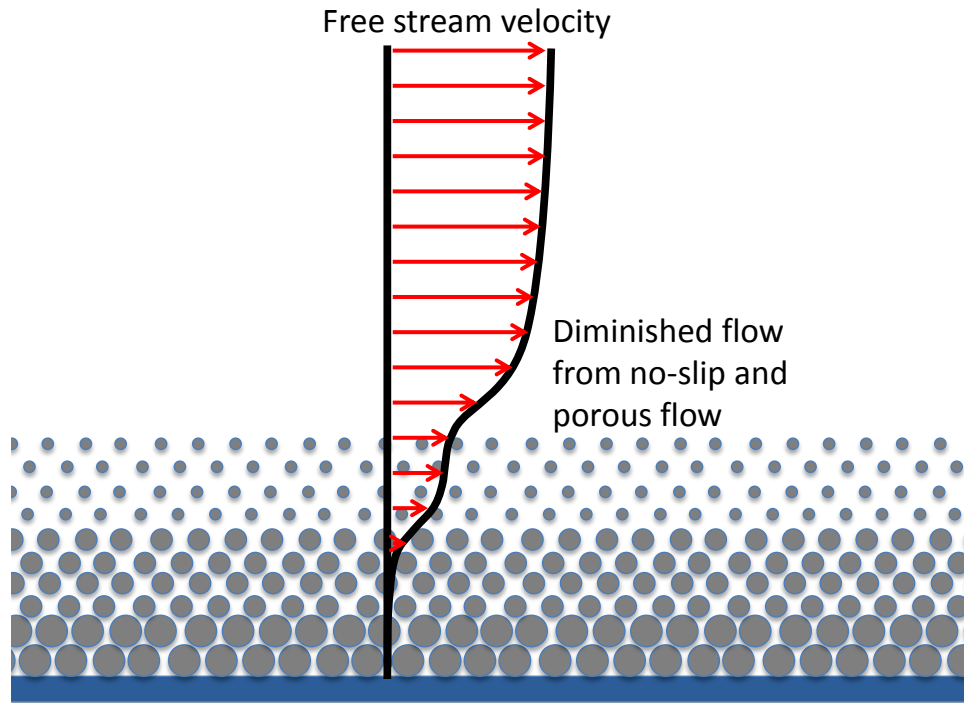


Figure 6.26: Porous flow diagram

### 6.3 Conclusions

The in-situ visualization rig was utilized to determine the thermal conductivity of a deposit layer formed in EGR heat exchanger systems.

The calculated thermal conductivity of a 379  $\mu\text{m}$  thick deposit layer on the downstream probe, developed over 24-hours, is approximately 0.046 W/mK. The deposit layer was seen to reduce in thickness after bake-out events, the first one at 120°C and the second at 150°C. The first bake-out demonstrated signs of mild layer shearing as evidenced by a reduction in measured surface area ratio and by a visually smoother layer. The second bake-out did not show a reduction in surface area ratio or produce visual evidence of shear however did produce a reduction in deposit thickness.

The bake-out events increased the heat transfer from the gas to the coolant. The increase in heat flux is not proportional to the decrease in layer thickness or surface area reduction. Further analysis shows an accompanying decrease in deposit conductivity and

modified behavior of conductivity with surface temperature as a result of the bake-out events. In addition, thermogravimetric analysis indicated the removal of low-end volatile species from pre-bake to post-bake deposit samples. The changes in thermal conductivity are hypothesized to result from layer compaction changing the behavior of thermal conductivity with surface temperature and layer volatile removal during thermal bake-out. The increase in conductivity expected from layer compaction may be offset by the decrease in conductivity resulting from layer volatilization.

The bake-out events constitute a mild recovery event since the heat transfer from the gas increases. This is directly proportional to an increase in heat exchanger effectiveness, even though the thermal conductivity of the layer decreased.

The introduction of isopropyl alcohol to the deposit layer immediately collapsed the porous structure of the layer. Using the pre-collapse layer thickness and the assumption of a solid layer post-collapse, porosity estimates of 88-93% for an undisturbed layer were calculated.

Heat transfer from the gas was measured to dramatically increase with the collapsed layer. This is due to the decreased thickness of the layer in addition to the increased thermal conductivity of the non-porous, collapsed layer.

Comparing frame-by-frame images of infrared thermal recordings generated evidence of porous-medium flow. Turbulent down sweeps of airflow were seen in the porous layer as determined by transient temperature variations while more steady temperatures were recorded for the collapsed layer. In addition, the collapsed layer produced an order of magnitude lower temperature variation due to the lack of porous flow.

The surface tension and high volatility of isopropyl alcohol created mud-cracks in the deposit surface. After the initial collapse of the deposit structure with the addition of alcohol, the deposit contracted as the alcohol evaporated. At the final stage of evaporation, the surface of the deposit was pulled apart by the evaporation process and



developed mud-cracks. These results coincide with observations of mud-cracks in field aged EGR coolers. Mud-cracks are often seen at the inlet of EGR coolers where the hot exhaust gas can evaporate volatiles in the deposit surface, drying out the deposit and creating mud-cracks.

The addition of high volatility hydrocarbons is seen to be a potential recovery mechanism, if appropriate temperatures and concentrations are met. The collapse of the deposit greatly increases the heat transfer from the gas and results in an increase in heat exchanger effectiveness. Care needs to be taken to avoid heavy fouling and plugging modes by selection of low temperature boiling point hydrocarbons.

## 6.4 References

- [1] Sluder, C. S., Storey, J., Lance, M. J., and Barone, T., "Removal of EGR Cooler Deposit Material by Flow-Induced Shear," *SAE Int. J. Engines*, vol. 6, no. 2, pp. 999-1008, 2013.
- [2] Abarham, M., Chafekar, T., Salvi, A., Hoard, J. W., Styles, D., Scott Sluder, C., and Assanis, D., "In-situ visualization of exhaust soot particle deposition and removal in channel flows," *Chemical Engineering Science*, vol. 87, no. 0, pp. 359-370, 2013.
- [3] Lance, M. J., Storey, J., Sluder, C. S., Meyer Iii, H., Watkins, B., Kaiser, M., and Ayyappan, P., "Microstructural Analysis of Deposits on Heavy-Duty EGR Coolers," SAE International, 2013.
- [4] Lance, M. J., Sluder, C. S., Wang, H., and Storey, J. M. E., "Direct Measurement of EGR Cooler Deposit Thermal Properties for Improved Understanding of Cooler Fouling," *SAE International*, 2009.
- [5] Çengel, Y. and Turner, R., *Fundamentals of Thermal-Fluid Sciences*. New York, NY: McGraw-Hill, 2001.

## **CHAPTER 7**

### **REMOVAL MECHANISMS**

The motivation for this chapter is to investigate and identify a deposit layer removal mechanism. Previous work has suggested that high gas velocity limits fouling through a reduction in particle trapping efficiency [1-4] and high velocities can result from a reduction in cross sectional flow area. Due to the large cross sectional area of the visualization rig, no significant change in gas velocities are expected, as described in Chapter 4. However, prior work from Malayeri suggested that a sudden change in pressure/flow of gas velocity might result in significant layer removal [5]. This chapter investigates whether deposit removal can be achieved due to either a change in pressure causing the lifting of the layer from the substrate or if velocity-based shear can cause layer removal.

To investigate the impact of sudden gas pressure/flow change on layer removal, the visualization rig, version 2, was used. A deposit layer was developed over a specified time interval and was subjected to a rapid change in ambient gas pressure and flow. Hypotheses on removal were investigated with an optical microscope and a high-speed camera.

## 7.1 Experimental Setup

### 7.1.1 Visualization rig

The visualization rig version 2 was utilized to develop a deposit layer and perform flow transient experiments. The rig takes exhaust from the high-pressure side of the 6.4L Ford diesel engine and flows a measured quantity at a set temperature and pressure through a simulated EGR heat exchanger (visualization rig version 2). The simulated EGR heat exchanger is comprised of a rectangular cross section of dimensions 21.5 x 12 x 300 mm with one side exposed to coolant and the other side enclosed by an optical window. A schematic of the setup is shown in Figure 7.1 and an image with the optical microscope and high-speed camera is shown in Figure 7.2.

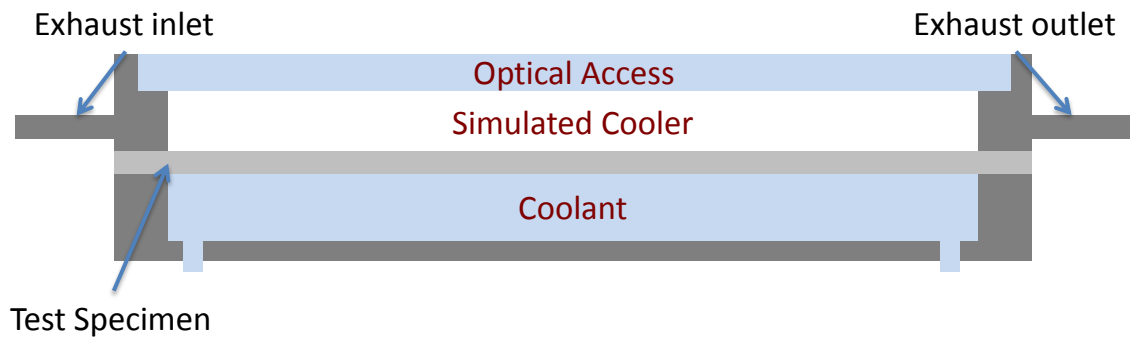
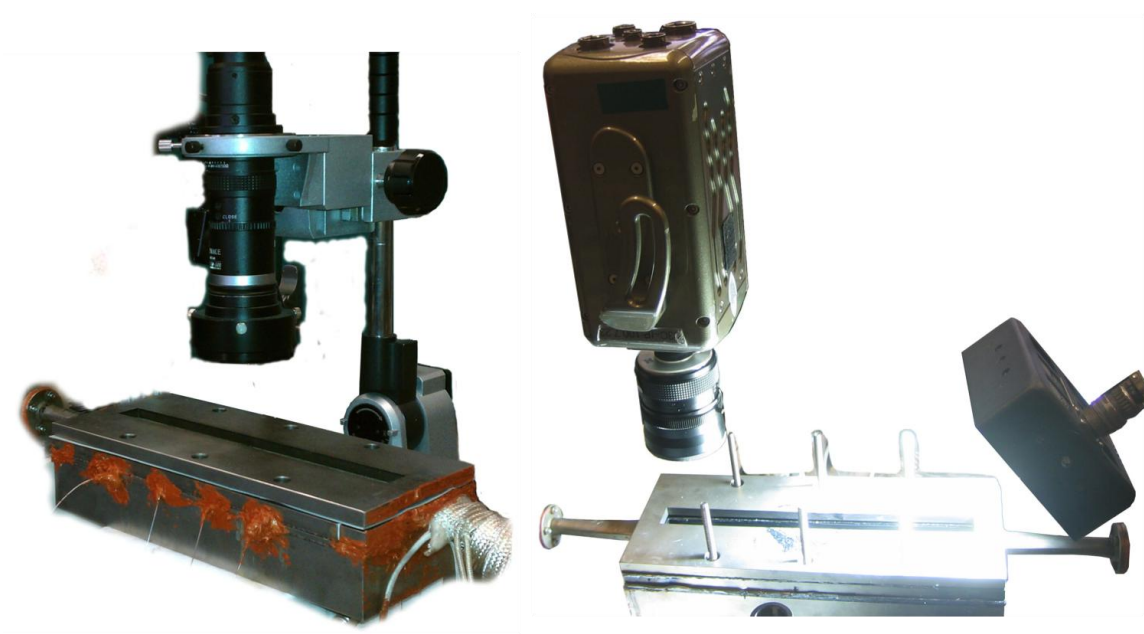


Figure 7.1: Visualization rig version 2 cross-section schematic



Optical microscope

High-speed camera at inlet with LED light box

Figure 7.2: Visualization rig version 2 image

Flow to the rig is controlled by a custom written Labview program. The rig can flow air or exhaust depending on experimental requirements. To investigate the effects of flow pressure/velocity on the deposit layer, a solenoid valve was installed at either downstream or upstream locations according to Figure 7.3.

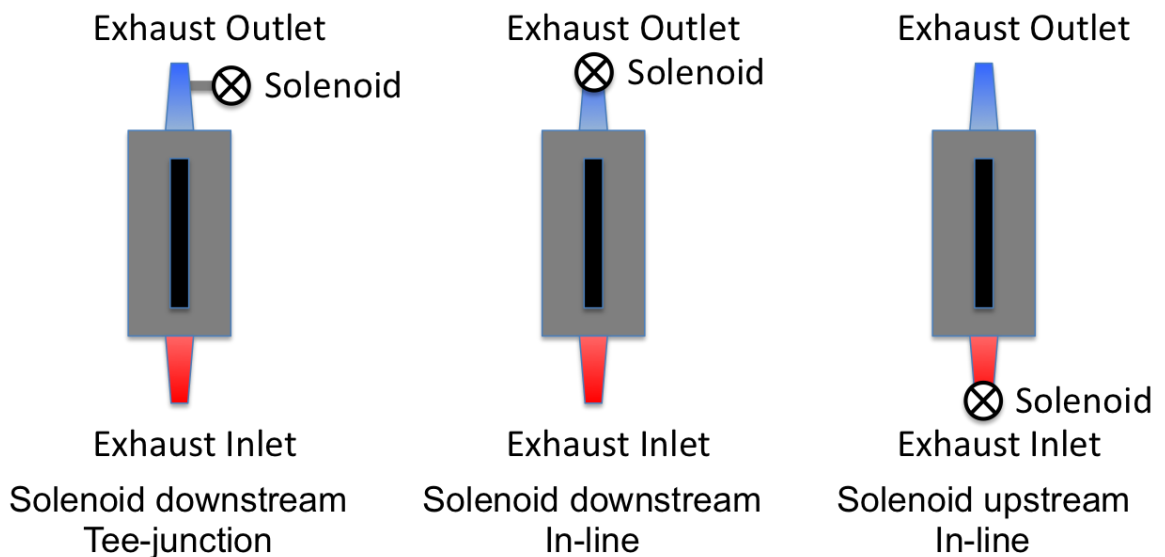


Figure 7.3: Solenoid locations on visualization rig version 2

### 7.1.2 Optical Equipment

The optical microscope is already described in Chapter 2 and will not be repeated here. The high-speed camera is a Vision Research Phantom v7.1 camera with a Navitar 50 mm F0.95 lens with 2 x 10 mm extensions. During the experiments, the high-speed camera is used in conjunction with the optical microscope to record transient events. The frame rate of the optical microscope is insufficient to capture the dynamics of the experiment, however the microscope captured high-resolution deposit surface images. The high-speed camera captured the dynamics of the experiment.

In addition, a high-powered LED light box supplied the lighting required to illuminate the deposit surface through multiple layers of optical glass.

## 7.2 **Results**

### 7.2.1 Downstream tee-junction solenoid

A schematic of the experimental setup is shown in “Solenoid downstream Tee-junction” in Figure 7.3, where the ½” solenoid valve is attached in a tee-junction downstream of the fixture. Various rig conditions prior to the flow transient were tested for removal, including:

1. High pressure, high flow
2. Low pressure, low flow
3. Low pressure, high flow
4. High pressure, low flow

Conditions 1 and 2 will be discussed together, followed briefly by condition 3, and finally concluded with condition 4. All conditions were developed using 1200 RPM, 7.5 bar BMEP with a 2 mg/stk at 30° aTDC post injection engine conditions.

### Conditions 1 and 2

A 6-hour deposit layer was generated and subjected to a pre-transient high pressure of 50 psia at a flow rate of 25 kg/hr at 211°C (~10.85 m/s) air for condition 1 and a different 6-hour layer to a low 22.5 psia at a low flow rate of 4.65 kg/hr at 209.7°C (~4.45 m/s) for condition 2. A cloth was wrapped around the outlet of the solenoid valve to capture any deposit layer blow out. Figure 7.4 qualitatively shows an increase in captured layer blow out for the low pressure, low flow rate of condition 2 compared to condition 1.

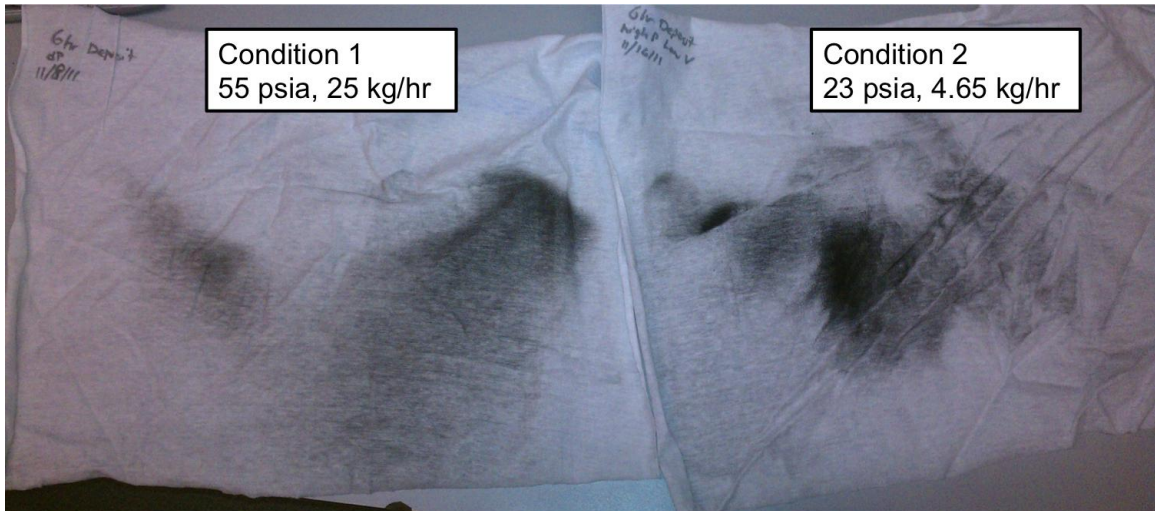


Figure 7.4: Qualitative analysis of deposit layer removal for condition 1 (high pressure, high flow) and condition 2 (low pressure, low flow)

Immediately following condition 2, the rig was pressurized to 45 psia at a flow rate of 4.65 kg/hr air at 32°C (~1.4 m/s) with the same layer that was exposed to the low pressure, low flow condition and another flow transient was performed. Figure 7.5 shows even further removal was achieved with high pressure, low flow on a layer previously subjected to a flow-transient. However, it appears the “easily” removed layer occurred mostly on the first low pressure, low flow transient. These transient conditions did not produce removal to bare metal, just thinned the deposit layer.

These results suggest that low flow rate might yield more removal. To verify this, a low pressure, high flow condition, condition 3, was investigated.

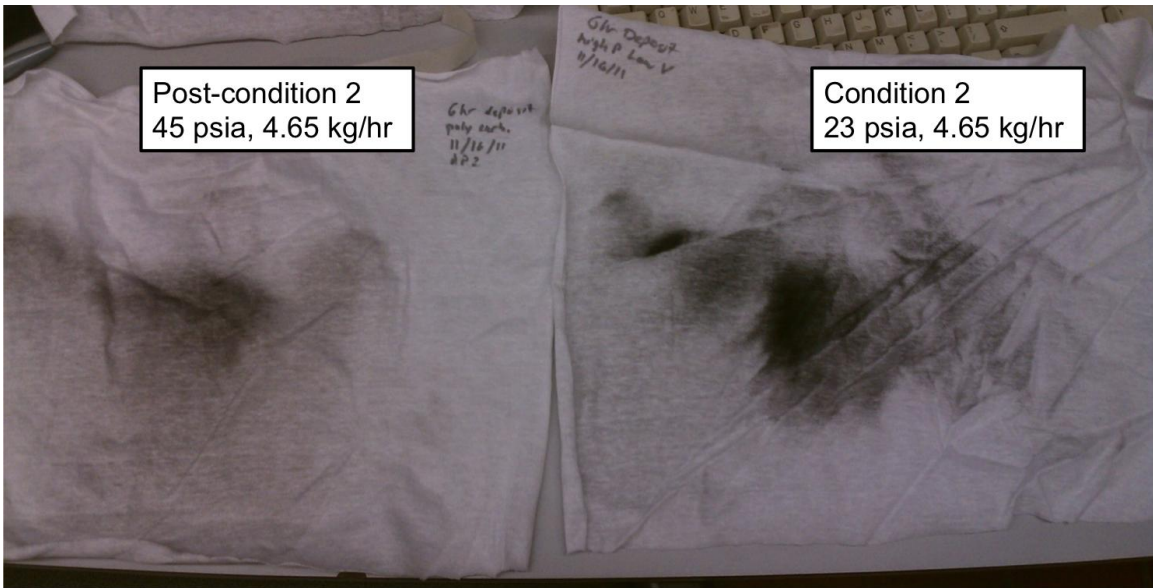


Figure 7.5: Qualitative analysis of condition 2 compared to post-condition 2 with high pressure and low flow

### Condition 3

A 3.5-hour layer was developed and subjected to a low pressure of 22.3 psia, high flow rate of 17.4 kg/hr of air at 315°C (~20.5 m/s). Pressure was dropped 7 psig from 23 psia to 16 psia. Figure 7.6 illustrates a reduction in the peaks of the deposit surface due to mild shearing, as demonstrated by a reduction in the shadows of the deposit layer. Overall, low pressure, high gas velocity pre-transient conditions did not produce strong removal.

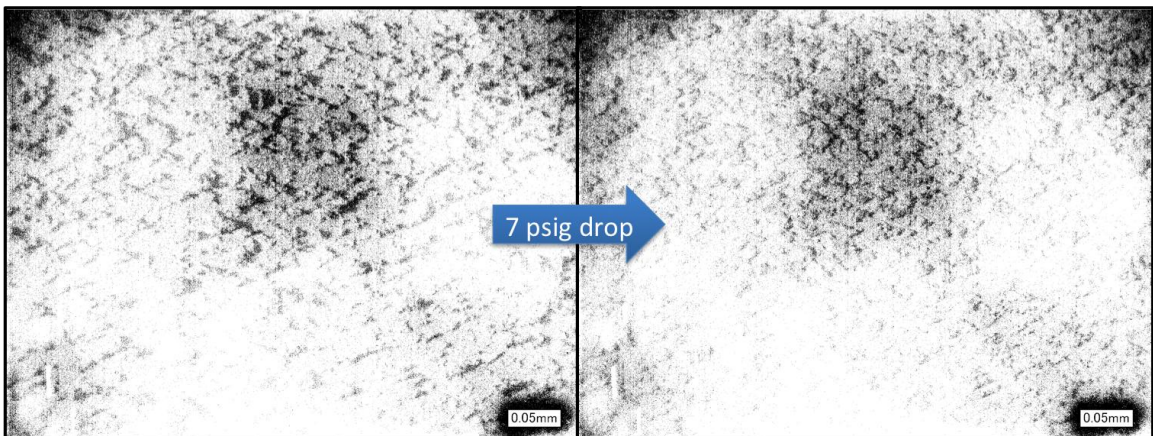


Figure 7.6: Low pressure, high flow mild shear removal during flow-transient on a 3.5-hour layer (image colors converted to black and white)



#### Condition 4

An 8-hour layer was developed and subjected to a high pressure of 51 psia, low gas flow of 9.3 kg/hr at 218°C (~4.03 m/s) pre-transient. The pressure dropped 36 psig to 15 psia during the transient. Assuming choked flow, the mass flow rate can be estimated using the following relationship:

$$\dot{m} = CA \sqrt{k \rho_0 P_0 \left( \frac{2}{k+1} \right)^{\frac{k+1}{k-1}}} \quad [6]$$

Where  $\dot{m}$  is the mass flow rate,  $C$  is the discharge coefficient,  $A$  is the discharge hole cross-sectional area,  $k$  is the ratio of specific heats of the gas,  $\rho_0$  is the gas density as upstream pressure and temperature, and  $P_0$  is the upstream pressure. Assuming a discharge coefficient of 1 and a choked flow area of 1.419E-4 m<sup>2</sup> (smallest flow path), an estimated flow rate of 258.7 kg/hr or 155.72 m/s was generated.

Optical microscope images show a significant shearing and thinning of the deposit surface after the transient event, as shown in Figure 7.7. Also in the figure is evidence of removal via particle bombardment, as illustrated by the large divot in the deposit surface. The leading and trailing grooves in the layer suggest the particle motion was parallel to the gas flow (left to right in the image). Large particles are seen in the pre-transient image and in prior work and are most likely responsible for impact removal [7, 8].

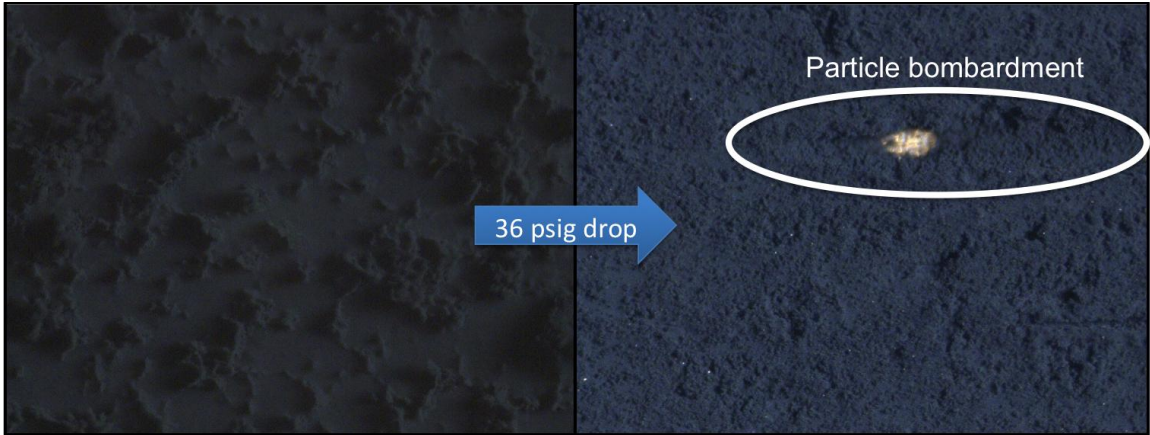


Figure 7.7: High pressure, low flow flow-transient layer shearing and particle bombardment

High-speed images at the channel inlet show layer removal much like sand dune wind erosion and are shown in Figure 7.8. High deposit surfaces are removed after which a ridge is created and is subsequently blown away. It appears as though the deposit layer is composed of two sections: the top layer that is easy to blow away and the bottom layer that remains on the surface after the top has blown away. It is apparent that this removal is based on velocity shear as there is no presence of a shock wave related to pressure change and the layer is not observed to lift from the metal substrate.

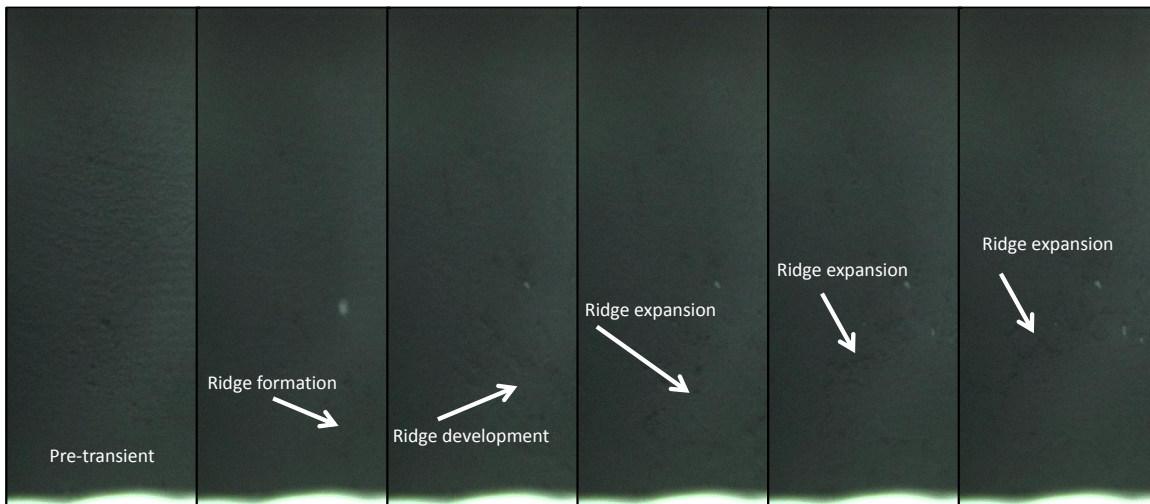


Figure 7.8: High-speed images of deposit shear

The high pressure, low flow condition produced more significant removal than the low pressure, high flow condition. The hypothesis as to why this happens is due to the

boundary layer development and thinning of the boundary layer in the high pressure, low flow condition and is shown in Figure 7.9.

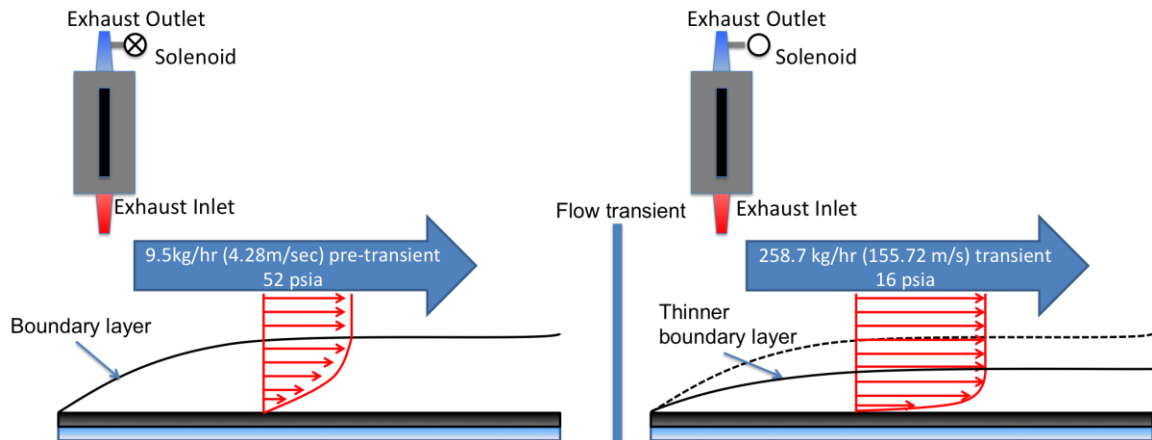


Figure 7.9: Schematic of flow-transient for high pressure, low flow condition

The pre-transient airflow creates a boundary layer over the deposit surface. When the solenoid opens and the high pressure in the rig is emptied to the atmosphere, the sharp increase in gas velocity decreases the boundary layer thickness and exposes the surface of the deposit to higher gas velocities. Increased velocity gradients on the deposit surface increase the shear stress according the shear stress relation for a viscous sublayer:

$$\tau = \mu \frac{dU}{dy}$$

Equation 7.1: Relationship between shear stress, velocity gradient, and viscosity [9]

Where  $\mu$  is the fluid viscosity,  $U$  is the fluid velocity,  $y$  is the height, and  $\tau$  is the shear stress. The shear force on the deposit surface during the transient event is stronger if the pre-transient flow velocity is low, minimizing the established boundary layer. This creates an even higher surface velocity gradient during a flow transient event and results in increased removal.

### 7.2.2 Upstream in-line solenoid

The solenoid was placed in-line with the gas flow upstream of the fixture with a 3-hour deposit layer. The in-line solenoid was used to create a stagnant, quiescent channel at ambient temperature and pressure. The solenoid was opened numerous times, labeled dP1, dP2, dP3, etc. in Figure 7.10, introducing airflow resulting from 54 to 68 psia pre-transient to 15 psia post-transient pressure drops. Figure 7.10 shows considerable layer removal with subsequent flow-transient events. After the 9<sup>th</sup> transient, approximately 30% of the channel was down to bare metal and can be seen in Figure 7.11.

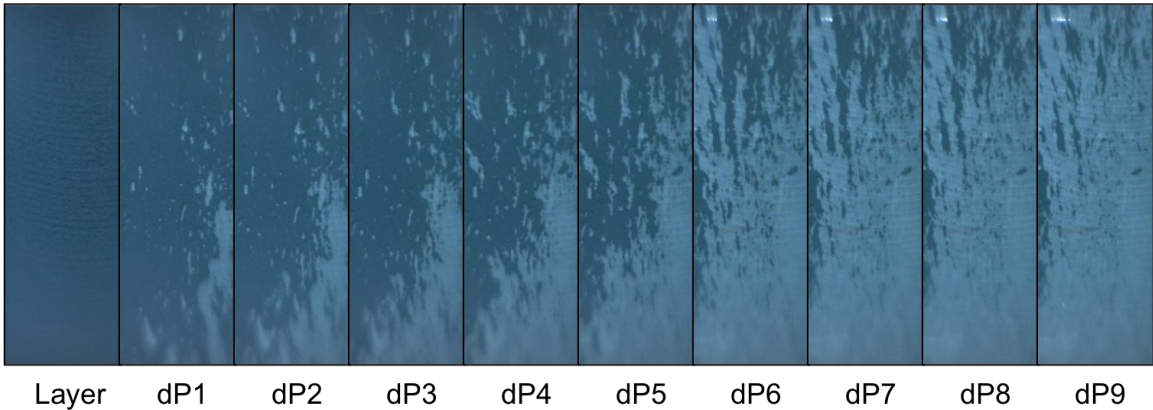


Figure 7.10: Flow-transients for upstream in-line solenoid valve; significant removal near inlet of channel

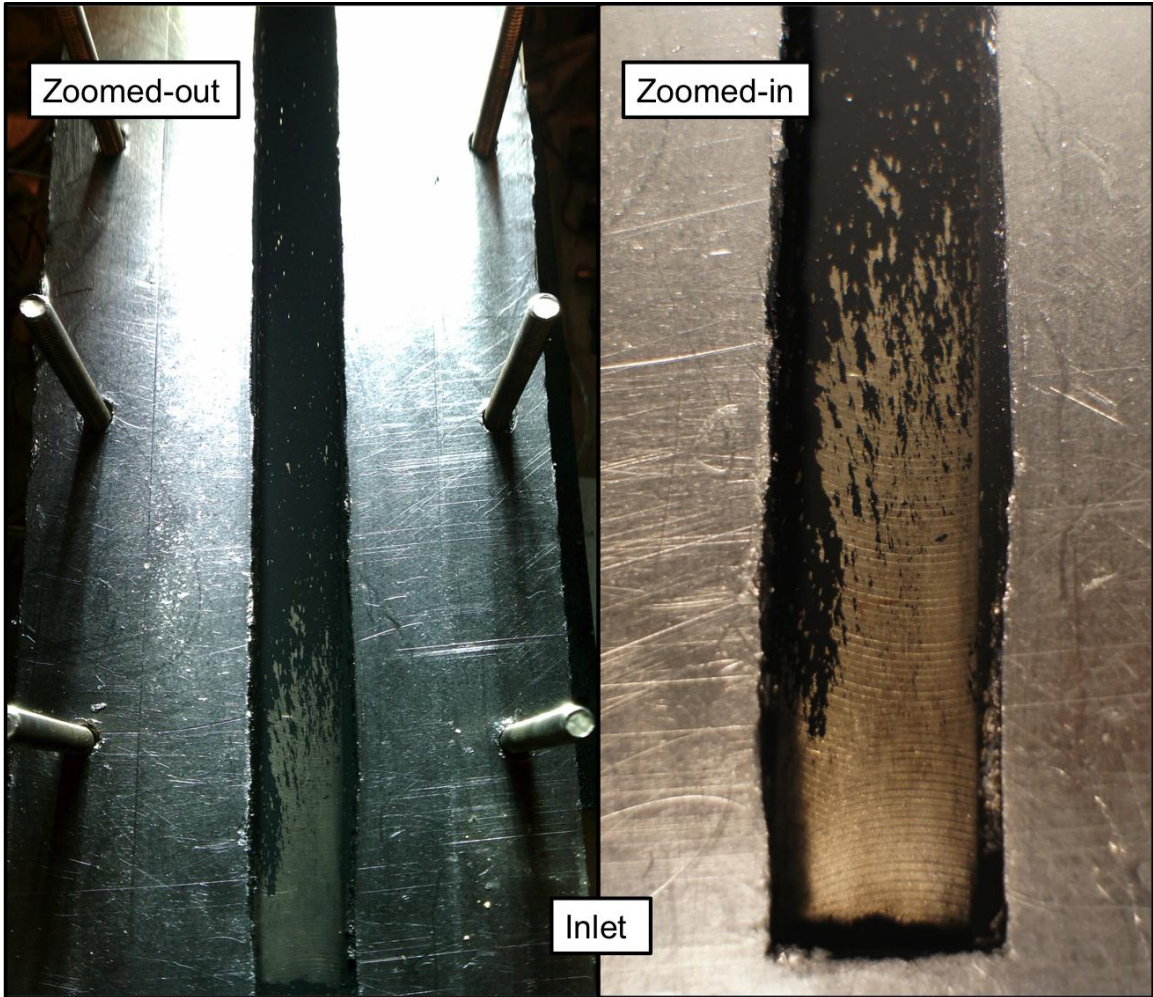


Figure 7.11: Zoomed-out and zoomed-in view at channel inlet of post-transient removal

Microscope images taken at mid-channel length show a significant layer shearing effect from the transient event, with pre-transient images in Figure 7.12 and post-transient images in Figure 7.13. The peaks of the deposit surface in the pre-transient image have been completely removed and replaced with a thinner, flatter surface.

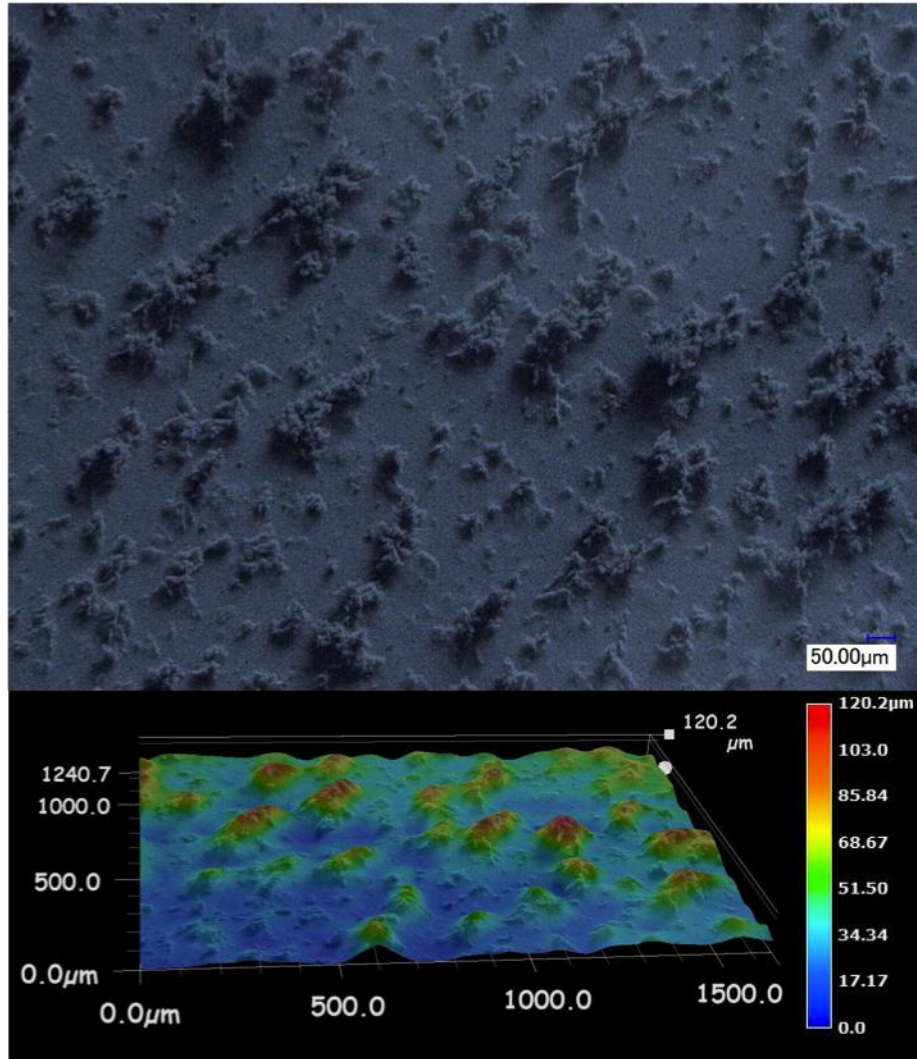


Figure 7.12: 3-hour pre-transient layer with upstream, in-line solenoid

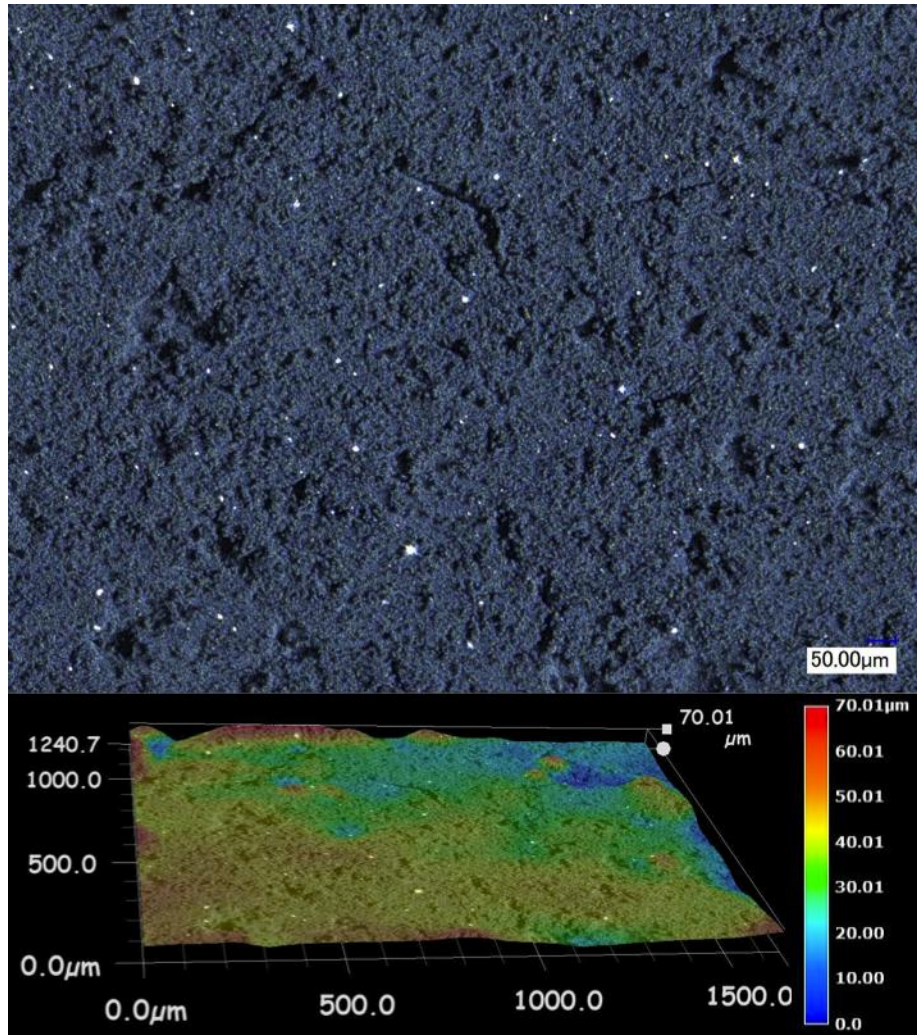


Figure 7.13: Optical surface images post-transient with upstream, in-line solenoid

The cause of this significant removal results from a negligible pre-transient boundary layer, in addition to the introduction of high velocity, turbulent air. Figure 7.14 shows a schematic of the flow conditions experienced in the channel during the transient event. The quiescent, stagnant air in the channel pre-transient eliminates an established boundary layer on the deposit surface. When the in-line solenoid valve opens, it introduces high velocity and highly turbulent air into the channel. The large velocity gradients and turbulent airflow is enhanced by the expansion of compressed air into the low-pressure channel. This large flow transient, or wind gust, flows across the deposit surface with no developed boundary layer and creates a high velocity gradient and shear

force on the deposit surface. As this gust progresses along the length of the channel into still stagnant air, a boundary layer starts to develop behind the initial gust and a shallower velocity gradient is experienced on the deposit surface. The wind gust is highly turbulent from flow rate and entrance effects, further reducing the development of a boundary layer. The flow is most turbulent at the inlet of the channel, hence why most of the layer removal is observed at that location and can be observed by the time-lapse high-speed images in Figure 7.15. These images also confirm removal is due to velocity shear and not due to a change in pressure causing the layer to lift off from the metal substrate.

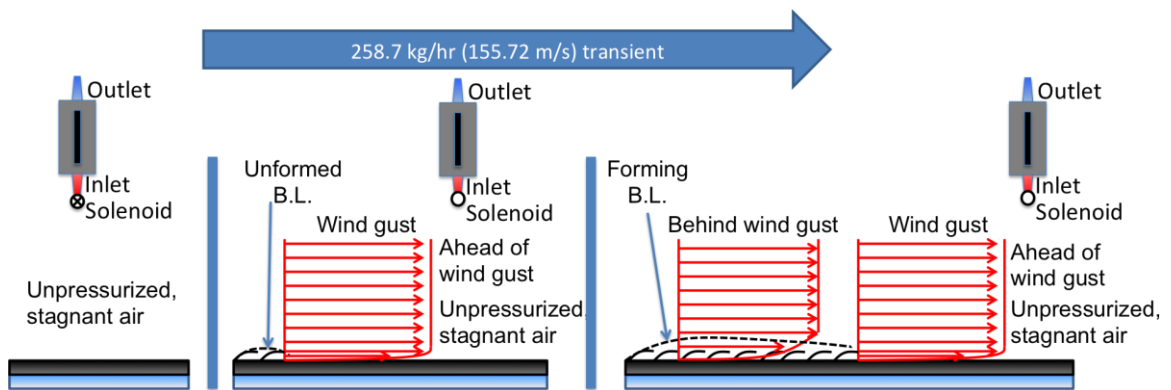


Figure 7.14: Flow schematic of upstream, in-line solenoid transient flow event

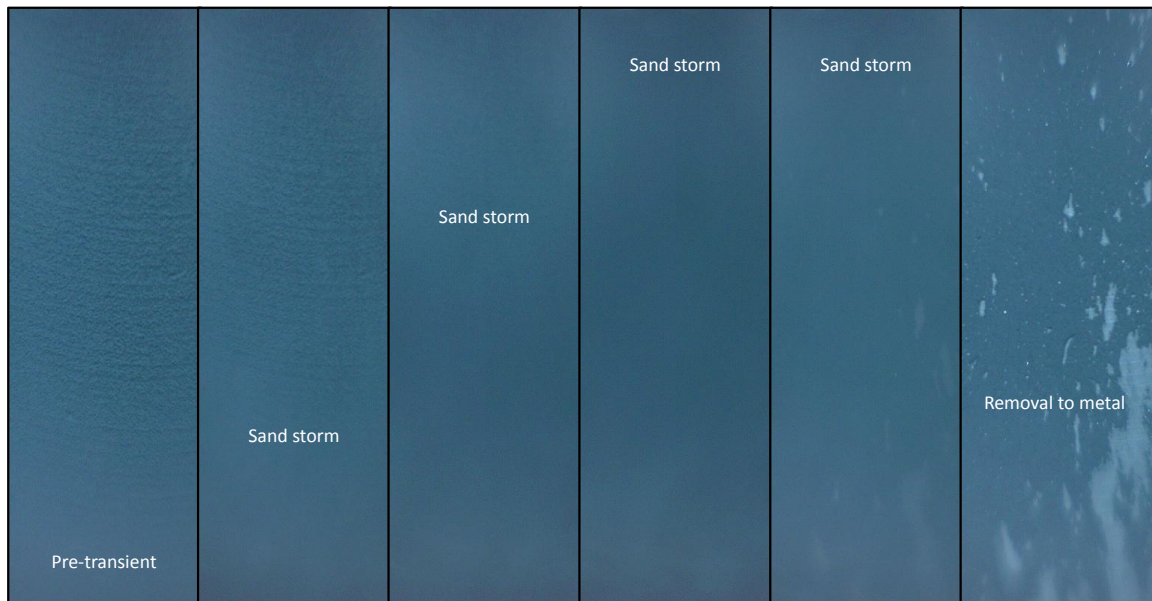


Figure 7.15: High-speed images of deposit layer removal caused by upstream solenoid



### Downstream in-line solenoid

The solenoid valve was placed downstream and in-line of the fixture to determine the effect of flow-transient on a quiescent but pressurized channel and eliminate the pressure expansion effect from an upstream, in-line solenoid. A 3-hour layer was generated and exposed to quiescent air at 52 psia. After opening the solenoid valve, minimal removal occurred and resulted in the shearing of the peaks of the deposit surface.

The solenoid valve was relocated to the upstream and in-line location and additional flow-transient events were conducted. In addition to successful layer removal with an unmodified layer discussed earlier in the upstream in-line solenoid experiment, the upstream in-line location also produced removal on an old and modified layer. Figure 7.16 shows the layer surface after removal with the upstream valve location. The pattern of removal is different from that in Figure 7.11. The unmodified layer in Figure 7.11 shows streaks of deposit layer removal whereas Figure 7.16 shows spots of removal. In addition, less bare metal is exposed in the modified layer compared to the unmodified layer.

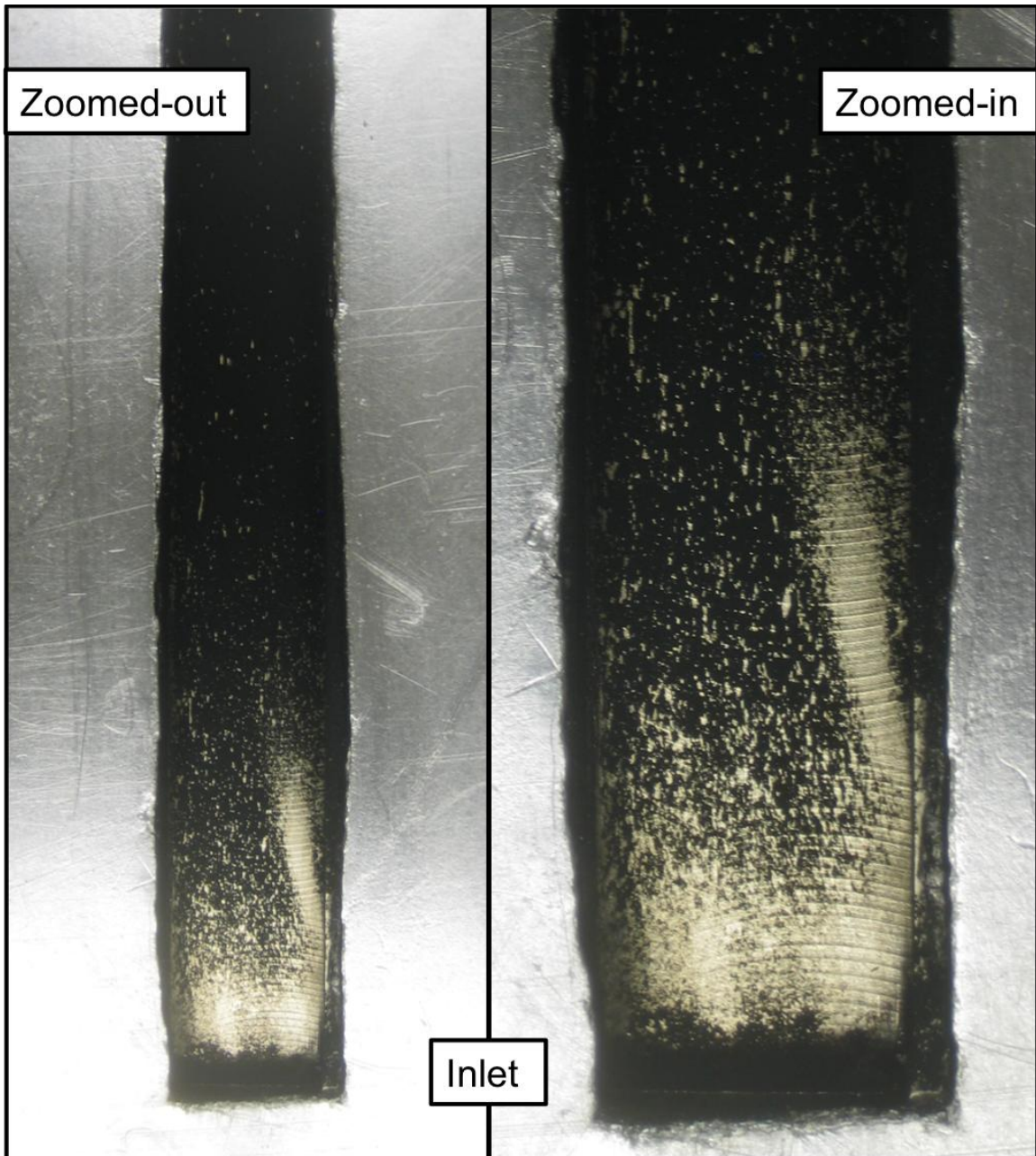


Figure 7.16: Layer removal on a previously modified deposit layer with an upstream, in-line solenoid

It is believed that the prior flow-transient events removed the peaks of the deposit surface but did not create the drastic removal noted with the upstream solenoid location due to the lack of pressure expansion into the channel. The removal of the peaks prevented significant removal when the solenoid valve was relocated upstream due to diminished shearing effects on a smoother layer. The peaks act to increase the shear force

due to their extension into higher velocity regions and are most susceptible to removal. After removal, these deposits can impact deposits downstream and create particle bombardment removal and further enhance the removal effect. In addition, the modified layer may have compacted during the downstream solenoid flow-transient event thus creating a more interlocked and stronger layer resistant to removal.

In terms of purely velocity-based removal, two parameters are important: quiescent channel and location of flow expansion. It is concluded that in addition to a quiescent channel, high-pressure air expansion into a low-pressure channel is required to generate the highly turbulent and high velocity flow needed for significant layer removal. It is noted, however, that achieving velocities of 155.72 m/s in an actual application, such as an engine, is not without a pressure loss or fuel economy penalty. To circumvent this issue, a strategy utilizing high-pressure boost from the turbo turbine during gearshifts or engine tip-out can be employed to regenerate EGR coolers. In addition, on-board air compressors can also be used to inject high-pressure air through the EGR cooler when engine load, and therefore intake manifold pressure, is low. This strategy creates a large pressure differential during low or no flow conditions, similar to condition 4 and the upstream solenoid, to create maximum cooler recovery.

### 7.2.3 Condensation and flow transient

The effect of exhaust gas condensation has been previously reported to effectively break apart and remove a deposit layer [8, 10]. A condensation experiment was performed on an old layer, previously modified via flow-transient experiments that thinned the layer. Coolant temperature was dropped to 16°C while engine exhaust was flowing through the visualization rig. The coolant temperature was below the dew point of the water vapor in the exhaust stream and led to the condensation of water in the channel. Previous experiments performed by Abarham et al. yielded a complete wash out

and recovery of the fouled channel [10]. During the current experiment, recovery and compaction of the layer was noticed however a complete wash out did not occur as shown in Figure 7.17.



Figure 7.17: Image of deposit surface after water condensation from exhaust gas

The water condensation experiment was repeated, however this time it was accompanied with a mild flow-transient induced from a 17 to 15 psia pressure drop with the solenoid valve in a tee-junction downstream of the fixture. The coolant temperature

was 4°C. The condensation in addition to flow-transient resulted in a significant removal and recovery event as shown in Figure 7.18.

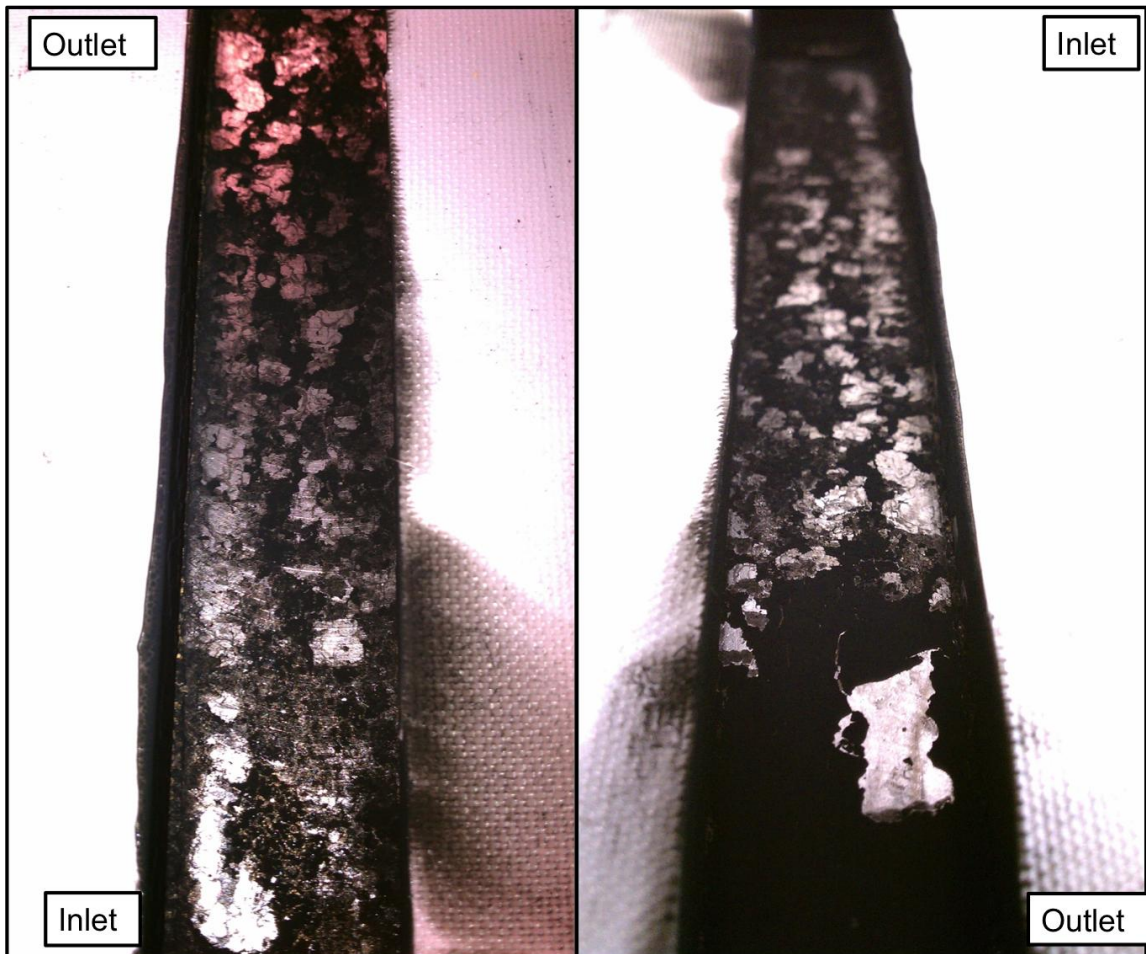


Figure 7.18: Water condensation plus flow-transient on a previously modified layer

The cold walls of the channel provide a condensation location for water vapor in the exhaust. The water vapor permeates through the layer and condenses underneath the deposit and on top of the cold wall [8]. The water cracks and lifts the deposit layer from the surface of the cooler wall. The mild flow transient provides sufficient shear force to blow away the already lifted and weakened layer, resulting in layer removal.

This recovery was more significant than shown in Figure 7.11, generating almost 50% metal recovery and required less pressure to achieve. This refreshment strategy could be used in application by flowing exhaust gas through cold EGR coolers, such as at

engine start-up or possibly delay circulation of coolant through the coolers, to encourage condensation. Since the flow-transient is not that severe, it could take place in low-load engine conditions. Caution needs to be observed to avoid heavy hydrocarbon fouling at initial engine start-up due to poor combustion and emissions light-off strategies.

#### 7.2.4 Angle of attack

To qualitatively determine the effect of boundary layer development on layer removal, experiments to determine the effect of airflow angle on deposit layer removal were conducted. The visualization rig was opened so the entire channel was exposed to ambient air. A compressed air line was positioned above the layer in various angles to determine the interaction between impacting airflow and the deposit surface. It was observed that as the angle of attack, as defined in Figure 7.19, of the airflow increased, deposit surface spallation increased. Spallation was not observed when the airflow was parallel to the deposit surface. The resulting deposit surface spallation is pictured in Figure 7.20

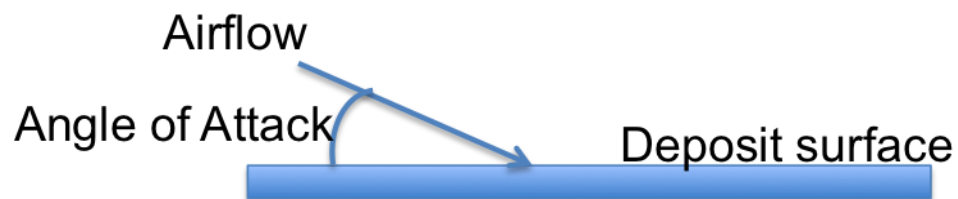


Figure 7.19: Definition of angle of attack



Figure 7.20: Deposit surface spallation resulting from angled airflow

The layer was not blown away in a puff, but was gradually broken apart. When the airflow was stopped and reinitialized with a sudden gust at 100 psia at an elevated angle of attack, the layer blew away in a puff. These results are related to the previous discussions about the formation of a boundary layer and subsequent thinning of that layer with velocity. As the angle of attack of airflow increases, the boundary layer on the deposit surface becomes thinner and the shear force on the deposit increases. As the shear force increases, deposit spallation occurs. The layer is seen to blow away when impacted with a gust of wind due to the lack of an existing boundary layer. In the absence of a developed boundary layer, the velocity gradient on the deposit surface is very large causing significant shear stress and removal of the deposit.

Utilizing this information, EGR coolers can mitigate fouling by using large angles of attack on surfaces to keep deposit build-up to a minimum. The reduction in boundary layer thickness will encourage deposit layer removal and improve heat transfer. Higher velocity flows will create an even thinner boundary layer and may reduce deposit

thickness further. Care needs to be taken to avoid significant pressure losses from too steep of an angle of attack, thereby reducing flow rates and incurring a fuel penalty.

### **7.3 Conclusions**

Investigations into deposit layer removal were performed on the visualization rig, version 2. A solenoid valve was placed at upstream and downstream locations; in either a tee-junction or in-line with the main gas flow path. An optical microscope and high-speed camera were utilized to determine the effects of various pre-flow-transient conditions on layer removal.

These investigations concluded that deposit removal is due to velocity-based shear and not to a change in pressure lifting up and removing the layer. It was determined that the upstream, in-line solenoid location produced the most significant velocity-based removal. When the solenoid was closed preventing flow, the quiescent rig channel was exposed to ambient pressure and a negligible boundary layer. When the valve opened, sharp velocity gradients were exposed to the deposit surface and resulted in large shear forces. The expansion of the airflow from high pressure into the low-pressure channel and inlet effects produced highly turbulent gas flow, thus increasing the shear force on the deposit surface. These effects caused dramatic layer removal to bare metal and after nine flow-transient events, approximately 30% of the channel experienced a full recovery. The solenoid valve was also placed in-line downstream of the fixture, however did not produce as significant of a removal event. This result highlights the importance of turbulent inlet air and diminished boundary layers created by the upstream solenoid valve location on removal. The upstream, in-line solenoid configuration also produced recovery to bare metal on previously flow-sheared layers.

High pressure, low flow conditions produced the next most significant removal as demonstrated by the solenoid valve being positioned downstream of the rig in a tee-



junction. While this orientation did not produce recovery to bare metal, it vastly thinned the deposit layer and is expected to regenerate a significant portion of a cooler's effectiveness.

The most significant recovery resulted by a combination of water condensation and flow-transients. A layer previously exposed to flow-transient shear but did not produce removal to metal was exposed to hot engine exhaust gases in the presence of cold coolant. The water vapor from the exhaust gas condensed on the cold surface of the heat exchanger and partially removed the layer. The same condensing conditions were performed again however with a low-pressure flow-transient after condensation occurred. The combination of the two produced the most significant deposit layer removal with approximately 50% bare metal recovery.

The angle of attack of the incoming gas flow to the deposit surface was also determined to be important. As the angle of attack increased from parallel to perpendicular, deposit layer spallation increased. This is due to the thinning of the boundary layer of the deposit surface, creating higher velocity-based shear on the surface. Using a high angle of attack and a quiescent channel, airflow was suddenly introduced to the surface. This resulted in the blowing away of the deposit surface instead of spallation and is attributed to the high velocity shear forces applied to the deposit surface due to a non-existing boundary layer.

#### **7.4 Acknowledgements**

I would like to thank Professor Margret Wooldridge at the University of Michigan for loaning me their high-speed camera and Mohammad Fatouraie for showing me how to properly operate it. In addition, I would like to thank Dr. Anand Gandhi at Ford Motor Company for lending me their LED light box to illuminate the deposit surface sufficiently for high-speed and optical microscope imaging.

## 7.5 References

- [1] Abarham, M., Hoard, J. W., Assanis, D., Styles, D., Sluder, C. S., and Storey, J. M. E., "An analytical study of thermophoretic particulate deposition in turbulent pipe flows," *Aerosol Science and Technology*, vol. 44, pp. 785-795, 2010.
- [2] Abd-Elhady, M. S., Zornek, T., Malayeri, M. R., Balestrino, S., Szymkowicz, P. G., and Müller-Steinhagen, H., "Influence of gas velocity on particulate fouling of exhaust gas recirculation coolers," *International Journal of Heat and Mass Transfer*, vol. 54, no. 4, pp. 838-846, 2011.
- [3] Abd-Elhady, M. S., Rindt, C. C. M., Wijers, J. G., van Steenhoven, A. A., Bramer, E. A., and van der Meer, T. H., "Minimum gas speed in heat exchangers to avoid particulate fouling," *International Journal of Heat and Mass Transfer*, vol. 47, no. 17-18, pp. 3943-3955, 2004.
- [4] Völk, P., Wachtmeister, G., Hörning, G., and Niessner, R., "Deposition mechanisms in exhaust heat exchangers," *MTZ*, vol. 73, pp. 58-64, 2012.
- [5] Malayeri, M. R., Zornek, T., Balestrino, S., Warey, A., and Szymkowicz, P. G., "Deposition of nano-sized soot particles in various EGR coolers under thermophoretic and isothermal conditions," in *International Conference on Heat Exchanger Fouling and Cleaning*, Crete Island, Greece, 2011.
- [6] *Handbook of Chemical Hazard Analysis Procedures*: Federal Emergency Management Agency, U.S. Department of Transportation, U.S. Environmental Protection Agency, 1989.
- [7] Hoard, J., Chafekar, T., Abarham, M., Schwader, R., Uplegger, S., and Styles, D., "Large particles in modern diesel engine exhaust," in *ASME 2012 Internal combustion engine division spring technical conference (ICES 2012)*, Torino, Italy, 2012.

- [8] Abarham, M., Chafekar, T., Salvi, A., Hoard, J. W., Styles, D., Scott Sluder, C., and Assanis, D., "In-situ visualization of exhaust soot particle deposition and removal in channel flows," *Chemical Engineering Science*, vol. 87, no. 0, pp. 359-370, 2013.
- [9] Kundu, P. and Cohen, I., *Fluid Mechanics*, 3rd ed. San Diego, CA: Elsevier Academic Press, 2004.
- [10] Abarham, M., Chafekar, T., Hoard, J., Styles, D., and Assanis, D., "A Visualization Test Setup for Investigation of Water-Deposit Interaction in a Surrogate Rectangular Cooler Exposed to Diesel Exhaust Flow," *SAE International*, 2012.

## CHAPTER 8

### UNCERTAINTY ANALYSIS

This chapter serves to determine the uncertainty associated with the in-situ measurement as well as provide mitigation strategies.

#### 8.1 Measurement uncertainty

##### 8.1.1 Accuracy

To determine the accuracy of the in-situ measurement, the partial derivative is applied to Equation 8.1 in terms of each measurement:

$$k = \frac{q'' \times y}{(T_{interface} - T_{wall})}$$

Equation 8.1: Thermal conductivity calculation in terms of relevant measurements

Where  $q''$  is the heat flux [ $\text{W}/\text{m}^2$ ] as measured by the heat flux probe,  $y$  is the thickness of the deposit [m] as measured by the optical microscope,  $T_{interface}$  is the gas-to-deposit interface temperature measured by the infrared camera, and  $T_{wall}$  is the deposit-to-probe wall temperature measured by the embedded thermocouple in the heat flux probe. The thermal conductivity accuracy uncertainties from each measurement are combined with each other to generate an overall uncertainty as shown in Equation 8.2:

$$\delta k = \left[ \left( \frac{\delta q'' \times y}{T_{interface} - T_{wall}} \right)^2 + \left( \frac{q'' \times \delta y}{T_{interface} - T_{wall}} \right)^2 + \left( - \frac{q'' \times y}{(T_{interface} - T_{wall})^2} \times \delta T_{interface} \right)^2 + \left( \frac{q'' \times y}{(T_{interface} - T_{wall})^2} \times \delta T_{wall} \right)^2 \right]^{1/2}$$

Equation 8.2: Total uncertainty introduced into the thermal conductivity calculation due to instrument uncertainty

Various instrument uncertainties are listed in Table 8.1 and are from manufacturer specifications.

Table 8.1: Instrument uncertainty for various parameters

Variable	Uncertainty
$\delta q''$	5% of measured value
$\delta y$	5 microns
$\delta T_{interface}$	2% of measured value or 2°C
$\delta T_{wall}$	0.75% of measured value or 2.2°C

The total uncertainty for heat flux probe 1 is shown in Figure 8.1 and the total uncertainty for heat flux probe 2 is shown in Figure 8.2 as a function of Reynolds number at various deposit thicknesses.

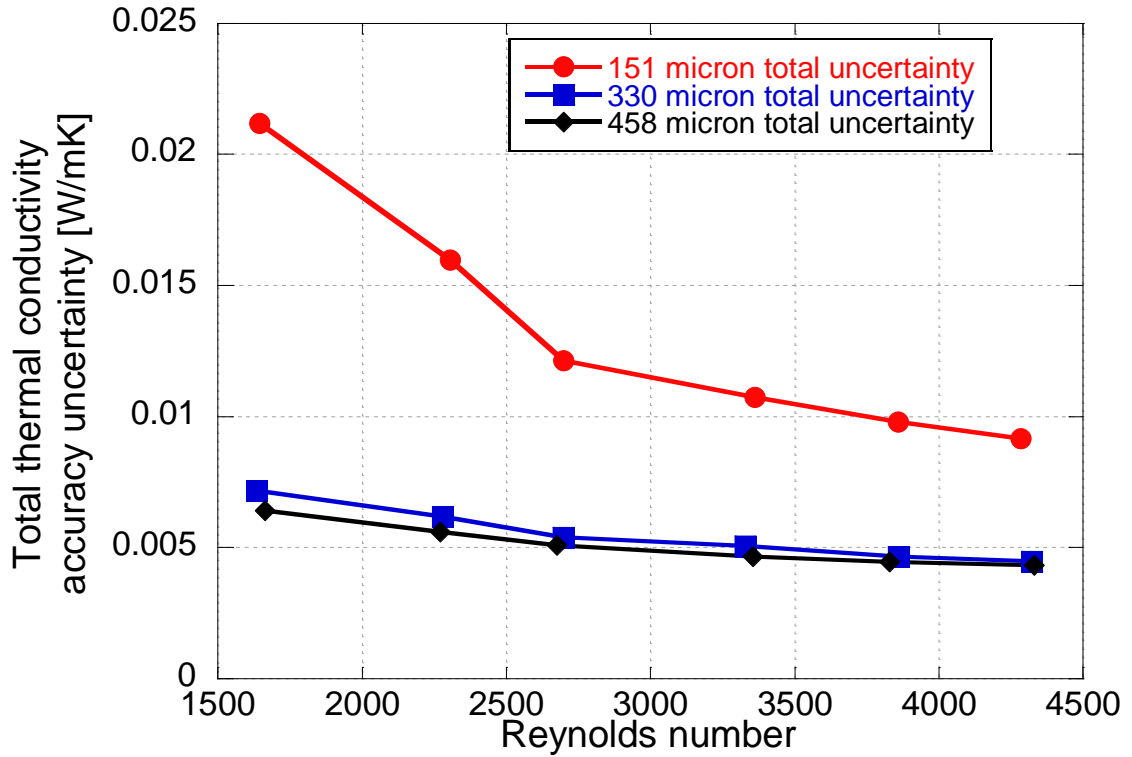


Figure 8.1: Total accuracy uncertainty as a function of Reynolds number at various thicknesses on heat flux probe 1

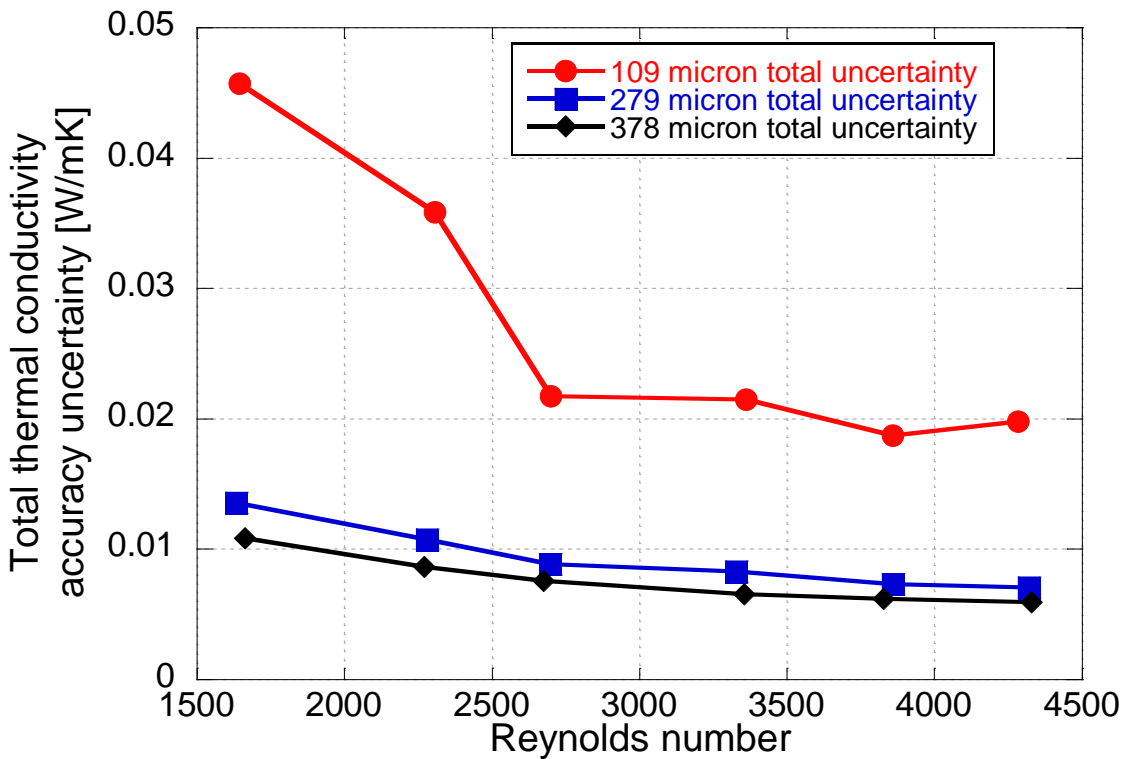


Figure 8.2: Total accuracy uncertainty as a function of Reynolds number at various thicknesses on heat flux probe 2

Figure 8.1 and Figure 8.2 represent the maximum uncertainty introduced by instrument tolerance specifications. It is clearly evident that the in-situ measurement uncertainty decreases significantly as deposit thickness increases. Also apparent is a decrease in uncertainty with increasing Reynolds number. To further understand these trends, the total uncertainty associated with the thinnest and thickest layers will be deconstructed into their constituent parts. This analysis will be performed for heat flux probe 2 as trends are similar for both probes but with slightly different values.

Figure 8.3 decomposes the total uncertainty for the 109 micron thick deposit on heat flux probe 2. The primary source of uncertainty results from the K-type wall thermocouple and infrared interface temperature. The uncertainties resulting from the heat flux probe and thickness measurement are an order of magnitude lower than that of the temperature measurements.

Figure 8.4 breaks down the uncertainty for 378 micron thick deposit on probe 2. The primary sources of uncertainty are still the K-type wall thermocouple and infrared interface temperature, however they are on the same order of magnitude as the uncertainty from the heat flux probe and thickness measurement.

The temperature measurements play a more significant role in the total uncertainty at thinner layers due to a smaller temperature differential across the layer. This is evidenced by the fact that as Reynolds number increases, and subsequently the temperature difference across the layer increases (Chapter 5), the uncertainty decreases. As the layer increases in thickness, the temperature difference across the layer also increases as described in Chapter 5. The increased temperature difference causes a decrease in the uncertainty stemming from the temperature measurements.

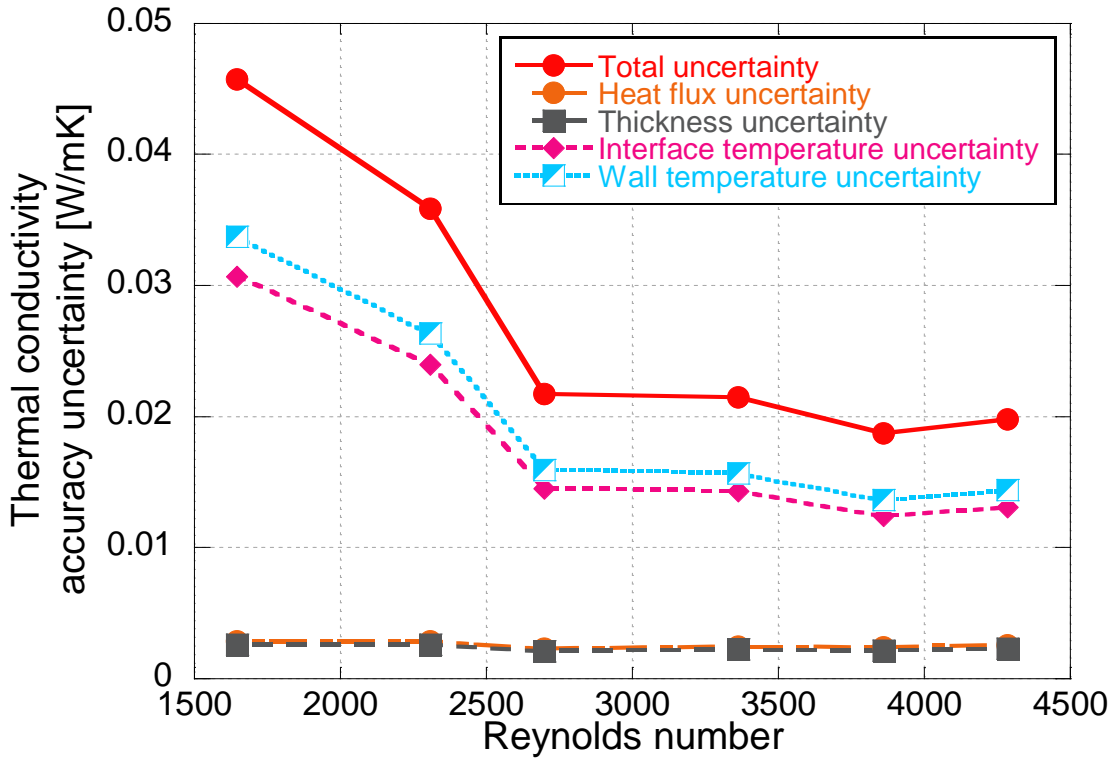


Figure 8.3: Thermal conductivity uncertainty breakdown for 109 micron thick deposit layer on heat flux probe 2

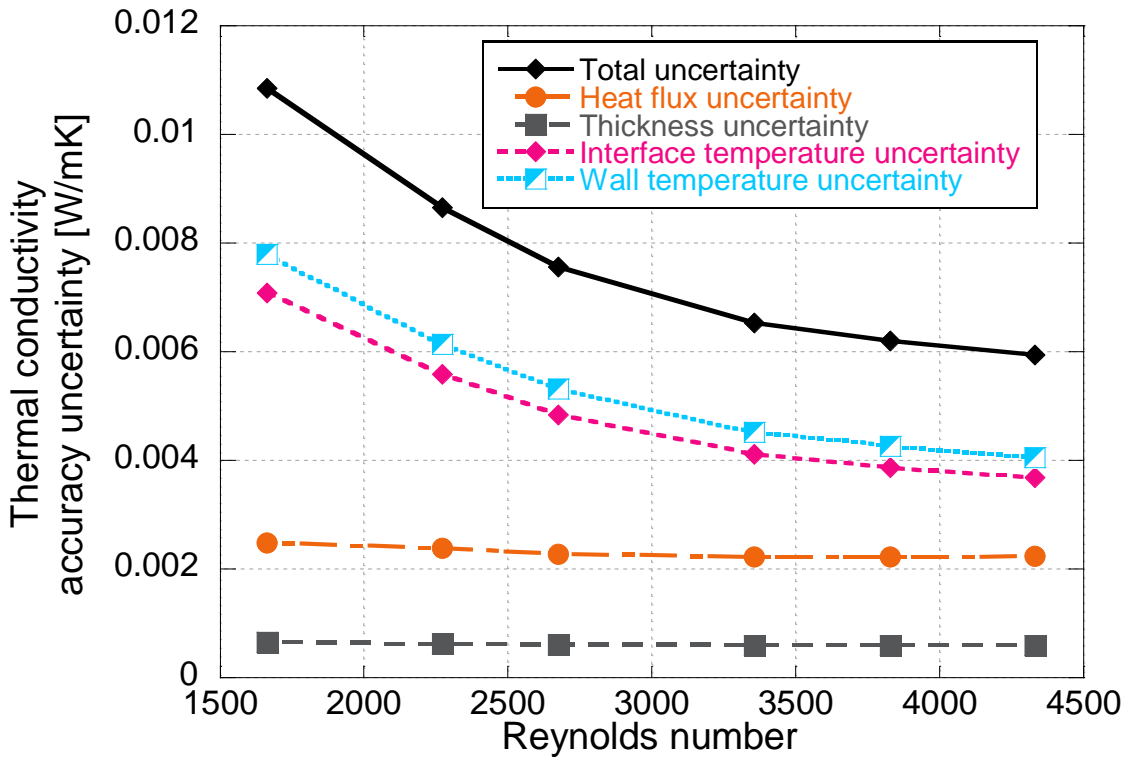


Figure 8.4: Thermal conductivity uncertainty breakdown for 378 micron thick deposit layer on heat flux probe 2



Combining the maximum instrument uncertainties for the 6-hour 109 micron thick layer, 18-hour 279 micron thick layer, and the 24-hour 378 micron thick layer with the measured conductivities from heat flux probe 2 yields the image in Figure 8.5. Trends are similar for heat flux probe 1 and will be omitted.

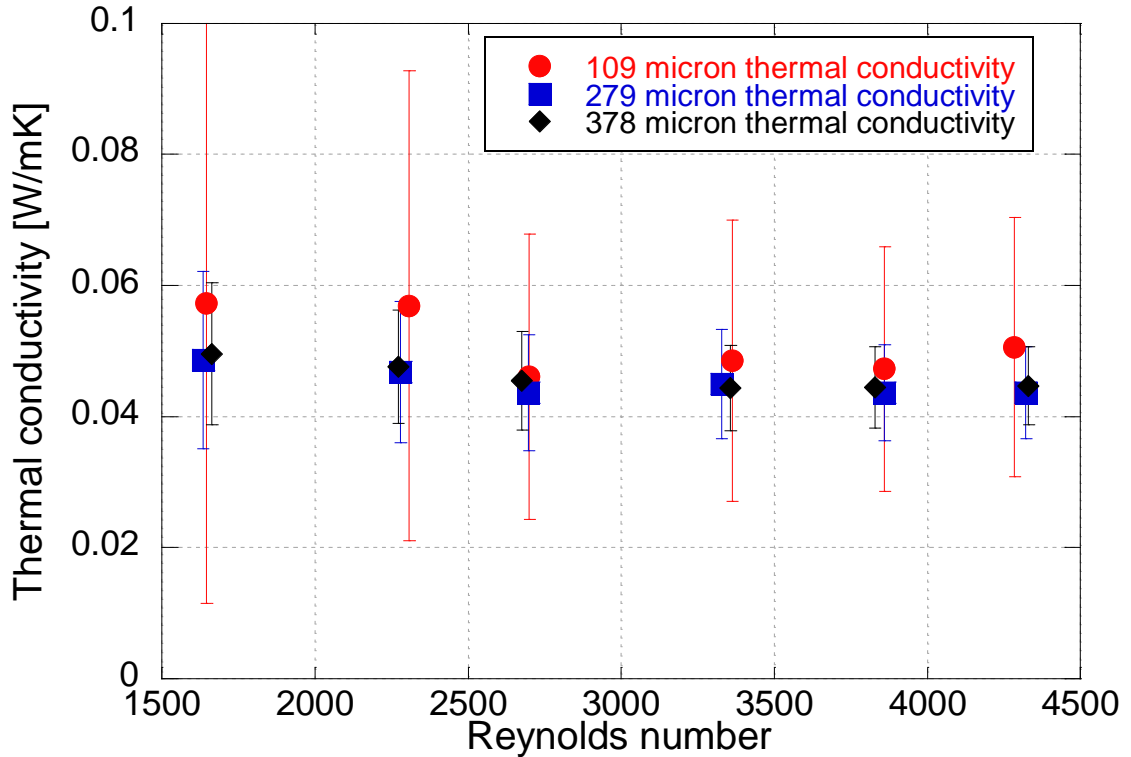


Figure 8.5: Thermal conductivity with maximum instrument uncertainty for 109, 279, and 378 micron thick deposit layers on heat flux probe 2

The maximum uncertainty represents the accuracy of the measurements and illustrates the potential to miscalculate the absolute value of the deposit thermal conductivity. At a 90% confidence interval, the deposit thermal conductivity may lie anywhere within this uncertainty band. This does not necessarily apply to the conductivity trends observed with surface temperature and volatile bake-out.

### 8.1.2 Precision

To determine the confidence in observed trends, the measurement precision needs to be considered and can be achieved by repeated measurements at similar Reynolds

number conditions. Repeated measurements were not recorded consecutively; the inlet flow rate and temperature was varied through the set points described in Chapter 5 and then the set was repeated. An example of this process is shown in Figure 8.6, which shows repeated interface temperature measurements on a 378 micron thick layer on heat flux probe 2. The precision uncertainty will be determined by the repeatability of each individual instrument measurement and then combined together to develop an overall conductivity precision uncertainty for each thickness interval. This process truly highlights the ability of the instruments to measure similar values after flow conditions change.

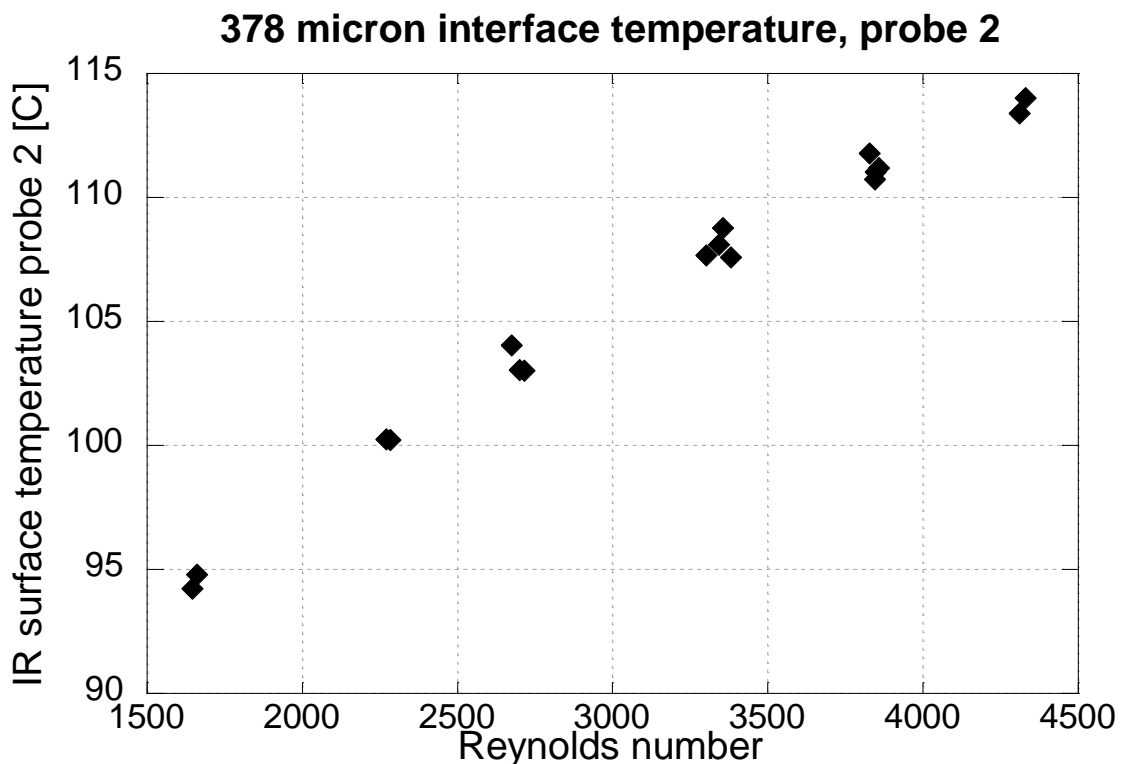


Figure 8.6: Precision of deposit interface temperature measurement on a 378 micron layer on heat flux probe 2

The precision uncertainty associated with the optical microscope in determining the thickness of the deposit layer varies with the thickness of the deposit. The uncertainty was established by performing multiple thickness measurements at various locations on the same thickness scratch on each heat flux probe and at different optical magnification

levels. The standard deviation of the mean deposit thickness for the multiple measurements is assumed to be the uncertainty associated with the measurement and is shown in Table 8.2 for the 24-hour interval and bake-out conditions.

Table 8.2: Optical microscope uncertainty at various experimental conditions

Experimental condition	Thickness measurement location	Standard deviation of mean [microns]
6 hour	Heat flux probe 1	1.75
	Heat flux probe 2	5.44
12 hour	Heat flux probe 1	5.41
	Heat flux probe 2	5.94
18 hour	Heat flux probe 1	11.24
	Heat flux probe 2	15.9
24 hour	Heat flux probe 1	21.4
	Heat flux probe 2	9.2
24 hour bake 1	Heat flux probe 1	23.0
	Heat flux probe 2	6.68
24 hour bake 2	Heat flux probe 1	18.5
	Heat flux probe 2	13.3

Incorporating the precision uncertainty from all the instruments yields Figure 8.7. The 6-hour, 109 micron layer exhibits large precision uncertainty, however the thicker layers are significantly more repeatable. While the accuracy uncertainty might yield different conductivity values, the precision uncertainty establishes confidence in the observed conductivity trends with Reynolds number and surface temperature as shown for the Reynolds number sweep on the 18-hour 279 micron layer in Figure 8.8. The same process is applied to the 24-hour bake-out data and is shown in Figure 8.9. The trends of diminishing conductivity are maintained as statistically significant, but only marginally for the pre-bake and bake 2 results.

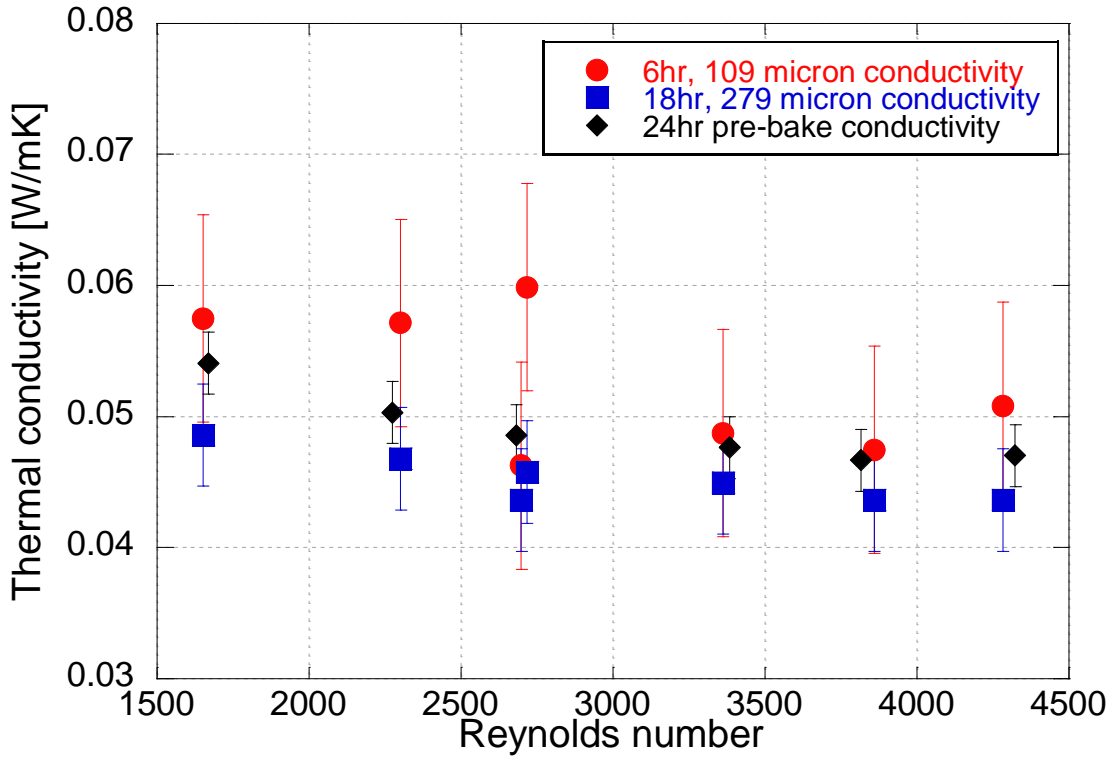


Figure 8.7: Precision uncertainty for the 6-hour 109 micron, 18-hour 279 micron, and 24-hour 378 micron layers on heat flux probe 2

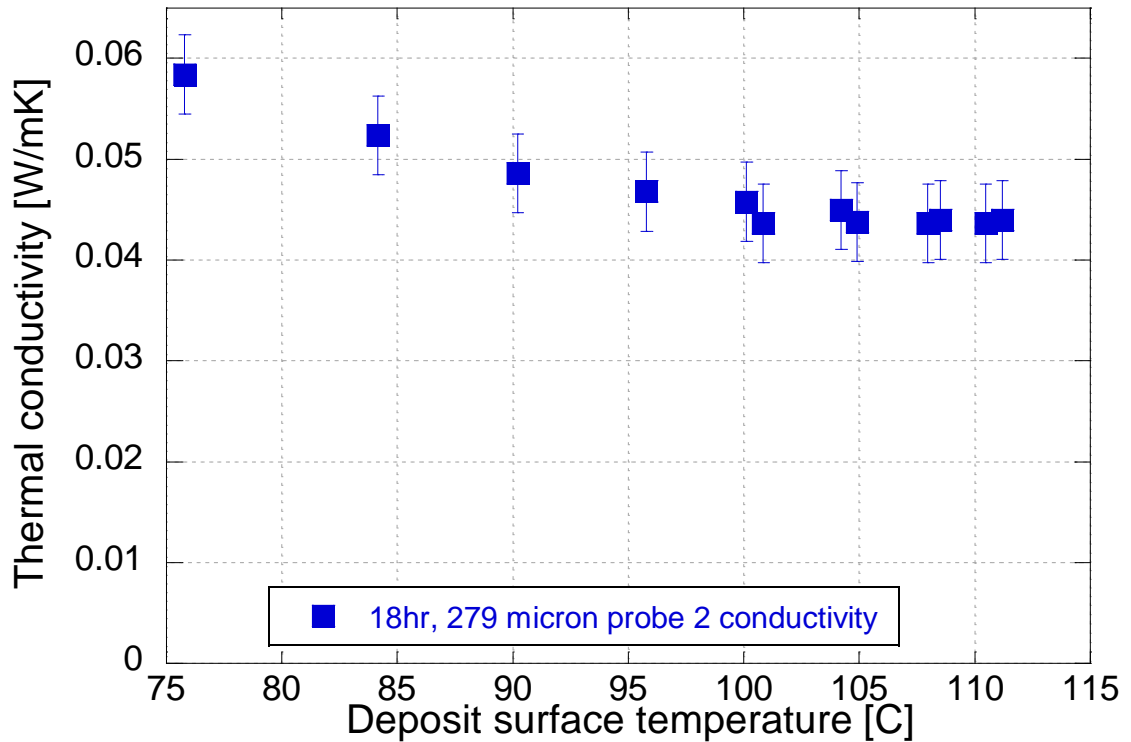


Figure 8.8: Precision uncertainty for thermal conductivity as a function of deposit surface temperature for the 18-hour, 279 micron layer on heat flux probe 2

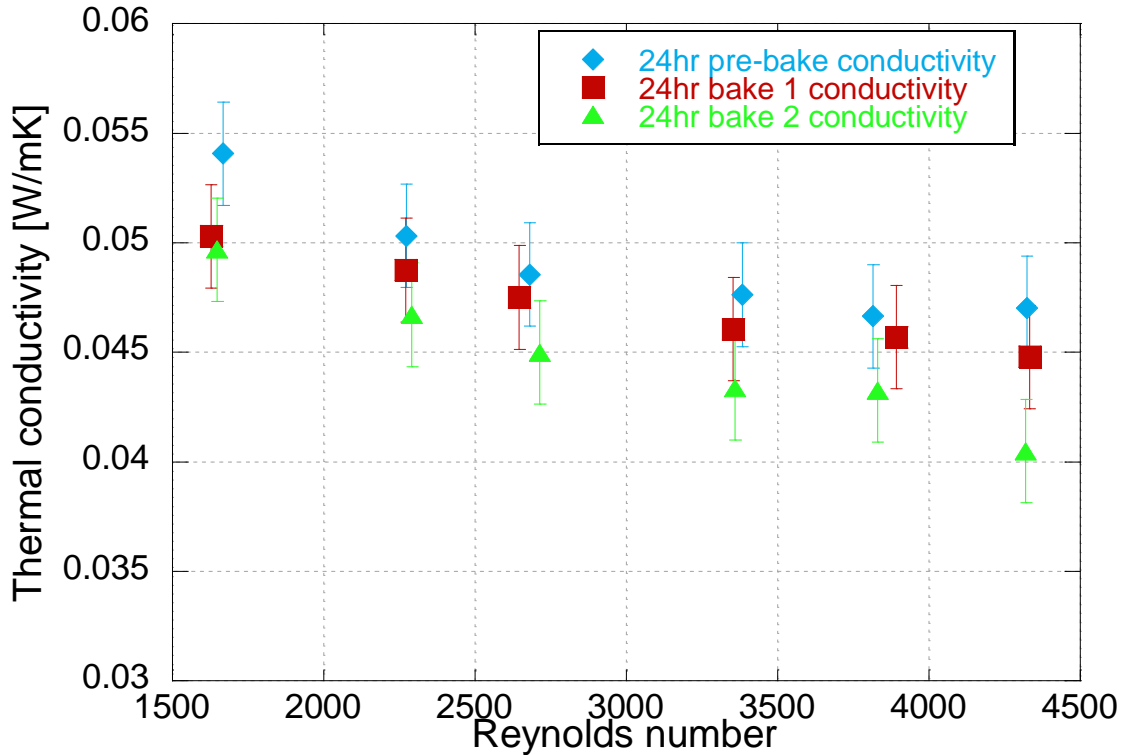


Figure 8.9: Thermal conductivity with precision uncertainty for the 24-hour bake-out layer on heat flux probe 2

### 8.1.3 Accuracy and precision uncertainty improvement

A few steps can be taken to increase the accuracy associated with the in-situ methodology. The most critical improvement is to increase the reliability of the measurement of the temperature difference across the deposit layer thickness. This can be achieved by:

1. Improving the accuracy of the temperature measurement device
2. Flowing hotter gas through the rig
3. Developing a thicker layer

Selecting higher accuracy instrumentation will assist in minimizing the total uncertainty of the measurement. It is, however, difficult to find production thermocouples and infrared cameras that offer such accuracy at a reasonable cost.

Flowing hotter gas through the rig increases the surface temperature of the deposit and the temperature difference across the layer. While this does serve to decrease the uncertainty associated with temperature measurement, caution needs to be observed not to exceed operational temperature limits of the heat flux probes or increase gas flow velocity to the point of velocity shear.

Finally, developing a thicker layer for measurement will also decrease uncertainty in the measurement. As the layer grows, the temperature difference across it increases due to the insulative properties of the deposit. This is a reliable method to reduce uncertainty, however it produces large errors at thinner layers. Thus, initially developing thin layers are more difficult to measure reliably.

## **8.2 Experimental error reduction**

### **8.2.1 Infrared camera**

Due to the porosity of the deposit layer, variations in the surface temperature were recorded as shown in Chapter 6. It is possible that if still infrared images of the layer were taken, the temperature of the layer could be measured to be higher/lower depending on the airflow. In essence, a high or low deposit temperature could be measured.

To resolve this issue, 5 second videos acquired at 25 Hz were recorded for each data point. The subsequent 125 frames were then averaged together to generate a representative deposit surface temperature. The 24-hour, 378 micron layer on heat flux probe 2 at 200°C inlet and 5.66 kg/hr airflow ( $Re = 3356$ ) is chosen as an example point. Figure 8.10 illustrates a potential peak-to-valley temperature difference of 0.97°C.

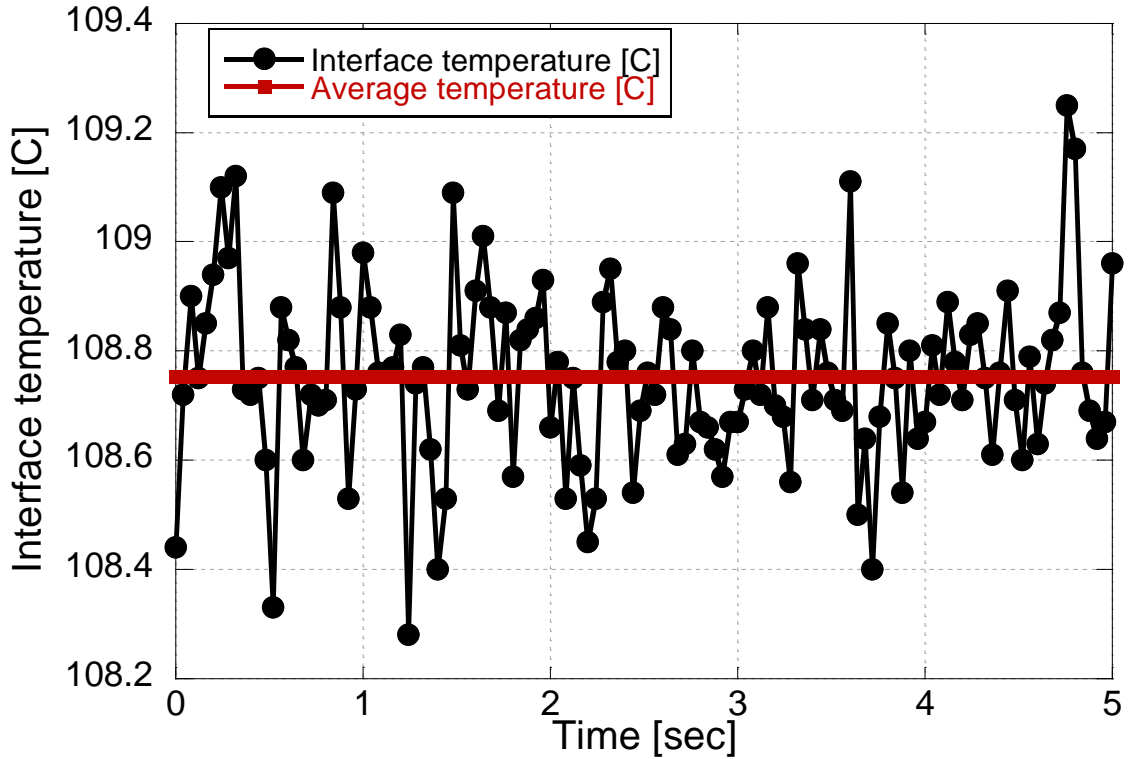


Figure 8.10: Interface temperature variation on a 378 micron thick layer using 5 second infrared video at 25 Hz

This temperature difference would manifest itself differently according to the thickness of the layer, but for this condition it translates to a maximum conductivity of 0.0453 W/mK and a minimum conductivity of 0.0433 W/mK, with a nominal conductivity of 0.0443 W/mK. This is approximately  $\pm 2.5\%$  of the nominal value, and a spread of 0.002 W/mK from the maximum to minimum conductivity values. This thermal conductivity variation is illustrated in Figure 8.11 as a function of Reynolds number.

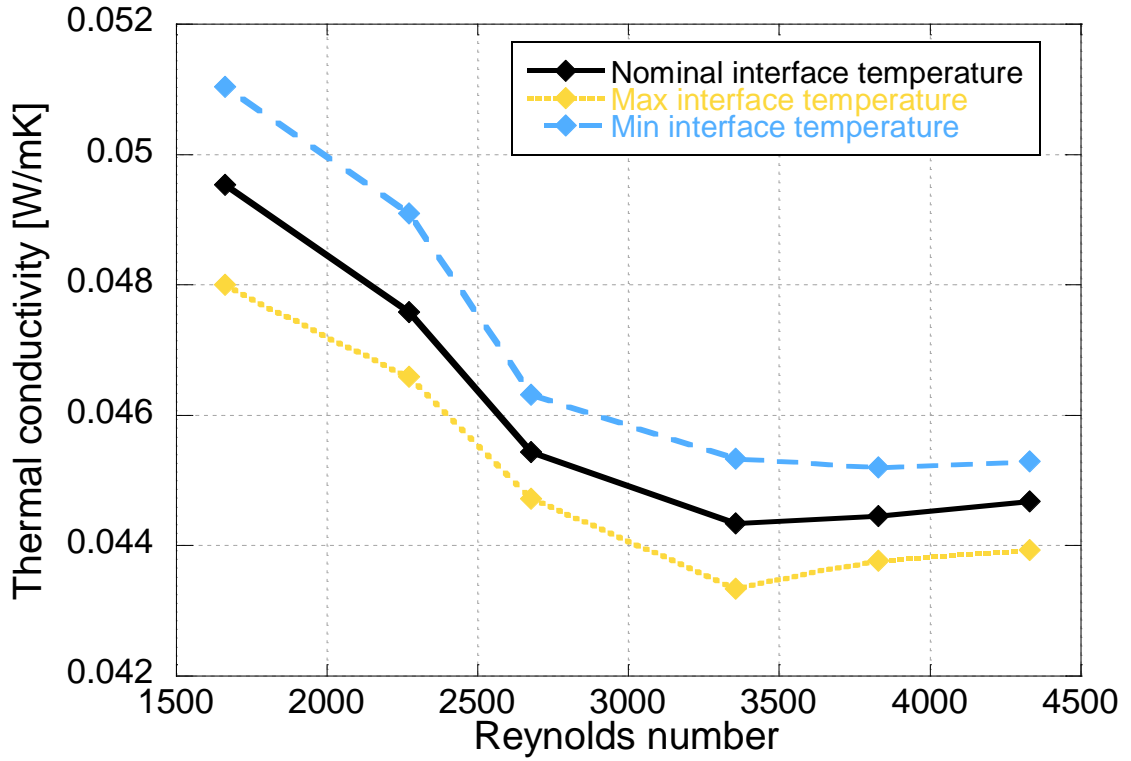


Figure 8.11: Variation of thermal conductivity due to temperature variations for the 378 micron thick layer on heat flux probe 2

The temperature variation and average temperature is shown in Figure 8.12 at the same condition for the 109 micron layer (200°C, 5.66 kg/hr, Re = 3360).



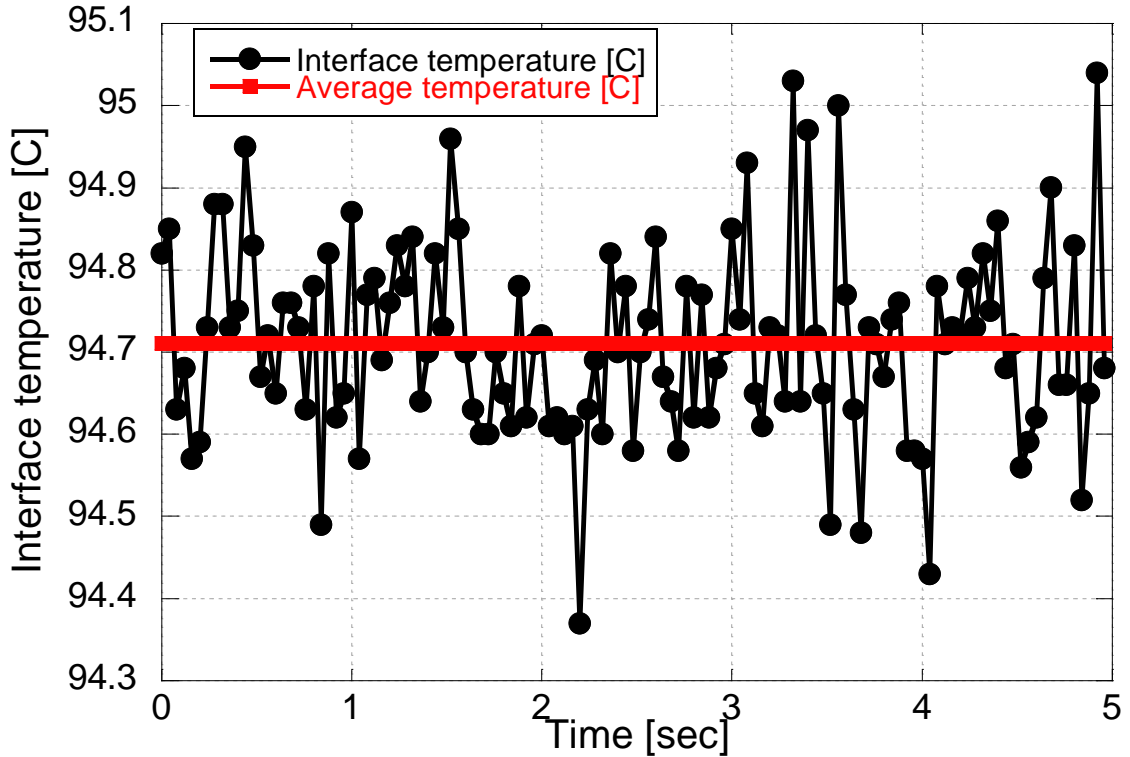


Figure 8.12: Interface temperature variation on a 109 micron thick layer using a 5 second infrared video at 25 Hz

Although the spread from the maximum and minimum temperature is only  $0.67^{\circ}\text{C}$ , the error increases to approximately  $\pm 5\%$  of the nominal conductivity value (nominal  $0.0485 \text{ W/mK}$ , max  $0.0510 \text{ W/mK}$ , min  $0.0463 \text{ W/mK}$ ). This signifies a difference of  $0.0047 \text{ W/mK}$  from the maximum to minimum conductivity values. The increase in error is due to the sensitivity of thermal conductivity to the measured temperature difference at thin deposit layers. The error in conductivity due to varying temperature is shown in Figure 8.13. By using the video averaging technique instead of still images, the potential source of error from still images is eliminated.

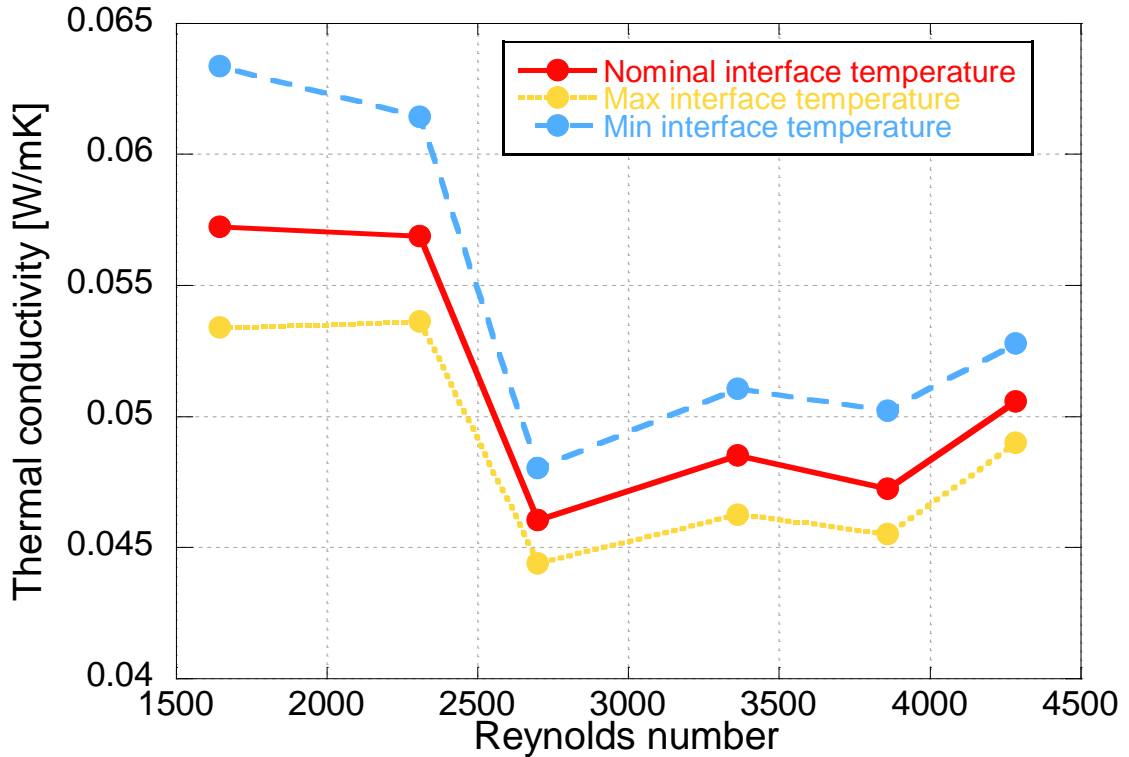


Figure 8.13: Variation of thermal conductivity due to temperature variations for the 109 micron thick layer on heat flux probe 2

### 8.2.2 Optical microscope

Imaging dark carbonaceous layers is a difficult process. Lighting is instrumental in highlighting the features of the deposit layer, as well as allowing the microscope to focus for thickness measurements. As microscope magnification increases, the less light is acquired making high magnification measurements difficult. It is, however, the higher magnification settings that make more accurate thickness measurements.

To increase the ability of the microscope to make such measurements, lighting is introduced at an angle creating shadows in the deposit layer. The enhanced lighting allows the microscope to detect surface features and the shadows add a depth perspective to the image. The effect of side lighting is shown in Figure 8.14.

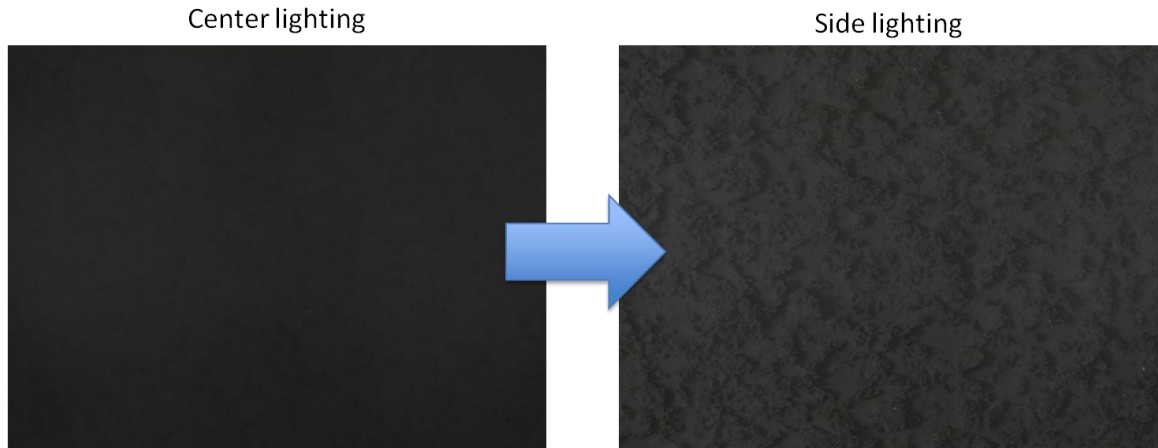


Figure 8.14: Effect of side lighting compared to center lighting on a deposit layer

### 8.2.3 Heat flux measurement

#### Surface mounted thermocouples

Initially, the heat flux through the deposit layer was to be determined by measuring the temperature difference across the stainless steel substrate and utilizing the 1-D heat conduction in Equation 8.1. To measure the temperature of the substrate, K-type thermocouple wire leads were silver epoxied to the surface. Silver epoxy was selected to electrically conduct voltage signals between the thermocouple leads. By locating the wire leads close together, the contact between the wires and the metal surface can be assumed to be at similar temperatures. Since the wires and metal are at similar temperatures, the electromotive force (EMF) will be a function of the temperature of the dissimilar thermocouple metals contacting the metal surface, and thus will measure the metal temperature. This is proven by calculating the EMF for the schematic shown in Figure 8.15, illustrating the aforementioned scenario.

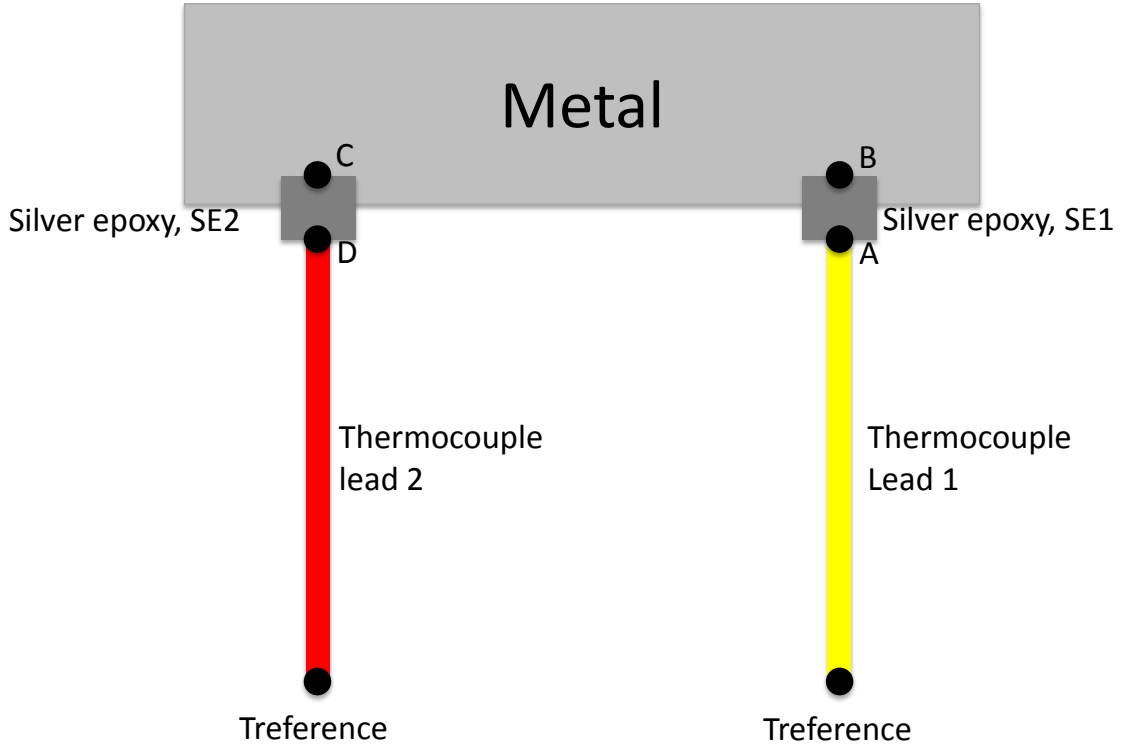


Figure 8.15: Schematic of surface mounted thermocouple

The net EMF is a function of temperature and is calculated from nodal point to nodal point. The net EMF is:

$$\begin{aligned}
 EMF_{net} = & EMF_{Lead1}(T_A) - EMF_{Lead1}(T_{Reference}) + EMF_{SE1}(T_B) - EMF_{SE1}(T_A) \\
 & + EMF_{Metal}(T_C) - EMF_{Metal}(T_B) + EMF_{SE2}(T_D) - EMF_{SE2}(T_C) \\
 & + EMF_{Lead2}(T_{Reference}) - EMF_{Lead2}(T_D)
 \end{aligned}$$

Equation 8.3: Net EMF for surface mounted thermocouple

In order to measure the temperature of the metal, the following conditions must be true:  $T_A = T_B$ ,  $T_C = T_D$ , and  $T_B = T_C$ . The net EMF then becomes:

$$\begin{aligned}
EMF_{net} &= EMF_{Lead1}(T_A) - EMF_{Lead1}(T_{Reference}) + EMF_{Lead2}(T_{Reference}) \\
&\quad - EMF_{Lead2}(T_D) \\
&= EMF_{Lead1}(T_{Metal}) - EMF_{Lead1}(T_{Reference}) + EMF_{Lead2}(T_{Reference}) \\
&\quad - EMF_{Lead2}(T_{Metal})
\end{aligned}$$

Equation 8.4: Net EMF to determine metal temperature

An experimental image of this configuration is shown in Figure 8.16, where the thermocouple is attached to the exhaust side of the metal substrate. A surface mounted thermocouple was also attached to the coolant side of the substrate. To verify the accuracy of this temperature measurement, a stick-on contact thermocouple was placed next to the surface mounted thermocouple (as shown in Figure 8.17). Hot coolant was then flowed beneath the metal, warming up the metal through conduction. After a brief amount of time, hot air was then introduced on the exhaust side. Figure 8.18 shows that the exhaust surface mounted thermocouple measured temperature as accurately as the stick-on thermocouple during the conduction heating (hot coolant only, time range 0-1900 seconds). When hot air was introduced (at 1900 seconds), the stick-on thermocouple deviated significantly from the surface mounted measurement due to the presence of convection. Since the stick-on thermocouple has a pre-made junction between the two dissimilar metals, the surrounding metal and convective air influenced its temperature measurement.

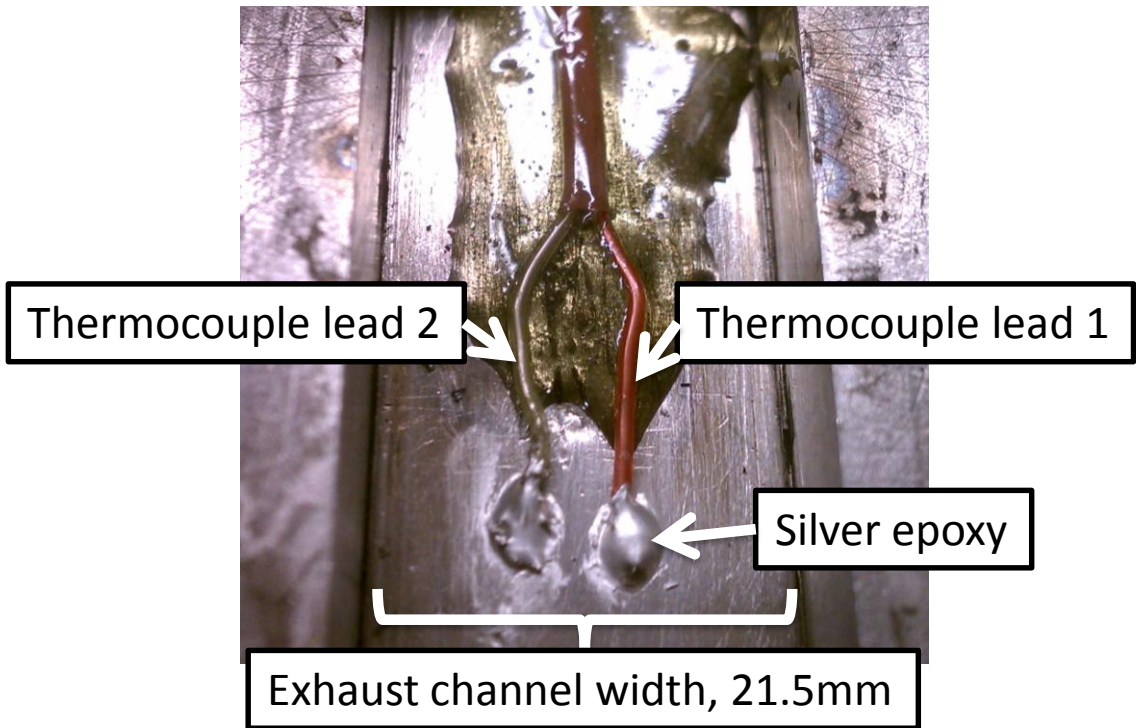


Figure 8.16: Experimental implementation of surface mounted thermocouple

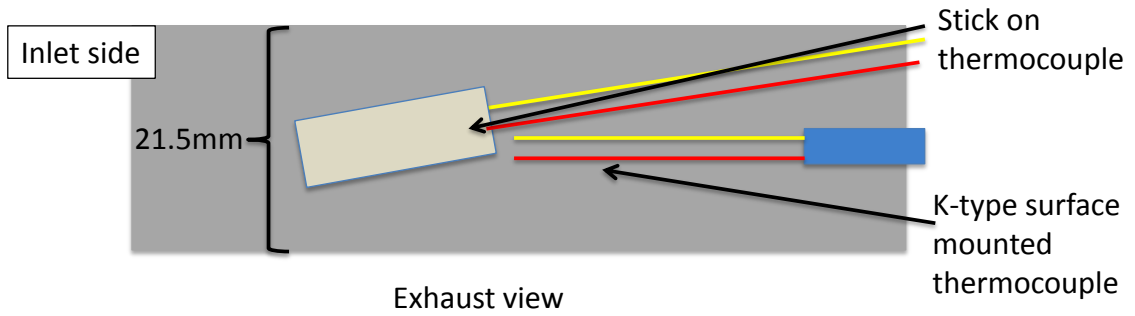


Figure 8.17: Exhaust side stick-on and surface mounted thermocouple schematic

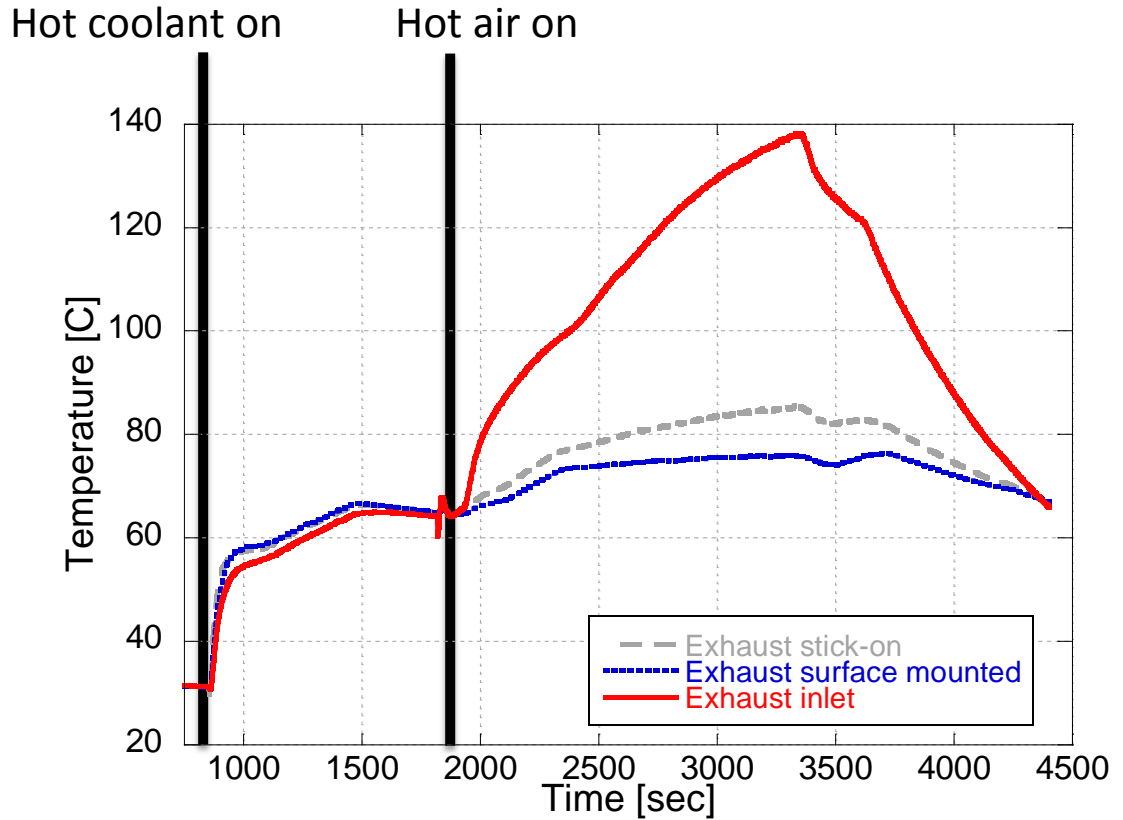


Figure 8.18: Exhaust side surface mounted, stick-on, and inlet temperature measurements

Temperature was measured on the coolant side with a surface mounted thermocouple as well as an exposed tip K-type thermocouple measuring the temperature of the coolant at the surface mounted location. Results in Figure 8.19 show that the surface mounted thermocouple measured temperatures similar to the exposed tip thermocouple during the hot coolant condition. The surface mounted thermocouple then detected an increase in the metal temperature when hot air was introduced on the other side of the substrate. When the hot air was turned off, the surface mounted thermocouple approached the same temperature recorded by the exposed tip thermocouple.

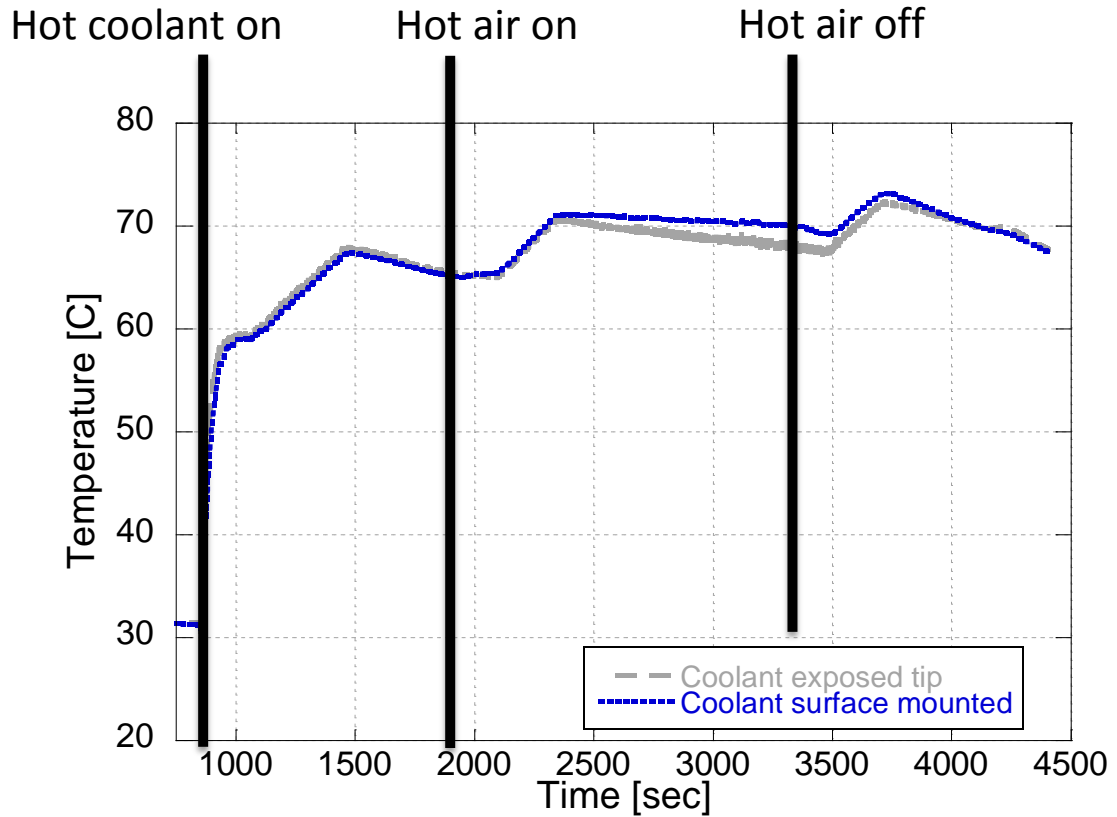


Figure 8.19: Surface mounted versus exposed tip thermocouple on coolant side

Both surface mounted thermocouples appear to be capable of measuring temperature accurately, and more accurately than a stick-on thermocouple when convection is present. Coupling the surface mounted thermocouple temperature information with the thermal conductivity and thickness of the stainless steel substrate (14.6 W/mK, 1mm respectively), the heat flux is calculated and is shown in Figure 8.20. The peak calculated heat flux was roughly  $8.5E4 \text{ W/m}^2$ .



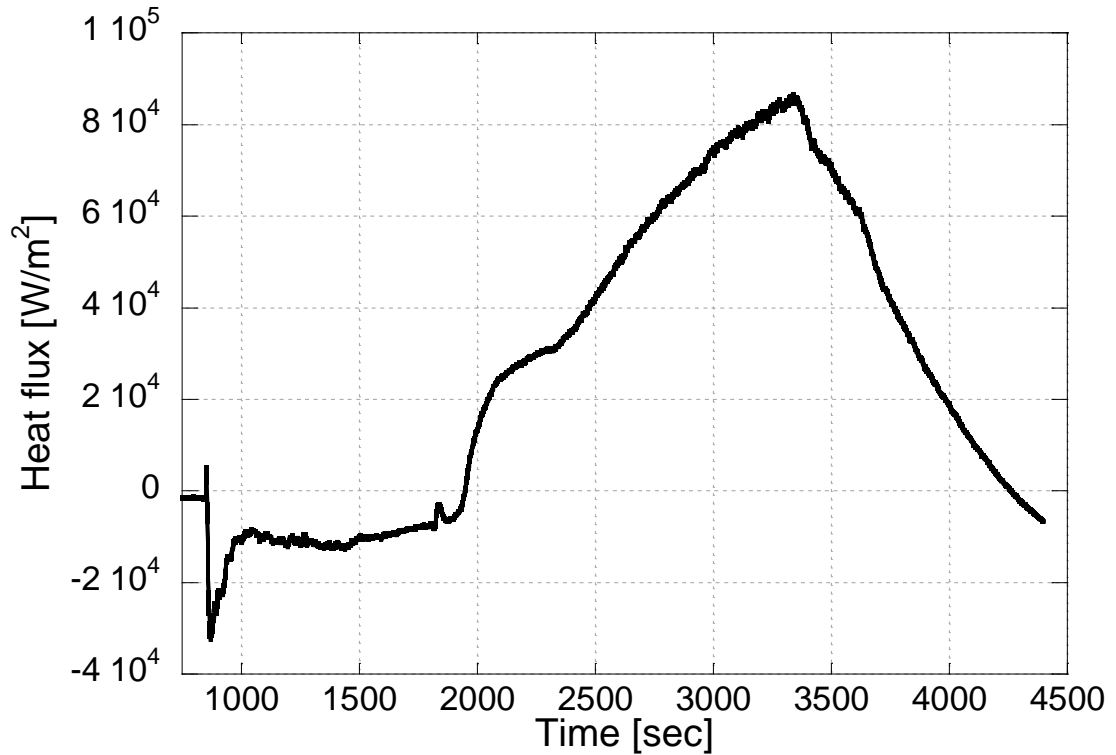


Figure 8.20: Calculated heat flux across a 1mm thick stainless steel substrate with a thermal conductivity of 14.6 W/mK and using the surface mounted thermocouple temperatures

An energy analysis of the hot airflow shows that the maximum possible heat flux is much lower than the measured heat flux, resulting in greater than an order of magnitude difference:

$$E = \dot{m}C_p\Delta T$$

$$E = (4.54 \text{ kg/hr}) \times (1.026 \text{ KJ/kgK}|_{\text{Air at } 200^\circ\text{C}}) \times (200^\circ\text{C} - 70^\circ\text{C})$$

$$E = 168.2\text{W}$$

$$\text{Area of channel} = 2 \times 21.5\text{mm} \times 280\text{mm} + 2 \times 12\text{mm} \times 280\text{mm} = 0.01876\text{m}^2$$

$$\text{Maximum heat flux} = \frac{E}{\text{Area of channel}} = 8965 \text{ W/m}^2$$

Equation 8.5: Maximum theoretical heat flux from hot air to channel surface

It is apparent that these thermocouples are still influenced by convection and therefore cannot be used to determine heat flux through the substrate.

### Heat flux probe

A heat flux probe was selected to measure the heat flux through the layer (Concept Engineering, specifications in Chapter 2). The probe was placed on the coolant side of the channel to observe the operational temperature range of the instrument. The addition of the probe increases the total thermal resistance of the channel and can alter the development of the deposit on the exhaust side. The low thermal conductivity of the probe (0.31 W/mK) resulted in an 84x increase in thermal resistance for the probe compared to the stainless steel. Assuming strictly conduction and ignoring convection and area, the resistance calculation is shown here and illustrated in Figure 8.21:

$$\begin{aligned}
 R_{Conduction\ total} &= \sum \frac{L}{kA} = \frac{L}{kA} \Big|_{Stainless\ steel} + \frac{L}{kA} \Big|_{Heat\ flux\ probe} \\
 R_{Conduction\ total} &= \frac{0.001[m]}{14.6 \left[ \frac{W}{mK} \right]} \Big|_{Stainless\ steel} + \frac{0.018[m]}{0.31 \left[ \frac{W}{mK} \right]} \Big|_{Heat\ flux\ probe} \\
 &= 6.85E - 5 \left[ \frac{m^2K}{W} \right] \Big|_{Stainless\ steel} + 0.0057 \left[ \frac{m^2K}{W} \right] \Big|_{Heat\ flux\ probe}
 \end{aligned}$$

Equation 8.6: Thermal resistance contribution of heat flux probe

Where L is the thickness, k is the thermal conductivity, and A is the area of the material.

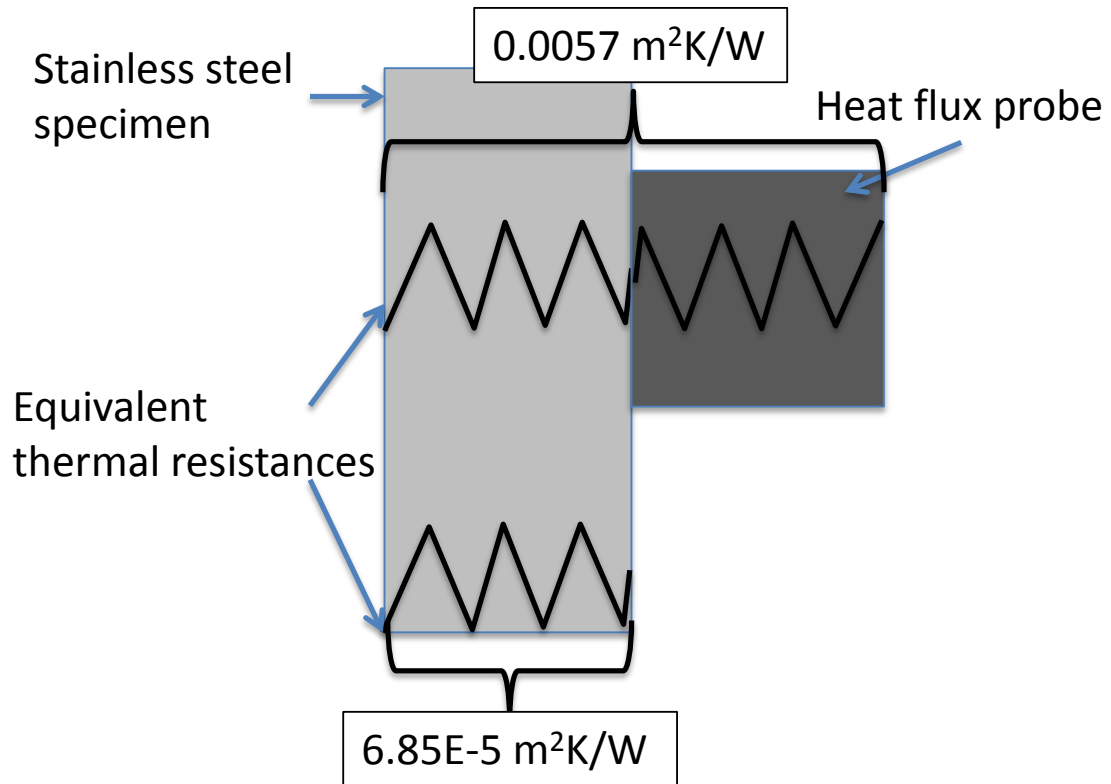


Figure 8.21: Thermal resistance schematic

Therefore, placing the heat flux probe on the coolant side would add a significant conduction resistance to the stainless steel and will create a “hot spot” on the exhaust side of the channel. The increased resistance indirectly creates a thinner deposit layer on the surface over the probe in addition to reducing the heat flux. Accounting for this inequality accurately on the exhaust side is difficult and would require significant simplifying assumptions, further contributing to the uncertainty of the in-situ conductivity measurement. Therefore, the heat flux probe is placed on the exhaust side of the channel so that the increased thermal resistance of the probe directly affects the deposit thickness and the probe directly measures the heat flux through that deposit layer. This scenario reduces the error associated with the probe since no simplifying assumptions are required and measurements of the layer properties can be made directly on the probe.

### Coolant temperature control

A thermostatic water heater was employed to keep the coolant temperature within a set temperature band. The thermostatic operation of the coolant heater created a saw tooth pattern in the coolant temperature, as illustrated in Figure 8.22. This saw tooth pattern also created fluctuations in the measured heat flux. This is due to the slow transient temperature response of the heat flux probe as well as a varying  $\Delta T$  from the exhaust stream to the coolant.

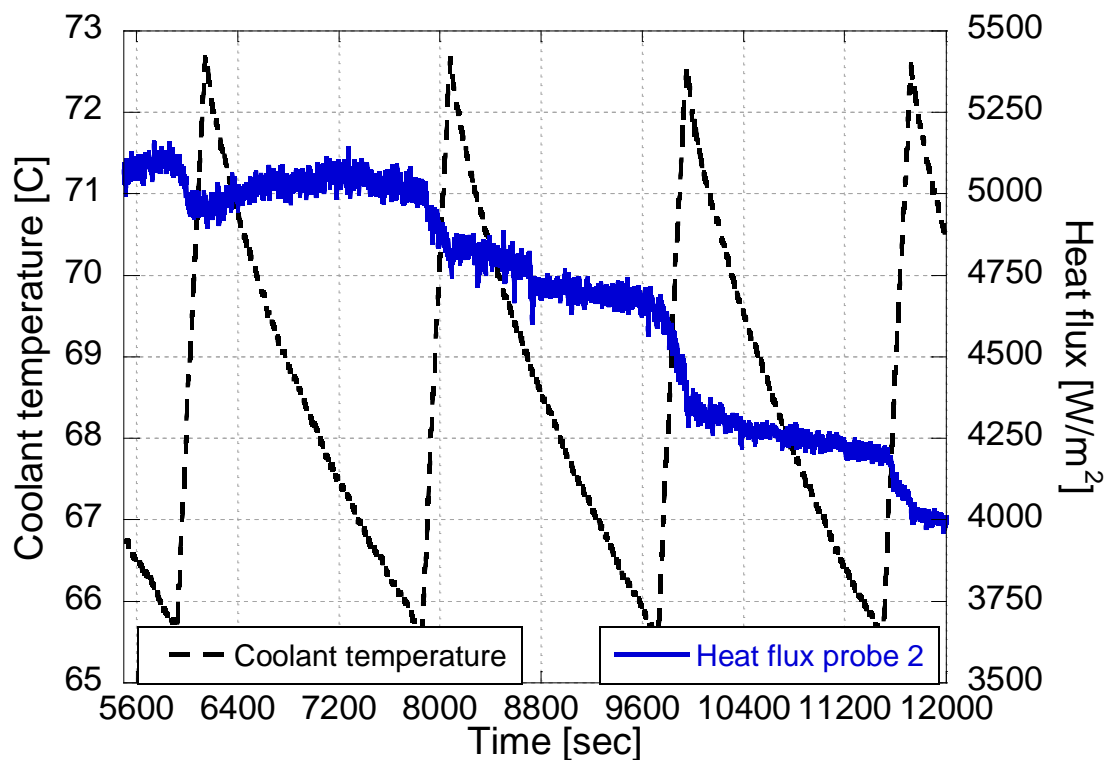


Figure 8.22: Thermostatic coolant heater influence on coolant temperature and measured heat flux

Assuming lumped system analysis is applicable (temperature of the probe is constant and changes uniformly with direction,  $T=f(T)$  not  $T=f(T, x, y, z)$ ) and that the probe is being heated from one side only (the coolant side), the response time to achieve 99% of the final temperature is determined:

$$\text{Energy transfer into body} = \text{Energy increase in body}$$

$$\text{Energy transfer via convection} = hA(T_{\infty} - T)dt$$

$$\text{Energy increase in body} = mC_p dT$$

$$hA(T_{\infty} - T)dt = mC_p dT$$

$$\frac{dT}{hA} = \frac{dT}{mC_p}$$

$$\frac{dT}{mC_p} = \frac{d(T - T_{\infty})}{-(T - T_{\infty})}$$

$$\text{Integrate } t = 0, T = T_i \text{ to } T = T(t)$$

$$\frac{T(t) - T_{\infty}}{T_i - T_{\infty}} = e^{-\frac{hA}{mC_p}t} = e^{-\frac{h}{\rho C_p * \text{probethickness}}t}$$

Equation 8.7: Transient thermal response calculation of heat flux probe

Assuming the probe thickness to be 0.002 m, probe Cp to be 700 J/kgK, probe density to be 968 kg/m<sup>3</sup>, and the convective heat transfer h to be 50 W/m<sup>2</sup>K, the response time to 99% of the final temperature is 124.8 seconds, or ~2 minutes.

To eliminate this thermal inertia effect and heat flux error, the inlet coolant line was supplemented with a PID controlled heat tape and maintained a constant inlet coolant temperature and is shown in Figure 8.23. The negative slope in both curves is due to a thickening deposit layer and a gradual reduction in the exhaust flow rate due to filter clogging.

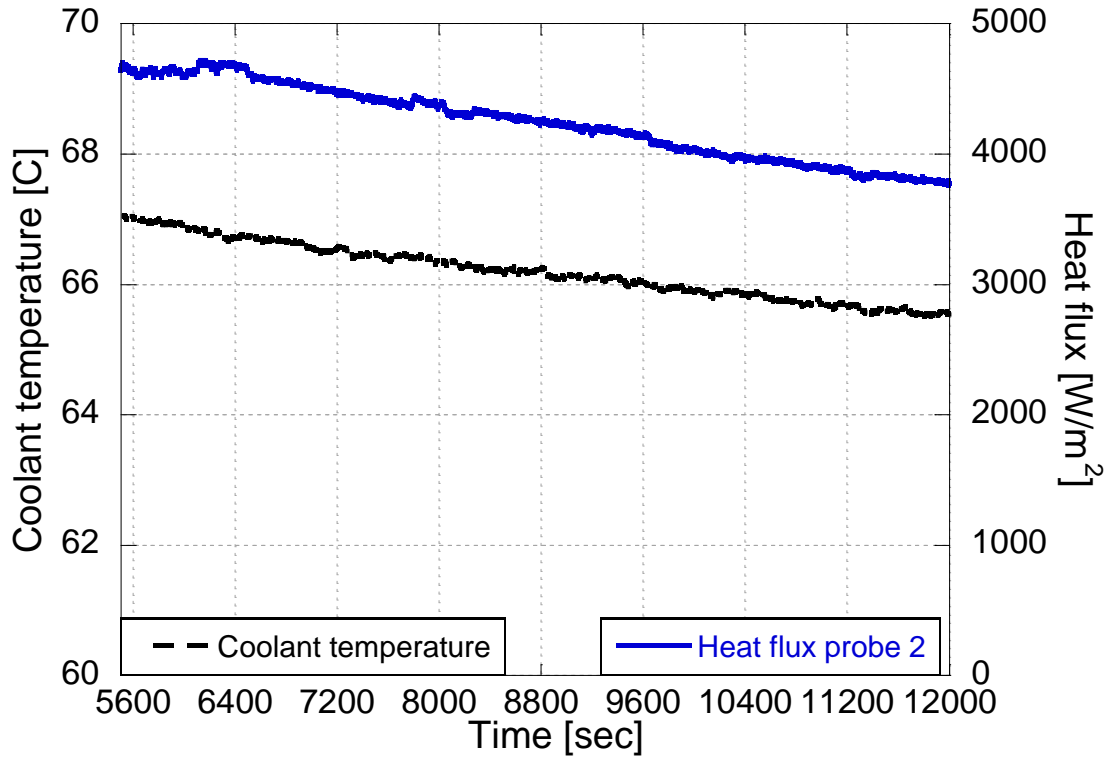


Figure 8.23: PID controlled coolant temperature

### 8.3 Conclusion

The uncertainty analysis indicates that the in-situ methodology improves in accuracy with a thicker deposit layer and a larger temperature differential across the layer thickness. At a Reynolds number of approximately 4300, the accuracy uncertainty for a 378 micron thick layer was approximately  $\pm 0.06$  W/mK. The dominant source of error is due to the accuracy uncertainty of the infrared and wall temperature measurement. At thin layers, the uncertainty due to the temperature measurements was an order of magnitude higher than the heat flux and thickness uncertainty. As the deposit layer increased in thickness, the uncertainty associated with the temperature measurements approached the values of uncertainty due to the heat flux and thickness instruments.

The precision uncertainty was determined by repeating similar inlet condition flows and measuring the repeatability of the instruments. The uncertainty from all of the instruments from the repeated points was combined to determine the precision

uncertainty. The results indicate confidence in the trends of deposit thermal conductivity with surface temperature and volatile composition.

## CHAPTER 9

### CONCLUSIONS, CONTRIBUTIONS, AND FUTURE WORK

A novel in-situ methodology was developed to better understand the thermo-physical properties of a deposit layer comprised of particulates and volatiles. A visualization rig was constructed with visual and infrared access to a deposit layer developed in a simulated exhaust gas recirculation heat exchanger. Using 1-D conduction, the thermal conductivity of the deposit layer was calculated at evolving deposit thicknesses and at varying deposit volatile fractions. The in-situ calculation was enabled by an optical microscope, an infrared camera, and a heat flux probe.

Insights were also developed into experimental deposit layer removal mechanisms using the visualization rig. Key parameters were identified for maximum heat exchanger recovery and recommendations for in-application recovery were suggested.

This chapter serves to summarize the conclusions and contributions of the in-situ research methodology and findings. In addition, suggestions for future work are presented.

#### **9.1 Summary of conclusions**

##### **9.1.1 In-situ measurement accuracy**

The novel in-situ measurement was developed to refine estimates of the thermal properties of deposit layers formed in exhaust gas recirculation heat exchangers. The



predominant source of accuracy uncertainty in the technique stems from the temperature measurement uncertainty of +/- 2% of the measured value for both the infrared and wall temperatures. This source of uncertainty makes conductivity measurements at thin deposit thicknesses unreliable. The accuracy uncertainty highlights the inability to determine the actual thermal conductivity of the deposit, however provides a range of values the conductivity could be as a result of instrument uncertainty.

Accuracy uncertainty can be reduced with thicker deposit layers and larger temperature gradients across the thickness of the deposit. Both of these parameters minimize the impact of the temperature uncertainty on the overall conductivity calculation. In addition, higher accuracy temperature instruments will reduce the accuracy uncertainty.

The precision uncertainty determined the in-situ measurement can be repeated and the trends in thermal conductivity with surface temperature and volatile fraction are statistically significant.

#### 9.1.2 Deposit conductivity with thickness

The in-situ thermal conductivity measurement suffers from large uncertainty with thin deposits, however becomes more accurate with thicker layers. Results indicate that the thermal conductivity does not change significantly as the deposit thickness grew over 24 hours to 379 microns. This conclusion is expected since the volatile composition of the deposit has most likely stabilized by this thickness interval. Unfortunately, due to the large uncertainty associated with the temperature measurements, the nascent layer where volatiles may play a larger role cannot be measured accurately.

### 9.1.3 Deposit conductivity with surface temperature

Deposit conductivity was calculated to change with the deposit surface temperature. At lower surface temperatures, the thermal conductivity of the solid fraction of the deposit layer is dominant. As deposit temperature increases, the conductivity reduces and approaches an inflection point where the thermal conductivity of the air becomes the dominant influence. This trade-off is due to the high porosity of the deposit layer and differing conductivity trends for the solid deposit and air filled voids of the layer. Confidence in this trend was established with a Reynolds number flow sweep at a thick deposit layer to minimize the uncertainty associated with the measurement. Results indicate a maximum spread of 0.0147 W/mK, or 33% of the minimum conductivity.

This conclusion highlights the fact that the thermal conductivity of the deposit is not a constant value and varies with temperature.

### 9.1.4 Volatile influence on deposit conductivity

The influence of volatiles on deposit thermal conductivity was determined by flowing hot air over the layer and baking out the low-end volatile fraction. Results indicate that the absence of low-end volatiles, as confirmed from a TGA, lowers the deposit thermal conductivity. The volatiles increase the deposit thermal conductivity due to the volatiles increased ability to conduct heat. By baking out the layer, the volatiles evaporate and are replaced by air and result in a lower apparent thermal conductivity.

The addition of liquid alcohol collapsed the structure of the deposit layer. The resulting layer was significantly thinner than the porous structure and constituted a significant recovery in terms of heat flux through the remaining deposit layer. Due to an extremely thin deposit, the thermal conductivity could not be established. However, it is expected to be similar to solid carbon (1.6 W/mK) due to the high carbon content of deposits.

#### 9.1.5 In-situ conductivity compared to previous results

The in-situ thermal conductivity differs from previously reported values. The incorporation of hotter ambient surrounding temperatures coupled with the influence of volatiles in the deposit results in a higher deposit thermal conductivity compared to ex-situ methods. More importantly, the in-situ methodology highlights the dependence of thermal conductivity on temperature. This has not been previously experimentally measured for deposits.

#### 9.1.6 Deposit surface area

Optical measurements of the deposit surface produced a very topographical surface. 3-D measurements of the layer enabled the calculation of deposit surface area and showed an increasing surface area with deposit thickness. Calculations and model results suggest a potential to increase the overall heat exchanger effectiveness directly with the increase in surface area. The increase in surface area may result in a 20% increase in effectiveness when compared to models assuming a flat deposit layer. Currently, deposition models do not account for an increase in deposit surface area and potentially introduce errors in the convective heat transfer coefficient and estimates of heat flux.

#### 9.1.7 Deposit porosity

Evidence of deposit porosity is apparent from infrared temperature measurements. Estimates of porosity were generated by comparing the experimental deposit thermal conductivity to that of the conductivity of an estimated porous graphite layer. Results indicate an approximate porosity of 98% for the deposit layer. However, due to the increase in conductivity with decreasing surface temperature, the deposit conductivity behaves like a lower porosity layer.

### 9.1.8 Velocity based removal

Deposit removal was achieved with flow transient events. The most significant velocity only removal was experienced with the introduction of high pressure flow into a quiescent channel. The lack of an established boundary layer in the quiescent channel pre-transient exposes the deposit surface to high shear forces from high gas velocities during the transient event. In addition, turbulence from entrance effects and expansion of flow into the channel increases the shear on the deposit surface. This strategy achieved approximately 30% deposit layer removal to bare metal.

Combining a flow transient with engine exhaust condensation produced approximately 50% deposit removal. The condensation of water from the exhaust stream is encouraged with low coolant temperatures. The water vapor permeates through the deposit layer and condenses on the cold metal substrate. This breaks up and lifts the layer from the substrate. When condensation is coupled with a mild flow transient, the deposit is easily removed from the channel.

## **9.2 Summary of contributions**

This work developed a novel in-situ methodology to non-destructively measure the evolution of deposit layers in a simulated exhaust gas recirculation heat exchanger. Previous methods to measure deposit properties were performed ex-situ and used destructive or discontinuous techniques. A unique heat exchanger with optical and infrared access to a deposit layer was constructed and visualized the growth of a deposit layer in-situ.

A novel in-situ measurement was developed and quantified the thermo-physical properties of an evolving deposit layer. Results indicate that surface area, deposit volatile fraction, and deposit temperature are significant to deposit heat transfer. These

parameters are typically not accounted for in heat exchanger models, which may lead to erroneous model predictions.

Key strategies were identified for successful heat exchanger effectiveness recovery. Thinning of the deposit thickness produced an increase in deposit heat transfer and subsequently increased the heat exchanger effectiveness. A collapse of the deposit porosity also resulted in a significant increase in deposit heat transfer.

This work developed a methodology to determine more representative in-situ thermal properties of deposit layers. Establishment of this method and considerations for its limitations allows for identification of exhaust/heat exchanger parameters critical to heat exchanger effectiveness.

### **9.3 Recommendations for future work**

The development of a novel in-situ methodology enables numerous subsequent investigations and experiments. Recommended topics include the following:

#### **9.3.1 Porosity measurement**

Insights into the physical structure of the deposit can be developed by analyzing the porosity of the deposit. Porosity is estimated to be a significant factor in the apparent thermal conductivity of the deposit and therefore needs to be quantified. Tracking deposit porosity with deposit thickness can develop insights into layer compaction with layer evolution. Layer compaction and subsequent increase in thermal conductivity could help explain the long-term stabilization of heat exchangers.

Simple extractable coupons can be installed downstream of the heat flux probes in the rig. During deposition, a deposit layer will form on these coupons. Using an XRD or SAXS instrument, porosity can be determined.

### 9.3.2 Impact of hydrocarbons on the thermal properties of deposit layers

An immediate evolution to the work presented in this thesis is to vary the hydrocarbon concentration in the exhaust stream and measure its impact on deposit properties. Efforts to dope the exhaust stream with heavy-end hydrocarbons resulted in poor vaporization and were unsuccessful in reliably boosting the hydrocarbon content of the exhaust stream. A redesigned hydrocarbon injector with sufficient heating may aid the vaporization of the heavy-end hydrocarbons, however it is recommended to use a medium weight hydrocarbon, perhaps C15, which will vaporize more easily. In addition, the hydrocarbon concentration in the exhaust stream can be increased by changing the engine operating condition. An additional post-injection later into the expansion stroke will directly increase the unburned hydrocarbon emissions from the engine, and will therefore increase the hydrocarbon concentration in the visualization rig.

Measurements quantifying the increase in hydrocarbon upstream of the simulated heat exchanger will be required to verify an actual increase in concentration. Subsequently, measurements downstream of the rig will also be required to verify hydrocarbon condensation in the simulated cooler. Thermogravimetric measurements of the deposit will also verify an increase in volatile composition of the deposit.

In combination with the porosity measurement in 9.3.1, the impact of hydrocarbons on the porosity of the deposit can be determined. It is expected that higher hydrocarbons should reduce the porosity of the deposit and change the structure of the layer.

### 9.3.3 Full factorial experiment

Using the newly developed in-situ methodology, a full factorial experiment can be conducted to identify important variables on deposit conductivity. Sweeps of coolant temperature, PM levels, HC levels, NO<sub>x</sub> levels, exhaust temperature, exhaust flow rates,

etc. can be performed and the thermo-physical properties of the deposit measured. This factorial can be used to determine heavy/light fouling conditions and help develop strategies to mitigate heat exchanger fouling in production applications.

#### 9.3.4 Longer term exposure

The maximum deposition exposure presented in this thesis was 24 hours. Longer-term exposures may shed light onto heat exchanger stabilization phenomena. The large cross sectional area of the visualization rig makes comparison to actual EGR coolers difficult due to geometrical differences. While this does not necessarily affect the deposit thermal properties, it does affect the manner in which the deposit grows. The typical asymptotic deposit growth seen in actual EGR coolers is not seen in the rig and it is hypothesized that if deposition continued for a significantly longer time, this asymptotic behavior will be apparent. The point at which deposit growth slows down is where deposit layers show signs of stabilization. The in-situ methodology can be used to measure the thermo-physical properties of a stabilized layer and to investigate any potential differences compared to an evolving layer.

#### 9.3.5 Reduced cross sectional area

Inserts may be added to the visualization rig to reduce the cross sectional area of the channel. With a reduced channel area, deposit stabilization should be more likely and the in-situ methodology can be applied to determine the properties of a stabilized layer. These measurements should be combined with porosity and hydrocarbon speciation to fully understand the thermal properties of the deposit.

### 9.3.6 Live deposition

Previous attempts to monitor the deposition process in real time resulted in the fouling of the infrared window. Methods to prevent window fouling resulted in thermal stress and fracture of the window. An air pocket design was investigated to keep the window clean using a curtain of air (schematic in Figure 9.1). The design worked with limited success however created back flow of cold air into the channel, as illustrated by the sudden drop in deposit temperature in Figure 9.2. A physical separation between the window and the channel with the use of a pneumatically actuated gate valve should provide the means to monitor deposition on a time-lapse basis. In addition, the window can be removed for cleaning while the gate valve is closed further extending the deposition time interval without requiring the experiment to shut down. Live monitoring of the interface temperature and optical profile on the layer will provide understanding of how the surface temperature and surface area evolves with deposit thickness.

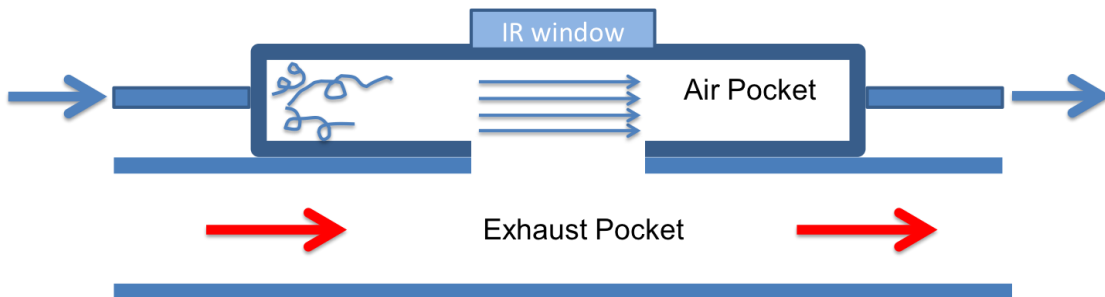


Figure 9.1: Air pocket design



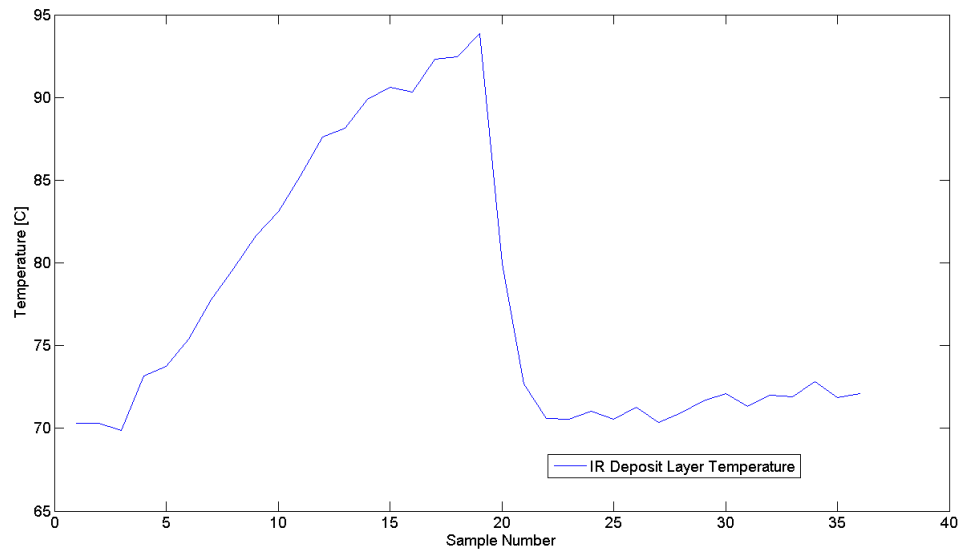


Figure 9.2: Live interface temperature

### 9.3.7 In-situ thickness measurement

The current in-situ methodology requires the removal of the infrared window for a scratch to be made in the deposit layer for thickness measurement. Developing the ability to measure deposit thickness without removing the window, such as with a remote deposit scraper, and enable deposit layer properties to be determined during deposition. This will shorten the time required for heat flux and optical measurements as described in this work.

Additionally, the ability to measure thickness without scratching the deposit surface will further enable longer-term deposition experiments. Currently, scratching the layer creates an area of altered deposit and limits the use of that area for future property measurement. A scratch is required to define a zero level for thickness measurements. Previous attempts to define a known height and measure the thickness relative to that, as shown in Figure 9.3, have proved difficult. The fixed height reference invariably moves due to thermal expansion or convection and changes the reference location. Another system for non-contact thickness measurement should be pursued.

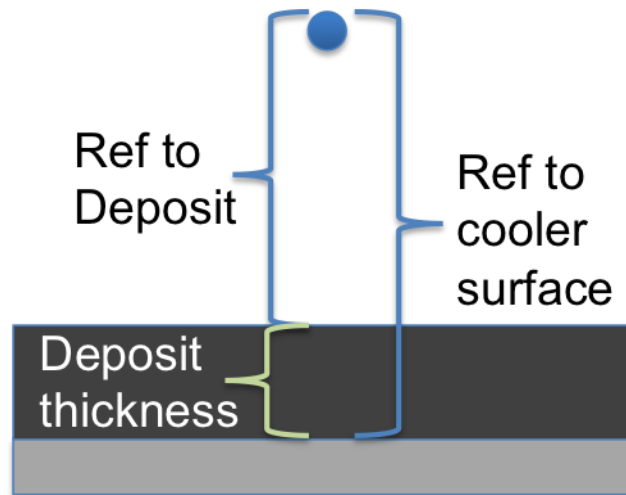


Figure 9.3: Top down fixed reference point thickness measurement

### 9.3.8 Flow geometry

The influence of the flow angle of attack was clearly seen in Chapter 7. Turbulence features in production EGR coolers attempt to exploit wavy fins or vortex features to minimize the development of a fouling layer. Surface features can be easily designed and installed into the visualization rig. The optical access from rig can determine which features are most successful at preventing a fouling layer. In addition, the in-situ methodology can determine the thermal properties of a layer formed, for example, on an incline surface. Combined with porosity measurements, the impact of layer compaction from impinging flow on the properties of the deposit can be determined.

### 9.3.9 Alternative fuels

A significant body of work exists discussing the impact of alternative fuels on engine combustion and emissions. Alternative fuels have a wide variety of physical and chemical properties and changes in these properties may affect the composition of the exhaust. For example, the lower volatility of biodiesel can produce a nucleation mode consisting of condensed hydrocarbons in the exhaust particle stream. As these fuels

become more popular, their impact on deposit formation must be addressed in order to determine potential problems with EGR cooler fouling.

## APPENDIX A

### A.1 MATLAB script for microscope image processing and surface area

```
clc;
clear all;
filename='HF2 left edge top.csv';    %enter name of image file in CSV format
outputfilename=filename(1:end-4);
M=csvread(char(filename));
Image=M(1:end-3,1:end-3);
contourf(Image,50);
saveas(gcf,char(outputfilename),'fig')
```

```
croppedrow_begin=input('Enter where you want to start image cropping on
vertical axis (min is 1):');
```

```
croppedrow_end=input('Enter where you want to end image cropping on vertical
axis (max is -3 from figure):');
```

```
croppedcolumn_begin=input('Enter where you want to start image cropping on
horizontal axis (min is 1):');
```

```
croppedcolumn_end=input('Enter where you want to end image cropping on
horizontal axis (max is -3 from figure):');
```

```

        cropped_image=Image(croppedrow_begin:croppedrow_end,croppedcolumn_begi
n:croppedcolumn_end);

        averaged_rows=mean(cropped_image);
        standard_dev_rows=std(cropped_image);
        ave_std=mean(standard_dev_rows);
        std_std=std(standard_dev_rows);
        image_average=mean(averaged_rows);
        averaged_rows=averaged_rows';
        max_image=max(max(cropped_image));
        min_image=min(min(cropped_image));

        dx=1;          % x-axis calibration
        dy=1;          % y-axis calibration
        Z=cropped_image;

        [m, n] = size(Z);
        cropped_image_area=(m-1)*(n-1);

        %Determine surface area by breaking square into triangles and performing
        %absolute crossproduct of vector components from 3D coordinates
        areas = 0.5*sqrt((dx*dy)^2 + (dx*(Z(1:m-1,2:n) - Z(1:m-1,1:n-1))).^2 +
(dy*(Z(2:m,1:n-1) - Z(1:m-1,1:n-1))).^2) + 0.5*sqrt((dx*dy)^2 + (dx*(Z(1:m-1,2:n) -
Z(2:m,2:n))).^2 + (dy*(Z(2:m,1:n-1) - Z(2:m,2:n))).^2);

        surfaceArea = sum(areas(:));
        SA_difference_percentage=(surfaceArea/cropped_image_area)*100;

```

## A.2 Close up infrared lens

Table A.1: Close up infrared lens specifications

Part number	T198059
Field of view (FOV)	32 x 24 mm
Magnifying factor	2.9x
Working distance	84 mm
Depth of field	0.65 mm
Focal length	78 mm
Spatial resolution (IFOV)	50 microns

## A.3 Heat flux conditions

Table A.2: Standard heat flux conditions

	Air flow rate [kg/hr]	Inlet air temperature [C]	Reynolds number
Point 1	4.56	200	2700
Point 2	5.66	200	3360
Point 3	6.48	200	3860
Point 4	7.24	200	4300
Point 5	3.89	200	2300
Point 6	2.79	200	1650
Point 7	4.57	200	2710

Table A.3: Heat flux conditions for Reynolds number sweep at 18-hour interval

	Air flow rate [kg/hr]	Inlet air temperature [C]	Reynolds number
Point 1	4.56	200	2700
Point 2	5.66	200	3360
Point 3	6.48	200	3860
Point 4	7.24	200	4300
Point 5	3.89	200	2300
Point 6	2.79	200	1650
Point 7	4.57	200	2710
Point 8	1.96	200	1166
Point 9	0.99	200	586